Title
Modeling and Optimization of Spatially Evolving Heat Sinks Using Volume Averaging Theory

Author
Sbutega, Krsto

Publication Date
2015

Peer reviewed|Thesis/dissertation

University of California
Los Angeles

Modeling and Optimization of Spatially Evolving Heat Sinks Using Volume Averaging Theory

A dissertation submitted in partial satisfaction
of the requirements for the degree
Doctor of Philosophy in Mechanical Engineering

by

Krsto Sbutega

2015

Abstract of the Dissertation

Modeling and Optimization of Spatially Evolving Heat Sinks Using Volume Averaging Theory

by

Krsto Sbutega

Doctor of Philosophy in Mechanical Engineering

University of California, Los Angeles, 2015

Professor Ivan Catton, Chair

Today's society has developed an ever-increasing dependence on electronic components, making it a critical challenge to match the rising demand for size reduction and performance reliability with efficient cooling strategies. Heat sinks are still the most common form of heat rejecting devices used in electronic cooling, and it has been shown in recent years that heat sinks with variable geometry can lead to efficiency improvement. The geometrical complexity and multi-scale nature of heat sinks make their modeling a challenging, and often time consuming, task. Volume Averaging Theory (VAT) has been shown to be a valid alternative to standard modeling techniques because of its ability to obtain accurate predictions of system performance parameters with a significant reduction in computational time.

In this work, the theoretical fundamentals of VAT are examined in detail. Its mathematical fundamentals are discussed, and analogies with other averaging procedures are presented to illustrate the bases of the averaging process. The VAT transport equations are then derived and closed. The developed VAT model is applied to heat sinks with non-uniform geometry. Two numerical solution methods are applied to efficiently solve the resulting set of partial differential equations: a Galerkin method and a fractional step finite difference method. The fractional step method, based on Strang splitting, is used to address the coupling between the VAT solid and fluid energy conservation equations. In addition, a variable time-step approach is derived to accelerate the convergence to steady state. A new solution method, based on a spectral decomposition of the interface temperature and a quasi-Newton iteration

method, is also proposed to address the coupling between the homogenous base of the heat sink and the geometrically homogenized heat sink channel. Overall, the solution method provides a significant improvement in computational time over previously used methods.

To determine the limits of applicability of the VAT model for systems with non-uniform geometry, a scaling procedure is applied to the governing equations. Through physical and mathematical arguments, it is determined that the momentum equation limits the applicability of the model, and it is shown that three non-dimensional parameters, M_1, M_2 and M_3, can be used to provide estimates of these limits. For heat sinks with constant geometry, it is found that the solution is accurate when the boundaries of the system do not significantly affect the solution in the bulk, and the parameter M_1 provides a quantitative estimate of these effects. For heat sinks with geometry variations in the cross-flow direction, it is determined that the accuracy of the solution is determined by the magnitude of the gradients induced by porosity variation, which are quantified through a parameter M_2. Finally, for the case in which the geometry changes in the stream-wise direction, the VAT model is observed to be accurate when porosity variations do not affect local flow. This is quantified by a third parameter M_3, which it is found to be Reynolds number dependent. In all three cases, it was shown that for low values of these parameters the VAT model is very accurate for a wide range of porosities, Reynolds numbers, geometries, and material combinations.

The vast improvement in computational speed, along with the defined limits, is exploited to carry a series of optimization studies to determine the effects of the added geometric degrees of freedom of the system on its performance. A Genetic Algorithm is employed to determine optimal solutions for entropy generation and thermal resistance for three types of micro-channel heat sink geometries: straight, trapezoidal, and converging (or diverging). It is found that although straight channels provide an optimal combination of pumping power and thermal resistance, the limited geometric degrees of freedom do not allow for efficient heat transfer improvement. It is determined that straight channels present no efficient means to improve heat transfer and, in order to reduce the thermal resistance of a straight channel heat sink by 20%, a 200% increase in pumping power is required. It is also concluded that trapezoidal channels do not provide significant advantages over straight channels for either

entropy generation or thermal resistance. On the contrary, an optimal converging channel configuration resulted in a 6% improvement in thermal resistance and a 23% decrease in pumping power, with respect to the thermally optimized straight channel. The results of the optimization studies are then combined to manually design a trapezoidal converging heat sink that features the same thermal performance of an optimal straight micro channel, but a 44% reduction in pumping power. Therefore, it is concluded that the added geometric degrees of freedom allow for a more efficient heat transfer improvement of the system.

The dissertation of Krsto Sbutega is approved.

Mladen Vučetić

Adrienne G. Lavine

Jeffrey D. Eldredge

Ivan Catton, Committee Chair

University of California, Los Angeles

2015

To my parents . . .

for not only giving me all the love that I could take,

but also the values that I live by.

Table of Contents

List of Figures

List of Tables

Nomenclature

α	Diffusivity
Δx	x direction grid spacing
Δz	z-direction grid spacing
$\dot{q}'''$	Volumetric Heat Generation
$\hat{}$	Scaled quantity
$\langle\rangle$	Superficial Average
$\mathbf{c}_f$	Skin Friction Drag Tensor
$\mathbf{c}_f$	Total Drag Tensor
$\mathbf{c}_{pd}$	Pressure Drag Tensor
$\mathbf{j}$	Flux
$\mathbf{K}$	Permeability
$\mathbf{n}$	Normal Vector
ν	Kinematic Viscosity
ν	Viscosity
Re	Reynold's Number
ψ	Arbitrary Function of Interest
ρ	Density
$\tilde{}$	Fluctuation Quantity
ε	Porosity

$_f$	Fluid phase
A_i	Interface Area within System
A_{fs}	Interface Area with a REV
C_b	Base aspect ratio
c_p	Specific Heat
C_x	x direction channel aspect ratio
C_z	z-direction channel aspect ratio
D	Diameter
D	Diameter
D_h	Standard hydraulic diameter
d_h	VAT-defined Hydraulic Diameter
$dotm$	Mass flow rate
F	Fluid energy equation scaling parameter
f_f	Fanning Friction Factor
g	Volumetric Generation
h	Heat Transfer Coefficient
H_c	Channel height
h_{REV}	REV height
k	Thermal Conductivity
K_1	Interface boundary conditions scaling parameter
L	Characteristic length scale of upper scale phenomena

L	Heat sink length scale
l	Characteristic length scale of lower scale phenomena
l_{Kol}	Komogorov Eddy Length Scale
l_{mfp}	Mean Free Path
L_{REV}	REV length
M	Momentum equation scaling parameter
N_c	Number of channels
Nu	Nusselt Number
p	Pressure
p_x	Longitudinal pitch
p_y	Transverse pitch
Pe	Peclet Number
q	Heat Flux
R	Radius
r_0	REV Length Scale
R_k	Porosity weighted thermal conductivity ratio
R_{th}	Thermal resistance
S	Solid equation scaling parameter
S_w	Specific Area with REV
T	Temperature
T_b	Temperature at bottom of base

t_b Base thickness

T_i Interface temperature

T_{in} Inlet temperature

U Average Velocity

u x direction velocity

V REV Volume

v Velocity

w z direction velocity

w_b Bottom width of trapezoidal micro-channel

w_c Channel width

w_c Non-dimensional width of non-uniform boxcar function

w_i Inlet width of converging (diverging) micro-channel

w_o Outlet width of converging (diverging) micro-channel

w_t Top width of trapezoidal micro-channel

x^* Non-dimensional thermal entry length

x_c Non-dimensional center of non-uniform boxcar function

$\langle\rangle^f$ Intrinisc Average over Fluid Phase

$\langle\rangle^s$ Intrinisc Average over Solid Phase

$\mathbf{k}_{f,disp}$ Dispersion Thermal Conductivity Tensor

$\mathbf{k}_{f,eff}$ Effective Thermal Conductivity Tensor

$\mathbf{k}_{f,stag}$ Stagnation Thermal Conductivity Tensor

$\dot{S}_{gen}$ Entropy generation

HSF Hot Spot Factor

PP Pumping Power

Acknowledgments

My wife Stacey, for loving, supporting and caring for me through these wonderful years, and for spending hours reviewing my publications.

My parents and my sisters, for letting me pursue my dreams, for always pushing me to be better while showing me unconditional love.

Manga, for sharing the best years of his life with me and giving me some of the best memories. Striko Branko for the love he gave me, the confidence he had in me and for encouraging me to always aim to the top.

Professor Catton, for believing in me, for being a great academic advisor and supporting me through these years. But most of all for the love, friendship and support that he provided in every other aspect of my life.

Susie Catton, for the love she showed me and the way she cared for me.

Blake Wellen, Milovan Radanovich, Adam Krikorian and Matt Armato, and for their effort in helping me to come to UCLA as an undergraduate water polo player. It is safe to say that I would not be where I am today if it wasnt for their vision, help and effort.

My Committee members, Professors Lavine, Eldredge, and Vucetic, for supporting and helpfully guiding me academically, professionally, and personally. Also, there are a number of other UCLA MAE faculty members who have made significant contributions towards cultivating my academic development during my ten years at the school.

Fellow students with whom I worked for their friendship and academic support. In par-

ticular, Mike Stubblebine, Jake Supowit, George DeMoulin, David Geb, Feng Zhou, Sean Reilly, Aanish Sikora, Angelo Lerro. Also, the staff in the Mechanical and Aerospace Engineering Department for their friendliness and support.

Lastly, the support of the Kerze-Cheyovich endowment, established by the late Prof. Novak Zuber, is gratefully acknowledged.

Vita

1999-2004	Diploma di Maturità, L.S.S A. Righi, Rome
2004–2009	Bachelor of Science, Mechanical Engineering, Henri Samueli School of Engineering and Applied Sciences, University of California, Los Angeles, California.
2010–2012	Masters of Science, Mechanical Engineering, Henri Samueli School of Engineering and Applied Sciences, University of California, Los Angeles, California.
2011	Teaching Assistant, MAE 133AL Thermodynamics Laboratory, Henri Samueli School of Engineering and Applied Sciences, University of California, Los Angeles, California.
2014	Teaching Assistant, MAE 136 Energy and Environment, Henri Samueli School of Engineering and Applied Sciences, University of California, Los Angeles, California.

Publications

Krsto Sbutega, David Geb and Ivan Catton, Modeling of Multi-scale Heat Transfer Systems using Volume Averaging Theory, *Advances in Heat Transfer*, 2015

Krsto Sbutega, and Ivan Catton, Galerkin Method Solution of Volume Averaged Model for Efficient Conjugate Heat Transfer Analysis, *Numerical Heat Transfer Journal: Part B*, 2015

Krsto Sbutega, and Ivan Catton, Analysis of Conjugate Heat Transfer in Micro-channels with non-uniform heat flux, *ASME-ATI-UIT 2015 Conference on Thermal Energy Systems: Production, Storage, Utilization and the Environment*, 17 - 20 May, 2015, Napoli, Italy

David Geb, Angelo Lerro, **Krsto Sbutega**, and Ivan Catton, Internal Transport Coefficient Measurements in Random Fiber Matrix Heat Exchangers, *Journal of Thermal Science and Engineering Applications*, 6(1):011005, 2014

Krsto Sbutega, and Ivan Catton, Efficient Hydraulic and Thermal Analysis of Heat Sinks using Volume Averaging Theory and Galerkin Methods, *Multiphase Science and Technology*, 25(2-4), 2013

Krsto Sbutega, and Ivan Catton, Application of Fourier-Galerkin Method to Volume Averaging Theory Based Model of Heat Sinks, *ASME 2013 International Mechanical Engineering Congress and Exposition*, 2013

Angelo Lerro, David Geb, **Krsto Sbutega**, and Ivan Catton, A Single Blow Transient Test Technique With Volume Averaging Theory Modeling for Random Fiber Matrices, *ASME 2012 Heat Transfer Summer Conference collocated with the ASME 2012 Fluids Engineering Division Summer Meeting and the ASME 2012 10th International Conference on Nanochannels, Microchannels, and Minichannels*, 595-600, 2012

David Geb, **Krsto Sbutega**, and Ivan Catton, A New Technique for Measuring Convective Heat Transfer Coefficients in Solid Matrices for Compact Heat Exchanger Design, *ASME 2012 Heat Transfer Summer Conference collocated with the ASME 2012 Fluids Engineering Division Summer Meeting and the ASME 2012 10th International Conference on Nanochannels, Microchannels, and Minichannels*, 35-41, 2012

CHAPTER 1

Introduction

Electronic devices nowadays are not only an important part of our personal lives, but also a vital element in arguably every aspect of our society. The ever expanding use of computers, along with the advent and galloping advancement of hand held devices, has opened new doors in the field of communication, data storage, data management, and virtually any other technological or scientific field. It is estimated that by 2019, there will be approximately 10 billion devices containing integrated circuits in the world [1] (see Figure 1.1).

However, our society's dependency on integrated circuits makes their reliability and proper

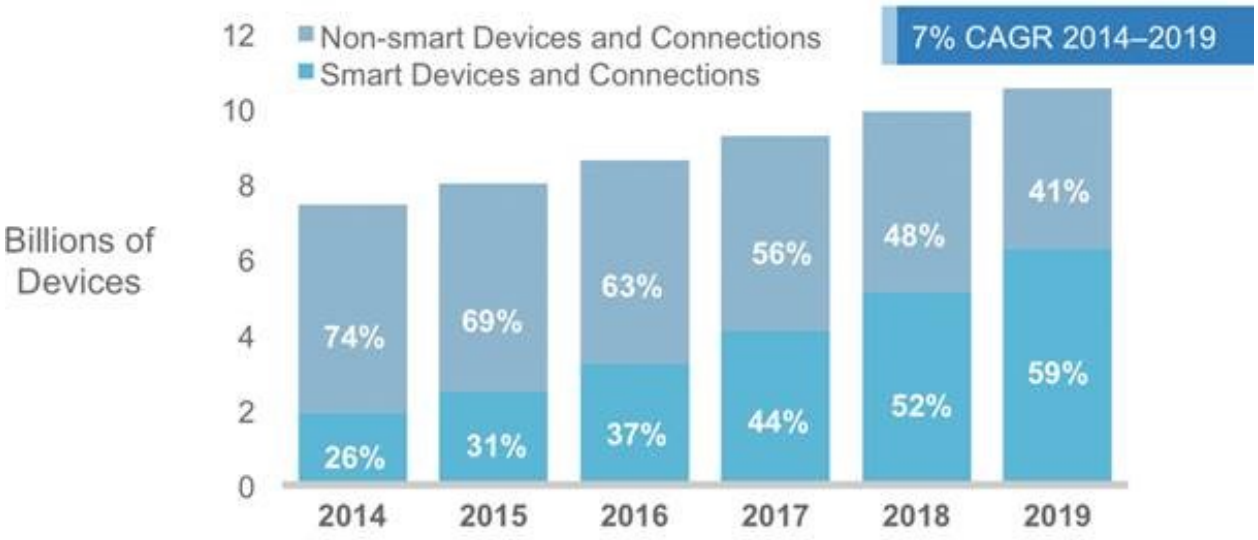

Figure 1.1: Predicted Global Growth of Smart Mobile Devices and Connections [1]

functioning a critical subject. Since computers are present in disparate applications in our everyday lives from entertainment systems to life supporting systems, gaming to missile defense, and economic activities to medical databases it can be easily understood why a failure in an electronic component can lead to severe and possibly life threatening scenarios.

Therefore, reliability of electronic devices is a key aspect in the present, and especially future, of our society.

Inter-diffusion, corrosion and electro-migration are the leading causes of degradation of reliability in electronics, and they all have thermally-activated components. Thus, as shown in Figure 1.2, the rate of reliability increases exponentially with decreasing temperature and an improvement in cooling devices. Furthermore, lower operating temperatures lead to reduc-

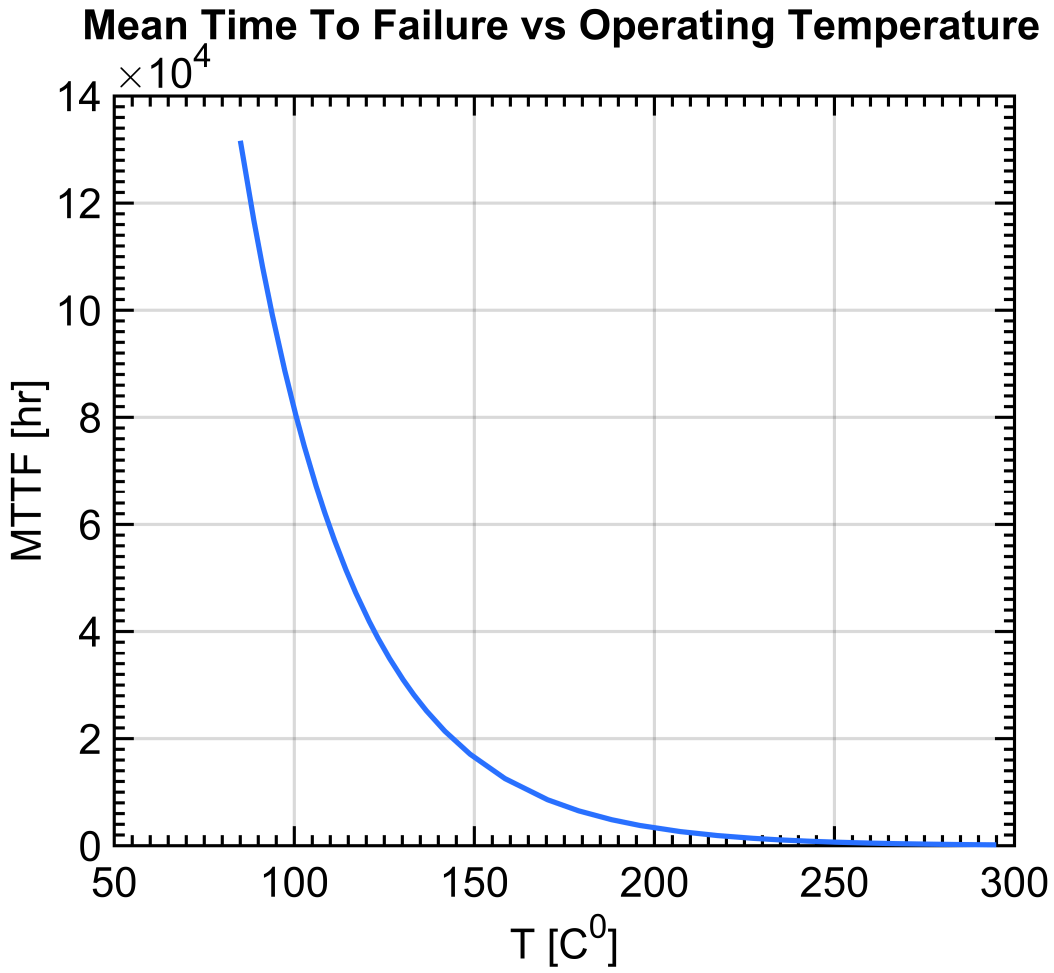

Figure 1.2: Predicted Mean Time To Failure (MTTF) vs Operating Temperature of a Typical Electronic Component [2]

tion in current leakage, therefore enhanced cooling solutions also improve chip performance. CMOS chip technology shows a 2% improvement in speed for every 10^0C reduction in chip temperature. Figure 1.3 shows the effect of operating temperature on a standard benchmark

performance test (Linpack score) as a function of the CPU operating temperature. The

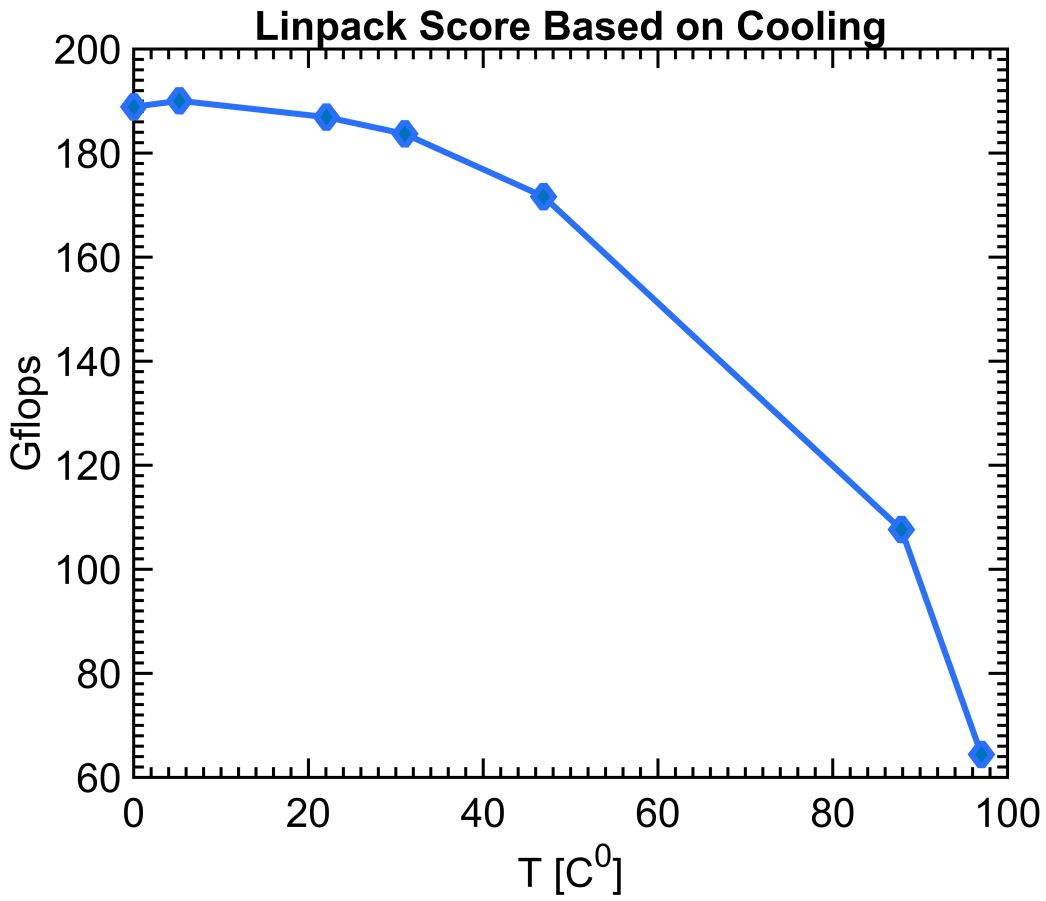

Figure 1.3: Linpack Score Based on Operating Temperature [3]

degradation in performance is clear, with about 70% degradation in performance when the CPU operates constantly above a temperature of 99^0C. These facts emphasize the importance of thermal management in electronic systems. Improved heat removal systems are further required because of the continuous increase of power density in microprocessors, as dictated by the infamous Moores law. At the same time, the need for reduction in weight and size of electronic components is reducing the space available and the choice of materials that can be employed for heat dissipation.

The increase in power density leads directly to an increase in chip heat flux as shown by Figure 1.4. We can see that by 2018, the predictions show that chips will need to dissipate as much as $190^{W}/_{cm^2}$. Since most electronic equipment needs to be maintained in a range

of $60 - 100^0C$, the need for very efficient heat exchangers is critical.

In the early stages of electronic cooling, the components were cooled by natural convection directly from the PCB. As the power density increases, heat sinks were added on top of the CPU (which is the most heat productive component) but natural convection was still the cooling mechanism. As the heat load increased, a fan was added to the system directly on top of the heat sink to enhance heat convection. In recent years, the growing number of GPUs, increasing heat load of CPUs, and the need for space reduction has stimulated the use of flattened heat pipes to transport heat from the PCB to a heat sink, which is placed in a different part of the system.

Air cooled heat sinks (ACHS) are the most common heat rejection devices because of their ready availability, ease of application, and low cost [4]. Furthermore, because of the lack of moving parts, connections, or valves, they are more reliable and applicable in a wide variety of conditions. Several types of ACHS have been developed, and numerous studies have been carried out to optimize their performance and design. Although there have been several studies on different shapes, heights, lengths, diameters, and pitches, and the two most common ACHS are shown in Figure 1.5. A base of high conducting material (usually Aluminum or Copper) is augmented with fins. Air flows over the structure and removes heat by convection. At steady state, all the heat produced by the electronic component is transferred to the solid and then to the fluid while friction causes a pressure drop in the fluid that needs to be overcome by a blower or fan. The reduction in size of the heat generating component, along with the improvements in micro-fabrication, has lead to development of water-cooled micro channel heat sinks (also shown in Figure 1.5). The cooling mechanism through water-cooled micro channel heat sinks is equivalent to the mechanism used by ACHS, except that the features of the system are smaller, and a higher specific heat fluid (water) is used to improve performance. Several new technologies are under development to satisfy the cooling needs of new generation chips. The most promising solutions are [5]:

- Improved Air Cooling
- Liquid flow in Microchannels

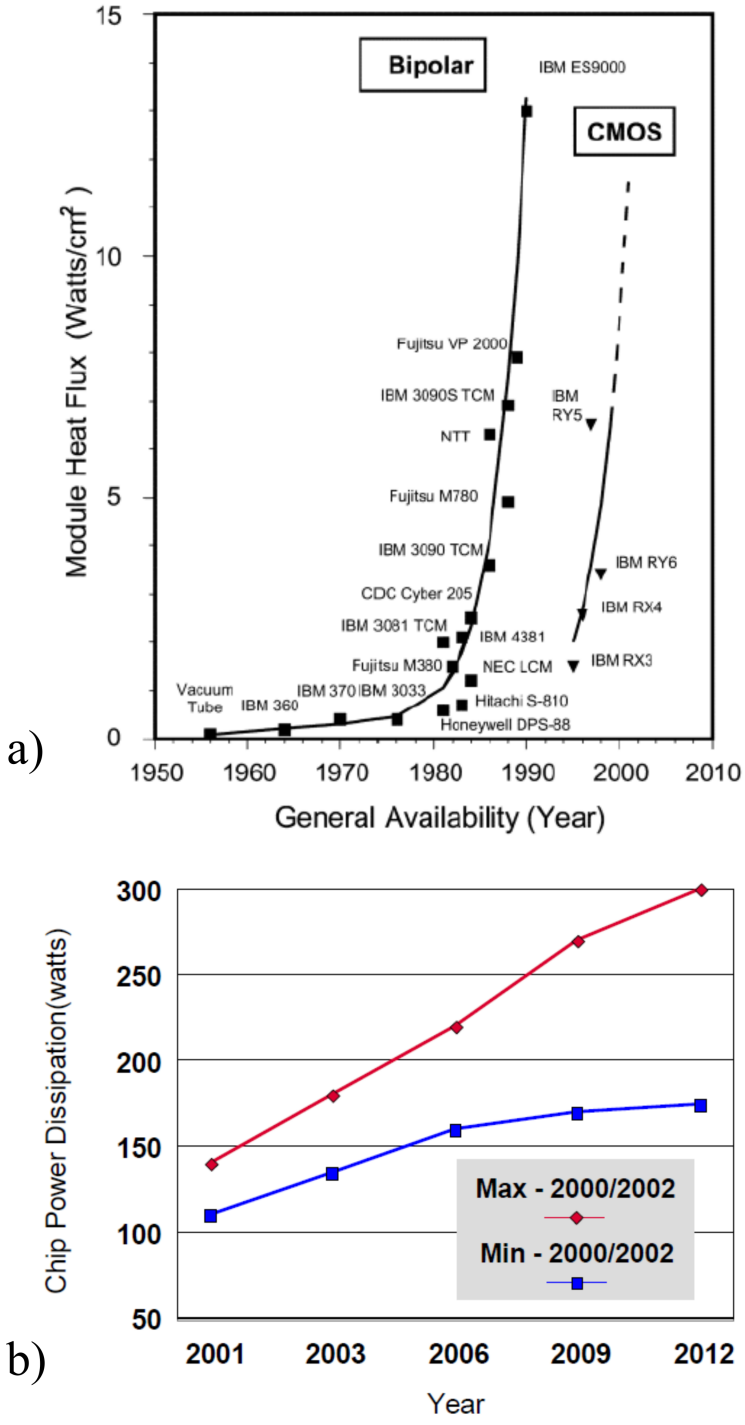

Figure 1.4: Trends in a) Chip Heat Flux and b) Chip Power

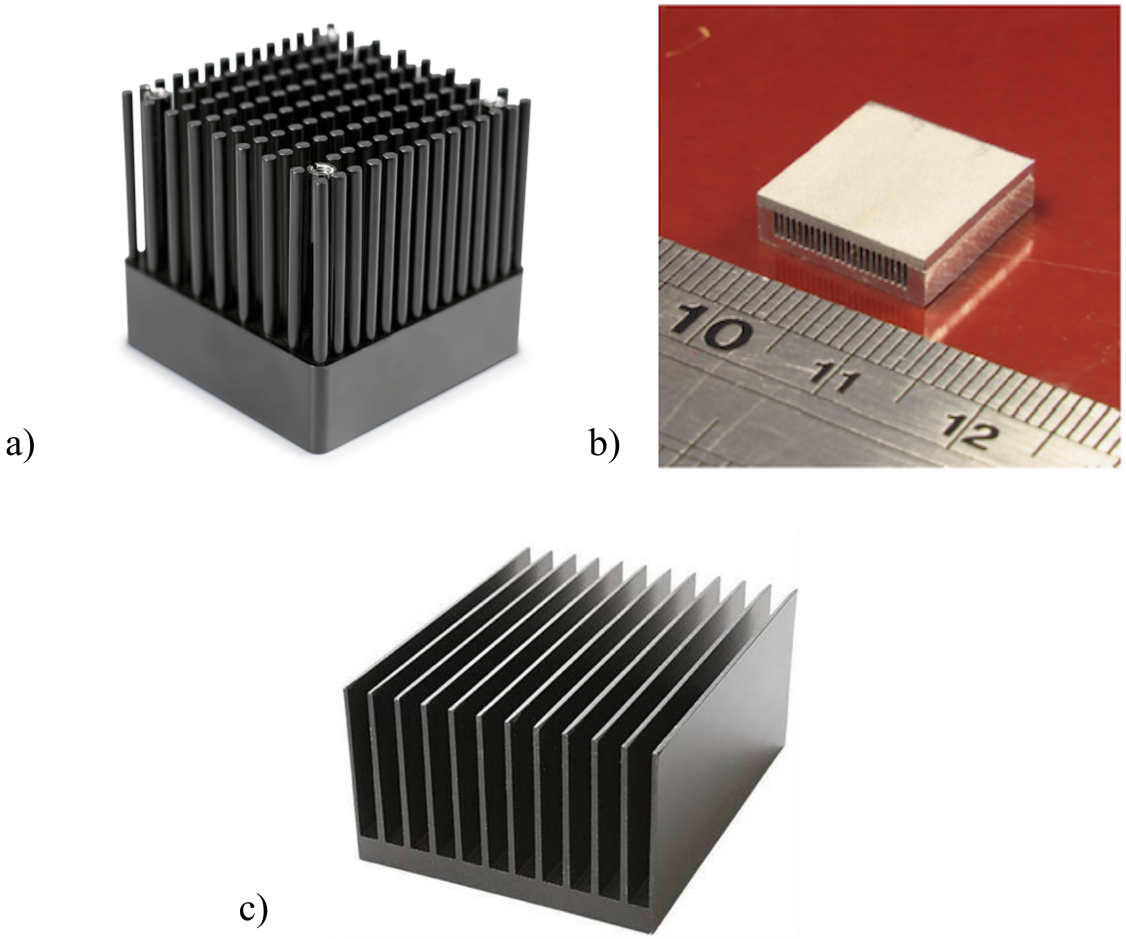

Figure 1.5: Example of a a) Pin Fin Heat Sink b) Microchannel Heat Sink and c) Plane Fin Heat Sink

- Thermoelectric Cooling
- Nanomaterials for property enhancement
- Compression refrigeration cycle

This work will concentrate on the first two solutions. The reliability and simplicity of ACHS make them the most commonly adopted and preferred solution, spurring great interest in the study of their performance and optimization. Hannenman [6] and Azar [7] have shown that no real barriers exist that would make air cooled technologies obsolete for most applications. Presently, we have reached goals in air cooled thermal management that were beyond the limits put on such technologies in the 1980s [8, 9]. The beginning of analysis of air cooled heat sinks starts with the analytical study of pin conduction and fin efficiency by Gardner [10]. Later, Elenbaas [11, 12] studied natural convection in parallel plate channels under different heating conditions. He correlated the date by using Rayleigh and Nusselt number correlations. Starner and McManus [13], Van de Pol and Tierney [14], Aihara and Maruyama [15] further developed these results to different shapes and arrays of fins. Radiation in U-shaped channels was analyzed by Ellison [16] using gray body assumptions. At about the same time, Zukauskas et al. [17, 18] used an impressive number of experimental results to correlate Nusselt number to Reynolds number for tubes in cross flow for a wide set of geometrical parameters. Whitaker [19] used a porous media derived hydraulic diameter to collapse date and correlate flow in packed beds and tube bundles which are often used in ACHS. Tuckerman and Pease [20] introduced the concept of micro-channels for cooling of high power electronic components, opening the doors to a whole new area of research in the field of heat transfer. The development in micro and nano manufacturing processes has increased the interest in microsystems for cooling because of their high heat transfer surface and small dimensions. With the increase interest in such systems, several modeling techniques have been developed to model air cooled heat sinks and several metrics have been used to optimize them. All of the studies mentioned before used analytical models or experimental results to guide the design of air cooled thermal management systems. Qu [21], Bowers [22], Dae-Whan [23] and Bar-Cohen [24], along with many others, investigated single

and two-phase flow and heat transfer in micro-channels.

Modeling techniques for all forms of heat rejection systems can be divided in four main areas:

- Analytical
- Experimental
- Numerical
- Averaged

All the studies discussed thus far belong to the experimental or analytical modeling of heat sinks. In most cases the quantities of interest are average pressure drop and average heat transfer coefficient across the heat sink, which are directly related respectively to the energy required to run the system and the amount of heat that can be dissipated by the system for a fixed temperature increase. Each method has its supporters, the advantages and disadvantages of each method are listed in Table 1.1. The advancement in computational hardware has made CFD methods the most popular analysis method for heat sinks. Because of the relative simplicity of CFD analysis with todays packages, a significant amount of work has been done in heat sink analysis and heat sink optimization, but very few brought innovative concepts to the field. Some of the first analysis using CFD was done by Linton and Agonafer [25] on modeling of a plane fin heat sink and by Chapman and Lee [26] for elliptical pin fin heat sinks. Liu and Garimella [27] analyzed micro-channel heat sinks using a full CFD simulation. Walchli et al. [28] combined CFD and analytical network models to obtain accurate results for micro-channels.

Averaging methods such as Volume Averaging Technique (VAT) were developed for flow through complex porous structures in the 1960s and 1970s, and have been successfully applied to modeling of heat and momentum transport in heat sinks. The advantages of averaging methods are that performance parameters can be obtained very quickly and the efficiency of the system can be evaluated in computational time, which is several orders of magnitude less than CFD finite element methods. On the other hand, the averaging process leads to some loss of information about the flow structure and requires development

Table 1.1: Comparison of different modeling techniques for heat sinks

Method	**Advantages**	**Disadvantages**
Analytical	No computational time Direct correlation of quantities of interest	Limited to simple geometries
Experimental	Comprehensive Does not need validation Produces directly quantities of interest Independent of geometry and problem conditions	Time consuming Expensive
Averaged	Reduced computation time Produces directly quantities of interest	Requires Closure Needs validation
Numerical	Accurate Applicable to wide range of geometries and flow conditions	Time consuming Needs validation

of closure schemes. Closure variables are geometry and flow dependent; however, schemes have been developed for a wide variety of applications. The foundations of the theory are discussed in detail in the next chapter, and several references are provided. Quintard and Whitaker [29, 30, 31, 32, 33, 34, 35] and Gray [36, 37] developed the mathematical foundation and theoretical basis for VAT application for heat transfer in porous media. Unlike geophysical porous media where the determination of the geometry is also part of the averaging process, for man-made heat management devices, the geometry is well defined and some of the assumptions can be relaxed and more accurate results can be obtained. Travkin and Catton [38] set the foundation for application of VAT to laminar and turbulent convective heat transfer in complex heat management systems. They applied these concepts with experimental closure to analyze flat channels with rough walls [39], structures with random pore distributions [40], and several other structures [41, 42, 43]. Horvat [44, 45] modeled pin fin heat sinks and heat exchangers while Vadjnal [46, 47] modeled a vapor chamber and a micro-channel heat sink using VAT. Kuwahara and Nakayama developed several closure correlations [48, 49] and studied convection in generalized geometric structures [50, 51] using VAT. However, in all of these studies, closure schemes for the momentum and energy equations were used with the assumption that the structure has constant porosity and periodic geometry. The problem of flow through geometrical heterogeneous media was first analyzed by Plumb and Whitaker [52] and Quintard [53, 35]. Goyeau [54] analyzed the limits of periodic closure for flow through a dendritic system with evolving nonlocal heterogeneity. Cushman [55] developed a general averaging and closure scheme for diffusion and dispersion for continuously evolving heterogeneity scales. Still, the author is not aware of any studies of heat transfer through such systems. Moreover, the heat sink problem is a conjugate problem where the conduction in the base can have a significant impact on the system performance. Because the volume averaged equations are true in the average sense while the base solution is point-wise true, the treatment of the interface presents a very important challenge. Sahraoui and Kaviany [56] assumed continuous heat flux and developed a temperature jump condition in terms of a parameter α. However, Nakayama [49] showed that the temperature equilibrium at the interface leads to more accurate results. Horvat [57] and Hu [58]

solved the conjugate problem by assuming temperature equilibrium at the interface and by using iteration to obtain an energy conserving flux interface. This leads to accurate results, but the iteration procedure is very expensive in terms of computational time. Nield and Kuznetsov [59] developed a quite arbitrary uniformity principle boundary condition for the conjugate problem for the case of negligible axial conduction in the fluid and in the base. The treatment of the interface condition for the general case of axial conduction in both base and channel still lacks some rigor and needs to be developed to refine and expand the use of VAT in modeling of general ACHS.

Although there have been an immense number of publications in heat sink technology, most of them have concentrated on spatially periodic structures. Recently, there have been few studies that have suggested that non-periodic, multi-scale heterogeneous geometries can greatly improve heat transfer and reduce pressure drop in heat dissipating devices [60, 61, 62]. This tendency was proposed by Bejan in his constructal law [63] and is supported by the scarcity of periodic structures in natural flow systems. The main challenges that have prevented extensive studies on these systems, has been the extensive computational times required to model such systems with conventional modeling techniques. The multi scale nature of the problem implies that, for discretization methods such as FEM/CFD, the minimum mesh size has to be on the order of magnitude of the lowest feature. When the system length scale disparity is very large, this means that very large meshes are required to discretize the system, which implies large memory and CPU requirement for the solution of the equations. This computational drawbacks have limited the exploration of more complicated non-uniform geometries, and have limited the amount of optimization studies that can be conducted. Fortunately, multi-scale problems arise constantly and several techniques have been developed to tackle the challenges they present.

Nature, in all its beauty and diversity, presents itself in an amazing range of physical and time scales. From the light-year scale of astronomical distances and eons of geological time scales, to the Planck length and time scales of string theory, the diversity of scales around us is astonishing. Nature being the inspiration and subject of engineering, leads to the ubiquitous presence of multi-scale problems in engineering applications. Since the scope of engineer-

ing is design, modeling of system behavior and determination of performance parameters is crucial. In most cases, models that are accurate and practical over a certain scale range, are inaccurate and/or inefficient over a different range. For example, although all design parameters for a system could be obtained by studying the motion of elementary particles (e.g. atoms, photons, phonons etc.) in it and around it, such an approach is undoubtedly not practical in designing a cargo ship. The study of transport phenomena through multi-scale systems is no different. In the study of transport phenomena, scale disparities arise from the physics and mathematics of the problem, such as in singularly perturbed problems (e.g. boundary layers) and turbulence, or they can result from the geometrical features of the system, such as in a porous medium. In both cases, modeling challenges are similar, and it will be shown in this paper that certain mathematical approaches to modeling systems that present length disparities are indeed very similar. The hot debate about climate change has sparked strong interest in Global Circulation Models (GCM), to study environmental transport phenomena on a global scale. This is clearly a multi-scale problem, with scales ranging from the size of small cities to earths radius. Furthermore, recent development in technology and manufacturing have given us access to micro (and lower) time and length scale and, have opened amazing new possibilities in all fields of engineering and science. It is not uncommon now, to have man-made large scale systems that contain both micro and nano scale features to improve their performance. Therefore, development of multi-scale models is a crucial aspect in engineering, and it is not surprising that research interest in the field has been exponentially growing in the last decade. There are several approaches to modeling of transport phenomena in multi scale modeling, each one with its advantages and disadvantages. The most accurate approach is to solve the problem directly at the smallest scale of interest l, and nowadays these are mostly carried out computationally. Example of these types of approaches are: molecular dynamics simulation of diffusion, direct numerical simulations of turbulence, pore scale simulation in porous media flow. These methods are essential to understand the physics of the problem at the lowest scale of interest, and could be applied to the entire system, although at great computational cost. Nonetheless, studying phenomena on the system scale L using this approach is not realistic when the length scale

disparity is large:

$$l \ll L \tag{1.0.1}$$

To avoid these shortcomings, in multi-scale systems, the scales are often separated, and the lower and upper scale models are solved separately (or iteratively). The main assumptions of these methods is that the large scale disparity leads to a weak coupling between the two problems. As it will be discussed later, the length scale disparity, Eqn. (1.0.1), is given different names in different multi-scale problems and results from different physical arguments. The earliest example of such methods are matched asymptotic studies of singularly perturbed equations. In these problems, a small boundary layer is present in which quantities vary significantly allowing an inner solution to the boundary layer and an outer solution to be defined and solved. Another approach involves averaging the lower scale equations on an intermediate scale; this allows the study of the phenomena at the intermediate scale, while still incorporating the effects of the lower scale through some closure parameters. Examples of these approaches are: continuum approximation in mechanics, Reynolds Averaged Navier Stokes (RANS), Large Eddy Simulations (LES) studies of turbulence, and, what will be the subject of this paper, Volume Averaging Theory (VAT) for geometrical multi-scale heterogeneous systems. Although not discussed in this work, it has been shown that all three of these methods can be mathematically unified through asymptotic expansion analysis [64, 65, 66]. Any averaging process leads to a loss of information about the underlying functions, therefore, some additional information about the effects of the lost information on the parameters of interest is usually required to close the problem. Quoting Einstein, the key step in the closure of an equation is to make it as simple as possible, but not simpler. The advantage of these averaged types of solutions is that the derived model can be solved much more efficiently, and, when the effects of lower scale quantities are properly defined and modeled, their effects are still taken into account. Another advantage of these averaged models is that they allow easier comparison with lab experiments. In most cases, it is very challenging, if not impossible, to directly determine the lower scale quantities, and lab measurement provide averaged quantities. For example, velocity and temperature in a macro system can be measured in a lab, therefore, it makes sense to have a model that directly predicts those

quantities such that its accuracy can be measured. At the same time, experimental validation of a method that predicts position and momentum of molecules throughout the same system is not really feasible. Similarly, for a porous medium with a complex geometrical structure, it could be impossible to obtain velocities and temperatures inside the pores, and average quantities (e.g. average pressure drop, average temperature increase) are usually measured. Therefore, it seems fit to have methods that predicts quantities which can be measured.

The focus of this work will be on VAT and its application to modeling, design and optimization of heat transfer systems. Although VAT was developed for study of transport phenomena in porous media, which are intrinsically multi-scale and heterogeneous, its features and rigor, make it very useful in any multi-scale heterogeneous medium, independent of whether or not it is porous in the true meaning of the word. This work is divided into five chapters. The first chapter is dedicated to the presentation of the problem and the solution methods proposed. The second chapter is dedicated to the derivation of system scale conservation equation, along with mathematical and physical explanations of the method. Although rigorous mathematical foundations for VAT have been laid out by Whitaker [67, 68], Quintard [69], and Gray [36], empirical variations are still widespread. The authors will attempt to show that the VAT approach is a rigorous approach that leads to exact equations which lead to a geometrically simplified but physically accurate model of the system under consideration. Approximation in the solution are introduced in the definition and determination of the closure parameters, therefore the closure problem will be discussed in depth. The second chapter will be dedicated to the application of the VAT model to heat sinks with variable geometry, and derivation of efficient numerical solutions to the resulting set of Partial Differential Equations (PDEs). A VAT two-dimensional model of a heat sink will be presented, and scaling arguments will be discussed to further simplify the equations. In the second part of the chapter, a Galerkin method and finite difference solution of the resulting set of PDEs will be presented. Significant attention will be dedicated to the issues that arise from the length scale disparity between the homogenous base and the channel. The accuracy and limits of the model are discussed in the fourth chapter. The solution method is

validated against experimental and numerical results, and the scaling developed in Chapter 3 is used to determine the limits of applicability of the theory. Finally, the drastic reduction in computational time is used to carry out an optimization study to determine optimal design parameters for heat sinks with variable geometry. System performance parameters of optimized heat sinks with uniform, trapezoidal and converging geometries are compared. The effects of the added geometric degrees of freedom are investigated, and it is determined that they are indeed an efficient way to improve heat transfer.

CHAPTER 2

Theoretical Fundamentals of Volume Averaging Theory

The omnipresence of porous media in geological systems has spurred strong interest over the last century in effective modeling of transfer processes through such media. The first well-known study in such systems is attributed to Darcy [70] in 1856, where in his Appendix D he states the most famous law for flow through porous media

$$\langle \mathbf{v} \rangle = -\frac{1}{\mu} \mathbf{K} \cdot \nabla p \tag{2.0.1}$$

where $\langle \mathbf{v} \rangle$ is the seepage velocity, $\mu$is the viscosity and $\mathbf{K}$ is the permeability tensor. For the sake of accuracy, it should be noted that in its original form given by Darcy, the equation is one dimensional and permeability is a constant. This equation relates the average velocity through the porous medium to the pressure gradient across it. This equation has been proven to be valid only for slow viscous flow of a Newtonian fluid and since then, several empirical modification to this law have been made to extend its validity. Some of the most important of these modifications are the additions by Brinkman [71] and Forchheimer [72], who added correction factors to extend Darcys law to higher speed flows and non-Newtonian fluids. These additions result in the Brinkman-Forchheimer extended Darcy equation

$$0 = -\nabla \langle p_f \rangle + \mu_{eff} \nabla^2 \langle \mathbf{v} \rangle - \frac{\mu_f}{\mathbf{K}} \langle \mathbf{v} \rangle - \frac{\rho_f c_1}{\mathbf{K}^{1/2}} \langle \mathbf{v} \rangle^2 = 0 \tag{2.0.2}$$

Although these equations have been used for many years to model flow through different porous media with good results, they are purely experimental and lack a solid theoretical foundation. These equations can be very useful in practice, for cases in which their limits and the empirical constant on which they are dependent have been determined; however, since they are purely empirical they cannot give a correct description of the physics of the problem, and it is unclear how to apply them to new problems.

On the other hand, it will be shown that direct integration of the Navier-Stokes equation (or other forms of the momentum conservation equations for non-Newtonian fluids) using VAT will give a physical description of the transport in a porous medium. Furthermore, using VAT, a theoretically based expression relating empirical properties such as permeability and effective viscosity to the geometry of the porous media and physical properties of fluid can be obtained. Thus, VAT allows, with proper closure, to efficiently obtain mean values of velocity, temperature, electric charge, etc. for several porous media geometries and different fluids. VAT was first proposed in the sixties by Anderson and Jackson , Slattery [73], Marle [74], Whitaker [68], Gray [36] and Zolotarev and Radushkevich [75] and has since been extended by the work of numerous investigators such as Quintard [30, 31, 32, 33, 34, 53], Carbonell [76], Plumb [52, 77], Travkin and Catton [38], Bear [78], Kaviany [79], Kuwahara [50, 48] and Nakayama [80, 81, 49], Hsu [82], Ochoa-Tapia [83], and Lemos [84]. This list is not intended to be comprehensive, as it is not possible to cite all contributors to the advancement of VAT in the last several decades. Recently, VAT has been applied to several new fields and in the last decade has found a lot of applications in biological systems and their modeling. Diffusive and convective flows through multi-scale systems are extremely common in biological applications. Species diffusion plays a key role in delivering nutrients through scaffoldings to cells for tissue growth, delivering drugs through tissue to defective cells for drug treatments, and spreading contrast fluid through joints to damaged areas for imaging. Lasseux et al [85] developed a three-phase model based on VAT for species reaction and transport during in-vitro tissue growth. Khanafer and Vafai [86] used VAT to study diffusion for MRI imaging and drug delivery systems. Fluid flow, convective species transport and heat transfer also play a key role in the intricate multi-scale circulatory system. Nakayama [87, 88, 89] developed a general bioheat equation to study transport phenomena in circulatory systems. Khanafer and Vafai [90, 91] also used VAT to developed models for transport in arterial walls, treatment of brain aneurysm and blood perfusion. The fast advancement in biotechnology and the growing interest in the field has opened an entirely new area for application of VAT, and its applications in biological systems are expected to grow exponentially in next few years. The main features of VAT will be described in great

detail in the core of this paper, however, it is important point out here that the VAT averaging process produces equations that are exact. However, the result is a set of partial integro-differential equation that contain a mix of averaged, fluctuation and point-wise quantities. Since the ultimate goal is to obtain equations in the average quantities alone, a closure scheme is introduced to model the effect of these fluctuation and point-wise quantities on the average values, and this is where approximations are introduced. Thus, approximations to the solution of the equations are introduced in the closure scheme, not in the derivation of the equations themselves. It is then obvious that closure is usually problem specific, and the key to achieving good results using VAT is a closure scheme that will correctly portray the physics and geometry of the problem at hand. First, it is shown that the VAT approach is similar to other common approaches in multi-scale problems.

2.1 Analogy with other averaging techniques

The continuum approach is today such an established technique that its underlying assumptions are sometimes forgotten. Following Bear [78], a short review is provided here in order to show the parallel between the continuum approach in fluid flow and the volume averaging approach in porous media. Because of the widespread use of the continuum approach, showing an analogy between it and VAT, will help demystify the VAT approach, and at the same time elucidate its limits of applicability and some of its issues. Since the rest of this work will deal with two-scale systems, the smaller scale will be defined as micro scale and given the symbol l (with appropriate subscript), while the upper scale will be defined as the macro scale L. While the micro scale is defined by lower scale phenomena, the macro scale depends on the problem under consideration, therefore it is not given any subscript. For the different averaging theories discussed in this section, the actual order of magnitude of micro and macro scales can be significantly different, however, because of the context in which they arise, no confusion should arise.

Fluids are composed of a large number of molecules contained in vacuum and in their perpetual motion they collide with each other and with the solid walls of the container in which

they are placed. Given initial position and momentum of each particle, hypothetically classical mechanic theories could be used to fully describe a given system of molecules and predict the future position of each molecule. However, even with todays most powerful computers, it is impossible to determine the motion of 10^{23} molecules in one gram of gas. Thus, instead of treating the problem at the molecular level, a statistical approach is usually used. This means that average quantities are defined that allow the study of motion of a large group of molecules and consider the fluid as a continuum. Essential to the continuum approach is the definition of particle. A particle is an ensemble of molecules contained in a small volume. In order for this averaging to have statistical value, its size has to be much bigger than the mean free path of the molecules, l_{mfp}. However, it should also be small compared to the entire fluid domain in order to allow its changes through the domain. The averaging process starts by taking a mathematical point P (which has no mass or volume), associating to it an elementary volume, of which P is the centroid, and calling it a physical or material point. Now, at every physical point density can be defined as the ratio of the mass Δm contained in a volume ΔU. The question is what should the size of the volume be for the density to be a good representation of the number of particles that are in the volume? Let's consider a point P in space, and take a volume ΔU_i around it, of which P is the centroid. Let Δm_i define the mass of the molecules in it. The average density of the fluid is then defined as their ratio $\rho_i = \Delta m_i / \Delta U_i$. Obviously, if ΔU_i is too big, say the size of the domain, it is meaningless to assign such a value to P because it cannot be used to study changes in ρ within the domain. To determine the correct size ofΔU, the behavior of density at P as the volume increase can be studied. Starting from the volume-less mathematical point, the size of the volume is increased and its effects on the density are shown in Figure 2.1. For small values of ΔU_i, few molecules will be present in the volume, and increasing its size will add a considerable amount of mass, and the value of the density will fluctuate significantly. As ΔU_i increases further, small variations in its size, produce smaller variations in the number of molecules added relative to the ones already contained. At a value of $\Delta U_i \geq \Delta U_0$, further increase in the volume size has negligible effects on ρ and fluctuations die down. As the value of ΔU_i is increased even further, if the fluid is inhomogeneous (or compressible), smooth changes in

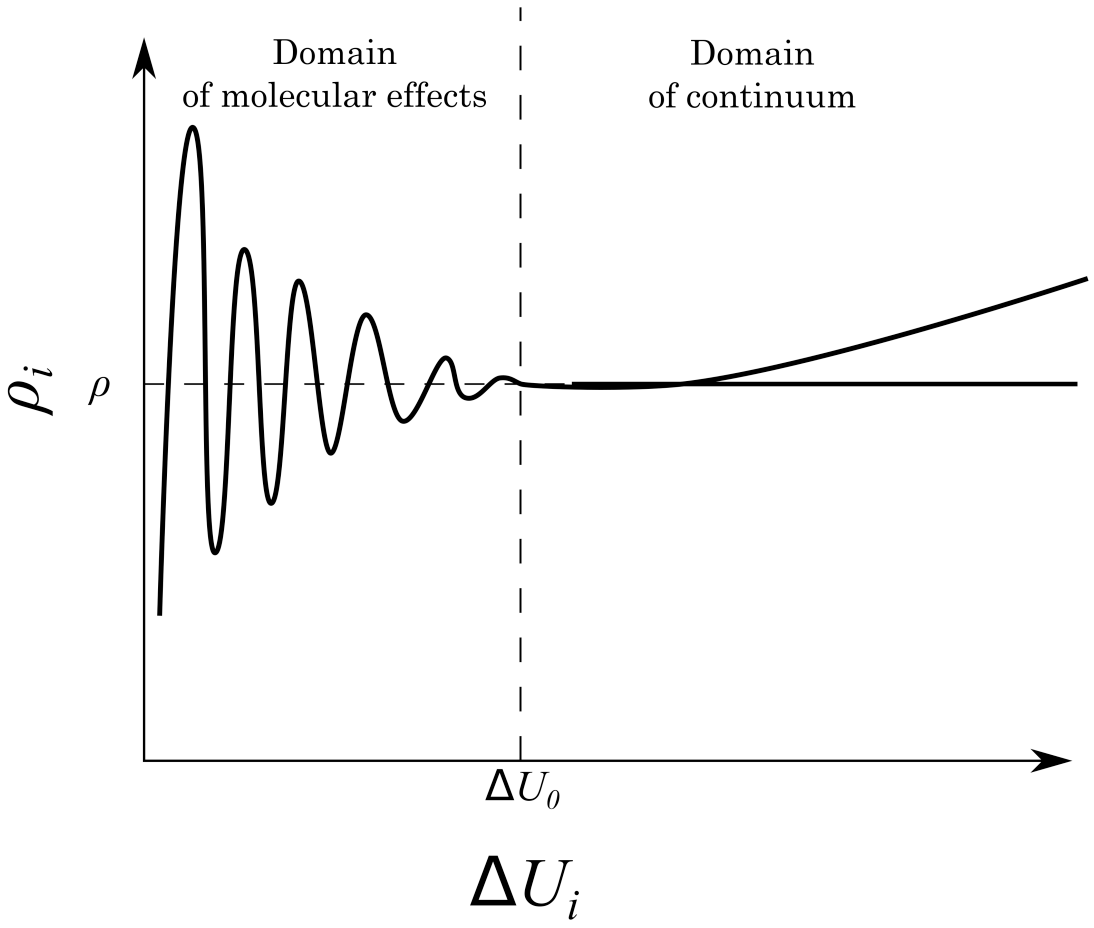

Figure 2.1: Definition of density and particle

ρ are present, otherwise it will be constant. From a statistical point of vie, Figure 2.1 can be interpreted by considering ρ as a probability, and as the sample size increases, its mean value will reach a constant value (or slowly varying). Going back to Figure 2.1 the size of the averaging volume should be taken $\Delta U_i \approx \Delta U_0$, because it is a good representation of the density of the system, while still allowing its variation through the system to be studied. The density at a physical point P is thus defined as

$$\rho\left(P\right) = \lim_{\Delta U \to \Delta U_0} \left(\frac{\Delta m_i}{\Delta U_i}\right) \tag{2.1.1}$$

The volume ΔU_0 may now be identified with the volume of a particle at the physical point P. Through this procedure, a fluid made of collection of molecules in a vacuum is replaced by a continuum filling the entire space and a fictitious smooth medium called fluid is defined at every point in space. As a consequence density has becomes a smooth function. Following this discussion, it is not a surprise that shock waves, whose size is on the order of l_{mfp}, give rise to discontinuities in density. When the fluid is inhomogeneous (or compressible), a higher length scale over which macroscopic changes in density occur can be defined as

$$L = \frac{\rho}{\partial\rho/\partial l} \tag{2.1.2}$$

The volume L^3 may be used as the upper limit for the size of the averaging volume ΔU, and

$$\frac{\partial\rho}{\partial l} = \lim_{\Delta l \to \Delta l_0} \frac{\rho\left(l + \Delta l/2\right) - \rho\left(l - \Delta l/2\right)}{\Delta l} \tag{2.1.3}$$

where $l_{mfp} < \Delta l_0 < L$ and $\left(\Delta l_0\right)^3 \approx \Delta U_0$. Similar arguments can be made to find the size of the fluid particle that gives smooth variations in other averaged quantities such as velocity, pressure, temperature etc. The size of the particle volume ΔU_0 to be associated to a point P should then be the largest one that makes these quantities smooth.

The Knudsen number is defined as a dimensionless parameter that defines the validity of the continuum approach

$$Kn = \frac{l_{mfp}}{L} \tag{2.1.4}$$

When $Kn \ll 1$, the continuum approach is valid. On the other side, when $Kn \approx 1$ the flow is in the slip flow regime, and for $Kn > 1$ the flow is usually defined as free molecular

or Knudsen flow. In these low Knudsen number flows, the continuum approach cannot be used, and use of Navier-Stokes equation would lead to incorrect results. This averaging process results in a loss of information because the effects of molecular motion still need to be taken into account, thus some closure is required. In the passage from molecular to continuum, this closure is obtained through the introduction of constitutive laws such as Newtons law of viscosity, Fouriers law, Ficks law etc. which define physical properties such as viscosity, diffusivity, thermal conductivity etc. These parameters describe the effect of molecular motion on average quantities (e.g. velocity, temperature, mass fraction). Note that the size of the particle volume does not enter in the averaged equations (e.g. Navier-Stokes, energy conservation), however, it can be important when the closure parameter need to be determined.

Similar to the transformation obtained through the continuum approach from a discrete molecular scale to a continuous medium, is the transformation obtained through the volume averaging approach from a discrete pore space to a homogenous medium. Hypothetically, it would be possible to solve the full Navier-Stokes equations for the fluid phase in the pores of a porous medium to obtain the velocity everywhere in the domain. However, it is computationally expensive, or sometimes impossible, to do so except for simple geometries such as capillary tubes. Thus, in order to obtain equations that can be solved efficiently, the lower scale governing equations are averaged over a volume and the discrete space is homogenized. The central issue is, again, to determine the size of the averaging volume that will give meaningful results. Following the procedure carried out for the continuum approach, given a mathematical point P, it is important to determine the size of the representative averaging volume (REV) around it. Clearly, this volume should be much larger than a single pore and much smaller than the entire porous medium domain. Analogous to the fluid density, defined as the ratio of the mass of the molecules in the volume and the volume itself, is the volumetric porosity ε, defined as the ratio of the volume of fluid in the REV to the volume of the REV itself. In both cases, the metric is taken as something that quantifies the amount of elements at the lower scale (molecules for continuum, pore space for porous media) per unit of representative volume (control volume for continuum, REV for porous

media). Returning to the issue of the size of the averaging volume, let P be a mathematical point inside a domain occupied by porous media. Let P be the centroid of a volume ΔU_i and define volumetric porosity as

$$\varepsilon_i = \frac{(\Delta U_v)_i}{\Delta U} \tag{2.1.5}$$

where $(\Delta U_v)_i$ is the volume of the pore space within ΔU_i. Repeating the procedure that was used for continuum, starting from a single point, the size of the REV is increased and the resulting plot is shown in Figure 2.2. Assuming that the initial point it is located in the fluid, the porosity is equal to 1. As the size of ΔU_i increases, some of the solid phase will be included and ε will start changing significantly. As the size of ΔU_i increases further, it start becoming a better representation of the actual phase distribution in the system and the porosity becomes a smooth function. The analogy to Figure 2.1 is clear. The size of the REV should be then taken as $\Delta U_i \approx \Delta U_0$, since it represents the smallest value that will give porosity as a smooth function, and allow the study of its variation throughout the domain. Hence, the volumetric porosity at point P is defined as

$$\varepsilon(P) = \lim_{\Delta U_i \to \Delta U_0} \frac{(\Delta U_v)_i}{\Delta U_i} \tag{2.1.6}$$

The volume ΔU_0 is therefore the REV of the porous media corresponding to the mathematical point P. A characteristic length L can be defined as

$$L = \frac{\varepsilon}{\partial\varepsilon/\partial l} \tag{2.1.7}$$

where

$$\frac{\partial\varepsilon}{\partial l} = \lim_{\Delta l \to \Delta l_0} \frac{\varepsilon\left(l + {}^{\Delta l}/_{2}\right) - \varepsilon\left(l - {}^{\Delta l}/_{2}\right)}{\Delta l} \tag{2.1.8}$$

and $(\Delta l_0)^3 \sim \Delta U_0$. Similar analysis can be carried for average velocity, average temperature etc., which would possibly result in different REV restriction. The actual size of the REV should be chosen as the largest one that will produce smooth functions for all the quantities of interest. Also, equivalent to the Knudsen number for continuum, a length scale ratio can be defined as

$$\frac{l_{por}}{L} \tag{2.1.9}$$

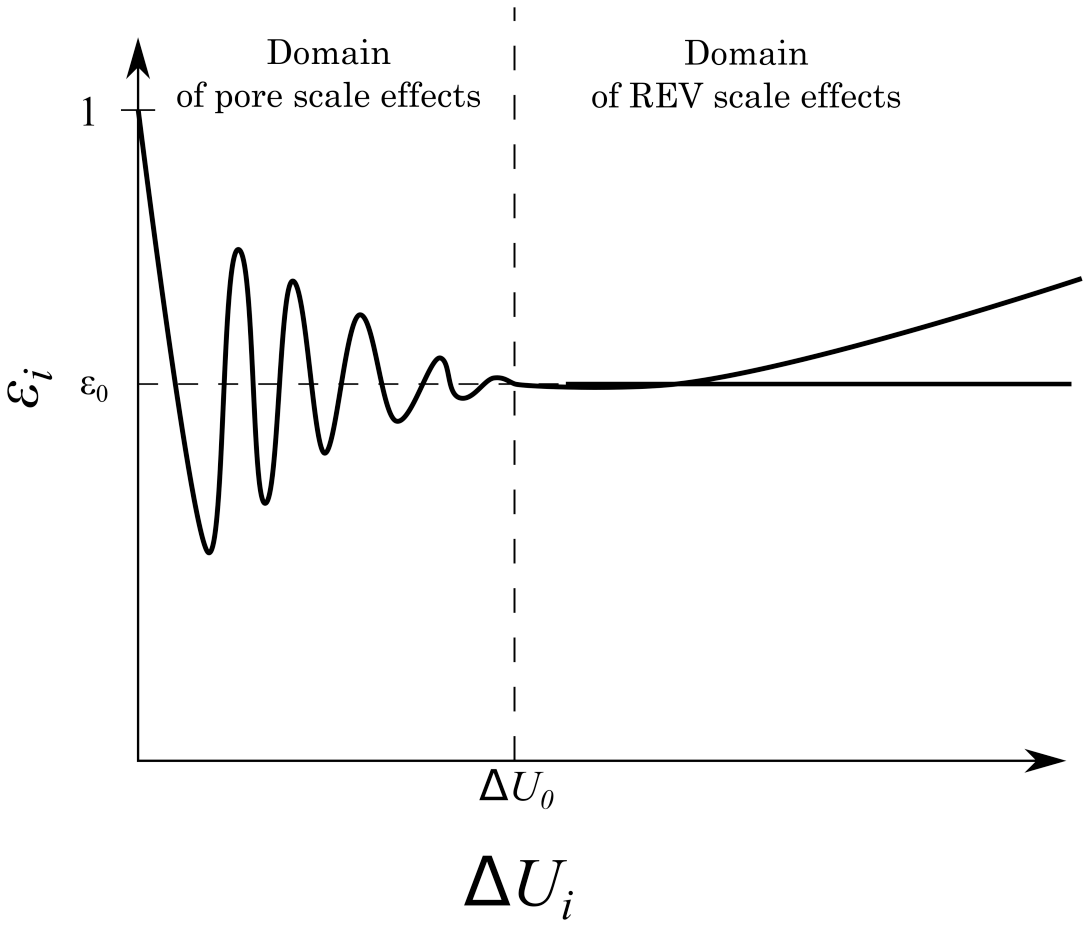

Figure 2.2: Definition of porosity and representative elementary volume

where l_{por} is the length scale associated with the pore space. When this quantity is small, the VAT approach will give meaningful results. When this quantity is on the order of unity, the system under consideration only has a few large pores and a regular approach with N-S equations should be used. It can be seen that, similarly to a shock wave, regions in which the pore geometry changes on the scale of l_{por}, will lead to discontinuity in the porosity.
By introducing the concept of porosity and the definition of REV, the actual porous media has been replaced by a fictitious smooth medium in which values of any property (fluid or solid) can be assigned to any mathematical point P. Once again, the averaging process causes a loss of information requiring some constitutive relations to associate the effects of lower level phenomena onto averaged quantities. In VAT, several different closure relations are available, and they define parameters such as the effective diffusivity, permeability, effective thermal conductivity etc. Also, the size of the averaging volume does not enter directly in the resulting averaged equations, however, its size has to be considered in the determination of the closure parameters. Since pictures are worth a thousand words (and equations), the discussion about the analogy between these two approaches is graphically shown in Figure 2.3. Both approaches take a discrete space, they average it over a representative volume, and produce a homogeneous space in which the lower effects are modeled through closure parameters.

Another example of an approach that takes advantage of length scale disparities is the Large Eddy Simulation (LES) method for turbulence modeling. The complexity of the physics of turbulence has (and will continue to) produce papers and books, and this is not in any way intended to be an extensive review of it. Only a few established physical behaviors will be highlighted to show how the LES approach is indeed very similar to the VAT approach. Kolmogorov's hypothesis states that for large Reynolds numbers the lowest scale eddies are independent of the mean flow scales and boundary conditions, and have a universal form that depends only on viscosity and dissipation rate. The length scale ratio between the mean flow scale L and the length scale of these lowest scale eddies l_{Kol} (Kolmogorovs length scale), can be then shown to be

$$\frac{l_{Kol}}{L} \sim \mathrm{Re}^{-3/4} \tag{2.1.10}$$

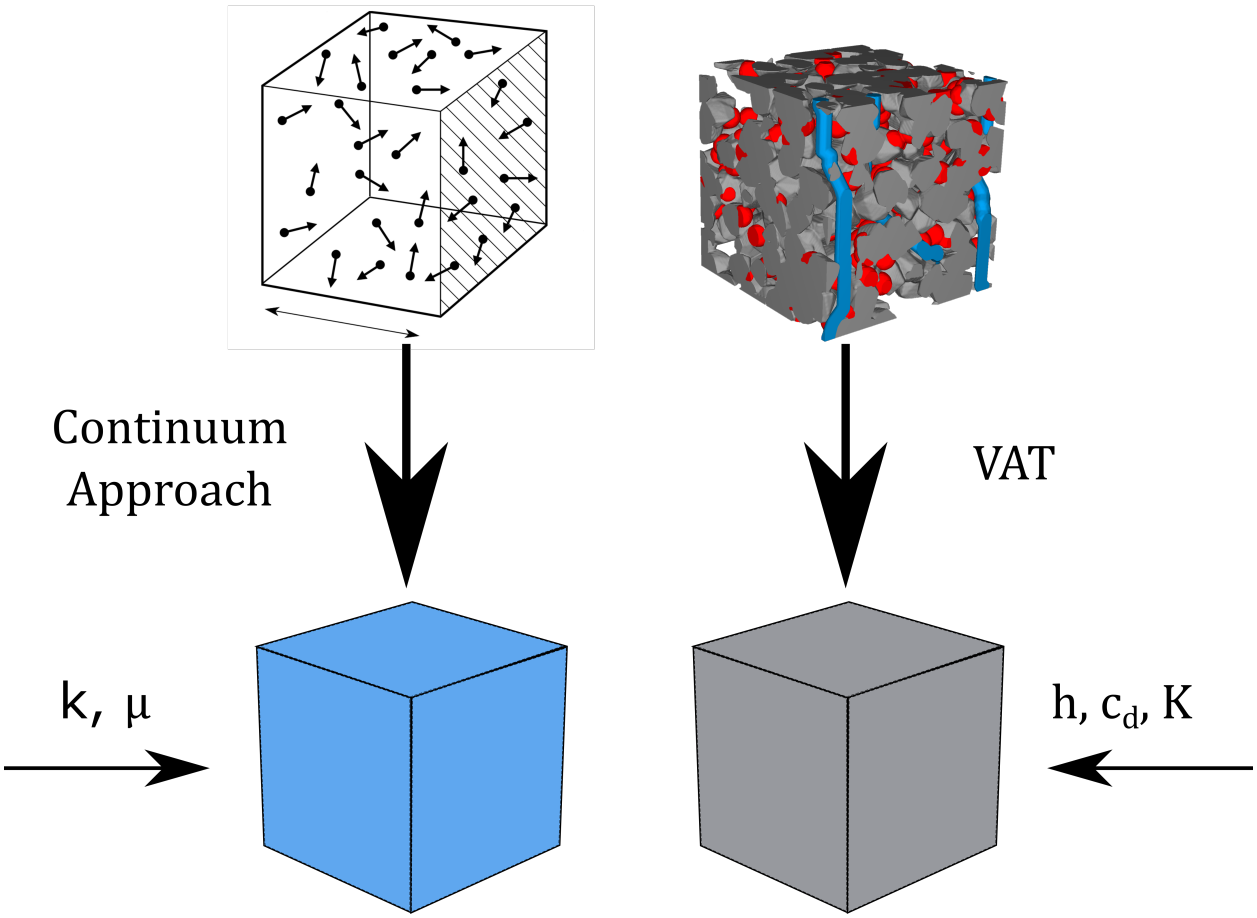

Figure 2.3: Graphical description of average analogy between continuum and VAT approaches

Comparing this equation with Eqn. (2.1.4) and Eqn. (2.1.9), it can be seen that they all define a conditions in which a length scale disparity is present. A large Reynold's number imply that the Kolmogorov length scale is much smaller than the system scale, and the two problems can be separated. This is the idea behind the LES approach, in which Navier-Stokes equations are averaged (filtered or resolved) over a volume at an intermediate scale between the largest and smallest eddies to obtain equations that are very similar to the VAT equations. In the averaging process, some information about the lower scale eddies (residual or subgrid) is lost, and their effect on the large scale eddies needs to be modeled through a closure scheme. Direct Numerical Simulations (DNS) of turbulence have been performed in recent years for moderate Reynolds numbers, however, they are not of practical use because of the need for very fine grids to resolve the Kolomgorov scale phenomena. The LES approach allows coarser grids to be used, and it is therefore more efficient while still maintaining a good degree of accuracy. The strong mathematical similarity between the LES approach and VAT provides opportunities for an exchange of knowledge from one to the other. This is particularly clear in the weighted VAT formulation which was proposed and discussed in detail by Quintard and Whitaker [30, 31, 32, 33, 34], in which the weight functions and their properties are equivalent to filter functions in LES.

These two analogies show that the mathematical and physical approaches behind VAT, are well established and VAT is indeed a rigorous technique. In the next sections, governing equations for transport phenomena will be derived, and it will be shown that they can be successfully applied to efficiently model complex multi-scale systems.

2.2 Derivation of the generalized VAT transport equation

In this section, first the averaging operators are defined, and their properties and useful theorems are discussed. Then, the operators are applied to a general point-wise transport equation, to develop the volume averaged form of the general transport equation. To illustrate the general feature of VAT without additional complications, the effects of turbulence are initially ignored and are included in a separate section. The notation and derivation are

taken mostly from the work of Whitaker [67] and Carbonell and Whitaker [76]. The term point-wise equations will be used throughout the section to define equations that are defined only at points within its phase (e.g. Navier-Stokes equations are defined only in points within the fluid). The averaging process and its discussion will be given for a two phase (fluid-solid) system; due to the linearity of the averaging operators defined, the extension to multiple immiscible phases is not very different (see [92]). The homogenization process of complex multi-scale geometry starts by associating to every point $\mathbf{x}$ in the domain, a volume V of which $\mathbf{x}$ is the centroid. The vector $\mathbf{y}_f$locates points in the fluid relative to $\mathbf{x}$, while $\mathbf{r}_f$locates points within the fluid relative to the fixed origin. Then it is easy to see that $\mathbf{r}_f = \mathbf{x}+\mathbf{y}_f$ (see Figure 2.4). Throughout the work, plain symbols will be used to denote scalar quantities, lowercase bold symbols will denote vectors (geometric and mathematical), and uppercase bold symbols will denote tensors and matrices. Two types of averaging operators are used in averaging the equations: a superficial average and an intrinsic average. The superficial average of a given variable ψ, at any point$\mathbf{x}$ in the domain is defined as

$$\langle\psi\rangle|_{\mathbf{x}} = \frac{1}{V(\mathbf{x})}\int\limits_{V_f(\mathbf{x})} \psi(\mathbf{x}+\mathbf{y}_f)\,dV \tag{2.2.1}$$

while the intrinsic average is defined as

$$\langle\psi\rangle^f\Big|_{\mathbf{x}} = \frac{1}{V_f(\mathbf{x})}\int\limits_{V_f(\mathbf{x})} \psi(\mathbf{x}+\mathbf{y}_f)\,dV \tag{2.2.2}$$

where V_f is the volume of fluid within the averaging volume. It can be easily shown that the relationship between these two averages is

$$\langle\psi\rangle|_{\mathbf{x}} = \frac{V_f(\mathbf{x})}{V(\mathbf{x})}\langle\psi\rangle^f\Big|_{\mathbf{x}} = \varepsilon_f(\mathbf{x})\ \langle\psi\rangle^f\Big|_{\mathbf{x}} \tag{2.2.3}$$

and ε_f is defined as the fluid volume fraction (also known as porosity). It is important to note here that the superficial average of a constant a is not equal to the constant itself

$$\langle a\rangle = a\left(\frac{1}{V}\int\limits_{V_f} dV\right) = a\varepsilon_f \tag{2.2.4}$$

On the other hand, the intrinsic average of a constant is equal to the constant itself, suggesting that, in most cases, it is more suitable for study of transport through porous media.

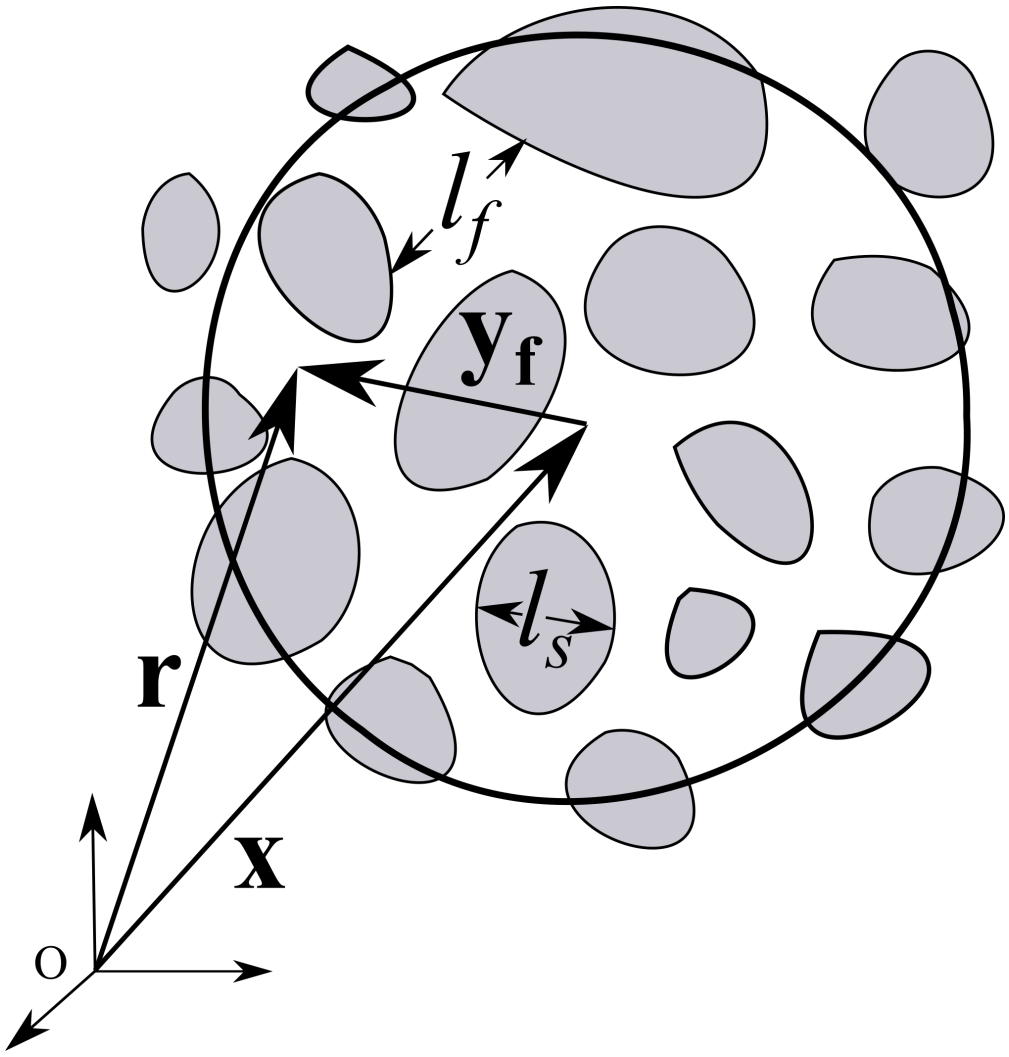

Figure 2.4: Position vectors associated with an averaging volume

Several arguments can be made on the preferred type of average for the study of transport in a porous medium, and there is not a right answer. In general, the value of the intrinsic average will be closer to point values that are measured with a probe, and therefore it is easier to interpret physically. On the other side, if instead of using the VAT upscaling approach, in which the governing equations are averaged starting from the point-wise equations, the derivation is started from a continuum view of a porous media, and the governing equations are obtained through a control volume approach, superficial averages seem to make more sense. These two approaches are equally valid, however, due to the familiarity of most researchers with point-wise equations and their physical meaning, the upscaling approach seems easier to grasp, and it will be described in this paper. Although the authors are not aware of a full derivation of the governing equations from a continuum view of the porous medium, Adler [93] and Brenner [94] give arguments that involve such an approach.

The application of these averaging operators to the governing equations leads to averages of gradients, and averages of products. In order to obtain equations that define changes of average quantities throughout the domain, these terms have to be dealt with. The average of a gradient can be related to the gradient of the average, using what is known as Slattery's Spatial Averaging Theorem (SAT). The theorem states

$$\langle \nabla \psi \rangle = \nabla \langle \psi \rangle + \frac{1}{V} \int_{A_{fs}} \mathbf{n}_{fs} \psi dS \tag{2.2.5}$$

where $\mathbf{n}_{fs}$ is the outward normal to A_{fs}, which represents the fluid-solid interface in the REV. This theorem is an extension of Leibnitzs rule, and will be used extensively throughout the rest of the derivations. A proof of the SAT can be found in [95] and [67]. The theorem also applies to the average of the divergence of a variable

$$\langle \nabla \cdot \psi \rangle = \nabla \cdot \langle \psi \rangle + \frac{1}{V} \int_{A_{fs}} \mathbf{n}_{fs} \cdot \psi dS \tag{2.2.6}$$

The average of a product, which usually stems from advective terms, also need to be related to products of averages. This is achieved by decomposing the point-wise values as a sum of its intrinsic average and fluctuation part

$$\psi_f = \langle \psi_f \rangle^f + \tilde{\psi}_f \tag{2.2.7}$$

This decomposition is indeed a decomposition of length scales, because at the basis of our derivation is the assumption that average quantities vary over the macro scale L, while fluctuation vary over the micro scale l_f. This assumption is a key argument in the derivation of the equations and their closure, therefore, it will be discussed in detail when necessary.
A crucial assumption that will be used in the derivation of the equations is that averaged values are constant (or vary negligibly) within the averaging volume. This can be expressed mathematically as

$$\langle\psi\rangle^f\Big|_{\mathbf{x}+\mathbf{y}_f} \approx \langle\psi\rangle^f\Big|_{\mathbf{x}} \tag{2.2.8}$$

where $|\mathbf{y}_f| \leq r_0$ (see Figure 2.4). Based on the discussion about the determination of an REV given in the previous section, this condition makes sense, and it simply states that the length scale of changes in the average quantity is much larger than the REV length scale, and ψwill vary smoothly throughout the domain. Some insight into this assumption can obtained by expanding the right hand side of Eqn. (2.2.8) in a Taylor series about the centroid$\mathbf{x}$

$$\langle\psi_f\rangle^f\Big|_{\mathbf{x}+\mathbf{y}_f} = \langle\psi_f\rangle^f\Big|_{\mathbf{x}} + \mathbf{y}_f \cdot \nabla\langle\psi_f\rangle^f\Big|_{\mathbf{x}} + \mathbf{y}_f\mathbf{y}_f : \nabla\nabla\langle\psi_f\rangle^f\Big|_{\mathbf{x}} + ... \tag{2.2.9}$$

Although this expression is not enlightening in terms of the physics of the problem, it shows that the difference between the average at the centroid and at a point relatively close to it, will depend on changes in the average quantity through the derivatives, and on the REV geometry through $\mathbf{y}_f$ and its moments. Rearranging Eqn. (2.2.9), the relative error in the approximation given in Eqn. (2.2.8), assuming that the average is not zero, can be written as

$$R|_{\mathbf{x}+\mathbf{y}_f} = \frac{\langle\psi_f\rangle^f\Big|_{\mathbf{x}+\mathbf{y}_f} - \langle\psi_f\rangle^f\Big|_{\mathbf{x}}}{\langle\psi_f\rangle^f\Big|_{\mathbf{x}}} = \frac{1}{\langle\psi_f\rangle^f\Big|_{\mathbf{x}}}\mathbf{y}_f \cdot \nabla\langle\psi_f\rangle^f\Big|_{\mathbf{x}} + \frac{1}{\langle\psi_f\rangle^f\Big|_{\mathbf{x}}}\mathbf{y}_f\mathbf{y}_f : \nabla\nabla\langle\psi_f\rangle^f\Big|_{\mathbf{x}} + ... \tag{2.2.10}$$

Defining the following length scales

$$\frac{\nabla\langle\psi_f\rangle^f\Big|_{\mathbf{x}}}{\langle\psi_f\rangle^f\Big|_{\mathbf{x}}} = O\left(\frac{1}{L_\psi}\right), \frac{\nabla\nabla\langle\psi_f\rangle^f\Big|_{\mathbf{x}}}{\langle\psi_f\rangle^f\Big|_{\mathbf{x}}} \sim O\left(\frac{1}{L_{\psi_1}}\right) \tag{2.2.11}$$

and, since $\max|\mathbf{y}_f| \sim r_0$, the relative residual can be expressed as

$$R|_{\mathbf{x}+\mathbf{y}_f} = O\left(\frac{r_0}{L_\psi}\right) + O\left[\left(\frac{r_0}{L_{\psi_1}}\right)^2\right] \tag{2.2.12}$$

Therefore, the error associated with the assumption that the intrinsic average is constant within the averaging volume will be negligible when

$$\frac{r_0}{L_\psi} \ll 1, \qquad \left(\frac{r_0}{L_{\psi_1}}\right)^2 \ll 1, \tag{2.2.13}$$

This shows again that changes in averaged quantities should occur over length scales much larger than the averaging volume scale. Two important properties of averaging stem from this assumption. The average of an averaged variable is the averaged variable itself

$$\left\langle \langle\psi\rangle^f \right\rangle^f = \langle\psi\rangle^f \tag{2.2.14}$$

and, the average of the product of averaged quantities is the product of the quantities

$$\left\langle \langle\psi\rangle^f \langle\zeta\rangle^f \right\rangle^f = \langle\psi\rangle^f \langle\zeta\rangle^f \tag{2.2.15}$$

or, equivalently

$$\left\langle \langle\psi\rangle^f \langle\zeta\rangle^f \right\rangle = \varepsilon_f \langle\psi\rangle^f \langle\zeta\rangle^f \tag{2.2.16}$$

Although these relations are shown for the fluid, they are indeed independent of the phase over which the averaging is carried out. Another assumption that will be used in the derivation of the governing equations is that the average of the fluctuations is zero

$$\left\langle \tilde{\psi} \right\rangle^f = 0 \tag{2.2.17}$$

These conditions are strongly reminiscent of the conditions required for Reynolds averaging of turbulent equations. In turbulent fluctuations, the assumption that the average of the fluctuations is zero is due to the random nature of time fluctuations in turbulence. In porous media, since the averaging is spatial, there will be a relationship between the morphology of the medium and the fluctuation. This is most easily seen by combining Eqn. (2.2.8) & Eqn. (2.2.9), to obtain an expression for the fluctuation of a variable as

$$\left\langle \tilde{\psi} \right\rangle^f = -\langle\mathbf{y}_f\rangle^f \cdot \nabla\langle\psi\rangle^f - \frac{1}{2}\langle\mathbf{y}_f\mathbf{y}_f\rangle^f : \nabla\nabla\langle\psi\rangle^f - ... \tag{2.2.18}$$

Intuitively, when the fluid phase is well distributed within the REV, such as in isotropic systems, the average of $\mathbf{y}_f$and its moments will be zero. A similar argument can be made for cases in which the geometry is spatially periodic, and the averaging volume is taken as a multiple integer of its period. For more complicated geometries, the validity of this assumption needs to be checked on a case to case basis. For more details on this discussion, refer to Whitaker [67], Carbonell and Whitaker [76]. Governing equations can be derived for cases where these conditions are not satisfied, and they are usually defined as non-local problems; however their solution is usually so complex that they end up losing their practicality, and when possible, a DNS approach would be more accurate and just as complex. In the rest of this work, it will be assumed that these assumptions are always verified, but they will be highlighted when necessary.

Now all the tools are in place, to start the derivation of averaged conservation equations through porous media. It will be assumed that the solid phase of the porous medium is rigid (does not deform under the influence of forces applied to it) and it has zero velocity. Furthermore, coupling between conservation equations will be ignored. Coupling is present for example when mass transfer affects material properties, exothermic or endothermic reactions and/or buoyancy effects need to be considered. In the absence of coupling, a general point-wise conservation equation for quantity ψin the fluid phase can be expressed in the following form

$$\frac{\partial \psi_f}{\partial t} + \nabla \cdot (\mathbf{v}\psi_f) = -\nabla \cdot \mathbf{j}\,(\psi_f) + g_f \tag{2.2.19}$$

The tensor $\mathbf{j}$ is the flux of ψ_f in and out of the volume and g_f is volumetric generation. Usually a constitutive relation (e.g. Newtons Law of viscosity, Fouriers Law etc.) is used to relate the flux to the gradient of ψ_f. The parameter ψ_f can be the any parameter that is conserved in a system e.g. mass, momentum, energy, concentration. Following our length scale separation, the boundary conditions can be divided into two types of boundary conditions: interfacial boundary conditions and system boundary conditions. Interfacial boundary conditions apply to the internal interfaces which have a characteristic length scale l_f. In general, they express conservation at the interfaces between the different phases within

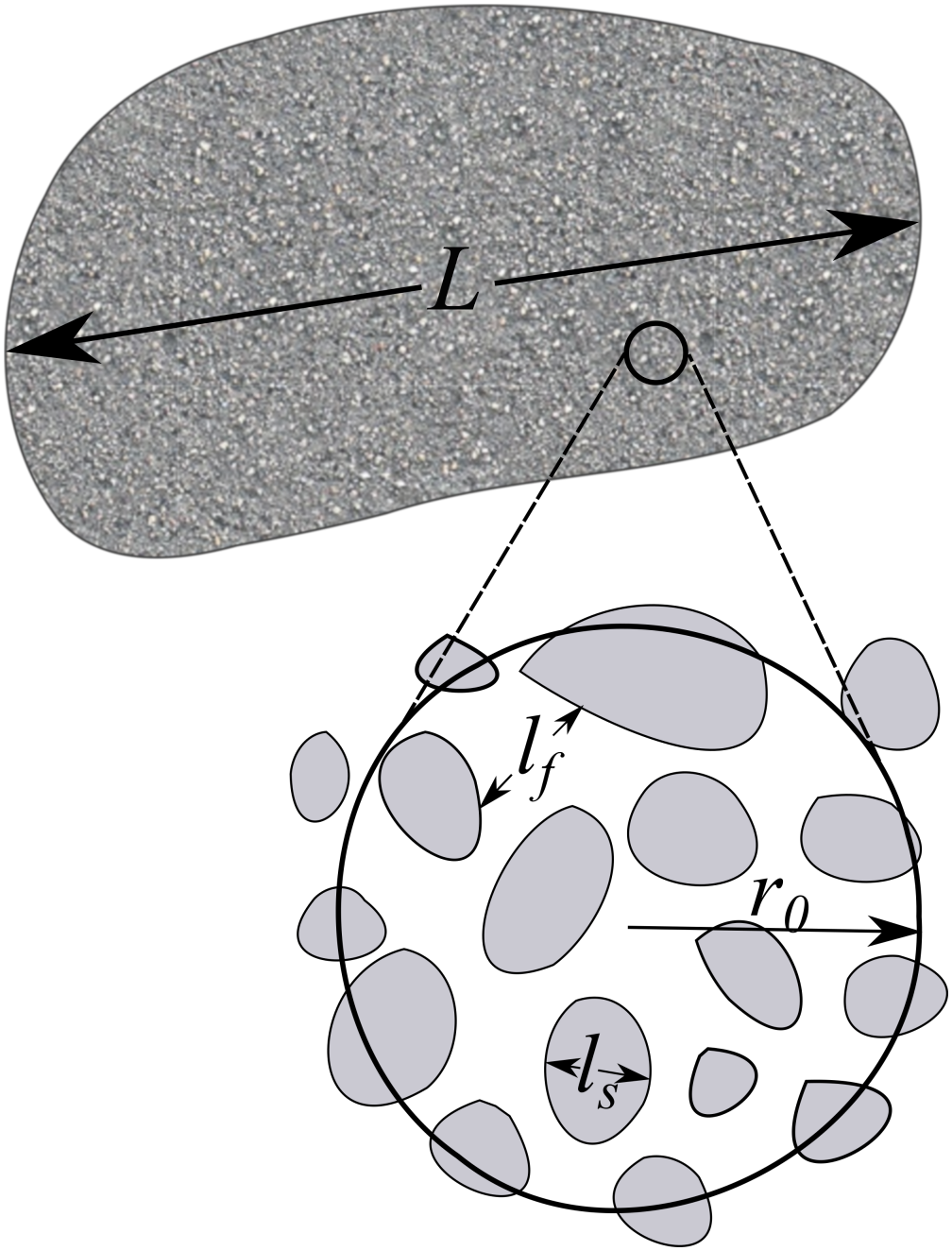

Figure 2.5: Macroscopic region and averaging volume

the system

$$\left.\begin{array}{c} \psi_f = \psi_s + f_1(\mathbf{r},t) \\ \textit{and} \\ \mathbf{n}_i \cdot \nabla\psi_f = \mathbf{n}_i \cdot \nabla\psi_s + f_2(\mathbf{r},t) \end{array}\right\} \textit{on } A_i \tag{2.2.20}$$

where A_i is the fluid-solid interfacial area inside the entire porous medium, and the functions f_1 and f_2 represent possible surface generation. It will be shown later, that these interfacial boundary conditions will be directly incorporated in the equations, and their effect on averaged quantities will be taken into account through the closure problem. System boundary conditions are inputs that are provided on the system boundaries, which have characteristic length scale L, and they lead to changes in average quantities (see Figure 2.5). These could be of the general form

$$\gamma_1\psi_f + \gamma_2\mathbf{n}_{fe} \cdot \nabla\psi_f = f_3(\mathbf{r},t) \textit{ on } A_{fe} \tag{2.2.21}$$

where A_{fe} is the area of the fluid phase at the system boundaries, $\gamma_1 \& \gamma_2$ are given functions and f_3 is the boundary forcing applied to the system. It is important to note that Eqn. (2.2.19) is defined only in the fluid domain Ω_f, and for complex geometries, the difficulty in its solution lies in the mathematical definition of the domain, and the intricate interfacial area A_i. Further, the fluid and solid equations are coupled through their interaction over the interfacial boundary conditions. For unsteady problems, an initial condition also needs to be provided,

$$\psi_f = f_4(\mathbf{x},0) \tag{2.2.22}$$

Similarly, a general conservation equation in the solid phase has the form,

$$\frac{\partial\psi_s}{\partial t} = -\nabla \cdot \mathbf{j}(\psi_s) + g_s \tag{2.2.23}$$

For a two-phase system, the interfacial area is the same, and interfacial boundary conditions are of the form

$$\left.\begin{array}{c} \psi_s = \psi_f - f_1(\mathbf{r},t) \\ \textit{and} \\ \mathbf{n}_i \cdot \nabla\psi_s = \mathbf{n}_i \cdot \nabla\psi_f - f_2(\mathbf{r},t) \end{array}\right\} \textit{on } A_i \tag{2.2.24}$$

The, system boundary conditions and initial condition are given, for example, by

$$\gamma_3\psi_s + \gamma_4\mathbf{n}_{se} \cdot \nabla\psi_f = f_5(\mathbf{r},t) \textit{ on } A_{se} \tag{2.2.25}$$

$$\psi_s = f_6(\mathbf{x}, 0) \tag{2.2.26}$$

where A_{se} is the solid part of the system boundaries, γ_3&γ_4 are given functions,$f_4$is a solid boundary forcing term, and f_6 is the solid initial condition. Again, the governing transport equation in the solid, Eqn. (2.2.23), is defined only in the solid domain Ω_s, and the difficulty in its solution lies in the definition of the complex geometrical domain. Conservation in the fluid phase is considered first, because the discussion dedicated to convective terms leads to extra complications, which are not present in the solid phase. The averaging process starts by applying the superficial averaging operator to every term in Eqn. (2.2.19)

$$\frac{1}{V}\int_{V_f}\frac{\partial\psi_f}{\partial t}dV + \frac{1}{V}\int_{V_f}\left[\nabla\cdot(\mathbf{v}\psi_f)\right]dV = -\frac{1}{V}\int_{V_f}\left[\nabla\cdot\mathbf{j}(\psi_f)\right]dV + \frac{1}{V}\int_{V_f} g_f dV \tag{2.2.27}$$

Assuming that the averaging volume is constant in time, the transient term can be rearranged by reversing the order of integration and differentiation

$$\frac{1}{V}\int_{V_f}\frac{\partial\psi_f}{\partial t}dV = \frac{\partial}{\partial t}\left(\frac{1}{V}\int_{V_f}\psi_f dV\right) = \frac{\partial\langle\psi_f\rangle}{\partial t} \tag{2.2.28}$$

For cases in which the volume V_f changes in time due to phase change (e.g. boiling, melting or solidification), this relationship cannot be used. Quintard et al [69, 96, 97, 98] and Whitaker [99] studied the application of VAT for two-phase flows, and developed tools to analyze them. Phase change phenomena are not included in this work, and Eqn. (2.2.28) is always assumed to be valid. Next, the convective term is considered. This term involves the average of a divergence thus, application of the SAT gives

$$\langle\nabla\cdot(\mathbf{v}\psi_f)\rangle = \nabla\cdot\langle\mathbf{v}\psi_f\rangle + \frac{1}{V}\int_{A_{fs}}\mathbf{n}_{fs}\cdot(\mathbf{v}\psi_f)\,dA \tag{2.2.29}$$

The first term is still expressed as the average of a product, and it will need additional consideration. Moving on to the flux term, application of the SAT gives

$$\langle\nabla\cdot\mathbf{j}(\psi_f)\rangle = \nabla\cdot\langle\mathbf{j}(\psi_f)\rangle + \frac{1}{V}\int_{A_{fs}}\mathbf{n}_{fs}\cdot\left[\mathbf{j}(\psi_f)\right]dA \tag{2.2.30}$$

The volumetric generation term can simply be rewritten as

$$\frac{1}{V}\int_{V_f} g_f dV = \langle g_f\rangle \tag{2.2.31}$$

Substituting back into Eqn. (2.2.27), a form of the averaged equation is

$$\begin{aligned}\frac{\partial \langle \psi_f \rangle}{\partial t} + \nabla \cdot \langle \mathbf{v}\psi_f \rangle + \frac{1}{V}\int\limits_{A_{fs}} \mathbf{n}_{fs} \cdot (\mathbf{v}\psi_f)\, dA = \\ = -\nabla \cdot \langle \mathbf{j}\,(\psi_f) \rangle - \frac{1}{V}\int\limits_{A_{fs}} \mathbf{n}_{fs} \cdot [\mathbf{j}\,(\psi_f)]\, dA + \langle g_f \rangle\end{aligned} \tag{2.2.32}$$

It should be noted that this form of the equation is exact and no assumptions or approximations have been made. Also, this is an averaged transport equation in terms of superficial averages, thus all quantities are per unit volume of porous media. An alternative form to Eqn. (2.2.32) expressed per unit volume of fluid phase can be obtained by using Eqn. (2.2.3),

$$\begin{aligned}\varepsilon_f \frac{\partial \langle \psi_f \rangle^f}{\partial t} + \nabla \cdot \left(\varepsilon_f \langle \mathbf{v}\psi_f \rangle^f \right) + \frac{1}{V}\int\limits_{A_{fs}} \mathbf{n}_{fs} \cdot (\mathbf{v}_f\psi_f)\, dA = \\ = -\nabla \cdot \left(\varepsilon_f \langle \mathbf{j}\,(\psi_f) \rangle^f \right) - \frac{1}{V}\int\limits_{A_{fs}} \mathbf{n}_{fs} \cdot [\mathbf{j}\,(\psi_f)]\, dA + \varepsilon_f \langle g_f \rangle^f\end{aligned} \tag{2.2.33}$$

It can be seen that the interfacial boundary conditions enter directly into the equations through the integral terms. Eqns. (2.2.32) and (2.2.33) still involve the average of a product in the convective term, and are not yet in a form that can be solved for the averaged quantities. To address this issue, the decomposition given in Eqn. (2.2.7) can be used,

$$\psi_f = \langle \psi_f \rangle^f + \tilde{\psi}_f, \qquad \mathbf{v} = \langle \mathbf{v} \rangle^f + \tilde{\mathbf{v}} \tag{2.2.34}$$

which allows one to rewrite the convective term as

$$\langle \mathbf{v}\psi_f \rangle = \left\langle \langle \mathbf{v} \rangle^f \langle \psi_f \rangle^f + \langle \mathbf{v} \rangle^f \tilde{\psi}_f + \tilde{\mathbf{v}} \langle \psi_f \rangle^f + \tilde{\mathbf{v}}\tilde{\psi}_f \right\rangle \tag{2.2.35}$$

Then, using the linearity of the averaging operator, and Eqn. (2.2.16) , the convective term simplifies further

$$\langle \mathbf{v}_f\psi_f \rangle = \varepsilon_f \langle \mathbf{v} \rangle^f \langle \psi_f \rangle^f + \langle \mathbf{v} \rangle^f \left\langle \tilde{\psi}_f \right\rangle + \langle \tilde{\mathbf{v}} \rangle \langle \psi_f \rangle^f + \left\langle \tilde{\mathbf{v}}\tilde{\psi}_f \right\rangle \tag{2.2.36}$$

Given the assumption that the average of fluctuations is zero, a final form of the convective term is obtained

$$\langle \mathbf{v}\psi_f \rangle = \varepsilon_f \langle \mathbf{v} \rangle^f \langle \psi_f \rangle^f + \left\langle \tilde{\mathbf{v}}\tilde{\psi}_f \right\rangle \tag{2.2.37}$$

Carbonell and Whitaker [76] give a lengthy discussion on this simplification of the convective term, and they state that the approximation is valid when the following length scale condition is satisfied

$$\frac{l_f}{L_\psi} \gg \frac{r_0^2}{L_\psi L_\varepsilon} \tag{2.2.38}$$

where L_ψ and L_ε are the length scale over which there are significant changes in $\langle\psi_f\rangle$ and ε_f respectively. Using this result, Eqn. (2.2.34) can be rewritten as

$$\begin{aligned} \varepsilon_f \frac{\partial \langle\psi_f\rangle^f}{\partial t} + \nabla\cdot\left(\varepsilon_f \langle\mathbf{v}\rangle^f \langle\psi_f\rangle^f\right) + \frac{1}{V}\int\limits_{A_{fs}} \mathbf{n}_{fs}\cdot(\mathbf{v}\psi_f)\, dA = \\ = -\nabla\cdot\left(\varepsilon_f \langle\mathbf{j}\left(\psi_f\right)\rangle^f\right) - \frac{1}{V}\int\limits_{A_{fs}} \mathbf{n}_{fs}\cdot\left[\mathbf{j}\left(\psi_f\right)\right] dA - \nabla\cdot\left(\varepsilon_f\left\langle\tilde{\mathbf{v}}\tilde{\psi}_f\right\rangle^f\right) + \varepsilon_f\langle g_f\rangle^f \end{aligned} \tag{2.2.39}$$

If the solid phase is impermeable the area integral on the left hand side will be zero because of the no-flow through boundary condition

$$\mathbf{v} = 0 \quad on \quad A_{fs} \tag{2.2.40}$$

In case blowing or suction at the solid wall are present, this integral will not be zero and it will have to be dealt with. For the rest of this work, it will be assumed that the walls are impermeable and the integral term will be dropped. Up to this point no assumptions about the flux terms have been made. However, in most scalar transports, the flux can be modeled by a general constitutive relationship in which the flux is proportional to the gradient of ψ_f

$$\mathbf{j}\left(\psi_f\right) = -\alpha_f \nabla\psi_f \tag{2.2.41}$$

and the proportionality constant α_f is the diffusivity of ψ_f in the medium (e.g. thermal or molecular diffusivity). Substituting this expression in Eqn. (2.2.39), the general transport equation becomes

$$\begin{aligned} \varepsilon_f \frac{\partial \langle\psi_f\rangle^f}{\partial t} + \nabla\cdot\left(\varepsilon_f \langle\mathbf{v}\rangle^f \langle\psi_f\rangle^f\right) = \nabla\cdot\left(\varepsilon_f\langle\alpha_f\nabla\psi_f\rangle^f\right) + \\ + \frac{1}{V}\int\limits_{A_{fs}} \mathbf{n}_{fs}\cdot\left[\alpha_f\nabla\psi_f\right] dA - \nabla\cdot\left(\varepsilon_f\left\langle\tilde{\mathbf{v}}\tilde{\psi}_f\right\rangle^f\right) + \varepsilon_f\langle g_f\rangle^f \end{aligned} \tag{2.2.42}$$

It can be seen that the first term on the right hand side contains the average of a gradient. Although the diffusion coefficient can vary significantly in the entire domain, it is usually

safe to assume that it is constant within the REV. Physically, this implies that changes in the diffusion coefficient occur over the macro length scale L, therefore, changes over the length scale r_0 are negligible. Using these assumptions and the SAT, the diffusive term can be rewritten as

$$\nabla \cdot \left(\varepsilon_f \langle \alpha_f \nabla \psi_f \rangle^f \right) = \nabla \cdot \left(\alpha_f \langle \nabla \psi_f \rangle \right) = \nabla \cdot \left[\alpha_f \left(\nabla \langle \psi_f \rangle + \frac{1}{V} \int\limits_{A_{fs}} \mathbf{n}_{fs} \psi_f dA \right) \right] \tag{2.2.43}$$

Substituting this result into Eqn. (2.2.42), and using Eqn. (2.2.3), the first form of the VAT conservation equation results

$$\begin{aligned} \varepsilon_f \frac{\partial \langle \psi_f \rangle^f}{\partial t} + \nabla \cdot \left(\varepsilon_f \langle \mathbf{v} \rangle^f \langle \psi_f \rangle^f \right) = \nabla \cdot \left[\alpha_f \nabla \left(\varepsilon_f \langle \psi_f \rangle^f \right) \right] + \\ + \nabla \cdot \left(\frac{\alpha_f}{V} \int\limits_{A_{fs}} \mathbf{n}_{fs} \psi_f dA \right) + \frac{1}{V} \int\limits_{A_{fs}} \mathbf{n}_{fs} \cdot \left[\alpha_f \nabla \psi_f \right] dA - \nabla \cdot \left(\varepsilon_f \left\langle \tilde{\mathbf{v}} \tilde{\psi}_f \right\rangle^f \right) + \varepsilon_f \langle g_f \rangle^f \end{aligned} \tag{2.2.44}$$

This form involves integrals of point-wise quantities, and certain closure schemes relate average quantities directly to these integrals. In other cases, it is required to obtain equations that involve only average and fluctuation quantities, or a mix of the two. This can be achieved by again using the decomposition given in Eqn. (2.2.7) to rewrite the first integral term as

$$\frac{1}{V} \int\limits_{A_{fs}} \mathbf{n}_{fs} \psi_{fs} dA = \frac{1}{V} \int\limits_{A_{fs}} \mathbf{n}_{fs} \langle \psi_f \rangle^f \Big|_{\mathbf{r}_f} dA + \frac{1}{V} \int\limits_{A_{fs}} \mathbf{n}_{fs} \tilde{\psi}_f \Big|_{\mathbf{r}_f} dA \tag{2.2.45}$$

The area integral of the intrinsic average is evaluated at a point other than the centroid, which would lead to a non-local form. Since it has already been assumed that the intrinsic average does not change within the REV (see Eqn. (2.2.8)), its value is constant also at interfaces within the REV, and Eqn. (2.2.45) can be written as

$$\frac{1}{V} \int\limits_{A_{fs}} \mathbf{n}_{fs} \psi_{fs} dA = \langle \psi_f \rangle^f \left[\frac{1}{V} \int\limits_{A_{fs}} \mathbf{n}_{fs} dA \right] + \frac{1}{V} \int\limits_{A_{fs}} \mathbf{n}_{fs} \tilde{\psi}_f \Big|_{\mathbf{r}_f} dA \tag{2.2.46}$$

In cases where the advective and/or inertial terms are negligible (e.g. geological porous media) or not present (e.g. solid phase), the assumptions invoked during the simplification of the convective term are not necessary. For such cases, Quintard and Whitaker [31, 32]

developed a set of definitions and length constraints that ensure that the simplification involved with the removal of the average from the area integral term in Eqn. (2.2.45) is physically valid. They found that this approximation is valid when

$$\nabla \langle \mathbf{y}_f \rangle \ll \mathbf{I}, \qquad \frac{r_0^2}{L_{\psi_1} L_\varepsilon} \ll 1 \tag{2.2.47}$$

where $L_{\psi_1}$is the length scale over which significant changes in $\nabla\nabla\langle\psi_f\rangle^f$ occur. It can be seen that in general, these are less restrictive conditions than Eqn. (2.2.38). Moving on, the integral of the normal over the interface area can be obtained by a clever application of the SAT

$$\langle \nabla 1 \rangle = \nabla \underbrace{\left(\frac{1}{V} \int\limits_{V_f} dA \right)}_{\varepsilon_f} + \frac{1}{V} \int\limits_{A_{fs}} \mathbf{n}_{fs} dA \rightarrow \frac{1}{V} \int\limits_{A_{fs}} \mathbf{n}_{fs} dA = -\nabla \varepsilon_f \tag{2.2.48}$$

and the area integral can be written as

$$\frac{1}{V} \int\limits_{A_{fs}} \mathbf{n}_{fs} \psi_{fs} dA = -\nabla \varepsilon_f \langle \psi_f \rangle^f + \frac{1}{V} \int\limits_{A_{fs}} \mathbf{n}_{fs} \tilde{\psi}_f \Big|_{\mathbf{r}_f} dA \tag{2.2.49}$$

Using this relation, another form of the diffusive term is obtained

$$\langle \alpha_f \nabla \psi_f \rangle = \varepsilon_f \alpha_f \nabla \langle \psi_f \rangle^f + \frac{\alpha_f}{V} \int\limits_{A_{fs}} \mathbf{n}_{fs} \tilde{\psi}_f dA \tag{2.2.50}$$

Substituting this result into Eqn. (2.2.42), another expression of the VAT governing equation is given by

$$\begin{aligned} \varepsilon_f \frac{\partial \langle \psi_f \rangle^f}{\partial t} + \nabla \cdot \left(\varepsilon_f \langle \mathbf{v} \rangle^f \langle \psi_f \rangle^f \right) = \nabla \cdot \left(\alpha_f \varepsilon_f \nabla \langle \psi_f \rangle^f \right) + \\ + \nabla \cdot \left(\frac{\alpha_f}{V} \int\limits_{A_{fs}} \mathbf{n}_{fs} \tilde{\psi}_f dA \right) + \frac{1}{V} \int\limits_{A_{fs}} \mathbf{n}_{fs} \cdot \left[\alpha_f \nabla \psi_f \right] dA - \nabla \cdot \left(\varepsilon_f \left\langle \tilde{\mathbf{v}} \tilde{\psi}_f \right\rangle^f \right) + \varepsilon_f \langle g_f \rangle^f \end{aligned} \tag{2.2.51}$$

This equation, unlike the point-wise equations from which it was derived, is defined everywhere in the porous medium; its domain is then $\Omega = \Omega_f \cup \Omega_s$. It can be seen how some closure will be required to model the fluctuation and area integral terms that appear in this equation. These fluctuations will depend on the microscopic structure of the porous media and will transmit information from the lower microscopic scale to the macroscopic scale. The

correct modeling of these terms is the key to obtaining good results in the study of transport using VAT.

The approximations used are generally safe everywhere in a porous media, except close to the boundaries of the porous media. In these areas, the geometry, and average quantities have steep gradients, which implies that the length scale L_ε and L_ψ are comparable to $r_0$and a different type of analysis needs to be carried out. The interface with homogenous media is particularly problematic, and a review of the treatment of boundary conditions will be given in a later section.

The derivation of a solid phase general transport equation follows closely the fluid phase derivation, except that obviously there is no flow, and all the velocity terms are equal to zero. Thus, by simply applying the SAT to Eqn. (2.2.23), and assuming that the flux is proportional to the gradient, a form of the equation is given by

$$\begin{aligned}\varepsilon_s \frac{\partial \langle \psi_s \rangle^s}{\partial t} = \nabla \cdot \left[\alpha_s \nabla \left(\varepsilon_s \langle \psi_s \rangle^s \right) \right] + \nabla \cdot \left(\frac{\alpha_s}{V} \int\limits_{A_{sf}} \mathbf{n}_{sf} \psi_s dA \right) + \\ + \frac{1}{V} \int\limits_{A_{sf}} \mathbf{n}_{sf} \cdot \left[\alpha_s \nabla \psi_s \right] dA + \varepsilon_s \langle g_s \rangle^s\end{aligned} \tag{2.2.52}$$

Since most of the assumptions were made to simplify the convective term, the only assumption for this form of the transport equation is the length scale disparity

$$\frac{l_s}{L} \ll 1 \tag{2.2.53}$$

where l_s is the size of the solid particles. It is again of interest to express the first integral term on the right hand side in terms of intrinsic averages and fluctuations from it. Similar to the analysis conducted for the fluid phase, the point-wise value is decomposed, the averaged value is taken out of the integral and the result given in Eqn. (2.2.48) is applied to obtain the following alternative form

$$\begin{aligned}\varepsilon_s \frac{\partial \langle \psi_s \rangle^s}{\partial t} = \nabla \cdot \left(\alpha_s \varepsilon_s \nabla \langle \psi_s \rangle^s \right) + \nabla \cdot \left(\frac{\alpha_s}{V} \int\limits_{A_{fs}} \mathbf{n}_{sf} \tilde{\psi}_s dA \right) + \\ + \frac{1}{V} \int\limits_{A_{fs}} \mathbf{n}_{sf} \cdot \left[\alpha_s \nabla \psi_s \right] dA + \varepsilon_s \langle g_s \rangle^s\end{aligned} \tag{2.2.54}$$

and the length constraints associated with this simplification are given by

$$\nabla \langle \mathbf{y}_f \rangle \ll \mathbf{I}, \qquad \frac{r_0^2}{L_{\psi_1} L_{\varepsilon_s}} \ll 1 \tag{2.2.55}$$

Note, that in this case L_{ψ_1} is the length scale associated with changes in$\nabla\nabla\langle\psi_s\rangle^s$, and in general, it is not equal to L_{ψ_1} defined in Eqn. (2.2.47).

Since in the rest of the study, only steady problems will be considered, little attention will be devoted to the effects of time variations. For cases in which transport is linear but unsteady, similar arguments to the ones carried out for the length scales, can be carried out for time scales. If it can be assumed that the time scales associated with changes in micro scale phenomena are much smaller than the time scale associated with macro scale quantities, the closure problem can be considered quasi-steady, and no additional complications arise in the derivation or closure. On the other hand, when the time scales of variations in the micro and macro scale phenomena are comparable, these problems are coupled in time and are much more difficult to solve. Turbulent conservation equations, which are implicitly unsteady, are treated in a separate section due to the extra complications, and the incomplete state of the theory. Now that averaged forms of the generalized VAT transport equations in the fluid and solid have been developed, they can be applied to individual variables to obtain the VAT form for mass, momentum and energy equations.

2.3 Development of the VAT Continuity Equation

The VAT mass conservation equation can be obtained by defining $\psi_f = \rho_f$. Furthermore, no diffusion or generation of mass are present, therefore $\alpha_f = 0$ and $g_f = 0$. Substituting these definitions in Eqn. (2.2.44), a first form of the VAT mass conservation equation is obtained

$$\varepsilon_f \frac{\partial \langle \rho_f \rangle^f}{\partial t} + \nabla \cdot \left(\varepsilon_f \langle \mathbf{v} \rangle^f \langle \rho_f \rangle^f \right) + \nabla \cdot \left(\varepsilon_f \langle \tilde{\mathbf{v}} \tilde{\rho}_f \rangle^f \right) = 0 \tag{2.3.1}$$

A few studies have been carried out for compressible flow in porous media using VAT [100, 53, 101]; however, there are few examples in which compressible flow models are necessary in a porous medium. Moin et al. [102] developed a widely used model for LES simulation in compressible flow, in which the mass conservation equation is very similar to Eqn. (2.3.1). Sirignano [103], in his analysis of turbulent spray flows, provides an interesting analysis of both the LES and VAT approach. In all cases considered in the rest of this work, it will be assumed that the flow is incompressible, and the continuity equation becomes

$$\nabla \cdot \langle \mathbf{v} \rangle = 0 \tag{2.3.2}$$

An alternative form is obtained by using the intrinsic average

$$\nabla \cdot \left(\varepsilon_f \langle \mathbf{v} \rangle^f \right) = \nabla \varepsilon_f \cdot \langle \mathbf{v} \rangle^f + \varepsilon_f \nabla \cdot \langle \mathbf{v} \rangle^f = 0 \tag{2.3.3}$$

thus

$$\nabla \cdot \langle \mathbf{v} \rangle^f = -\frac{\nabla \varepsilon_f}{\varepsilon_f} \cdot \langle \mathbf{v} \rangle^f \tag{2.3.4}$$

Note that, when porosity is not constant, the superficial velocity is solenoidal (divergence-free) while the intrinsic velocity is not. This is an important difference since several analytic and numerical solution methods take advantage of the divergence-free nature of the velocity vector field, which suggests that, for variable porosity, it is advantageous to solve for the superficial velocity.

2.4 Development of the VAT Momentum Equation

The particular form of the flux term in the momentum equation, leads one to start the development from an earlier form of the governing equations. The quantity conserved is

momentum, therefore $\psi_f = \rho_f \mathbf{v}$. For a Newtonian incompressible fluid the flux is given by $\mathbf{j}(\rho_f \mathbf{v}) = -\nu_f \nabla(\rho_f \mathbf{v}) + p_f \mathbf{I}$, and the only body force considered is gravity, $g_f = \rho_f \mathbf{g}$. Substituting these definitions into Eqn. (2.2.39), the following result is obtained

$$\begin{aligned} &\frac{\partial \langle \rho_f \mathbf{v} \rangle}{\partial t} + \nabla \cdot \left(\varepsilon_f \langle \rho_f \mathbf{v} \rangle^f \langle \mathbf{v} \rangle^f + \varepsilon_f \langle \rho_f \tilde{\mathbf{v}} \tilde{\mathbf{v}} \rangle^f \right) + \frac{1}{V} \int\limits_{A_{fs}} \mathbf{n}_{fs} \cdot (\rho_f \mathbf{v} \mathbf{v}) \, dA = \\ &= \nabla \cdot \langle \nu_f \nabla \cdot (\rho_f \mathbf{v}) - p_f \mathbf{I} \rangle - \frac{1}{V} \int\limits_{A_{fs}} \mathbf{n}_{fs} \cdot [-\nu_f \nabla \cdot (\rho_f \mathbf{v}) + p_f \mathbf{I}] \, dA + \langle \rho_f \mathbf{g} \rangle \end{aligned} \tag{2.4.1}$$

Following the discussion in the previous section, it is important to point out that this form is only valid when the average velocity vector can be considered constant within the REV, and the average of fluctuations is zero. For incompressible flow, impermeable solid phase, and constant gravity, Eqn. (2.4.1) becomes

$$\begin{aligned} \rho_f \frac{\partial \langle \mathbf{v} \rangle}{\partial t} + \rho_f \nabla \cdot \left(\varepsilon_f \langle \mathbf{v} \rangle^f \langle \mathbf{v} \rangle^f \right) = -\nabla \langle p_f \rangle + \nabla \cdot \langle \mu_f \nabla \mathbf{v}_f \rangle + \\ -\frac{1}{V} \int\limits_{A_{fs}} \mathbf{n}_{fs} \cdot [-\mu_f \nabla \mathbf{v}_f + p_f \mathbf{I}] \, dA - \rho_f \nabla \cdot \left(\varepsilon_f \langle \tilde{\mathbf{v}}_f \tilde{\mathbf{v}}_f \rangle^f \right) + \varepsilon_f \rho_f \langle \mathbf{g} \rangle^f \end{aligned} \tag{2.4.2}$$

The convective term can be further simplified using continuity, Eqn. (2.3.3),

$$\begin{aligned} &\nabla \cdot \left(\varepsilon_f \langle \mathbf{v} \rangle^f \langle \mathbf{v} \rangle^f \right) = \nabla \cdot \left(\langle \mathbf{v} \rangle \langle \mathbf{v} \rangle^f \right) = \\ &= (\nabla \cdot \langle \mathbf{v} \rangle) \langle \mathbf{v} \rangle^f + \langle \mathbf{v} \rangle \cdot \nabla \langle \mathbf{v} \rangle^f = \varepsilon_f \langle \mathbf{v} \rangle^f \cdot \nabla \langle \mathbf{v} \rangle^f \end{aligned} \tag{2.4.3}$$

If viscosity changes only over the macro-length scale, it can be taken out of the integral and the diffusive term simplifies to

$$\nabla \cdot \langle \mu_f \nabla \mathbf{v} \rangle = \nabla \cdot (\mu_f \langle \nabla \mathbf{v} \rangle) \tag{2.4.4}$$

Using the SAT, the velocity gradient tensor can be rewritten as

$$\langle \nabla \mathbf{v} \rangle = \nabla \langle \mathbf{v} \rangle + \frac{1}{V} \int\limits_{A_{fs}} \mathbf{n}_{fs} \cdot \mathbf{v} dA \tag{2.4.5}$$

and, for no flow-through at the interface, the integral term is zero,

$$\langle \nabla \mathbf{v} \rangle = \nabla \langle \mathbf{v} \rangle \tag{2.4.6}$$

Substituting Eqns. (2.4.3) and (2.4.6), into Eqn. (2.4.2), and using Eqn. (2.2.3) a first form of the VAT equation is obtained

$$\rho_f \varepsilon_f \frac{\partial \langle \mathbf{v} \rangle}{\partial t} + \rho_f \varepsilon_f \langle \mathbf{v} \rangle^f \cdot \nabla \langle \mathbf{v} \rangle^f = -\nabla \left(\varepsilon_f \langle p_f \rangle^f \right) + \nabla \cdot \left[\mu_f \nabla \left(\phi_f \langle \mathbf{v} \rangle^f \right) \right] + \\ + \frac{1}{V} \int\limits_{A_{fs}} \mathbf{n}_{fs} \cdot \left[-p_f \mathbf{I} + \mu_f \nabla \mathbf{v} \right] dA - \rho_f \nabla \cdot \left(\varepsilon_f \langle \tilde{\mathbf{v}} \tilde{\mathbf{v}} \rangle^f \right) + \rho_f \varepsilon_f \langle \mathbf{g} \rangle^f \tag{2.4.7}$$

The first integral term contains the integral of the pressure and drag forces at the interface. It will be shown later, that some closure schemes close these point-wise integral terms directly. Other closure schemes work on equations that are given entirely in terms of velocity and fluctuations. These equations can be derived by again using the decomposition of velocity and pressure into their intrinsic average and fluctuation values, and expressing the pressure and velocity gradient tensor inside the integrals as

$$\frac{1}{V} \int\limits_{A_{fs}} \mathbf{n}_{fs} \cdot (\mu_f \nabla \mathbf{v}) \, dA = \frac{1}{V} \int\limits_{A_{fs}} \mathbf{n}_{fs} \cdot \left(\mu_f \nabla \langle \mathbf{v} \rangle^f \right) dA + \frac{1}{V} \int\limits_{A_{fs}} \mathbf{n}_{fs} \cdot (\mu_f \nabla \tilde{\mathbf{v}}) \, dA \tag{2.4.8}$$

$$\frac{1}{V} \int\limits_{A_{fs}} \mathbf{n}_{fs} p_f dA = \frac{1}{V} \int\limits_{A_{fs}} \mathbf{n}_{fs} \langle p_f \rangle^f dA + \frac{1}{V} \int\limits_{A_{fs}} \mathbf{n}_{fs} \tilde{p}_f dA \tag{2.4.9}$$

In the decomposition of the convective term, it has been assumed that changes in average velocity within the REV are negligible. To remove $\nabla \langle \mathbf{v} \rangle^f$ and $\langle p_f \rangle^f$ from the integrals, it needs to be further assumed that changes in these quantities are also negligible within the REV. With these assumptions, and using Eqn. (2.2.48), it can be shown that

$$\frac{1}{V} \int\limits_{A_{fs}} \mathbf{n}_{fs} \cdot (\mu_f \nabla \mathbf{v}) \, dA = -\mu_f \nabla \varepsilon_f \nabla \langle \mathbf{v} \rangle^f + \frac{\mu_f}{V} \int\limits_{A_{fs}} \mathbf{n}_{fs} \cdot (\nabla \tilde{\mathbf{v}}) \, dA \tag{2.4.10}$$

$$\frac{1}{V} \int\limits_{A_{fs}} \mathbf{n}_{fs} p_f dA = -\nabla \varepsilon_f \langle p_f \rangle^f + \frac{1}{V} \int\limits_{A_{fs}} \mathbf{n}_{fs} \tilde{p}_f dA \tag{2.4.11}$$

Whitaker [67] developed some length constraints that need to be satisfied for this assumption to be valid

$$\nabla \langle \mathbf{y}_\beta \rangle \ll \mathbf{I}, \quad \frac{r_0^2}{L_\phi L_{v_2}} \ll 1, \quad \frac{r_0^2}{L_\phi L_{p_1}} \ll 1 \tag{2.4.12}$$

where L_ε, L_{v_2}, and L_{p_1} are the length scale associated with changes in $\nabla \varepsilon_f$,$\nabla \nabla \nabla \langle \mathbf{v} \rangle^f$ and $\nabla \nabla \langle p_f \rangle^f$, respectively. Substituting these results, into Eqn. (2.4.7), a second form of the

VAT momentum equation is obtained

$$\rho_f \varepsilon_f \frac{\partial \langle \mathbf{v} \rangle^f}{\partial t} + \rho_f \varepsilon_f \langle \mathbf{v} \rangle^f \cdot \nabla \langle \mathbf{v} \rangle^f = -\varepsilon_f \nabla \langle p_f \rangle^f + \nabla \cdot \left(\mu_f \varepsilon_f \nabla \langle \mathbf{v} \rangle^f \right) + \\ + \frac{1}{V} \int_{A_{fs}} \mathbf{n}_{fs} \cdot \left[-\tilde{p}_f \mathbf{I} + \mu_f \nabla \tilde{\mathbf{v}} \right] dA - \rho_f \nabla \cdot \left(\varepsilon_f \langle \tilde{\mathbf{v}} \tilde{\mathbf{v}} \rangle^f \right) + \varepsilon_f \rho_f \langle \mathbf{g} \rangle^f \tag{2.4.13}$$

which is entirely in terms of average quantities and fluctuations. It is important to summarize the assumptions made to develop the two forms of the VAT momentum equation, Eqns. (2.4.7) and (2.4.13). It has been assumed that the fluid is Newtonian, flow is incompressible, solid boundaries are impermeable, and viscosity is constant within the REV. Furthermore, it has been assumed that the intrinsic average of velocity does not change significantly within the REV, the average of the fluctuations is zero. The form given in Eqn. (2.4.13) also implies that the length constraints given by Eqn. (2.4.12) are valid. Several form of the VAT momentum equation can be developed to suit different type of closure. However, independently of their form, in order to obtain an equation that involves only the average velocity, a closure scheme needs to be developed to model the fluctuation terms and area integrals. Proper modeling of these terms is crucial in order to obtain accurate results and most of the research in recent years has been geared towards the analysis of these terms.

2.5 Development of the VAT Energy Equation

The VAT energy equation for the fluid phase can be derived by substituting $\psi_f = \rho_f c_{pf} T_f$in the general VAT transport equation Eqn. (2.2.42). The diffusivity is given by the thermal diffusivity $\alpha_f = \kappa_f = k_f / \rho_f c_{pf}$, and a constant volumetric heat source is considered $g_f = \dot{q}_f'''$ (e.g. Joule heating).

$$\varepsilon_f \frac{\partial \langle \rho_f c_{pf} T_f \rangle^f}{\partial t} + \nabla \cdot \left(\varepsilon_f \langle \rho_f c_{pf} T_f \rangle^f \langle \mathbf{v} \rangle^f \right) + \frac{1}{V} \int_{A_{fs}} \mathbf{n}_{fs} \cdot \left(\mathbf{v} \rho_f c_{pf} T_f \right) dA = \\ = \nabla \cdot \langle \kappa_f \nabla \rho_f c_{pf} T_f \rangle + \frac{1}{V} \int_{A_{fs}} \mathbf{n}_{fs} \cdot \left[\kappa_f \nabla \rho_f c_{pf} T_f \right] dA - \nabla \cdot \left(\varepsilon_f \left\langle \rho_f c_{pf} \tilde{T}_f \tilde{\mathbf{v}} \right\rangle^f \right) + \varepsilon_f \left\langle \dot{q}_f''' \right\rangle^f \tag{2.5.1}$$

In the derivation of this form, following the discussion in the previous section, it is implied that the averaged values do not change significantly within the REV, and that the average of fluctuating quantities is zero. Assuming that flow is incompressible, and specific heat is a constant, Eqn. (2.5.1) simplifies to

$$\begin{aligned}\rho_f c_{pf}\varepsilon_f\frac{\partial\langle T_f\rangle^f}{\partial t}+\rho_f c_{pf}\nabla\cdot\left(\varepsilon_f\langle T_f\rangle^f\langle\mathbf{v}\rangle^f\right)+\rho_f c_{pf}\frac{1}{V}\int\limits_{A_{fs}}\mathbf{n}_{fs}\cdot(\mathbf{v}T_f)\,dA=\\ =\nabla\cdot\langle k_f\nabla T_f\rangle+\frac{1}{V}\int\limits_{A_{fs}}\mathbf{n}_{fs}\cdot[k_f\nabla T_f]\,dA-\rho_f c_{pf}\nabla\cdot\left(\phi_f\left\langle\tilde{T}_f\tilde{\mathbf{v}}_f\right\rangle^f\right)+\varepsilon_f\left\langle\dot{q}_f'''\right\rangle^f\end{aligned}\tag{2.5.2}$$

Assuming also that the solid phase is impermeable, and using continuity, Eqn. (2.5.2) can be further simplified to obtain

$$\begin{aligned}\varepsilon_f\rho_f c_{pf}\frac{\partial\langle T_f\rangle^f}{\partial t}+\varepsilon_f\rho_f c_{pf}\langle\mathbf{v}\rangle^f\cdot\nabla\langle T_f\rangle^f=\\ =\nabla\cdot\langle k_f\nabla T_f\rangle+\frac{1}{V}\int\limits_{A_{fs}}\mathbf{n}_{fs}\cdot[k_f\nabla T_f]\,dA-\rho_f c_{pf}\nabla\cdot\left(\phi_f\left\langle\tilde{\mathbf{v}}\tilde{T}_f\right\rangle^f\right)+\varepsilon_f\left\langle\dot{q}_f'''\right\rangle^f\end{aligned}\tag{2.5.3}$$

Next, the diffusive terms on the right hand side needs to be expressed in terms of gradients of averaged quantities. Assuming that the thermal conductivity is constant within the REV, and using the SAT, the diffusive term can be rewritten as

$$\nabla\cdot\langle k_f\nabla T_f\rangle=\nabla\cdot\left(k_f\langle\nabla T_f\rangle\right)=\nabla\cdot\left(k_f\nabla\langle T_f\rangle+\frac{k_f}{V}\int\limits_{A_{fs}}\mathbf{n}_{fs}T_f dA\right)\tag{2.5.4}$$

Substituting Eqn. (2.5.4) back into Eqn. (2.5.3), and expressing everything in terms of intrinsic values, a first form of the VAT energy equation is obtained

$$\begin{aligned}\varepsilon_f\rho_f c_{pf}\frac{\partial\langle T_f\rangle^f}{\partial t}+\varepsilon_f\rho_f c_{pf}\langle\mathbf{v}\rangle^f\cdot\nabla\langle T_f\rangle^f=\nabla\cdot\left[k_f\nabla\left(\varepsilon_f\langle T_f\rangle^f\right)+\frac{k_f}{V}\int\limits_{A_{fs}}\mathbf{n}_{fs}T_f dA\right]+\\ +\frac{1}{V}\int\limits_{A_{fs}}\mathbf{n}_{fs}\cdot[k_f\nabla T_f]\,dA-\rho_f c_{pf}\nabla\cdot\left(\phi_f\left\langle\tilde{\mathbf{v}}\tilde{T}_f\right\rangle^f\right)+\varepsilon_f\left\langle\dot{q}_f'''\right\rangle^f\end{aligned}\tag{2.5.5}$$

In most closure schemes, the interface flux term, is closed in terms of the heat transfer coefficient based on the point-wise terms, therefore, the decomposition will be applied only

to the first term on the right hand side of Eqn. (2.5.5)

$$\begin{aligned}\nabla\cdot\left(k_f\nabla\left(\varepsilon_f\langle T_f\rangle^f\right)+\frac{k_f}{V}\int\limits_{A_{fs}}\mathbf{n}_{fs}T_f dA\right)=\\ =\nabla\cdot\left(k_f\nabla\left(\varepsilon_f\langle T_f\rangle^f\right)+\frac{k_f}{V}\int\limits_{A_{fs}}\mathbf{n}_{fs}\langle T_f\rangle^f dA+\frac{k_f}{V}\int\limits_{A_{fs}}\mathbf{n}_{fs}\tilde{T}_f dA\right)\end{aligned} \tag{2.5.6}$$

Since average temperature variations have already been assumed negligible within the REV (in the derivation of the convective terms), the intrinsic average can be taken out of the integral without additional constraints. Following the development from the previous sections, the diffusion term becomes

$$\begin{aligned}\nabla\cdot\left[k_f\nabla\left(\varepsilon_f\langle T_f\rangle^f\right)-k_f\nabla\varepsilon_f\langle T_f\rangle^f+\frac{k_f}{V}\int\limits_{A_{fs}}\mathbf{n}_{fs}\tilde{T}_f dA\right]=\\ =\nabla\cdot\left(\varepsilon_f k_f\nabla\langle T_f\rangle^f\right)+\nabla\cdot\left(\frac{k_f}{V}\int\limits_{A_{fs}}\mathbf{n}_{fs}\tilde{T}_f dA\right)\end{aligned} \tag{2.5.7}$$

Using this result in Eqn. (2.5.3), a second form of the VAT energy equation for the fluid phase is obtained

$$\begin{aligned}\varepsilon_f\rho_f c_{pf}\frac{\partial\langle T_f\rangle^f}{\partial t}+\varepsilon_f\rho_f c_{pf}\langle\mathbf{v}\rangle^f\cdot\nabla\langle T_f\rangle^f=\nabla\cdot\left(\varepsilon_f k_f\nabla\langle T_f\rangle^f\right)+\nabla\cdot\left(\frac{k_f}{V}\int\limits_{A_{fs}}\mathbf{n}_{fs}\tilde{T}_f dA\right)+\\ +\frac{1}{V}\int\limits_{A_{fs}}\mathbf{n}_{fs}\cdot\left[k_f\nabla T_f\right]dA-\rho_f c_{pf}\nabla\cdot\left(\varepsilon_f\left\langle\tilde{\mathbf{v}}_f\tilde{T}_f\right\rangle^f\right)+\varepsilon_f\left\langle\dot{q}_f'''\right\rangle^f\end{aligned} \tag{2.5.8}$$

The development of the solid equation is carried out in a similar way. Substituting $\psi_s = \rho_s c_{ps} T_s$, $\alpha_s = \kappa_s = {}^{k_s}/_{\rho_s c_{ps}}$ and $g_s = \dot{q}_s'''$ in Eqn. (2.2.52), a first form of the equation is given by

$$\begin{aligned}\varepsilon_s\frac{\partial\langle\rho_s c_{ps}T_s\rangle^s}{\partial t}=\nabla\cdot\left[\kappa_s\nabla\left(\varepsilon_s\langle\rho_s c_{ps}T_s\rangle^s\right)\right]+\nabla\cdot\left(\frac{\kappa_s}{V}\int\limits_{A_{sf}}\mathbf{n}_{sf}\rho_s c_{ps}T_s dA\right)+\\ +\frac{1}{V}\int\limits_{A_{sf}}\mathbf{n}_{sf}\cdot\left[\kappa_s\nabla\rho_s c_{ps}T_s\right]dA+\varepsilon_s\left\langle\dot{q}_s'''\right\rangle^s\end{aligned} \tag{2.5.9}$$

Assuming that $\rho_s c_{ps}$ is constant, Eqn. (2.5.9) can be rearranged as

$$\varepsilon_s \rho_s c_{ps} \frac{\partial \langle T_s \rangle^s}{\partial t} = \nabla \cdot \left[k_s \nabla \left(\varepsilon_s \langle T_s \rangle^s \right) \right] + \nabla \cdot \left(\frac{k_s}{V} \int\limits_{A_{sf}} \mathbf{n}_{sf} T_s dA \right) + \\ + \frac{1}{V} \int\limits_{A_{sf}} \mathbf{n}_{sf} \cdot \left[k_s \nabla T_s \right] dA + \varepsilon_s \left\langle \dot{q}_s''' \right\rangle^s \tag{2.5.10}$$

Assuming that changes in the intrinsic average of the solid temperature are negligible within the REV, it can be taken out of the integral, and another form of energy conservation in the solid is given by

$$\varepsilon_s \rho_s c_{ps} \frac{\partial \langle T_s \rangle^s}{\partial t} = \nabla \cdot \left[\varepsilon_s k_s \nabla \langle T_s \rangle^s \right] + \nabla \cdot \left(\frac{k_s}{V} \int\limits_{A_{sf}} \mathbf{n}_{sf} \tilde{T}_s dA \right) + \\ + \frac{1}{V} \int\limits_{A_{sf}} \mathbf{n}_{sf} \cdot \left[k_s \nabla T_s \right] dA + \varepsilon_s \left\langle \dot{q}_s''' \right\rangle^s \tag{2.5.11}$$

This last assumption implies that the following length conditions are satisfied

$$\nabla \langle \mathbf{y}_f \rangle \ll \mathbf{I}, \quad \frac{r_0^2}{L_\varepsilon L_{T1}} \ll 1 \tag{2.5.12}$$

where L_{T1} is the length scale associated with changes in $\nabla \nabla \langle T_s \rangle^s$. Since $\varepsilon_s = 1 - \varepsilon_f$, the length scale associated changes in porosity, L_ε, will be the same for both phases. The governing VAT mass, momentum and continuity equations were rigorously derived by applying the averaging operator, and making certain assumptions about the behavior of the averaged functions. These assumptions are relatively safe for most real porous media and multi-scale engineered structures. Modeling of the integral and fluctuation terms is still needed to obtain closed form of the equations, however, before discussing closure, the development of the turbulence equations is carried out.

2.6 Closure

The accuracy of the analysis of transport phenomena using VAT is strongly dependent on the accuracy of the closing scheme. Although some assumptions about length scale disparities are used in the derivation of the governing equations, most of the approximations are

introduced in the closure models. For natural porous media, the determination of geometric properties, such as porosity and internal structure can be a challenge and will introduce further approximations. In man-made multi-scale systems such as heat exchangers, heat sinks and packed beds, the determination of these properties is usually much simpler, and can be obtained analytically. In these systems, the challenges in the solution of the governing equations all lie in the determination of the integral and fluctuation terms for different flow conditions. The first step is the definition of the closure parameters. A few closure schemes will be mentioned, and the closure scheme developed by Travkin and Catton [38] will be discussed in detail. The second challenge is in the determination of the defined closure parameters. Three main methods to obtain closure variables are available:

- Analytical
- Experimental
- Numerical

Analytical solutions are usually possible only for very simple geometries, and involve several approximations and will therefore not be treated in this paper. Experimental closure, when carried out accurately, is usually the most accurate method and should always be used to validate results obtained through other means. A review of a few important correlations will be given in this section. Development of experimental techniques and their implementation is often time consuming and expensive. As a result, and due to the improvement in commercially available CFD software, and increase in commonly available computational power, numerical simulations have quickly become the most common technique to obtain closure relations. Furthermore, numerical simulations provide solution at any point in the (discretized) domain and therefore they allow the determination of certain closure parameters that are experimentally very hard to measure. The procedure developed by Zhou [104] to obtain closure through CFD will be presented, along with selected numerical results. Following the structure of the first section, the laminar equations are closed first, followed by a discussion of the closure parameters. Closure of the turbulent transport equations, requires

further closure and approximation due to the double averaging procedure, and it is treated in a separate section.

2.6.1 Closure of VAT Momentum Equation

In Section 2.4, the laminar VAT momentum equations were rigorously derived by using averaging operators on the point-wise momentum equation, and several forms of the equations were provided. The closure scheme defined by Travkin and Catton [38] for the laminar momentum equation is best applied by starting from Eqn. (2.4.7), which is repeated here in tensor notation

$$\begin{aligned}\rho_f \varepsilon_f \frac{\partial \langle v\rangle_i^f}{\partial t} + \rho_f \varepsilon_f \langle v\rangle_j^f \frac{\partial \langle v\rangle_i^f}{\partial x_j} = -\frac{\partial}{\partial x_i}\left(\varepsilon_f \langle p_f\rangle^f\right) + \frac{\partial}{\partial x_j}\left[\mu_f \frac{\partial}{\partial x_j}\left(\varepsilon_f \langle v\rangle_i^f\right)\right] + \\ + \frac{1}{V}\int\limits_{A_{fs}} n_{fs,j}\left[-p_f\delta_{ij} + \mu_f \frac{\partial v_i}{\partial x_j}\right] dA - \rho_f \frac{\partial}{\partial x_j}\left(\varepsilon_f \langle \tilde{v}_i \tilde{v}_j\rangle^f\right) + \rho_f \varepsilon_f \langle g\rangle_i^f\end{aligned} \tag{2.6.1}$$

The pressure drag resistance integral term is closed by defining a diagonal form drag tensor

$$c_{pd,ii} = \frac{\left[\frac{1}{V}\int\limits_{A_{fs}} n_{fs} p_f dA\right]_i}{{}^1\!/_2 \rho_f \left(\langle v\rangle_i^f\right)^2 S_{wp}} \tag{2.6.2}$$

where $S_{wp} = A_{fs,p}/V$ is the cross flow interface projected area per unit volume. The pressure integral term can then be closed

$$\left[\frac{1}{V}\int\limits_{A_{fs}} n_{fs} p_f dA\right]_j \delta_{ij} = \frac{1}{2}\rho_f S_{wp} c_{dp,ij}\left(\langle v\rangle_j^f\right)^2 \tag{2.6.3}$$

Similarly, the velocity gradient integral, can be closed using a skin friction drag tensor

$$c_{f,ij} = \frac{\left[\frac{1}{V}\int\limits_{A_{fs}} n_{fs}\left(-\mu_f \frac{\partial v_i}{\partial x_j}\right) dA\right]_j}{{}^1\!/_2 \rho_f \left(\langle v\rangle_i^f\right)^2 S_w} \tag{2.6.4}$$

where $S_w = A_{fs}/V$, and the traction integral can be closed

$$\left[\frac{1}{V}\int\limits_{A_{fs}} n_{fs,j}\mu_f \frac{\partial v_i}{\partial x_j} dA\right]_j = \frac{1}{2}\rho_f S_w c_{f,ij}\left(\langle v_f\rangle_j^f\right)^2 \tag{2.6.5}$$

The product of the velocity fluctuations has been treated in several different ways throughout the literature. Analogy with turbulent dispersion and physical intuition suggests that the momentum dispersion term should be closed by assuming it will improve momentum diffusion. Therefore, similar to the eddy viscosity, a scalar geometrical diffusivity ν_g is defined as

$$-\langle\tilde{v}_i\tilde{v}_j\rangle = \nu_g \frac{\partial\langle v\rangle_i}{\partial x_j} \tag{2.6.6}$$

Substituting this definition into Eqn. (2.6.1) , and dividing through by density yields a closed form of the VAT momentum equation,

$$\begin{aligned}\varepsilon_f\frac{\partial\langle\mathbf{v}\rangle^f}{\partial t} + \varepsilon_f\langle\mathbf{v}\rangle^f\cdot\nabla\langle\mathbf{v}\rangle^f = -\nabla\left(\varepsilon_f\langle p_f\rangle^f\right) + \\ +\nabla\cdot\left[\nu_{eff}\nabla\left(\varepsilon_f\langle\mathbf{v}\rangle^f\right)\right] - \frac{1}{2}S_w\left(\mathbf{c}_{dp}\frac{S_{wp}}{S_w}+\mathbf{c}_f\right)\cdot\left(\langle\mathbf{v}\rangle^f\right)^2 + \varepsilon_f\langle\mathbf{g}\rangle^f\end{aligned} \tag{2.6.7}$$

where $\nu_{eff} = \nu_f + \nu_g$. Although this seems to be a more rigorous approach, difficulties with measurements of the dispersion terms, and the historical importance of models such as Darcys law, and the Brinkmann-Forcheimer models, the velocity fluctuation terms are usually included in the momentum sink term. Travkin and Catton [38] define an overall drag coefficient that includes the fluctuation terms,

$$c_{d,ij} = c_{dp,ij}\frac{S_{wp}}{S_w} + c_{f,ij} + \frac{\rho_f\frac{\partial}{\partial x_j}\left(\langle\tilde{v}_i\tilde{v}_j\rangle^f\right)}{{}^1\!/_2\rho_f\left(\langle v\rangle_i^f\right)^2 S_w} \tag{2.6.8}$$

Using this definition, the closed VAT momentum equation is given,

$$\begin{aligned}\varepsilon_f\frac{\partial\langle\mathbf{v}\rangle^f}{\partial t} + \varepsilon_f\langle\mathbf{v}\rangle^f\cdot\nabla\langle\mathbf{v}\rangle^f = -\nabla\left(\varepsilon_f\langle p_f\rangle^f\right) + \\ +\nabla\cdot\left[\nu_f\nabla\left(\varepsilon_f\langle\mathbf{v}\rangle^f\right)\right] - \frac{1}{2}S_w\mathbf{c}_d\cdot\left(\langle\mathbf{v}\rangle^f\right)^2 + \varepsilon_f\langle\mathbf{g}\rangle^f\end{aligned} \tag{2.6.9}$$

It can be seen that the drag term acts as a momentum sink that is proportional to the square of the velocity. Note that the macroscale kinetic energy is dissipated through the drag term by the no slip condition at the lower scale fluid-solid interfaces. This is quite similar to the energy cascade in turbulence where energy is transferred from the mean flow to the lower scale eddies and is then dissipated through viscous effects. Travkin and Catton [38] also argue that the drag coefficient has the following form

$$c_{d,ij} = \frac{A_{ij}}{\mathrm{Re}_{d_h}} + B_{ij} \tag{2.6.10}$$

where the Reynolds number is based on the magnitude of the intrinsic velocity $\left|\langle \mathbf{v} \rangle^f\right|$, and the VAT hydraulic diameter is defined as

$$d_h = \frac{4\varepsilon_f}{S_w} \tag{2.6.11}$$

The ratio of the porosity to specific surface area defines a length scale that naturally arises from the non-dimensionalization of the closed VAT momentum and equations. Another approach to arrive at this ratio for the characteristic length scale of lower scale phenomena, is by arguing that at the micro scale, information about the macro scale has been lost, and all the momentum losses are due to the intricate geometry. After homogenization, the only parameters that describe the geometry are indeed the porosity and the specific surface, and using scaling arguments they can be combined to obtain their ratio as the length scale. It was shown by Travkin and Catton [38], that the factor of 4 was a natural consequence of scaling both globular and capillary geometries. The VAT momentum equation can be directly related to the Brinkmann-Forchimer equation, a purely empirical but extensively used model of flow in porous media. This Brinkmann-Forchimer equation was originally developed for one dimensional flow, and by substituting the proposed form of the drag coefficient in the one dimensional form of Eqn. (2.6.9) , the following equation is obtained

$$\varepsilon_f \frac{\partial \langle u \rangle^f}{\partial t} + \varepsilon_f \langle u \rangle^f \frac{\partial \langle u \rangle^f}{\partial x} = -\frac{\varepsilon_f}{\rho_f} \frac{\partial \langle p_f \rangle^f}{\partial x} + \varepsilon_f \nu_f \frac{\partial^2 \langle u \rangle^f}{\partial x^2} - \frac{1}{2} S_w \left(\frac{A}{\mathrm{Re}} + B \right) \left(\langle u \rangle^f \right)^2 \tag{2.6.12}$$

Then, assuming that the flow is steady and fully developed, rearranging the drag term and multiplying both sides by the density, Eqn. (2.6.12) becomes

$$-\frac{\partial \langle p_f \rangle}{\partial x} + \varepsilon_f \mu_f \frac{\partial^2 \langle u \rangle^f}{\partial x^2} - \frac{1}{2} S_w \frac{\mu_f A}{d_h} \langle u \rangle^f - \rho_f B \left(\langle u \rangle^f \right)^2 = 0 \tag{2.6.13}$$

Expressing the two constants as

$$A = \frac{2 d_h}{S_w K}, \quad B = \frac{c_1}{K^{1/2}} \tag{2.6.14}$$

Eqn. (2.6.13) is the Brinkmann-Forcheimer model that was given at the beginning of this work, Eqn. (2.0.2). Eqn. (2.6.13) however, is developed by a rigorous upscaling procedure and closure model. The assumptions behind its derivation can be directly verified, and all

terms have a physical meaning. It can also be seen that there is a direct correlation between the drag coefficient defined in Eqn. (2.6.10) and the commonly used permeability tensor. The form of the drag tensor closely resembles correlations that have been developed for the Fanning friction factor. It can be shown that these two are indeed strongly related. This can be illustrated using the definition of the Fanning friction factor

$$f_f = \frac{1}{4}\frac{\Delta P}{L}\frac{d_h}{{}^1/_2\rho U^2} \tag{2.6.15}$$

Assuming that the velocity scale is $U = \langle u_f \rangle^f$, and the length scale is the VAT defined hydraulic diameter, the expression for the Fanning friction factor can be written

$$\frac{1}{2}\rho_f S_w f_f \Big(\langle u_f \rangle^f\Big)^2 = \varepsilon_f \frac{\Delta P}{L} \tag{2.6.16}$$

The closed VAT momentum equation, Eqn. (2.6.9), for one dimensional, steady, fully developed flow and negligible diffusion becomes

$$0 = -\frac{\varepsilon_f}{\rho_f}\frac{\partial \langle p_f \rangle^f}{\partial x} - \frac{1}{2} S_w c_d \Big(\langle u_f \rangle^f\Big)^2 \tag{2.6.17}$$

Integrating over the entire x domain, multiplying through by the density and rearranging, this equation becomes

$$\frac{1}{2}\rho_f S_w c_d \Big(\langle u_f \rangle^f\Big)^2 = \varepsilon_f \frac{\Delta P}{L} \tag{2.6.18}$$

and comparison of Eqn. (2.6.16) & Eqn. (2.6.17), shows that

$$c_d = f_f \tag{2.6.19}$$

In general, this will not be a strong equality, but it is expected that the drag coefficient can be closely approximated by the Fanning friction factor, $c_d \approx f_f$. This relationship is particularly useful, because correlations for the Fanning friction factor have been experimentally and numerically developed for a large number and variety of geometries and, even though they are not always expressed in the form given by Eqn. (2.6.10), and are based on different velocity and length scales, they can be recast in the proper form and with the proper scaling. The form of the drag coefficient expressed in Eqn. (2.6.10) has been widely used to correlate

pressure drops for packed and fluidized beds. Arguably the most popular correlation for the Darcy friction factor, was proposed by Erguns [105]

$$f_{ERG} = \frac{150}{\mathrm{Re}_p}\frac{(1-\varepsilon_f)^2}{\varepsilon_f^3} + 1.75\frac{(1-\varepsilon_f)}{\varepsilon_f^3} \tag{2.6.20}$$

where the friction factor is based on the superficial velocity and a characteristic particle diameter. It can be shown that using the definition of the Fanning friction factor given by Eqn. (2.6.16), and the VAT hydraulic diameter, the porosity dependence of the coefficients can be removed, and the Ergun equation becomes

$$f_f = \frac{33.3}{\mathrm{Re}_{d_h}} + 0.5833 \tag{2.6.21}$$

The first term is dominant in the viscous (also known as Darcy) regime when $\mathrm{Re}_p < 1$, while the constant term prevails in the inertial range (also known as Forcheimer) regime $\mathrm{Re}_p > 100$. Amaral Souto and Moyne [106, 107], in their study of two dimensional arrays of inline, staggered and random media found that the viscous regime is usually accurate up to $\mathrm{Re}_p = 20 - 30$, and confirmed the dependence of the friction factor with the square of the velocity in the inertial regime, $\mathrm{Re}_p > 100$. They also found that in the intermediate range, the pressure drop has a cubic dependence on the Reynolds number. Erguns equation was originally developed by a combination of physical arguments and empirical data. In its original form, it was assumed that the fluid flows through a bundle of tortuous capillaries with a uniform average cross-sectional area, and that the solid phase was composed of randomly distributed uniform sized spheres. It was also assumed that the system includes a large enough number of particles, so the effects of porosity and flow variations at the boundaries could be neglected. Since its original publication, this equation has been shown to give surprisingly accurate results for a wide variety of geometries and flow conditions. Macdonald [108], extended Erguns correlation by extending the curve fit for a large variety of data, and found that for engineering purposes a modified of the Ergun equation can be used for a wide variety of shapes and over a wide range of porosities

$$f_{MCD} = \frac{180}{\mathrm{Re}_p}\frac{(1-\varepsilon_f)^2}{\varepsilon_f^3} + 1.8\frac{(1-\varepsilon_f)}{\varepsilon_f^3} \tag{2.6.22}$$

Once again, by using the Fanning friction factor and the VAT hydraulic diameter, the porosity dependence of the constants is removed, and the equation reduces to

$$f_f = \frac{45}{\mathrm{Re}_{d_h}} + 0.45 \tag{2.6.23}$$

Several other modifications of these equations are found in the literature for different geometries, based on curve fits of numerical or experimental data. More recently, Du Plessis [109] used a combination of the VAT approach, with a generalized REV, to give a physical and geometrically based arguments for the derivation of the Ergun equation, its modifications, and its dependence on parameters of the problem. It is well known that surface roughness or micro scale structures also affect the pressure drop, therefore they have to be taken into account. Since the scale of these structures is usually orders of magnitude smaller than the sizes of the REV, their effects are included in the constants of the friction factor. In the viscous regime, usually these effects are negligible, therefore, they enter the correlations through the inertial term B. Macdonald [108], in the same work, presented a modified version of Eqn. (2.6.22) for rough particles

$$f_{MCD} = \frac{180}{\mathrm{Re}_p}\frac{(1-\varepsilon_f)^2}{\varepsilon_f^3} + 4\frac{(1-\varepsilon_f)}{\varepsilon_f^3} \tag{2.6.24}$$

although what rough means is not clear. For cases in which the drag coefficient has not been determined, it can be obtained through experimental or Computational Fluid Dynamics (CFD) studies. Zhou and Catton [110, 111, 112, 113, 114, 115, 116, 117, 118, 119, 120, 121, 122, 123, 124] conducted a large number of numerical studies using commercial CFD software to obtain the VAT defined drag coefficients for a wide variety of heat sink and heat exchangers geometries. Although it may seem counter intuitive to use DNS to obtain closure of the VAT equations, since the computational cost of such studies is what motivated the use of VAT in the first place, the DNS studies can be carried out over only one (or a few) properly selected REVs providing significant advantages over a full DNS study of the entire system. It is also important that closure of the governing equations using CFD software be carefully executed, in order to ensure that the results obtained do not depend on the number of REVs considered, and/or meshes and numerical methods used. Zhou [104] developed a five step procedure for the evaluation procedure

1. Selection of the REV,

2. Determination of the closure length scale,

3. Validation of the model with experimental data,

4. Determination of the number of REVs required, and

5. Correlation of results.

In the first step, the REV for the current geometry is selected such that it is spatially periodic in the main flow direction. If the system under consideration can be treated as a spatially periodic porous medium, in most cases, it can be assumed that spatial fluctuations of the lower scale fields are themselves spatially periodic with period equal to the REV period, and they do not have a significant effect on the averaged equations. This fact allows simplifications because the fluctuation field is not always easy to calculate numerically or experimentally, and the local closure parameters can be obtained from a single REV with periodic boundary conditions. In the second step, the VAT hydraulic diameter is calculated by determining the porosity ε and specific surface S_w. For heat transfer systems such as heat exchangers and heat sinks, an analytical expression for these parameters is easily obtained in terms of geometrical parameters such as transverse and longitudinal pitches, diameter, thickness etc. This fact implies one of the key features/assumptions of the porous media modeling of these systems: the multi-parameter, complex micro scale geometric structure can be reduced to only two macro scale parameters. In the third step, the results obtained numerically are compared to available experimental data to ensure that meshing and numerical errors are negligible. In the fourth step, the number or REVs is increased to study the effects of multiple REVS on the closure parameters. Following the discussion from Section 2.1, the number of REVs, which is the size of the closure volume, should be chosen such that the averaged quantities of interest become smooth functions. For example, the heat transfer coefficient determined using only one REV, might be quite different than the one obtained by using two REVs, and so forth. Once a certain amount of REVs is reached, this volume is a good overall representation of the heat transfer processes and adding further REVs will not significantly

change the heat transfer coefficient. In the last step, simulations are carried out for a range of Reynolds numbers and Prandtl numbers, and the data is correlated using the definition of friction factor and VAT hydraulic diameter.

As demonstrated by Erguns and Macdonalds correlations, closure parameters for different micro scale geometries, can be collapsed onto a single curve by using a length scale defined in terms of the porosity and specific surface, which are combined in the VAT hydraulic diameter. Erguns correlation has been shown to provide good results for a wide number of packed beds and for several different materials. Macdonalds correlation, given by Eqn. (2.6.22), is accurate to within 20% for 14 different types of natural and man-made lower scale geometries. Zhou et al [124] were able to collapse the closure parameter for six different fin-and-tube heat exchanger tube diameters and pitches for a large range of Reynolds numbers onto a single curve (see Figure 2.6). Vadnjal [46] also found that one REV, with periodic boundary conditions, was enough to obtain a good approximation of the drag coefficient in a packed bed of spheres. Improvements in micro and nano fabrication techniques has made surface micro structures a popular method to enhance heat transfer due to their ability to increase mixing and surface area. These structures, unlike surface roughness which is not designed and is commonly characterized statistically, are coherent and can be defined through parameters similar to those used for regular geometries (e.g. diameter, pitch, height etc.). Zhou [114, 112], in his study of the effects of fish-scale shape on heat transfer enhancement and pressure drop, found that the effects of variation in these structures cannot be collapsed onto one curve simply by using the VAT velocity and hydraulic diameter. This can be explained by recalling that the main assumption behind the collapse of friction factor curves using VAT was that the momentum loss in the system is all due to no-slip conditions at surfaces with the REV geometry, which can be completely characterized by porosity and specific surface. However, varying the micro structure geometric parameters affects the porosity negligibly, while significantly affecting the flow field, therefore, the porosity is not a good descriptor of changes in the micro structure. It should be pointed out that this fact does not mean that micro enhanced surfaces cannot be studied using VAT; it is only meant to point out that the effects of changes in micro structures parameters cannot be taken into account simply

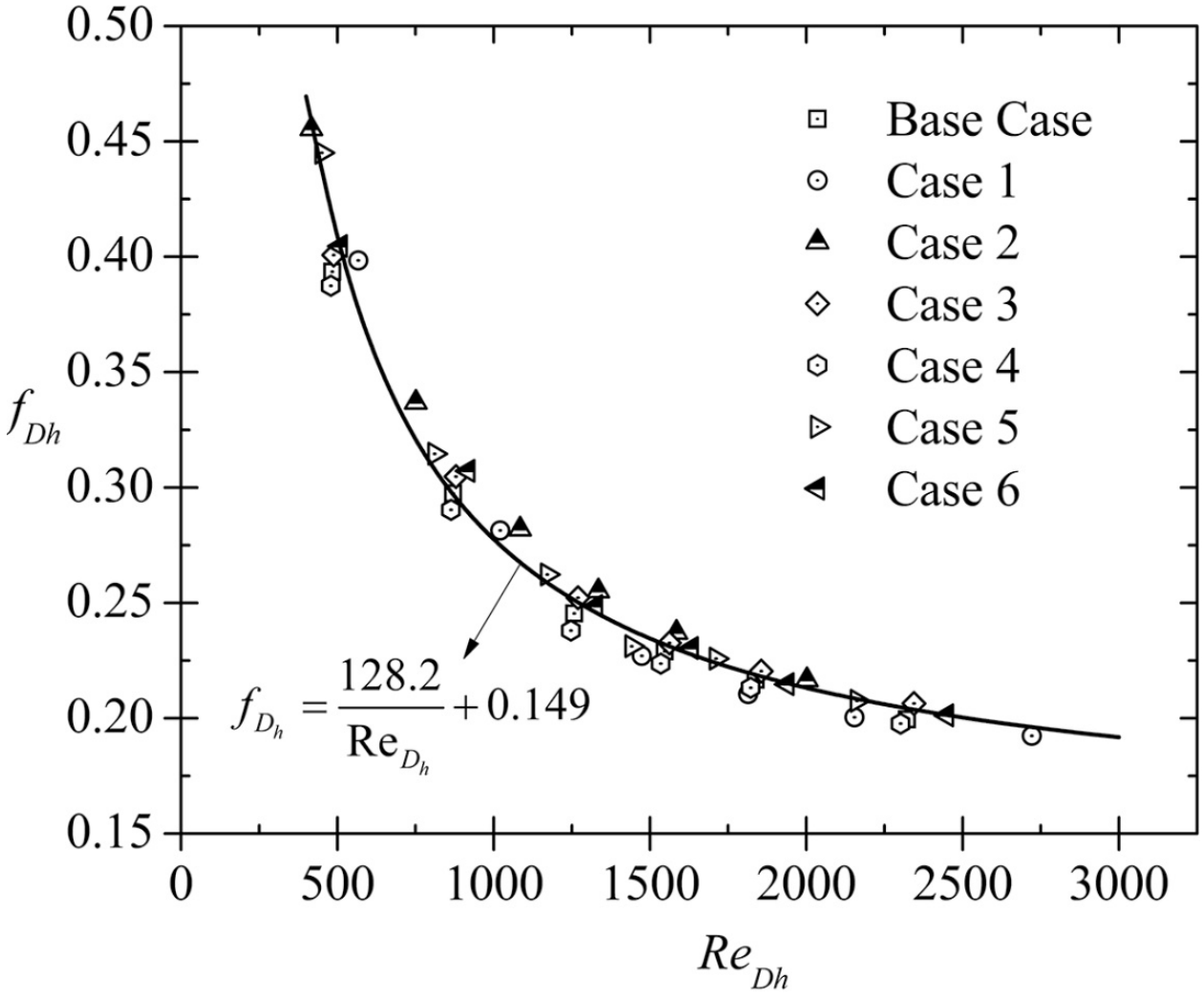

Figure 2.6: Friction factor for different Fin-and-Tube Heat Exchanger geometries

through changes in the VAT hydraulic diameter.

2.6.2 Closure of VAT Energy Equation

The laminar VAT based energy equations were rigorously derived in the previous sections using an averaging operator on the microscale energy equation. There are three terms that require closure in Eqn. (2.5.8) and Eqn. (2.5.11). They are generally defined as

$$\begin{aligned}
&\nabla \cdot \left(\frac{k_f}{V} \int\limits_{A_{fs}} \mathbf{n}_{fs} \tilde{T}_f dA \right) : \text{ tortuosity} \\
&\frac{1}{V} \int\limits_{A_{fs}} \mathbf{n}_{fs} \cdot [k_f \nabla T_f] \, dA : \text{ interfacial flux} \\
&\nabla \cdot \left\langle \tilde{T}_f \tilde{\mathbf{v}}_f \right\rangle : \text{dispersion}
\end{aligned} \tag{2.6.25}$$

The same terms, except for the dispersion term, are also found in the solid energy equation. The non-closed form of the VAT energy equations best suited for the derivation of the closure scheme are given by Eqn. (2.5.5)

$$\begin{aligned}
&\rho_f c_{pf} \varepsilon_f \frac{\partial \langle T_f \rangle^f}{\partial t} + \rho_f c_{pf} \varepsilon_f \langle \mathbf{v}_f \rangle^f \nabla \langle T_f \rangle^f = \\
&= \nabla \cdot \left(k_f \varepsilon_f \nabla \langle T_f \rangle^f \right) + \nabla \cdot \left(\frac{k_f}{V} \int\limits_{A_{fs}} \mathbf{n}_{fs} \tilde{T}_f dA \right) + \frac{1}{V} \int\limits_{A_{fs}} \mathbf{n}_{fs} \cdot [k_f \nabla T_f] \, dA + \\
&- \rho_f c_{pf} \nabla \cdot \left\langle \tilde{T}_f \tilde{\mathbf{v}}_f \right\rangle + \varepsilon_f \left\langle \dot{q}_f''' \right\rangle^f
\end{aligned} \tag{2.6.26}$$

$$\begin{aligned}
\rho_s c_{ps} \varepsilon_s \frac{\partial \langle T_s \rangle^s}{\partial t} &= \nabla \cdot (\varepsilon_s k_s \nabla \langle T_s \rangle^s) + \nabla \cdot \left(\frac{k_s}{V} \int\limits_{A_{fs}} \mathbf{n}_{sf} \tilde{T}_s dA \right) + \\
&+ \frac{1}{V} \int\limits_{A_{fs}} \mathbf{n}_{sf} \cdot [k_s \nabla T_s] \, dA + \varepsilon_s \left\langle \dot{q}_s''' \right\rangle^s
\end{aligned} \tag{2.6.27}$$

The tortuosity and dispersion terms are usually assumed to be proportional to the gradient of the average temperature, suggesting that they promote (or impair) diffusion. This assumption is reminiscent of improved diffusion due to turbulent dispersion, and it was first shown for laminar flow through a tube by Taylor [125] and Aris [126]. The interfacial flux

term is assumed to be proportional to the difference between the average fluid and solid temperatures. These schemes have been extensively used by Kuwahara, [48, 50, 127, 128] and Nakayama [129, 80, 81, 49]. The interfacial flux is closed by defining a local heat transfer coefficient

$$h_1 \equiv \frac{\frac{k_f}{V}\int\limits_{A_{fs}} \mathbf{n}_{fs}\cdot\nabla T_f dA}{S_w\left(\langle T_s\rangle^s - \langle T_f\rangle^f\right)} \tag{2.6.28}$$

The tortuosity and dispersion terms are closed by defining an effective thermal conductivity tensor

$$\mathbf{k}_{f,eff}\cdot\nabla\langle T_f\rangle^f = (\mathbf{k}_{f,stag} + \mathbf{k}_{f,dis})\cdot\nabla\langle T_f\rangle^f \tag{2.6.29}$$

The stagnation thermal conductivity is taken as the sum of the porosity weighted thermal conductivity and the tortuosity term

$$\mathbf{k}_{f,stag} = \varepsilon_f k_f \mathbf{I} + \frac{k_f}{V}\int\limits_{A_{fs}} \mathbf{n}_{fs}\tilde{T}_f dA \tag{2.6.30}$$

The dispersion terms are closed by defining a dispersion thermal conductivity tensor

$$\mathbf{k}_{f,dis}\cdot\nabla\langle T_f\rangle^f = -\rho_f c_{pf}\left\langle \tilde{T}_f\tilde{\mathbf{v}}_f\right\rangle \tag{2.6.31}$$

Using these closure parameters, a closed form of the VAT fluid conservation equation is given by

$$\begin{aligned}&\rho_f c_{pf}\varepsilon_f\frac{\partial\langle T_f\rangle^f}{\partial t} + \rho_f c_{pf}\varepsilon_f\langle\mathbf{v}_f\rangle^f\nabla\langle T_f\rangle^f = \\ &= \nabla\cdot\left(\mathbf{k}_{eff,f}\cdot\nabla\langle T_f\rangle^f\right) + h_1 S_w\left(\langle T_s\rangle^s - \langle T_f\rangle^f\right) + \varepsilon_f\left\langle\dot{q}_f'''\right\rangle^f\end{aligned} \tag{2.6.32}$$

Since dispersion effects do not enter directly into the solid energy equation, only the stagnation thermal conductivity and interfacial flux are defined, and the solid VAT energy equation is

$$\rho_s c_{ps}\varepsilon_s\frac{\partial\langle T_s\rangle^s}{\partial t} = \nabla\cdot(\mathbf{k}_{stag,s}\cdot\nabla\langle T_s\rangle^s) - h_1 S_w\left(\langle T_s\rangle^s - \langle T_f\rangle^f\right) + \varepsilon_s\left\langle\dot{q}_s'''\right\rangle^s \tag{2.6.33}$$

where the minus sign in the interfacial flux terms comes from the relation between the interface normal $\mathbf{n}_{sf} = -\mathbf{n}_{fs}$. Numerous studies have been carried out to determine the tortuosity and dispersion effects. Yang and Nakayama [130] developed a model based on a

unit cell model to obtain a general expression for stagnation and dispersion, and their results agreed well with experimental data for a different geometries. Hsu [131] developed a closure scheme for convective heat transfer in packed beds by considering a dilute array of spheres with a constant to account for the interaction between spheres. Nakayama and Kuwahara [50, 48] extended Hsus closure scheme to include convection. Souto [106, 107] studied the two-dimensional dispersion tensor for an inline, staggered and random array of square obstacles. The tortuosity terms are generally more important in a purely conductive system, while it will be negligible for convectively dominated flows. This can be demonstrated for the solid by considering the solid tortuosity term, and using spatial decomposition

$$\frac{k_s}{V}\int\limits_{A_{fs}} \mathbf{n}_{fs}\tilde{T}_s dA = \frac{k_s}{V}\int\limits_{A_{fs}} \mathbf{n}_{fs}\left(T_s - \langle T_s\rangle^s\right) dA \tag{2.6.34}$$

The difference between the point-wise temperature and the average temperature will depend on point-wise temperature gradients in the solid phase within the REV. When the Biot number is small, this gradient is negligible, therefore, it can be assumed that the temperature at the interface will be equal to the volume averaged temperature, $T_s = \langle T_s\rangle^s$. Therefore

$$\frac{k_s}{V}\int\limits_{A_{fs}} \mathbf{n}_{fs}\left(T_s - \langle T_s\rangle^s\right) dA \approx 0, \qquad Bi = \frac{hD}{k_s} \ll 1 \tag{2.6.35}$$

where D is a general particle diameter length scale. This also shows that in convective flows, this term depends on the local heat transfer coefficient, and its distribution. For example, if stagnation and recirculation areas are present in the flow, there might be areas in which the Biot number is relatively large, and this term can be significant. This link between tortuosity and the VAT heat transfer coefficient can be seen also by considering the fluid tortuosity term. When no reaction at the interface area is present, the point-wise temperatures will be

equal. Using this fact, and the definition of the decompositions it can be shown that

$$\begin{aligned}
&\frac{k_f}{V}\int\limits_{A_{fs}} \mathbf{n}_{fs}\tilde{T}_f dA = \frac{k_f}{V}\int\limits_{A_{fs}} \mathbf{n}_{fs}\left(T_f - \langle T_f\rangle^f\right) dA = \frac{k_f}{V}\int\limits_{A_{fs}} \mathbf{n}_{fs}\left(T_s - \langle T_f\rangle^f\right) dA = \\
&= \frac{k_f}{V}\int\limits_{A_{fs}} \mathbf{n}_{fs}\left(\langle T_s\rangle^s - \langle T_f\rangle^f\right) - \tilde{T}_s dA = \\
&= \frac{k_f}{V}\int\limits_{A_{fs}} \mathbf{n}_{fs}\left(\langle T_s\rangle^s - \langle T_f\rangle^f\right) dA - \frac{k_f}{k_s}\left(\frac{k_s}{V}\int\limits_{A_{fs}} \mathbf{n}_{fs}\tilde{T}_s dA\right)
\end{aligned} \tag{2.6.36}$$

The first term depends on the average temperature difference between the two phases and is directly linked to the local heat transfer coefficient. The second term is dependent on the ratio of the solid and fluid temperature, and the Biot number. Therefore, in general, the tortuosity depends on the heat transfer coefficient, the ratio of solid to fluid thermal conductivity and the Biot number. In most convective flows and material combinations, the thermal conductivity ratio and the Biot number are very small and the second term can be ignored. In the numerous studies of thermal dispersion, a relationship between the diagonal terms of the dispersion tensor is generally found in the form

$$\frac{k_{dis,ii}}{k_f} = C_i + D_i Pe^n \tag{2.6.37}$$

where the Peclet number is based on a lower length scale and the main direction flow velocity. In general, it is reported that $n \approx 2$, the constants C_i and D_i are dependent on the geometry, and that dispersion in the direction perpendicular to the main flow is much smaller than in the parallel direction. Yang [130] also reports that for convective flows, the constant D_i is inversely proportional to the Nusslet number. Dixon and Cresswell [132] also found that the effective thermal conductivity for both solid and fluid phases depends on the heat transfer coefficient. This shows that although tortuosity, dispersion and heat transfer terms are usually treated as separate entities, they are indeed linked to each other. Based on the observed dependence of the local heat transfer coefficient on tortuosity and dispersion, Travkin and Catton [38] used a different closure scheme for the energy equations. Starting again from the non-closed form of the equation, Eqn. (2.6.26), they define an overall heat

transfer coefficient as

$$h \equiv \frac{\frac{1}{V}\int\limits_{A_{fs}} \mathbf{n}_{fs}\cdot k_f \nabla T_f dA}{S_w\left(\langle T_s\rangle^s - \langle T_f\rangle^f\right)} + \frac{\nabla\cdot\left(\frac{k_f}{V}\int\limits_{A_{fs}} \mathbf{n}_{fs}\tilde{T}_f dA\right)}{S_w\left(\langle T_s\rangle^s - \langle T_f\rangle^f\right)} - \frac{\rho_f c_{pf}\nabla\cdot\left(\varepsilon_f\left\langle \tilde{T}_f\tilde{\mathbf{v}}_f\right\rangle^f\right)}{S_w\left(\langle T_s\rangle^s - \langle T_f\rangle^f\right)} \tag{2.6.38}$$

Applying this definition, a closed VAT fluid equation is obtained

$$\begin{aligned}&\varepsilon_f\rho_f c_{pf}\frac{\partial\langle T_f\rangle^f}{\partial t} + \varepsilon_f\rho_f c_{pf}\langle\mathbf{v}_f\rangle^f\nabla\langle T_f\rangle^f = \\ &= \nabla\cdot\left(\varepsilon_f k_f\nabla\langle T_f\rangle^f\right) + hS_w\left(\langle T_s\rangle^s - \langle T_f\rangle^f\right) + \varepsilon_f\left\langle\dot{q}_f'''\right\rangle^f\end{aligned} \tag{2.6.39}$$

This approach defines a heat source (or sink) in the fluid temperature that is dependent on the difference between the averaged solid and fluid, while leaving the diffusion coefficient unchanged. Therefore, dispersion and tortuosity effects are included in the heat transfer coefficient, and their effects are assumed to be proportional to fluid solid temperature difference. Defining the heat transfer coefficient this way greatly simplifies its experimental determination because it removes the added complications of the determination of tortuosity and dispersion. The two closure schemes discussed lead to the same equations for cases in which tortuosity and dispersion effects are negligible. To close the solid equations, they argue that conservation of energy dictates that energy entering the fluid must leave the solid, therefore the energy equation is closed as

$$\rho_s c_{ps}\varepsilon_s\frac{\partial\langle T_s\rangle^s}{\partial t} = \nabla\cdot\left(\varepsilon_s k_s\nabla\langle T_s\rangle^s\right) - hS_w\left(\langle T_s\rangle^s - \langle T_f\rangle^f\right) + \varepsilon_s\left\langle\dot{q}_s'''\right\rangle^s \tag{2.6.40}$$

The use of the same heat transfer coefficient for both equations might seem mathematically inconsistent due to the fact that the dispersion terms are not explicitly included in the solid equation. However, following the previous discussion, it has been shown that both tortuosity terms, and dispersion will depend on the local heat transfer coefficient. Neither one of these approaches is exact, because the effects of the coupling of the two equations cannot always be exactly limited to only one of the closure parameters. Quintard and Whitaker [133] present a different, more mathematically rigorous closure model, which includes coupling between the two equations in several terms. They define additional velocity terms that couple the convective fluid transport with convective-like terms that involve gradients in

the solid temperature. Furthermore, their definition of the effective thermal conductivity tensors also couples the fluid and solid temperatures. Quintard and Kaviany [134] solve those equations for several three dimensional configurations, and provide very useful insight in the dependence of the different terms on geometry, physical and flow characteristics of the system. This is a more comprehensive approach, and should be considered for new problems. However, its practicality is limited by the number of parameters that need to be determined and the mathematical complications. Each of the different closure schemes has its merits and in this work, expediency and simplicity are important, and the closure method discussed in the previous section have been shown to provide accurate results within their limitations. Much of the discussion of the determination of the closure parameters for the momentum equation is also valid for closure of the energy equations. In most cases, following conventional correlations, the Nusselt number can be expressed as

$$Nu_{d_h} = C\,\mathrm{Re}_{d_h}^{n} + D\,\mathrm{Re}_{d_h}^{m}\,\mathrm{Pr}^{1/3} \tag{2.6.41}$$

Handley and Heggs [135], in some of the earliest work done on the determination of the heat transfer coefficient in packed beds proposed the following correlation

$$Nu_p = \frac{0.255}{\varepsilon_f}\,\mathrm{Re}_p^{2/3}\,\mathrm{Pr}^{1/3} \tag{2.6.42}$$

for $\mathrm{Re}_p > 100$, where the length scale p is the average particle diameter . Wakao and Kaguei [136] used a combination of analysis and experimental data for packed beds to adjust the previous correlation, and extend it to the limit of zero Reynolds number

$$Nu_p = 2 + 1.1\,\mathrm{Re}_p^{0.6}\,\mathrm{Pr}^{1/3} \tag{2.6.43}$$

Whitaker [19], using the VAT defined hydraulic diameter (with a different constant) was able to collapse the data for a wide number of packed beds and inline and staggered tube bundles onto a single correlation

$$\begin{aligned} Nu_{d_h} &= 2\,\mathrm{Re}_{d_h}^{1/3}\,\mathrm{Pr}^{1/3}, \qquad \mathrm{Re}_{d_h} < 10^2 \\ Nu_{d_h} &= \left(0.5\,\mathrm{Re}_{d_h}^{1/2} + 0.2, \mathrm{Re}_{d_h}^{2/3}\right) \qquad \mathrm{Pr}^{1/3}10^2 < \mathrm{Re}_{d_h} < 10^5 \end{aligned} \tag{2.6.44}$$

Over the years, several new correlations have been proposed for different geometries. Recently, Kuwahara [51] suggested a new correlation based on two dimensional numerical studies for flow over an array of staggered squares

$$Nu_D = \left[2 + \frac{12\,(1-\varepsilon_f)}{\varepsilon_f}\right] + (1-\varepsilon_f)^{1/2}\,\mathrm{Re}_D^{0.6}\,\mathrm{Pr}^{1/3} \tag{2.6.45}$$

Zhou [111] in a numerical study of fin-and-tube heat exchangers, was able to collapse the heat transfer coefficient for several different heat exchanger geometries on a single curve using the VAT defined hydraulic diameter (see Figure 2.7). In general, it is of interest to

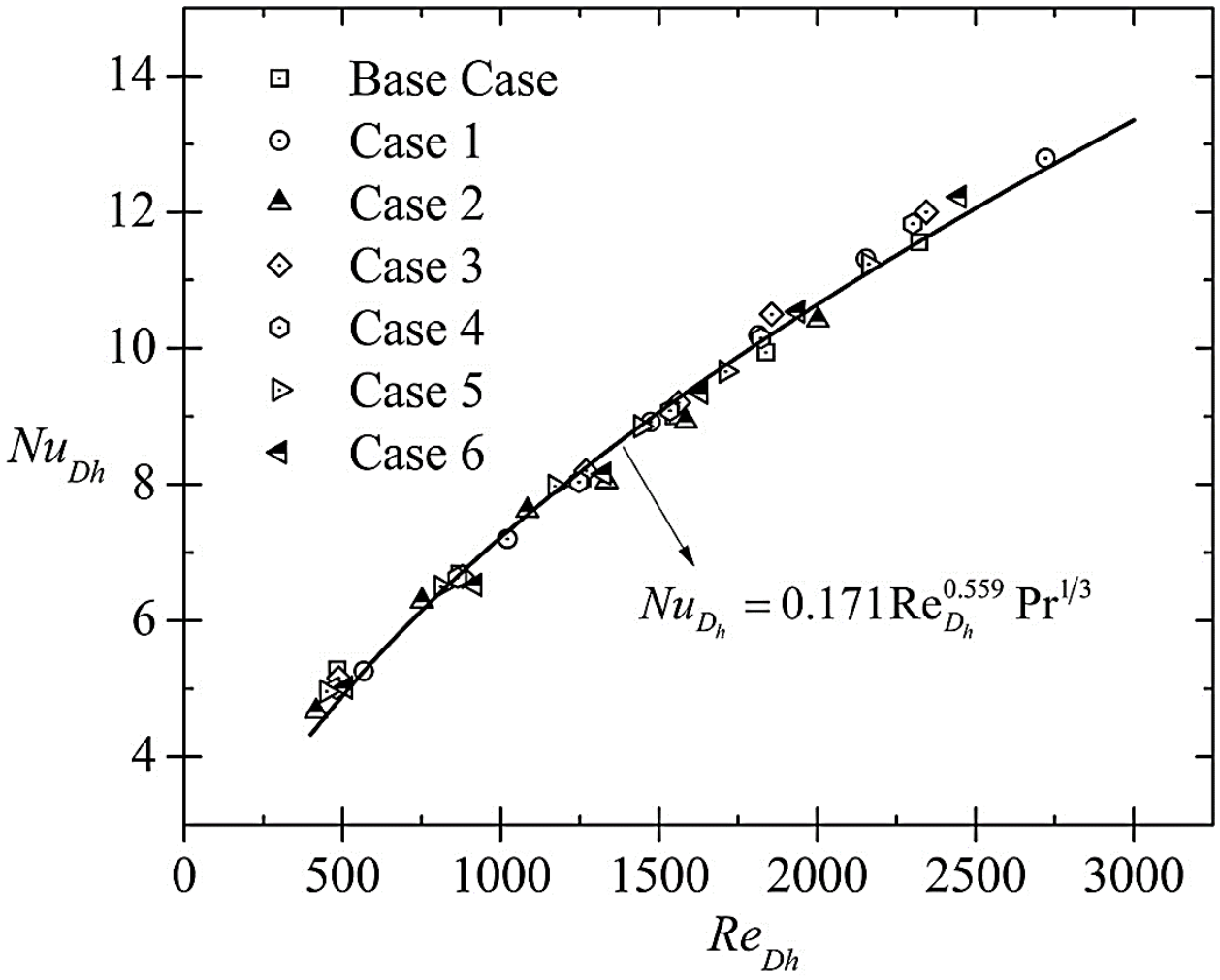

Figure 2.7: Fin Side Nusslet number for several Fin-and-Tube geometric configurations using VAT defined hydraulic diameter

develop some criteria that could allow the use of commonly available correlations for the

Nusslet number for VAT applications. This would allow one to use the large amount of literature for common geometries to determine the VAT defined heat transfer coefficient. In general, most experimental relations for Nusselt numbers are based on the following form

$$h_{\text{exp}} = \frac{Q}{A\left(T_s - T_{f,\infty}\right)} = \frac{q''}{\left(T_s - T_{f,\infty}\right)} \tag{2.6.46}$$

The definition of the VAT heat transfer coefficient, can be rearranged as

$$h_1 = \frac{\int\limits_{A_{fs}} \mathbf{n}_{fs} \cdot \left[k_f \nabla T_f\right] dA}{A_{fs}\left(\langle T_s \rangle^s - \langle T_f \rangle^f\right)} = \frac{q''_{avg}}{\left(\langle T_s \rangle^s - \langle T_f \rangle^f\right)} \tag{2.6.47}$$

where the average heat flux can be obtained from the integral using the mean value theorem. In general, the heat flux in reported experiments is the heat input divided by the area and it is generally closely approximated by its VAT equivalent. Following the discussion in the previous section, when the Biot number is large, it can be assumed that the average and point-wise solid temperatures will be close, $\langle T_s \rangle^s \approx T_s$. The definition of $T_{f,\infty}$, varies but the two most common forms are $T_{f,\infty} = T_{f,avg}$and $T_{f,\infty} = T_{in}$, where $T_{f,avg}$ is usually some averaged value over the domain. In general, the assumption that $T_{f,in} \approx \langle T_f \rangle^f$ is not physically accurate since the volume averaged temperature can vary significantly throughout the domain, while $T_{f,in}$ is a constant. Travkin and Catton [38] argue that using their definition of the heat transfer coefficient

$$h \equiv \frac{\frac{1}{V}\int\limits_{A_{fs}} \mathbf{n}_{fs} \cdot k_f \nabla T_f dA}{S_w\left(\langle T_s \rangle^s - \langle T_f \rangle^f\right)} + \frac{\nabla \cdot \left(\frac{k_f}{V}\int\limits_{A_{fs}} \mathbf{n}_{fs} \tilde{T}_f dA\right)}{S_w\left(\langle T_s \rangle^s - \langle T_f \rangle^f\right)} - \frac{\rho_f c_{pf} \nabla \cdot \left\langle \tilde{T}_f \tilde{\mathbf{v}}_f \right\rangle}{S_w\left(\langle T_s \rangle^s - \langle T_f \rangle^f\right)} \tag{2.6.48}$$

the variation in tortuosity and dispersion can take into account the difference between these definitions, and therefore $h \approx h_{\text{exp}}$. This allows the use of widely available data for the heat transfer coefficient in different geometry to be used directly in the VAT equations. This also implies that for a given Reynolds number, the heat transfer coefficient as defined above will also be constant in the domain. Although it seems difficult to completely understand the mathematical assumption of these relations, Vadnjal [46] carried out CFD simulations for convective heat transfer in a bed of spheres for two different Reynolds numbers, and found that, except for a small region near the inlet, the heat transfer coefficient is indeed constant

throughout the domain (see Figure 2.8). Zhou [104] found that the VAT defined heat transfer coefficient in heat exchangers, at larger Reynolds numbers, was also constant almost everywhere in the domain, which suggests that the this behavior is actually independent of the Reynolds number. When correlations are not readily available, experiments can be carried

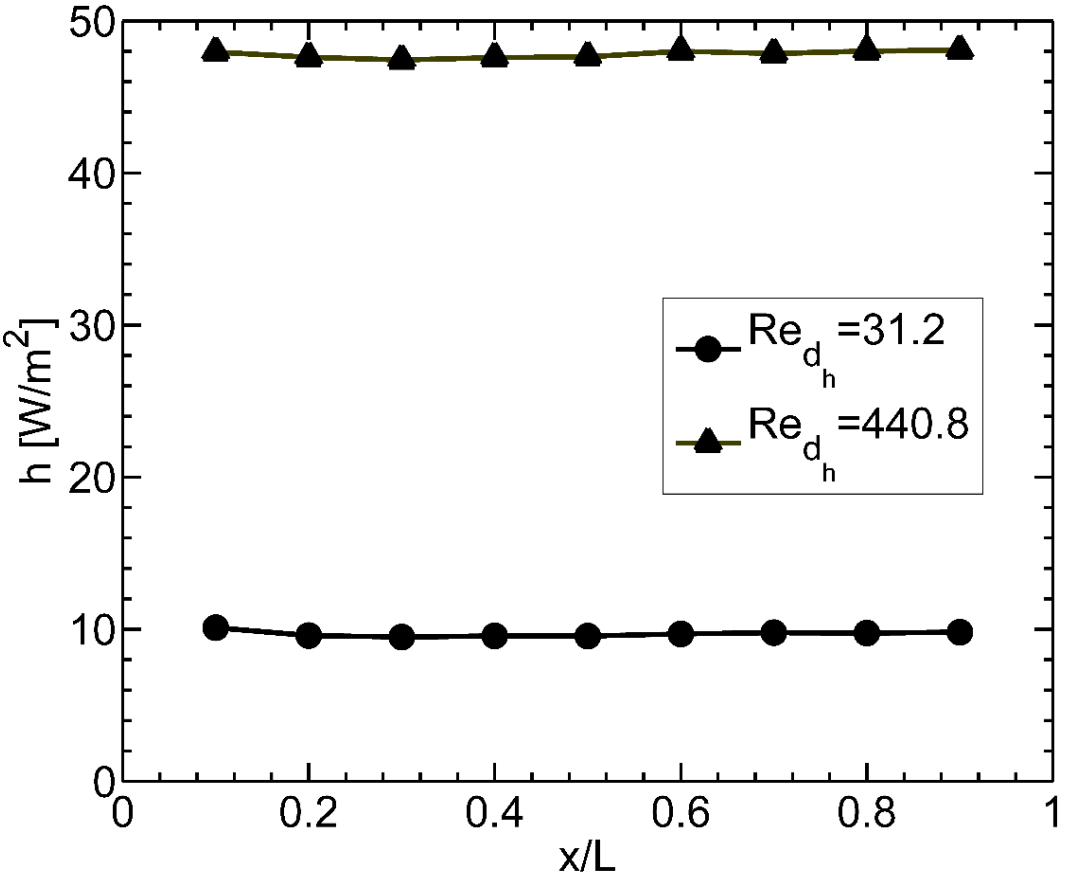

Figure 2.8: Local heat transfer coefficient variation along computational domain (replotted from [46])

out to determine these parameters. Geb [137] used a single-blow method to experimentally determine the heat transfer coefficient for random fiber matrices. By also using the VAT defined hydraulic diameter, and he was able to collapse data for six different random fiber matrices onto one correlation

$$\mathrm{Nu}_{d_h} = 0.103\,\mathrm{Re}_{d_h}^{0.998}\,\mathrm{Pr}^{1/3} \tag{2.6.49}$$

Geb [138, 139] also used an induction heating method to determine the VAT based heat transfer coefficient for cylinders and cross flow, mesh matrices and packed beds and found good agreement with commonly available correlations. The advancement in CFD has made numerical studies cheaper and faster than experiments. Using the same procedure discussed for the closure of the momentum equations, CFD studies can be carried out over an REV to determine the Nusslet number correlation for the given geometry. The number of REVs that need to be included in the numerical studies to obtain a good representation of the heat transfer processes in the system needs to be determined. Following the discussion of Section 2.1, this number does not need to be the same as the one used to determine the drag coefficient. Vadnjal [46] found that six REVs needed to be included in the computational domain to obtain a good representation of the heat transfer coefficient in a packed bed at low Reynolds numbers. Zhou [123], in his study on closure for heat exchangers at high Reynolds numbers, also found that six REVs were necessary to obtain a good representation of the VAT heat transfer coefficient. Also, different boundary conditions (constant temperature, constant heat flux, and constant volumetric heat generation) can be used to heat the solid phase in the numerical simulations, which one to use is not clear. Vadnjal [46] in his study found that the VAT-defined heat transfer coefficient was the same for all three types of boundary conditions (see [114, 112]), therefore either one of them can be used in the numerical simulations. These results show that using six REVs, and any type of boundary conditions, the heat transfer coefficient can be determined numerically, and used in the VAT energy equations. Following the discussion in the momentum section, the effect of changes in micro structures parameters cannot simply be taken into account using the VAT hydraulic diameter, therefore for different micro structures, the correlation does not collapse onto a single curve.

Once the geometry is defined, and the drag and heat transfer coefficients have been determined, Eqns. (2.6.9), (2.6.39) and (2.6.40) represent a closed set of partial differential equations (PDE) that can be solved to obtain the average velocities and temperatures in the entire system. The complex geometry, has now been substituted by a fictitious homogenous medium, and the governing equations are now defined everywhere in the domain. This ho-

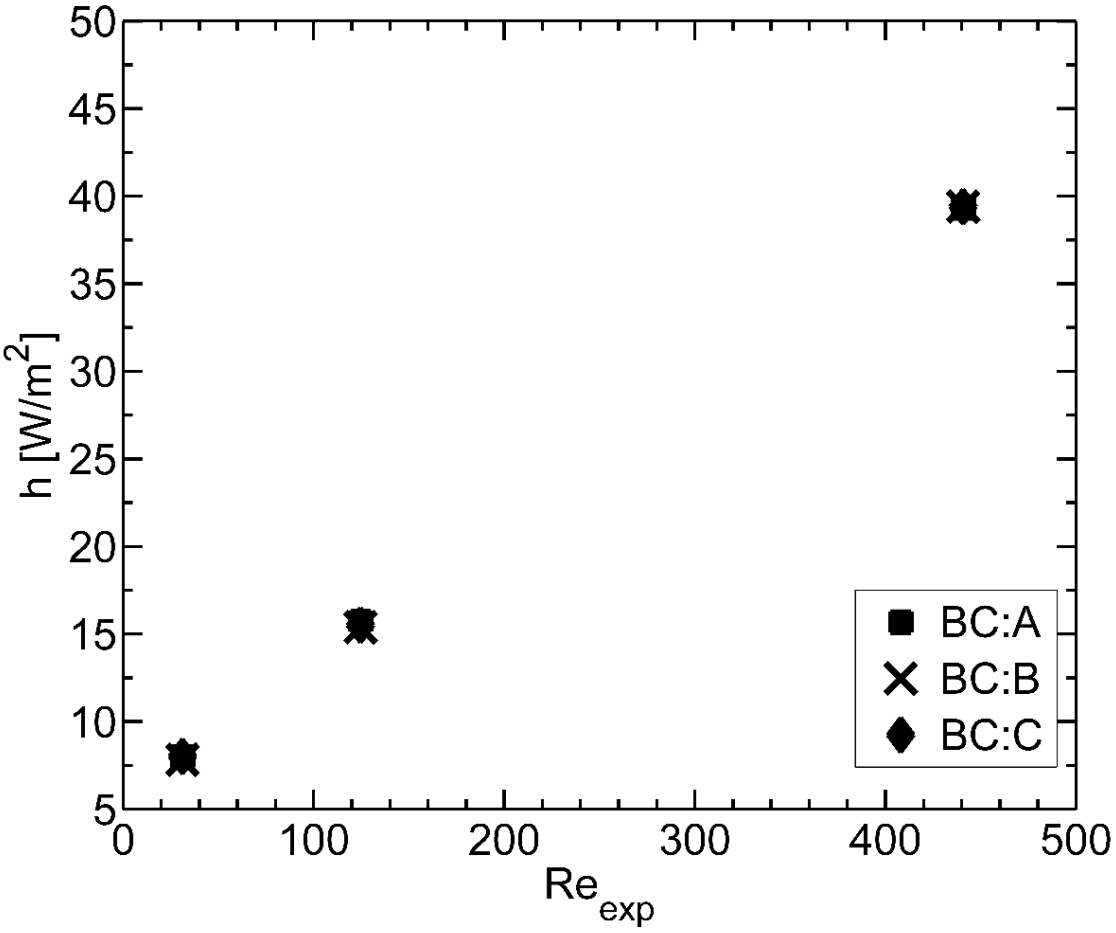

Figure 2.9: Local heat transfer coefficient for three types of heating. BC:A ⇒ constant heat flux heating, BC:B ⇒ constant wall temperature heating, BC:C ⇒ constant volumetric heating (replotted from [46])

mogenization process effectively bypasses the numerical issues that arise from the complex geometry, while including its effects through the closure coefficient.

2.7 Boundary Conditions

It is possible that in certain regions of the domain significant changes in the average quantities occur over the length scale l and the length scale disparities discussed previously are not locally verified. In these situations, the two scales cannot be considered separately and their interaction has to be accounted for. In these regions, the equations become non-local, and their solution is greatly complicated. In incompressible flow, this length scale breakdown is often due to sudden changes in geometry which can arise within the medium (e.g. step changes in geometry) or at the boundaries. At a porous-porous interface, if the difference in porosity and other average quantities is not too severe, this issue is avoided, however, it cannot be avoided when interfaces are between porous and homogenous media (e.g. porous-solid and porous-fluid interfaces). Continuing in our analogy with the continuum approach, this is similar to the breakdown in length scale disparity that is found at boundaries in microfluidics and shock formation in compressible flow. In these regions, changes in the quantities of interest occur at the mean free path scale where the local Knudsen number is below the continuum threshold and standard conservation equations and regular boundary conditions are not accurate. Molecular effects (lower scale effects) have to be included directly in the governing equations, and jump conditions, (e.g. slip velocity, Rankine-Hugoniot conditions), need to be defined allowing the lower scale and upper scale quantities to be directly related. Similarly, for cases where sudden changes in geometry are present, jump condition for the VAT equations need to be developed.

The development of these conditions is further complicated by noting that in the homogenous region the point-wise equations define quantities that are defined on the particle scale, while in the porous region, the VAT equations are averaged on the REV scale so temperatures and velocities across the interface have different meaning. To address this issue several approaches have been developed, with different degrees of rigor, to develop energy and mo-

mentum jump conditions at such interfaces. Ochoa-Tapia and Whitaker [83, 140, 141], in their work on the development of stress and heat transfer jump conditions at a porous-fluid interface, developed a rigorous mathematical framework for the derivation of jump conditions. As a first step, they average the homogenous equations over an REV to bridge the length scale disparity. Then, the non-local problem is solved by further averaging both equations over a larger scale to obtain an expression for the excess surface stresses and heat flux jump conditions. These conditions are given in terms of effective tensors that need to be closed, for the conditions to be used in practice. Valdes-Parada et al [142] developed a closure scheme for the aforementioned tensors for a momentum jump at a porous-fluid interface, and provided numerical values for a few geometries. Hassanizadeh and Grey obtain more abstract and general momentum and concentration jump conditions in terms of integrals of point quantities at the interface. Sharaoui and Kaviany [143, 144, 56], numerically studied the effect of different energy and momentum boundary conditions between porous and homogenous medium for convection-diffusion and pure diffusion. Vafai and Thiyagaraja [145] used asymptotic analysis to study porous-porous, porous-solid and porous-fluid interfaces for different flow conditions and pure conduction. Although all these studies have shed some light in the behavior of transport phenomena at the interface between porous and homogeneous media, a unified approach that defines rigorous but simple interface jump conditions, and gives closure parameters that can be obtained numerically still needs to be developed, and is one of the main issues that needs to be addressed.

In this work, VAT will be used for analysis of manufactured geometrically well-defined structures. This removes the complications resulting from geometry characterization at interfaces that are common in geological porous structures. In such cases, as shown in the closure section, direct numerical simulations using CFD software can be used to obtain insight into the behavior at the lower scale. This is true also for boundary conditions, and CFD solutions can be used to determine the distribution of heat fluxes at the interface and validate existing models. Jiang and Lu [146]used CFD to study temperature and heat flux distributions at the interface between a conducting solid wall and a porous medium composed of uniform size spheres under laminar convective heat transfer. They considered three different particle

sizes and two different fluid-solid material combinations to study the effects of particle size and thermal conductivity ratio on the temperature and heat flux distributions. They found that, if thermal contact resistances were included, the fluid and solid temperatures at the interface were quite different from each other, while the heat flux was uniform between the two phases. They also found, that if contact resistances were not included (e.g. sintered porous media), the difference in temperature at the interface was negligible, however the heat flux into the fluid phase was much less than the heat flux into the solid phase. For the case of negligible thermal contact resistance, they stated that the following energy jump boundary conditions at the interface best approximated the numerical results

$$\begin{aligned} \langle T_f \rangle^f &= \langle T_s \rangle^s \\ q_s &= \frac{k_s}{\varepsilon_f k_f + \varepsilon_s k_s} q_w \\ q_f &= \frac{k_f}{\varepsilon_f k_f + \varepsilon_s k_s} q_w \end{aligned} \tag{2.7.1}$$

where q_w is the heat flux applied at the base of the homogenous solid, and q_s and q_w are the heat fluxes going into the solid and fluid phase. Imani et al [147] conducted similar CFD studies to determine the effect of porosity, geometry configuration, Reynolds number and thermal conductivity ratio on heat flux distribution at the interface between a tube bundle (considered as a porous medium) and a homogeneous solid for convective heat transfer. Since contact resistances are not present in this geometrical configuration, they confirmed that temperature differences between the two phases at the interface are negligible, and, using a curve-fitting of their findings, they proposed the following correlation for the heat flux bifurcation

$$\begin{aligned} \langle T_f \rangle^f &= \langle T_s \rangle^s \\ \frac{q_s}{q_w} &= 1.244 \left(\frac{k_s}{k_f} \right)^{0.277} \varepsilon_f^{1.086} \, \mathrm{Re}_D^{-0.037} \\ \frac{q_s}{q_w} &= 1.244 \left(\frac{k_s}{k_f} \right)^{-0.406} \varepsilon_f^{0.771} \, \mathrm{Re}_D^{0.214} \end{aligned} \tag{2.7.2}$$

where the Reynolds number was based on the cylinder diameter but the velocity scale is not specified. The correlation given in Eqn. (2.7.2) are valid over a wide range of thermal conductivity ratios (0.83-335), porosities (0.39-0.87) and for Reynolds numbers between 1.4 and

44. Ouyang et al [148] developed a model to determine heat flux bifurcation and temperature distribution at the interface between porous and solid interfaces for the same condition, and found good agreement with CFD results. Although these studies provide practical confirmation of analytical studies and useful relationships for certain geometries, to our knowledge, there has not been a study that develops a porous-solid heat transfer jump condition that combines a rigorous mathematical approach based on VAT to defined closure variables, and direct numerical studies to determine their values.

CHAPTER 3

Heat Sink Model and Solution Methods

In this chapter, the governing VAT conservation equations developed in the previous section are applied to model fluid flow and heat transfer in a heat sink. Addition assumptions are discussed, boundary conditions are introduced, and governing equations are scaled. The developed scaling is used to simplify the equations, that are then solved numerically. The numerical methods used are discussed in detail, and particular attention is dedicated to the treatment of the interface boundary condition. A Finite Difference (FD) method and a Galerkin Method (GM) solution are developed for the governing equations.

3.1 Model

In addition to the assumption of separation of scale and smoothness, discussed in the previous section, in the current model, the following assumptions are made:

1. Flow and heat transfer phenomena are steady.
2. No heat generation or viscous dissipation are present.
3. Variations along the width (y-direction) can be ignored. The overall model is two dimensional.
4. Dispersion and tortuosity effects can be ignored.
5. Drag tensor is diagonal.
6. Fluid and solid temperature at the interface between the channel and the homogenous base are equal.

The first two approximations are related to the physics of the problem. It is of interest to look only at the steady state response of the system, therefore the transient behavior is not considered. There are no additional physical phenomena that could possibly generate heat within the solid phase, and the Eckert number is very small so viscous dissipation within the fluid can be ignored. The third assumption implies that the number of finned rows along the width is large, therefore variations from row to row are negligible. This will in general be true, except for regions close to the width boundaries, which will affect the flow. Following the discussion in Section 2.6, dispersion effects are important only for high Peclet number flows, and tortuosity effects are significant only for large Biot numbers. In this work, due to the relatively low Peclet numbers considered and the high thermal conductivities of the solid phase, these effects will be negligible. The fifth assumption, as discussed in Section 2.6 has been shown to be true when the thermal conductivity ratio between the fluid and the solid is large. This is indeed the case in most common heat rejecting devices, and always the case in the ones considered here. Following these assumptions, the governing VAT conservation equations in a heat sink are given by mass conservation,

$$\frac{\partial \langle u \rangle}{\partial x} + \frac{\partial \langle w \rangle}{\partial z} = 0 \tag{3.1.1}$$

momentum conservation,

$$\langle u \rangle \frac{\partial \langle u \rangle^f}{\partial x} + \langle w \rangle \frac{\partial \langle u \rangle^f}{\partial z} = -\frac{\varepsilon_f}{\rho_f}\frac{\partial \langle p_f \rangle^f}{\partial x} + \nu_f \left(\frac{\partial^2 \langle u \rangle}{\partial x^2} + \frac{\partial^2 \langle u \rangle}{\partial z^2} \right) - \frac{1}{2} S_w c_{d,xx} \left(\langle u \rangle^f \right)^2 \tag{3.1.2}$$

$$\langle u \rangle \frac{\partial \langle w \rangle^f}{\partial x} + \langle w \rangle \frac{\partial \langle w \rangle^f}{\partial z} = -\frac{\varepsilon_f}{\rho_f}\frac{\partial \langle p_f \rangle^f}{\partial z} + \nu_f \left(\frac{\partial^2 \langle w \rangle}{\partial x^2} + \frac{\partial^2 \langle w \rangle}{\partial z^2} \right) - \frac{1}{2} S_w c_{d,zz} \left(\langle w \rangle^f \right)^2 \tag{3.1.3}$$

and fluid and solid energy conservation in the channel,

$$\rho_f c_{pf} \langle u \rangle \frac{\partial \langle T_f \rangle^f}{\partial x} = k_f \frac{\partial}{\partial x}\left(\varepsilon_f \frac{\partial \langle T_f \rangle^f}{\partial x} \right) + k_f \frac{\partial}{\partial z}\left(\varepsilon_f \frac{\partial \langle T_f \rangle^f}{\partial z} \right) + h S_w \left(\langle T_s \rangle^s - \langle T_f \rangle^f \right) \tag{3.1.4}$$

$$k_s \frac{\partial}{\partial x}\left(\varepsilon_s \frac{\partial \langle T_s \rangle^s}{\partial x} \right) + k_s \frac{\partial}{\partial z}\left(\varepsilon_s \frac{\partial \langle T_s \rangle^s}{\partial z} \right) - h S_w \left(\langle T_s \rangle^s - \langle T_f \rangle^f \right) = 0 \tag{3.1.5}$$

These equations are solved over the same domain $\Omega = \{(x,z) \in \mathbb{R}^2 : 0 \leq x \leq L; 0 \leq z \leq H_c\}$. In addition, energy conservation in the base is also solved over a different domain $\Omega_b = \{(x,z_b) \in \mathbb{R}^2 : 0 \leq x \leq L; 0 \leq z_b \leq t_b\}$

$$\frac{\partial^2 T_b}{\partial x^2} + \frac{\partial^2 T_b}{\partial z_b^2} = 0 \tag{3.1.6}$$

and the two are connected at the interface. Mathematically, these type of problems appear frequently, and are also known as Domain Decomposition Methods (DDM). A schematic of the system is shown in Figure 3.1. The governing equations are complemented by their

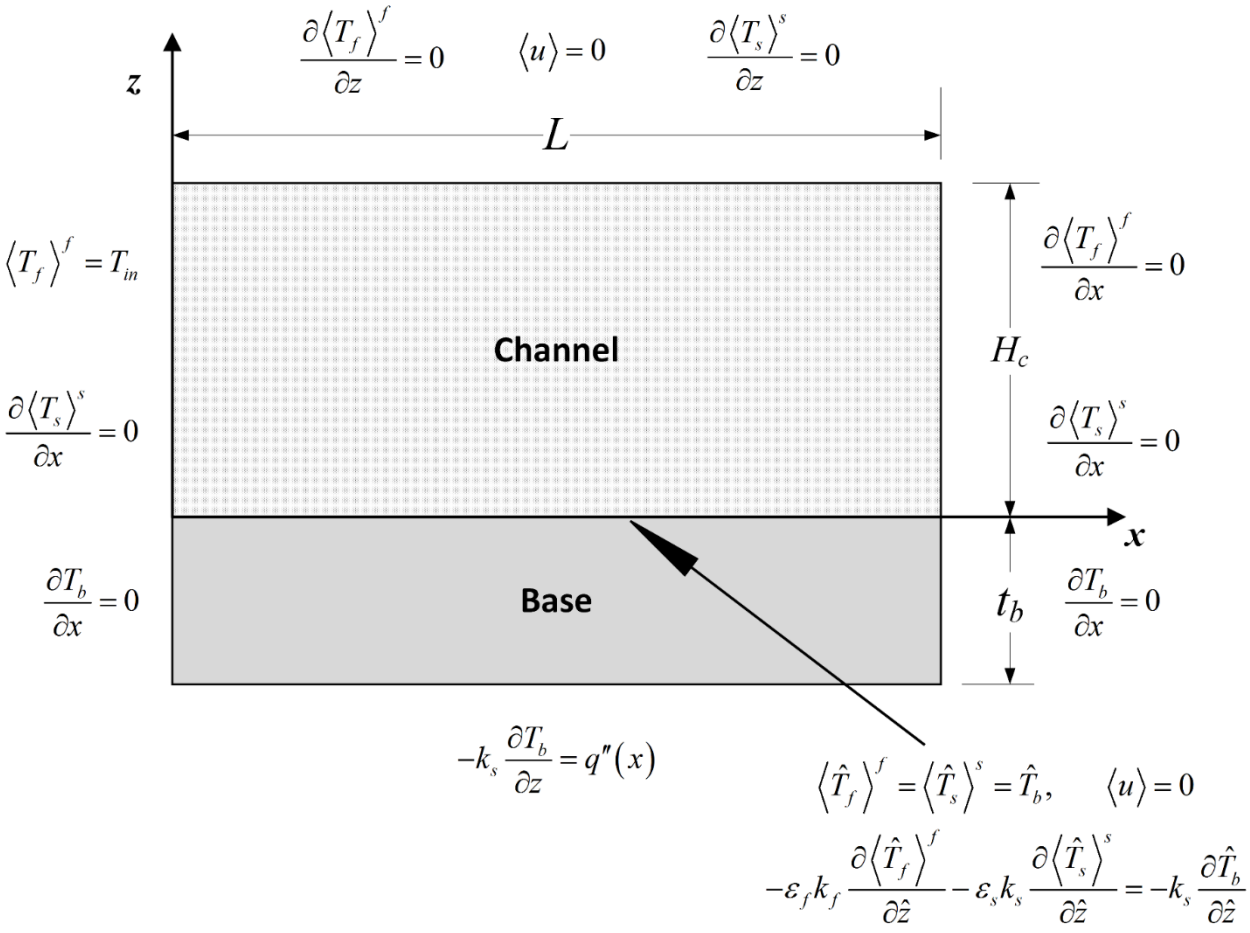

Figure 3.1: Schematic of System Geometry and Energy Boundary Conditions

boundary conditions, which are also shown in Figure 3.1. The boundary conditions for the momentum and continuity equation are no-slip and no-flow through at the top and bottom of the channel,

$$\langle \mathbf{v} \rangle = 0 \tag{3.1.7}$$

The fluid is assumed to be entering the system at constant temperature,

$$\langle T_f \rangle^f = T_{in} \tag{3.1.8}$$

the top of the heat sink is assumed to be adiabatic,

$$\left.\frac{\partial \langle T_f \rangle^f}{\partial z}\right|_{z=H_c} = 0 \tag{3.1.9}$$

and no heat enters through the outlet.

$$\left.\frac{\partial \langle T_f \rangle^f}{\partial x}\right|_{x=L} = 0 \tag{3.1.10}$$

It is also assumed that heat losses through the solid boundaries at the inlet, top and outlet are negligible.

$$\left.\frac{\partial \langle T_s \rangle^s}{\partial x}\right|_{x=0} = \left.\frac{\partial \langle T_s \rangle^s}{\partial x}\right|_{x=L} = \left.\frac{\partial \langle T_s \rangle^s}{\partial z}\right|_{x=H_c} 0 \tag{3.1.11}$$

Heat flux losses from the sides of the base are ignored,

$$\left.\frac{\partial T_b}{\partial x}\right|_{x=0} = \left.\frac{\partial T_b}{\partial x}\right|_{x=L} = 0 \tag{3.1.12}$$

and a known heat flux is applied at the bottom of the base,

$$-k_s \left.\frac{\partial T_b}{\partial z}\right|_{z=0} = q\left(x\right) \tag{3.1.13}$$

As discussed previously, at the interface it is assumed that the fluid, solid and base temperatures are equal,

$$\langle T_f \rangle^f = \langle T_s \rangle^s = T_b = T_i\left(x\right) \tag{3.1.14}$$

The interface temperature is not known a priori and it is obtained iteratively by requiring the system to satisfy the following energy conserving condition,

$$-\varepsilon_s k_s \left.\frac{\partial \langle T_s \rangle^s}{\partial z}\right|_{z=0} - \varepsilon_f k_f \left.\frac{\partial \langle T_f \rangle^f}{\partial z}\right|_{z=0} = -k_s \left.\frac{\partial T_b}{\partial z}\right|_{z=1} \tag{3.1.15}$$

This boundary condition represents a third boundary condition in the z-direction, while all the equations are second order. The numerical treatment of this extra boundary condition will be discussed in detail in the following sections.

3.2 Scaling of Conservation Equations

Before moving on to the numerical solution of the equations, it is always good practice to scale the governing equations to find possible simplifications, and identify important parameters.

Furthermore, well scaled equation will reduce computational round-off errors. In the rest of this section, the $\hat{}$ superscript will denote scaled quantities. First, the two domains are reduced to two unit squares, by applying the following scaling

$$\hat{x} = \frac{x}{L}, \quad \hat{z} = \frac{z}{H_c}, \quad \hat{z}_b = \frac{z_b}{t_b} \tag{3.2.1}$$

Next, starting from the momentum equation the governing equations are scaled.

3.2.1 Continuity and Momentum Equation

First, the x component of velocity is scaled

$$\langle \hat{u} \rangle = \frac{\langle u \rangle}{U} \tag{3.2.2}$$

In most cases, the average velocity or flow rate of the heat sink fan are provided, in which case the scale U is given. Substituting this scaling parameters in the continuity equation, Eqn. (3.1.1), the following form is obtained

$$\frac{U}{L}\frac{\partial u}{\partial x} + \frac{W}{H_c}\frac{\partial u}{\partial z} \rightarrow W \sim \left(\frac{H_c}{L}\right) U \tag{3.2.3}$$

Similarly, using the velocity and domain scaling given in Eqns. (3.2.1) and (3.2.2), the scaled x-momentum equation is

$$\begin{aligned} &\left(\frac{\varepsilon_f U^2}{L}\right)\left[\langle \hat{u} \rangle \frac{\partial \langle \hat{u} \rangle^f}{\partial \hat{x}} + \langle \hat{w} \rangle \frac{\partial \langle \hat{u} \rangle^f}{\partial \hat{z}}\right] = \\ &= -\frac{\varepsilon_f}{\rho_f}\frac{\partial \langle p_f \rangle^f}{\partial x} + \nu_f \left(\frac{U}{L^2}\frac{\partial^2 \langle \hat{u} \rangle}{\partial \hat{x}^2} + \frac{U}{H_c^2}\frac{\partial^2 \langle \hat{u} \rangle}{\partial \hat{z}^2}\right) - \frac{1}{2}U^2 S_w c_{d,xx}\left(\langle \hat{u} \rangle^f\right)^2 \end{aligned} \tag{3.2.4}$$

Note that the relation between superficial and intrinsic velocities led to the porosity appearance, and that the pressure gradient has not yet been scaled. Similarly, the same scaling is applied to the z-momentum equation

$$\begin{aligned} &\frac{\varepsilon_f U^2}{L}\left(\frac{H_c}{L}\right)\left[\langle \hat{u} \rangle \frac{\partial \langle \hat{w} \rangle^f}{\partial \hat{x}} + \langle \hat{w} \rangle \frac{\partial \langle \hat{w} \rangle^f}{\partial \hat{z}}\right] = -\frac{\varepsilon_f}{\rho_f}\frac{\partial \langle p_f \rangle^f}{\partial z} + \\ &+ \nu_f \left(\frac{H_c}{L}\right)\left(\frac{U}{L^2}\frac{\partial^2 \langle \hat{w} \rangle}{\partial \hat{x}^2} + \frac{U}{H_c^2}\frac{\partial^2 \langle \hat{w} \rangle}{\partial \hat{z}^2}\right) - \frac{1}{2}\left(\frac{H_c}{L}\right) U^2 S_w c_{d,zz}\left(\langle \hat{w} \rangle^f\right)^2 \end{aligned} \tag{3.2.5}$$

Up to this point, the scaling is quite similar to the scaling that is conducted for the fully developed assumption in channel flow. However, since our system is multi-scale, somewhere, the ratio of scales has to appear. This is found by dividing Eqn. (3.2.4) and Eqn. (3.2.5) by $S_w U^2$ and using the VAT hydraulic diameter defined in Eqn. (2.6.11),

$$\begin{aligned}
&\left(\frac{d_h}{4L}\right)\left[\langle\hat{u}\rangle\frac{\partial\langle\hat{u}\rangle^f}{\partial\hat{x}}+\langle\hat{w}\rangle\frac{\partial\langle\hat{u}\rangle^f}{\partial\hat{z}}\right]= \\
&=-\frac{d_h}{4\rho_f U^2}\frac{\partial\langle p_f\rangle^f}{\partial x}+\frac{1}{\varepsilon_f \mathrm{Re}_{dh}}\left[\left(\frac{d_h^2}{4L^2}\right)\frac{\partial^2\langle\hat{u}\rangle^f}{\partial\hat{x}^2}+\left(\frac{d_h^2}{4H_c^2}\right)\frac{\partial^2\langle\hat{u}\rangle^f}{\partial\hat{z}^2}\right]-\frac{1}{2}c_{d,xx}\Big(\langle\hat{u}\rangle^f\Big)^2
\end{aligned} \tag{3.2.6}$$

$$\begin{aligned}
&\left(\frac{d_h}{4L}\right)\left[\langle\hat{u}\rangle\frac{\partial\langle\hat{u}\rangle^f}{\partial\hat{x}}+\langle\hat{w}\rangle\frac{\partial\langle\hat{u}\rangle^f}{\partial\hat{z}}\right]= \\
&=-\frac{d_h}{4\rho_f U^2}\frac{\partial\langle p_f\rangle^f}{\partial x}+\frac{1}{\varepsilon_f \mathrm{Re}_{dh}}\left[\left(\frac{d_h^2}{4L^2}\right)\frac{\partial^2\langle\hat{u}\rangle^f}{\partial\hat{x}^2}+\left(\frac{d_h^2}{4H_c^2}\right)\frac{\partial^2\langle\hat{u}\rangle^f}{\partial\hat{z}^2}\right]-\frac{1}{2}c_{d,xx}\Big(\langle\hat{u}\rangle^f\Big)^2
\end{aligned} \tag{3.2.7}$$

where the Reynolds number is based on the average velocity and the hydraulic diameter

$$\mathrm{Re}_{dh}=\frac{U d_h}{\nu_f} \tag{3.2.8}$$

The length scale d_h represents the size of the lower scale geometry, and the length scale ratios represent the multi-scalicity of the problem. The goal is to find conditions for which the z component of the velocity will be negligible. It can be seen that there are three possibilities that would lead to this conclusion

1. The ratio H_c/L is small.
2. The product of the length ratios $(d_h/L\,)\,(H_c/L\,)$ is small and the z-component of the drag tensor is negligible.
3. The ratios $(d_h/L\,)$ and $(d_h/H_c\,)$ are small and the z-component of the drag tensor is negligible

The last condition would lead to an over simplification of the x-momentum equation, so it is assumed that one of the first two conditions are satisfied. With this in mind, the z-momentum equation implies that

$$\frac{\partial\langle p_f\rangle^f}{\partial z}=0,\quad \langle w\rangle=0 \tag{3.2.9}$$

Therefore, the continuity and x-momentum conservation equation become

$$\frac{\partial \langle \hat{u} \rangle}{\partial x} = 0 \tag{3.2.10}$$

$$\left(\frac{d_h}{4L}\right) \langle \hat{u} \rangle \frac{\partial \langle \hat{u} \rangle^f}{\partial \hat{x}} = -\frac{d_h}{4\rho_f U^2} \frac{d\langle p_f \rangle^f}{dx} + \frac{1}{\varepsilon_f \mathrm{Re}_{dh}} \left(\frac{d_h^2}{4H_c^2}\right) \frac{\partial^2 \langle \hat{u} \rangle}{\partial \hat{z}^2} - \frac{1}{2} c_{d,xx} \left(\langle \hat{u} \rangle^f\right)^2 \tag{3.2.11}$$

It can be noted that the scaling revealed that the advective and diffusive terms in the x-momentum equation will be much smaller than the momentum sink term. Physically this makes sense because it implies that most of the momentum loss in the system will be due to the no-slip conditions at the intricate lower scale surfaces, while the momentum loss due to the system boundaries will be much smaller. This also implies that the pressure term, which has to be significant, will balance the momentum sink. This assumption will be expanded and validated in Chapter 4 for several cases. With this in mind, a reference pressure is defined as

$$p_{ref} = \frac{2\rho_f c_d L}{d_h} \frac{U^2}{\varepsilon_f^2} \tag{3.2.12}$$

Since the superficial velocity is a divergence-free quantity, it is convenient to express everything in its terms. Substituting the scaled pressure and expressing everything in terms of superficial averages, Eqn. (3.2.11) becomes (the subscript xx in the drag term will be dropped from here on)

$$\left(\frac{d_h}{4L}\right) \langle \hat{u} \rangle \frac{\partial}{\partial \hat{x}} \left(\frac{\langle \hat{u} \rangle}{\varepsilon_f}\right) = -\frac{c_d}{2\varepsilon_f^2} \frac{d\langle p_f \rangle^f}{dx} + \frac{1}{\varepsilon_f \mathrm{Re}_{dh}} \left(\frac{d_h^2}{4H_c^2}\right) \frac{\partial^2 \langle \hat{u} \rangle}{\partial \hat{z}^2} - \frac{c_d}{2\varepsilon_f^2} \langle \hat{u} \rangle^2 \tag{3.2.13}$$

Note also that this derivation was carried out assuming that the porosity is constant. In cases in which the porosity and the hydraulic diameter are not constant, the scaling values given in Eqn. (3.2.11), are characteristic values, and can be denoted with a subscript c. In these cases, the scaled equation becomes

$$\begin{aligned} \frac{1}{\varepsilon_{f,c}} \left(\frac{d_{h,c}}{4L}\right) \langle \hat{u} \rangle \frac{\partial}{\partial \hat{x}} \left(\frac{\langle \hat{u} \rangle}{\hat{\varepsilon}_f}\right) = -\frac{c_{d,c}}{2\varepsilon_{f,c}^2} \hat{\varepsilon}_f \frac{d\langle p_f \rangle^f}{dx} + \\ + \frac{1}{\varepsilon_{f,c} \mathrm{Re}_{dh}} \left(\frac{d_{h,c}^2}{4H_c^2}\right) \frac{\partial^2 \langle \hat{u} \rangle}{\partial \hat{z}^2} - \frac{c_{d,c}}{2\varepsilon_{f,c}^2} \frac{\hat{S}_w \hat{c}_d}{\hat{\varepsilon}_f} \langle \hat{u} \rangle^2 \end{aligned} \tag{3.2.14}$$

Using the continuity equation, the convective term can be expressed in a more suitable form

$$\frac{\partial \langle \hat{u} \rangle}{\partial x} = \langle \hat{u} \rangle^f \frac{\partial \varepsilon_f}{\partial x} + \varepsilon_f \frac{\partial \langle \hat{u} \rangle^f}{\partial x} = 0 \rightarrow \frac{\partial}{\partial x} \left(\frac{\langle u \rangle}{\varepsilon_f}\right) = -\langle \hat{u} \rangle^f \frac{1}{\varepsilon_f} \frac{\partial \varepsilon_f}{\partial x} = -\langle \hat{u} \rangle \frac{1}{\varepsilon_{f,c} L} \frac{1}{\hat{\varepsilon}_f^2} \frac{\partial \hat{\varepsilon}_f}{\partial \hat{x}} \tag{3.2.15}$$

Substituting this relation back into Eqn. (3.2.14), and rearranging, a final form of the VAT momentum equation is obtained

$$\frac{2\varepsilon_{f,c}}{c_{d,c}\mathrm{Re}_{dh}}\left(\frac{d_{h,c}^2}{4H_c^2}\right)\frac{\partial^2\langle\hat{u}\rangle}{\partial\hat{z}^2}-\frac{1}{\hat{\varepsilon}_f^2}\left[\hat{S}_w\hat{c}_d-\frac{1}{c_{d,c}}\left(\frac{d_{h,c}}{2L}\right)\frac{\partial\hat{\varepsilon}_f}{\partial\hat{x}}\right]\langle\hat{u}\rangle^2=\hat{\varepsilon}_f\frac{d\langle p_f\rangle^f}{dx} \tag{3.2.16}$$

It can be seen that the porosity variation term in the x direction will act as an added momentum loss (or gain depending on the sign of the porosity gradient) proportional to the square of the velocity. The length scale ratios that arose in the previous derivation, will also be present in the scaling of the energy equations, therefore two parameters are defined

$$C_x=\frac{d_{h,c}}{2L},\quad C_z=\frac{d_{h,c}}{2H_c}, \tag{3.2.17}$$

The momentum equation can be rewritten as

$$M_1\frac{\partial^2\langle\hat{u}\rangle}{\partial\hat{z}^2}-\left[\hat{S}_w\hat{c}_d-M_3\frac{\partial\hat{\varepsilon}_f}{\partial\hat{x}}\right]\langle\hat{u}\rangle^2=\hat{\varepsilon}_f\frac{d\langle\hat{p}_f\rangle^f}{d\hat{x}} \tag{3.2.18}$$

where the parameters M_1 and M_2 are defined as

$$M_1=\frac{2\varepsilon_{f,c}}{c_{d,c}\mathrm{Re}_{dh}}C_z^2,\quad M_3=\frac{C_x}{c_{d,c}} \tag{3.2.19}$$

It is important to point out here that the scaling has shown that the momentum loss will be balanced by the drag term, therefore, the coefficients of these two terms are of order one. The other coefficients that are present in the equation will determine the importance of the other terms in the equation with respect to these two terms. This discussion is carried out in the next chapter.

3.2.2 Fluid Energy

Next, the fluid energy equation is scaled. The fluid temperature is scaled as follows

$$\left\langle\hat{T}_f\right\rangle^f=\frac{\langle T_f\rangle^f-T_{in}}{\langle T_f\rangle_{avg}^f-T_{in}}, \tag{3.2.20}$$

where integral conservation of energy implies that

$$\langle T_f\rangle_{avg}^f-T_{in}=\frac{Q}{\dot{m}c_{pf}} \tag{3.2.21}$$

and the mass flow rate is defined as

$$\dot{m} = \rho_f H_c W \int_0^1 \langle \hat{u} \rangle \, dz \tag{3.2.22}$$

Furthermore, the heat transfer coefficient and the specific surface are scaled using their average values

$$\hat{h} = \frac{h}{h_{avg}}, \quad \hat{S}_w = \frac{S_w}{S_{w,avg}} \tag{3.2.23}$$

Substituting these quantities in the VAT energy conservation equation, a scaled form of the energy equation is obtained

$$\begin{aligned} \frac{\mathrm{Re}_{dh}\mathrm{Pr}_f}{2Nu_{dh}} \frac{C_x}{\hat{\varepsilon}_{f,c}} \langle \hat{u} \rangle \frac{\partial \left\langle \hat{T}_f \right\rangle^f}{\partial \hat{x}} &= \frac{C_x^2}{Nu_{dh}} \frac{\partial}{\partial \hat{x}} \left(\hat{\varepsilon}_f \frac{\partial \left\langle \hat{T}_f \right\rangle^f}{\partial \hat{x}} \right) + \\ &+ \frac{C_z^2}{Nu_{dh}} \frac{\partial}{\partial \hat{z}} \left(\hat{\varepsilon}_f \frac{\partial \left\langle \hat{T}_f \right\rangle^f}{\partial \hat{z}} \right) + \hat{h} \hat{S}_w \left(\left\langle \hat{T}_s \right\rangle^s - \left\langle \hat{T}_f \right\rangle^f \right) \end{aligned} \tag{3.2.24}$$

where the non-dimensional parameters are defined as

$$Nu_{dh} = \frac{\hat{h}_{avg} \hat{d}_{h,avg}}{\hat{k}_f}, \quad \mathrm{Pr}_f = \frac{\hat{\nu}_f}{\hat{\alpha}_f} = \frac{\hat{\nu}_f}{\hat{k}_f / \hat{\rho}_f \hat{c}_{pf}}, \quad C_x = \frac{d_{h,avg}}{2L} \tag{3.2.25}$$

The equation can be rewritten in a simpler form as

$$F_1 \langle \hat{u} \rangle \frac{\partial \left\langle \hat{T}_f \right\rangle^f}{\partial \hat{x}} = F_2 \frac{\partial}{\partial \hat{x}} \left(\hat{\varepsilon}_f \frac{\partial \left\langle \hat{T}_f \right\rangle^f}{\partial \hat{x}} \right) + F_3 \frac{\partial}{\partial \hat{z}} \left(\hat{\varepsilon}_f \frac{\partial \left\langle \hat{T}_f \right\rangle^f}{\partial \hat{z}} \right) + \hat{h} \hat{S}_w \left(\left\langle \hat{T}_s \right\rangle^s - \left\langle \hat{T}_f \right\rangle^f \right) \tag{3.2.26}$$

where the non-dimensional parameters are

$$F_1 = \frac{\mathrm{Re}_{dh}\mathrm{Pr}_f}{2Nu_{dh}} \frac{C_x}{\varepsilon_{f,c}}, \quad F_2 = \frac{C_x^2}{Nu_{dh}}, \quad F_3 = \frac{C_z^2}{Nu_{dh}}, \tag{3.2.27}$$

This equation was scaled in such a way that F_4 is of order one. Therefore, the other parameters in the equation represent their relative importance to the interphase heat transfer term. The boundary equations are also scaled

$$\left\langle \hat{T}_f \right\rangle^f \Big|_{\hat{x}=0} = 0 \tag{3.2.28a}$$

$$\left.\frac{\partial\left\langle\hat{T}_f\right\rangle^f}{\partial\hat{x}}\right|_{\hat{x}=1} = \left.\frac{\partial\left\langle\hat{T}_f\right\rangle^f}{\partial\hat{z}}\right|_{\hat{z}=1} = 0 \tag{3.2.28b}$$

$$\left\langle\hat{T}_f\right\rangle^f\Big|_{z=0} = \frac{T_i(x) - T_{in}}{\langle T_f\rangle^f_{avg} - T_{in}} = \hat{T}_i(x) \tag{3.2.28c}$$

3.2.3 Solid Equation

Next, the solid equation is scaled. The solid equation is scaled using the same scaling factor used for the fluid equation, to avoid extra terms in the interphase heat transfer term and interface condition,

$$\left\langle\hat{T}_s\right\rangle^s = \frac{\langle T_s\rangle^s - T_{in}}{\langle T_f\rangle^f_{avg} - T_{in}} \tag{3.2.29}$$

Substituting this in the governing equation and rearranging, the following equation is obtained

$$\frac{R_k}{Nu_{dh}}C_x^2\frac{\partial}{\partial\hat{x}}\left(\hat{\varepsilon}_s\frac{\partial\left\langle\hat{T}_s\right\rangle^s}{\partial\hat{x}}\right) + \frac{R_k}{Nu_{dh}}C_z^2\frac{\partial}{\partial\hat{z}}\left(\hat{\varepsilon}_s\frac{\partial\left\langle\hat{T}_s\right\rangle^s}{\partial\hat{z}}\right) - \hat{h}\hat{S}_w\left(\left\langle\hat{T}_s\right\rangle^s - \left\langle\hat{T}_f\right\rangle^f\right) = 0 \tag{3.2.30}$$

where $R_k$is the ratio of porosity weighted thermal conductivities

$$R_k = \frac{\varepsilon_{s,c}k_s}{\varepsilon_{f,c}k_f} \tag{3.2.31}$$

This can be rewritten in compact form as

$$S_1\frac{\partial}{\partial\hat{x}}\left(\hat{\varepsilon}_s\frac{\partial\left\langle\hat{T}_s\right\rangle^s}{\partial\hat{x}}\right) + S_2\frac{\partial}{\partial\hat{z}}\left(\hat{\varepsilon}_s\frac{\partial\left\langle\hat{T}_s\right\rangle^s}{\partial\hat{z}}\right) - \hat{h}\hat{S}_w\left(\left\langle\hat{T}_s\right\rangle^s - \left\langle\hat{T}_f\right\rangle^f\right) = 0 \tag{3.2.32}$$

with

$$S_1 = \frac{R_k}{Nu_{dh}}C_x^2, \quad S_2 = \frac{R_k}{Nu_{dh}}C_z^2 \tag{3.2.33}$$

Once again, the coefficients S represent the magnitude of each term with respect to the interphase heat transfer term. The boundary conditions are also scaled

$$\left.\frac{\partial\left\langle\hat{T}_s\right\rangle^s}{\partial\hat{x}}\right|_{\hat{x}=0} = \left.\frac{\partial\left\langle\hat{T}_s\right\rangle^s}{\partial\hat{x}}\right|_{\hat{x}=1} = \left.\frac{\partial\left\langle\hat{T}_s\right\rangle^s}{\partial\hat{z}}\right|_{\hat{z}=1} = 0 \tag{3.2.34a}$$

$$\left\langle\hat{T}_s\right\rangle^s\Big|_{z=0} = \hat{T}_i(x) \tag{3.2.34b}$$

3.2.4 Base and Interface

The base is also non-dimensionalized using the same temperature scaling,

$$\hat{T}_b = \frac{T_b - T_{in}}{\langle T_f \rangle^f_{avg} - T_{in}} \tag{3.2.35}$$

Substituting this, in the governing Laplace equation, the following equation is obtained

$$\left(\frac{t_b}{L}\right)^2 \frac{\partial^2 \hat{T}_b}{\partial \hat{x}^2} + \frac{\partial^2 \hat{T}_b}{\partial \hat{z}_b^2} = 0 \tag{3.2.36}$$

or

$$C_b^2 \frac{\partial^2 \hat{T}_b}{\partial \hat{x}^2} + \frac{\partial^2 \hat{T}_b}{\partial \hat{z}_b^2} = 0 \tag{3.2.37}$$

where

$$C_b = \frac{t_b}{L} \tag{3.2.38}$$

The boundary condition at the bottom of the base becomes

$$\left.\frac{\partial \hat{T}_b}{\partial \hat{x}}\right|_{\hat{x}=0} = \left.\frac{\partial \hat{T}_b}{\partial \hat{x}}\right|_{\hat{x}=1} = 0 \tag{3.2.39a}$$

$$\left.\frac{\partial \hat{T}_b}{\partial \hat{z}}\right|_{\hat{z}=0} = -\frac{q_w(x)\, t_b}{\left(\langle T_f \rangle^f - T_{in}\right) k_s} = -\hat{q}_w(x) \tag{3.2.39b}$$

The scaled interface boundary condition is given by

$$\varepsilon_{s,c} \frac{t_b}{H_c} \hat{\varepsilon}_s \frac{\partial \left\langle \hat{T}_s \right\rangle^s}{\partial \hat{z}} + \frac{\varepsilon_{f,c} k_f}{\varepsilon_{s,c} k_s} \varepsilon_{s,avg} \frac{t_b}{H_c} \hat{\varepsilon}_f \frac{\partial \left\langle \hat{T}_f \right\rangle^f}{\partial \hat{z}} = \frac{\partial \hat{T}_b}{\partial \hat{z}} \tag{3.2.40}$$

which can be rewritten as

$$K_1 \hat{\varepsilon}_s \frac{\partial \left\langle \hat{T}_s \right\rangle^s}{\partial \hat{z}} + \frac{K_1}{R_k} \hat{\varepsilon}_f \frac{\partial \left\langle \hat{T}_f \right\rangle^f}{\partial \hat{z}} = \frac{\partial \hat{T}_b}{\partial \hat{z}} \tag{3.2.41}$$

where the coefficients K_1 is defined as

$$K_1 = \varepsilon_{s,avg} \frac{t_b}{H_c} \tag{3.2.42}$$

A closed set of scaled equations to model heat transfer and fluid flow through a heat sink have been developed. In the next section, numerical methods for the solution of the equations will be discussed in detail. Note that from now on, the superscript ˆ will be dropped and all the equations discussed will be the scaled equations derived in this section.

Table 3.1: Code Inputs

Geometry Type
Heat Sink Length [mm]
$W[mm]$
$H_c[mm]$
Transverse Pitch
Longitudinal Pitch $p_y[mm]$
Geometry Varying Direction (none=0, z=1, x=2, x & z =3)
Porosity Variation Function Type
Porosity Variation Function Parameters
Base Thickness $t_b[mm]$

3.3 Solution Methods

In this section, the solution methods employed for the calculation of the geometry, solution of the governing equations, and the interface matching is discussed.

3.3.1 Geometry

Three type of geometries are considered in this work: inline pin fins, staggered pin fins and plane fins (micro-channels). For each type of geometry, geometrical variations in the x- and z- direction are considered. In this cases, calculation of the VAT geometric parameters, porosity and specific surface require some discussion, which is carried out in this section. Since the geometric parameters that describe each of these geometries can be different, in order to develop an input interface to the code that was independent of the geometry, the definition of the parameters that describe the geometry are not always intuitive. The code is set up in such a way that the geometric inputs given in are required in all cases, In all geometries, the quantity that varies is specified by the size of the obstacles, D. For pin fins, this is obviously the diameter of the pins, while for micro-channels, it represents the thickness of the fins. In general, D is allowed to be a function of x- and z- and in the following

sections, the calculation of the VAT geometrical parameters for each configuration will be explained. Also, to reduce numerical errors in the integration process that is required to calculate these parameters, the geometric parameters are calculated on a $512x512$ grid, and then interpolated on the solution grid. The parameters to be calculated for each geometry are the total REV volume V , the fluid volume in the REV V_f and the interface are between the two phases A_{fs}. Given these parameters, the porosity, specific surface and hydraulic diameters are calculated using their definitions.

3.3.1.1 Inline Pin Fins

The assumed diameter variation in the x-direction for inline pin fins is shown in the top view of the REV given in Figure 3.2. The description of the z-direction variations are shown from a side view in Figure 3.3. These figures, as well as the ones in the next two sections, are not shown to scale, and they are only meant to elucidate the assumed geometry variations.

The volume of the REV is given by

$$V = p_x p_y h_{REV} \tag{3.3.1}$$

The volume of the solid at each REV location is

$$V_s = \frac{1}{8}\pi \left[\int_{z-h_{REV}/2}^{z+h_{REV}/2} \left[D\left(x,\tilde{z}\right)\right]^2 d\tilde{z} + \int_{z-h_{REV}/2}^{z+h_{REV}/2} \left[D\left(x+p_x,\tilde{z}\right)\right]^2 d\tilde{z} \right] \tag{3.3.2}$$

The interface area at each REV location is

$$A_{fs} = \pi \left[\int_{z-h_{REV/2}}^{z+h_{REV/2}} R\left(x,\tilde{z}\right) \sqrt{1+\left[R'\left(x,\tilde{z}\right)\right]^2} d\tilde{z} + \int_{z-h_{REV/2}}^{z+h_{REV/2}} R\left(x+p_x,\tilde{z}\right) \sqrt{1+\left[R'\left(x+p_x,\tilde{z}\right)\right]^2} d\tilde{z} \right] \tag{3.3.3}$$

where $R\left(x,z\right) = {}^{D(x,z)}/_{2}$.

3.3.1.2 Staggered Pin Fins

The assumed diameter variation in the x-direction for staggered pin fins is shown in the top view of the REV given in Figure 3.4. The description of the z-direction variations are shown

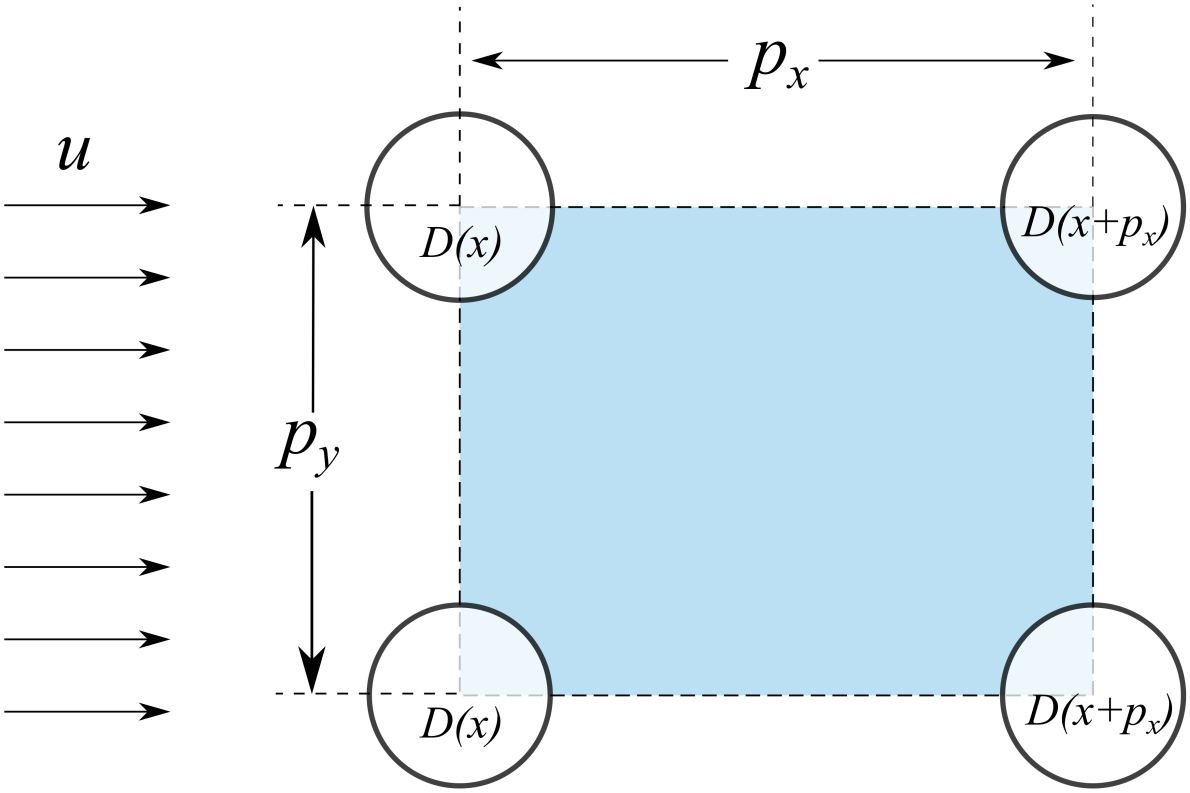

Figure 3.2: Top View of an Inline Pin Fin REV

from a side view in Figure 3.5. The volume of the REV is given by

$$V = 2p_x p_y h_{REV} \tag{3.3.4}$$

The volume of the solid at each REV location is

$$V_s = \frac{1}{8}\pi \left[3 \int_{z-h_{REV}/2}^{z+h_{REV}/2} \left[D\left(x, \tilde{z}\right)\right]^2 d\tilde{z} + \int_{z-h_{REV}/2}^{z+h_{REV}/2} \left[D\left(x+p_x, \tilde{z}\right)\right]^2 d\tilde{z} \right] \tag{3.3.5}$$

The interface area at each REV location is

$$A_{fs} = \pi \left[3 \int_{z-h_{REV/2}}^{z+h_{REV/2}} R\left(x, \tilde{z}\right) \sqrt{1 + \left[R'\left(x, \tilde{z}\right)\right]^2} d\tilde{z} + \int_{z-h_{REV/2}}^{z+h_{REV/2}} R\left(x+p_x, \tilde{z}\right) \sqrt{1 + \left[R'\left(x+p_x, \tilde{z}\right)\right]^2} d\tilde{z} \right] \tag{3.3.6}$$

where $R\left(x, z\right) = {}^{D(x,z)}/_{2}$.

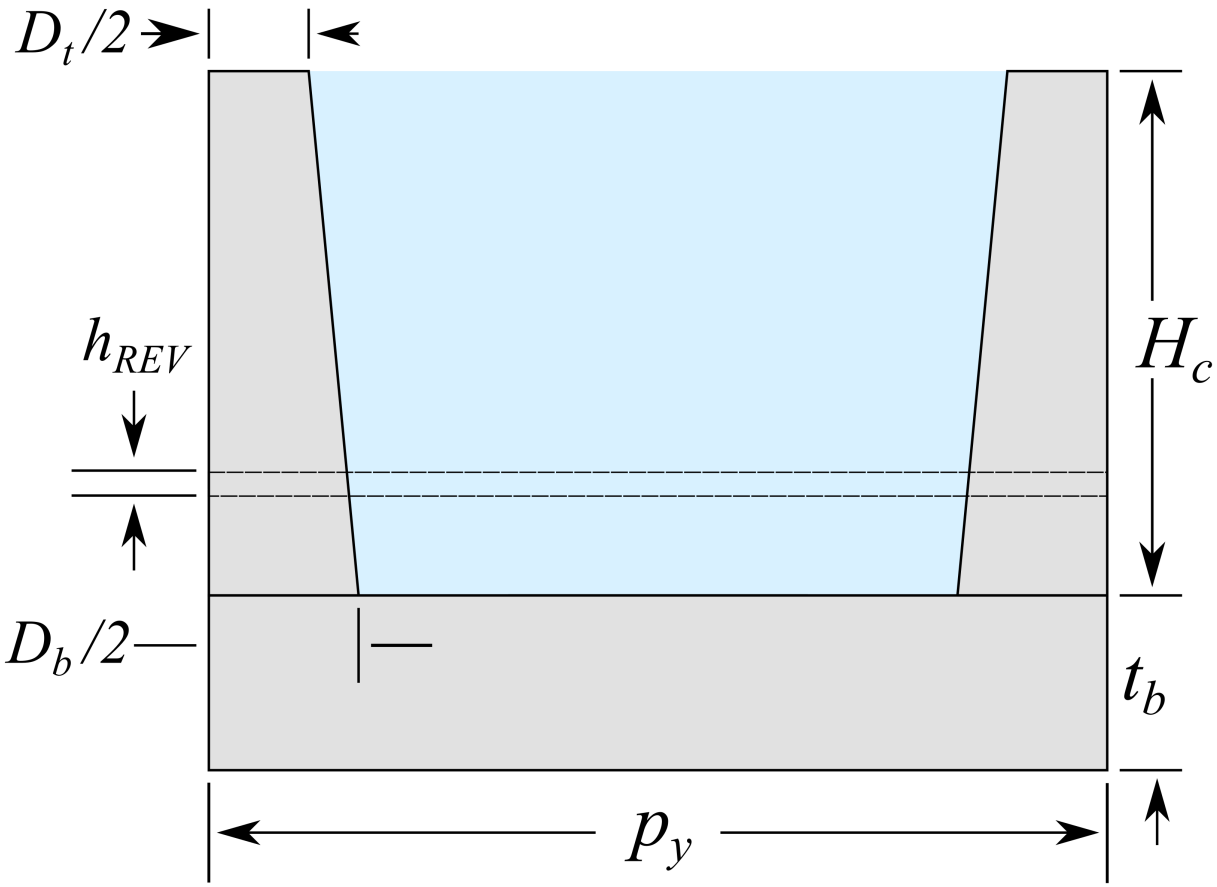

Figure 3.3: Front View of an Inline Pin Fin REV

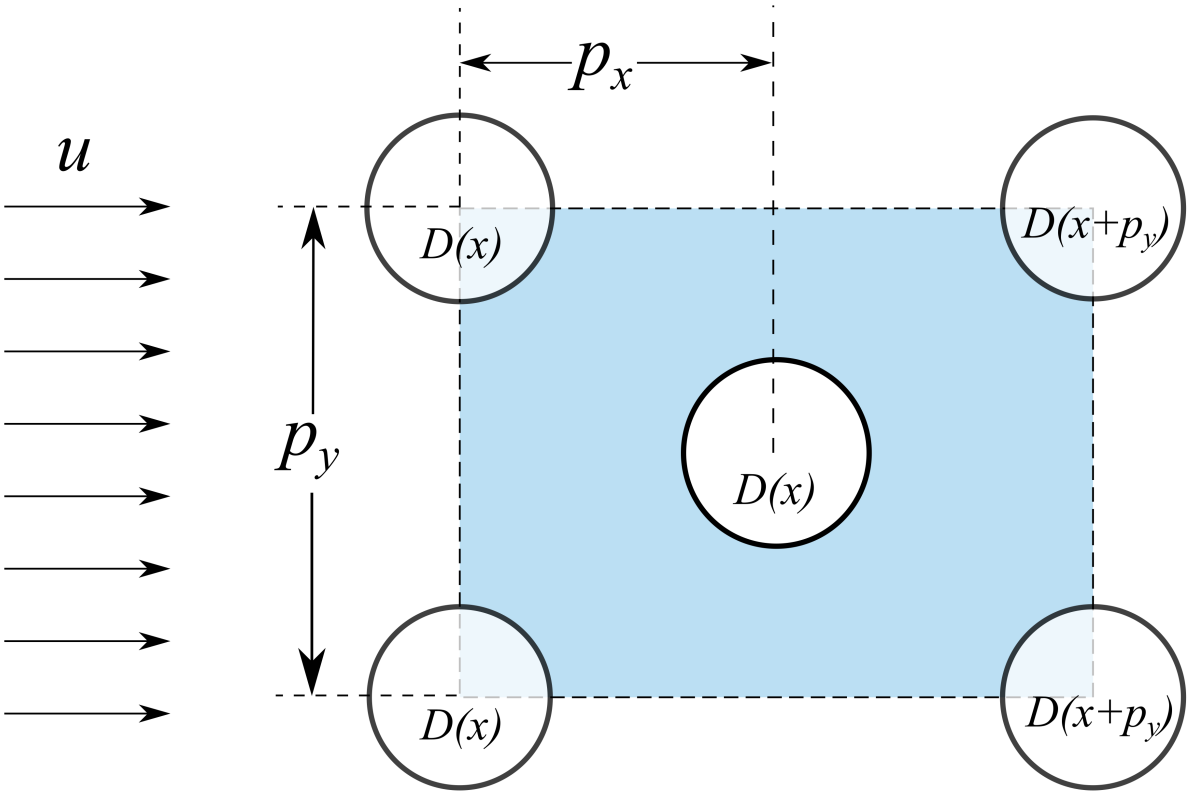

Figure 3.4: Top View of a Staggered Pin Fin REV

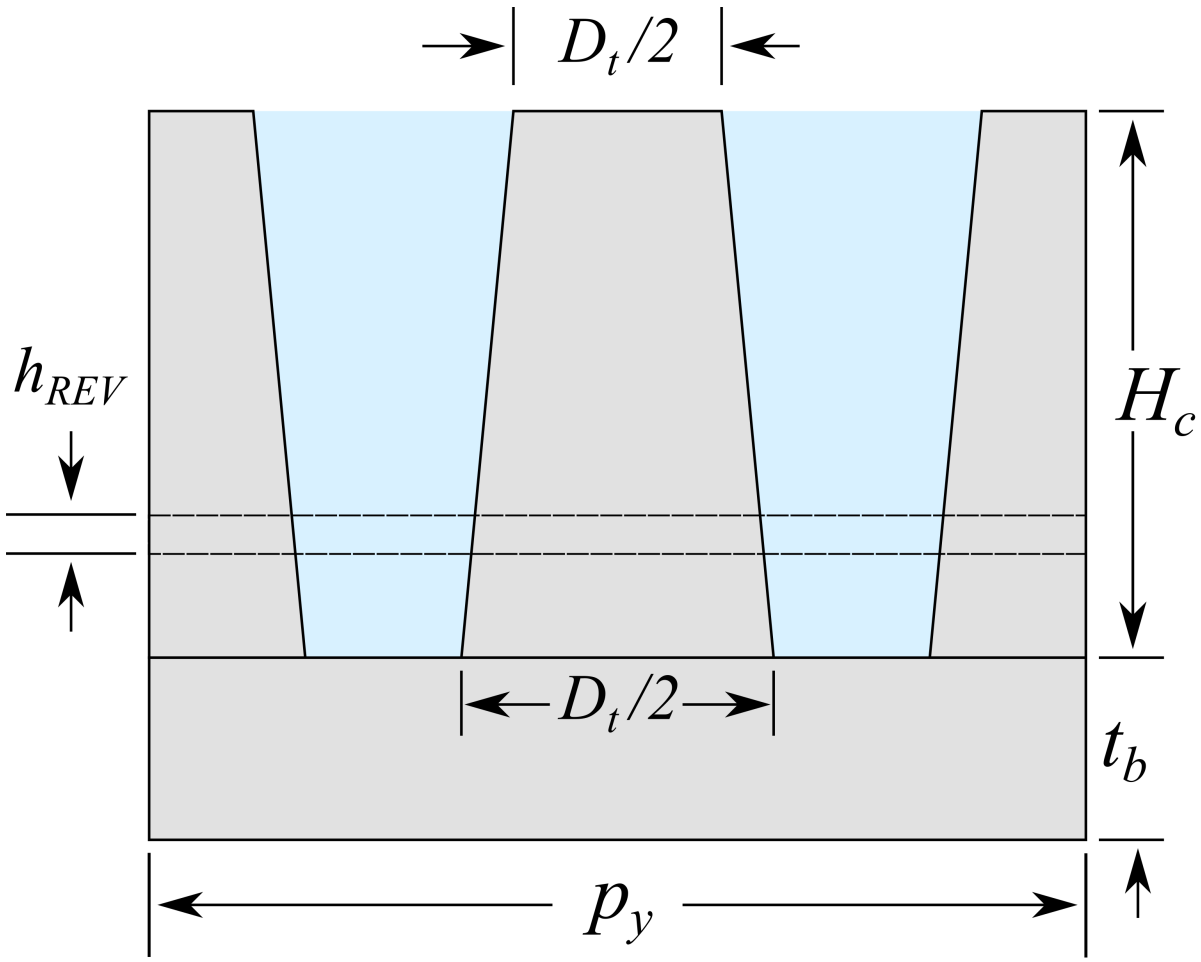

Figure 3.5: Schematic of Front View of a Staggered Pin Fin REV

3.3.1.3 Plane Fins

Plane fins are continuous, therefore the definition of the parameters is more straightforward. The top view and side views, with the definition of the parameters are given in Figure 3.6 and Figure 3.7, respectively. The volume of the REV is given by

$$V = p_y h_{REV} L_{REV} \tag{3.3.7}$$

The volume of the fluid is given by

$$V_f = \int_{x-L_{REV}/2}^{x+L_{REV}/2} \int_{z-h_{REV}/2}^{z+h_{REV}/2} w\left(\tilde{x}, \tilde{z}\right) d\tilde{z} d\tilde{x} \tag{3.3.8}$$

The interface area is given by

$$A_{fs} = 2 \int_{z-h_{REV}/2}^{z+h_{REV}/2} \int_{x-L_{REV}/2}^{x+L_{REV}/2} \sqrt{\left[\frac{\partial w}{\partial x}\right]^2 + \left[\frac{\partial w}{\partial z}\right]^2 + 1} d\tilde{x} d\tilde{z} \tag{3.3.9}$$

The determination of the lower scale geometric parameters obtained solving these integrals is indeed independent of the actual profile of the fins. For simple cases, such as constant or linear geometries, these integrals can be solved analytically, however, in the developed code they are solved numerically (with small grid spacing) such that any profile defined by a integrable function can be analyzed.

3.3.2 Continuity and Momentum Equations

The continuity and momentum equations were derived in the previous section and their scaled form, given in Eqns. (3.2.10) and (3.2.18), are repeated here for completeness

$$\frac{\partial \langle \hat{u} \rangle}{\partial x} = 0 \tag{3.3.10}$$

$$-M_1 \frac{\partial^2 \langle u \rangle}{\partial z^2} + M_3\left(x, z\right) \langle u \rangle^2 = \frac{d \langle p_f \rangle}{dx} \tag{3.3.11}$$

where

$$M_1 = \frac{2\varepsilon_{f,avg}}{\mathrm{Re}_{dh} f_{f,avg}} C_z^2, \quad M_3 = \frac{1}{\varepsilon_f^2}\left(S_w f_f - \frac{C_x}{f_{f,avg}} \frac{\partial \varepsilon_f}{\partial x}\right) \tag{3.3.12}$$

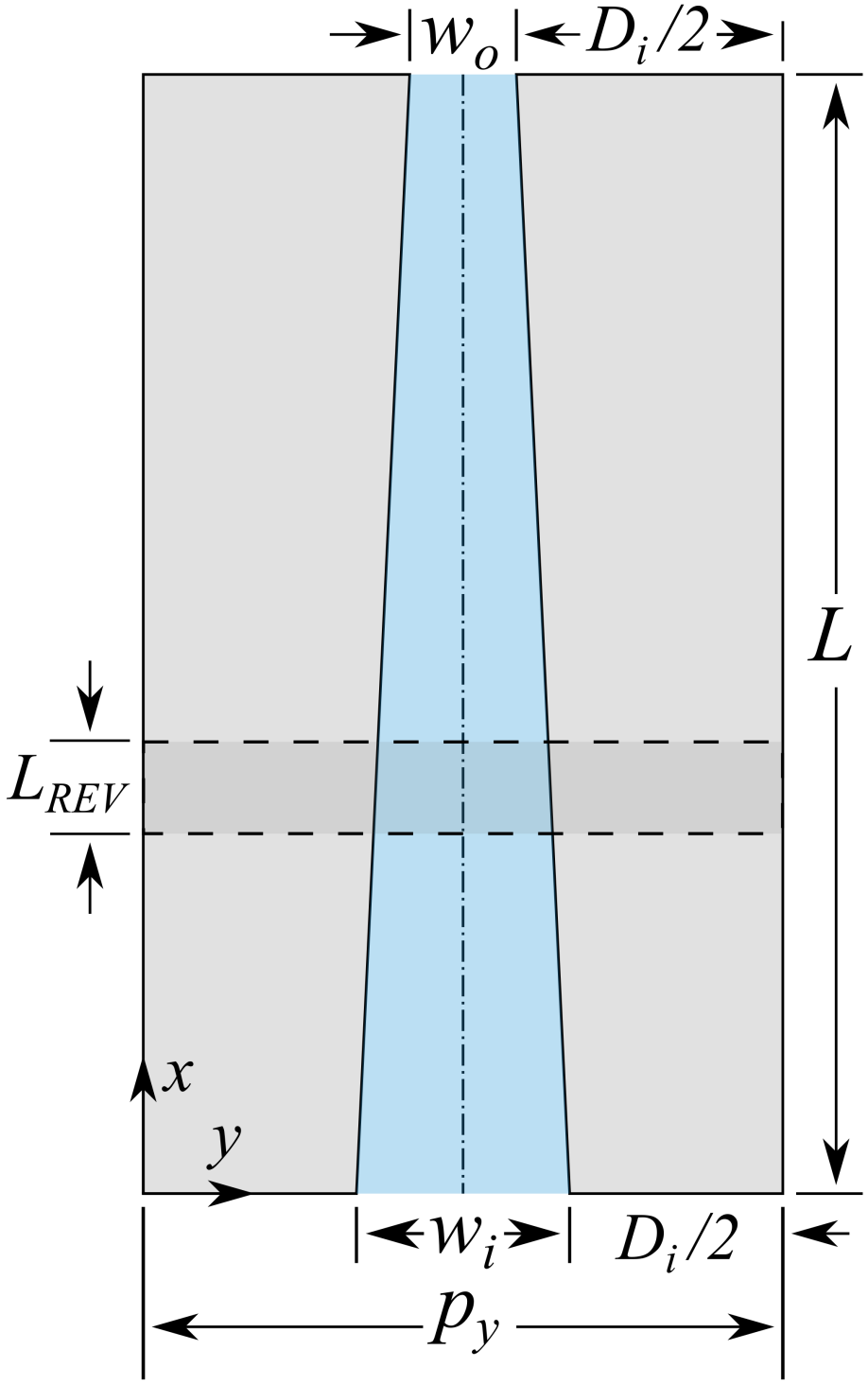

Figure 3.6: Schematic of Top View of Converging Micro-channel

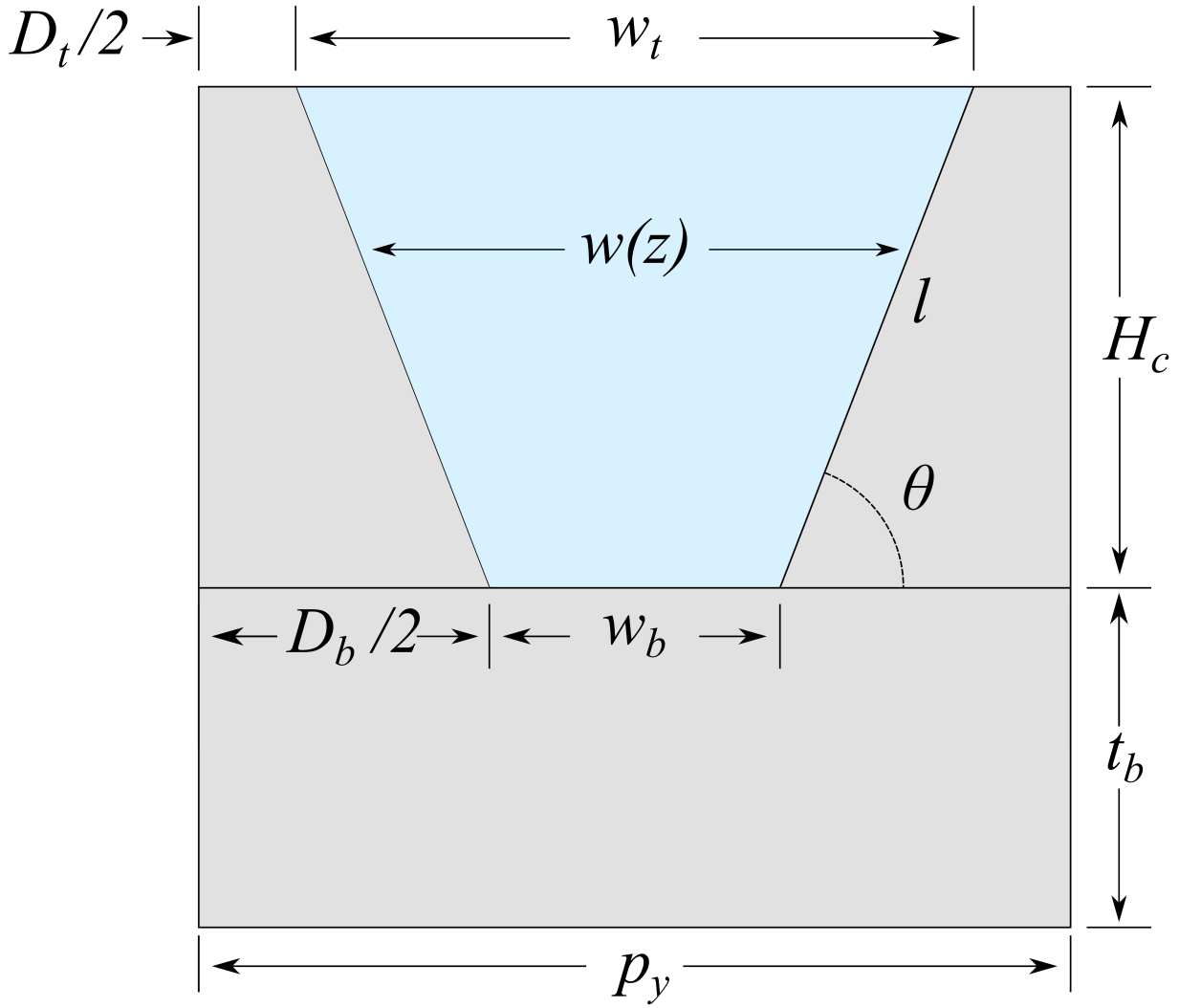

Figure 3.7: Schematic of Front View of Trapezoidal Microchannel

This is a non-linear equation in two dimensions for the superficial velocity, and can be solved using the methods discussed in the previous section. Using second order accurate finite difference schemes, the discretized equation is

$$-\frac{M_1}{\Delta z^2}\left(\langle u\rangle_{i,j-1}-2\langle u\rangle_{i,j}+\langle u\rangle_{i,j+1}\right)+M_{3,i,j}\langle u\rangle_{i,j}^2=\left.\frac{d\langle p_f\rangle}{dx}\right|_{i,j} \tag{3.3.13}$$

Note that the dependency on the x direction is only in the coefficient M_2 and the pressure gradient, therefore, the equations at each x location are independent of each other, and can be solved as such. The system of equations given by Eqn. (3.3.13), is a non-linear system and at each i location it is solved using a Newtons method, The discretized equations for point i at iteration k is given by

$$g_{i,j}\left(\langle u\rangle|^k\right)=-\frac{M_1}{\Delta z^2}\left(\langle u\rangle|_{i,j-1}^k-2\langle u\rangle|_{i,j}^k+\langle u\rangle|_{i,j+1}^k\right)+M_{3,i,j}\left(\langle u\rangle|_{i,j}^k\right)^2-\left.\frac{d\langle p_f\rangle}{dx}\right|_{i,j} \tag{3.3.14}$$

The Jacobian at each i location is calculated from Eqn. (3.3.14)

$$\left[J\left(\langle u\rangle^f\right)\right]_{jm}=\frac{\partial}{\partial u_m}\left[g_{i,j}\left(\langle u\rangle^f\right)\right]=\begin{cases}\dfrac{2M_1\langle u\rangle|^k{}_{i,j-1}}{\Delta z^2}, j=m-1\\ \dfrac{2M_1\langle u\rangle|^k{}_{i,j}}{\Delta z^2}+2M_{3,i,j}\langle u\rangle|_{i,j}^k, j=m\\ \dfrac{2M_1\langle u\rangle|^k{}_{i,j+1}}{\Delta z^2}, j=m+1\\ 0, otherwise\end{cases} \tag{3.3.15}$$

The algorithm is implemented by solving the tridiagonal linear system

$$\mathbf{J}\left(\langle\mathbf{u}\rangle^{\mathbf{f}}\Big|^k\right)\boldsymbol{\Delta}|^k=-\mathbf{g}\left(\langle\mathbf{u}\rangle^{\mathbf{f}}\Big|^k\right) \tag{3.3.16}$$

using Thomas algorithm [149] and updating the solution

$$\langle\mathbf{u}\rangle^{\mathbf{f}}\Big|^{k+1}=\langle\mathbf{u}\rangle^{\mathbf{f}}\Big|^k+\boldsymbol{\Delta}|^k \tag{3.3.17}$$

until $\left\|\boldsymbol{\Delta}|^k\right\|_2/\left\|\langle\mathbf{u}\rangle^{\mathbf{f}}\Big|^k\right\|_2\leq\sigma_{mom}$. The tolerance is chosen to be $\sigma_{mom}=\Delta z^2$. This choice is justified by the fact that, after the iterative process has converged, the numerical error at every point i, will be the sum of the local truncation error of the scheme and the iterative process tolerance. Therefore, lowering σ_{mom} much below the local truncation error would

not significantly improve the accuracy, but could significantly increase computational time. The assumption that the flow is locally fully developed assumption implies that the pressure gradient at each x location is independent of the pressure gradient at other x locations. Therefore, the pressure gradient is determined by enforcing mass flow rate conservation at each x location separately. In mathematical terms, pressure is simply a Lagrangian variable in the system that is used to enforce mass conservation. An initial pressure distribution is defined, then the function to be minimized at each location is

$$s\left(x_i\right) = \dot{m} - \int_0^1 u\left(x_i, \tilde{z}\right) d\tilde{z} \tag{3.3.18}$$

A Newton-Rhapson method is used for updating the pressure at each iteration,

$$\left.\frac{dp}{dx}\right|_i^{k+1} = \left.\frac{dp}{dx}\right|_i^{k} - \frac{s^k\left(x_i\right)}{S^k\left(x_i\right)} \tag{3.3.19}$$

where S is the gradient of the function s as a function of the pressure gradient

$$S^k\left(x_i\right) = \frac{s^k\left(x_i\right) - s^{k-1}\left(x_i\right)}{\left.\frac{dp}{dx}\right|_i^k - \left.\frac{dp}{dx}\right|_i^{k-1}} \tag{3.3.20}$$

In addition, it was found that for extreme values of the x gradient, an under relaxation factor was required for stability, and a value of 0.8 was chosen based on numerical experiments. Once the pressure gradient is obtained, the pressure distribution is obtained by simply numerically integrating the pressure gradient using a trapezoidal method, where the outlet value is set to zero. The local friction factor also depends on the local velocity, therefore, after the velocity and pressure distribution have converged, another fixed point iterative loop is used to obtain a final solution of the momentum equation. The algorithm for the solution is given in Figure 3.8. At each iteration, the linear system given in Eqn. (3.3.16) needs to be solved. In the current version of the code, the system is solved by generating a sparse matrix representation and solving the linear system using MATLABs sparse solver. The overall iterative procedure is found to converge on average within 50 iterations, which for a $128x128$ grid implies a computational time of about $0.3s$.

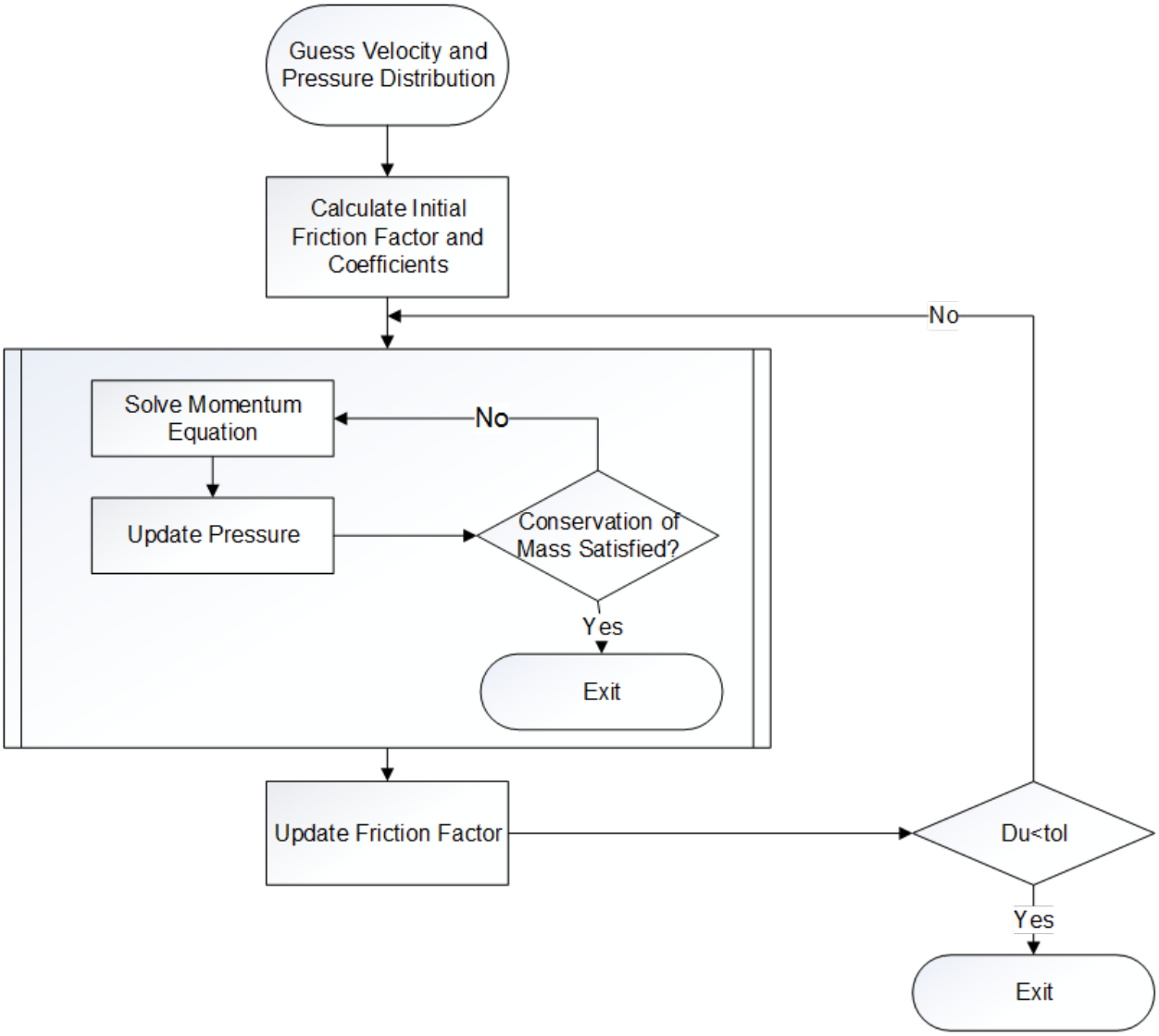

Figure 3.8: Momentum equation solution algorithm

3.3.3 Energy

The energy equations are a set of linear, two-dimensional, coupled partial differential equations. The coupling is due to the inter-REV heat transfer term, and the interface boundary conditions. Two different numerical methods have been developed to solve the governing equations: a Galerkin Method and a Finite Difference method. The Galerkin Method was developed only for constant porosity cases, while the finite difference method was developed for both constant and variable porosity cases.

3.3.3.1 Galerkin Method Solution

The Galerkin Method is a subclass of the larger group of spectral methods. The idea at the bottom of the Galerkin Method is that it is more advantageous to look for the unknown coefficients of a series expansion of the function, than to solve the domain on a grid. With this in mind, the fluid and solid temperatures are expanded in a tensor product of modified Fourier series [150] (using Einsteins summation convention)

$$\langle T_f \rangle^f = b_n \, \mathrm{c}\left(\varphi_n x\right) + \left[l_m + f_{nm} \, \mathrm{s}\left(\gamma_n x\right)\right] \mathrm{s}\left(\gamma_m z\right) \tag{3.3.21}$$

$$\langle T_s \rangle^s = b_n \, \mathrm{c}\left(\varphi_n x\right) + s_{nm} \, \mathrm{c}\left(\varphi_n x\right) \mathrm{s}\left(\gamma_m z\right) \tag{3.3.22}$$

where $\gamma_n = (2n+1)\,\pi/2$, $\varphi_m = m\pi/2$ and $m \in [0, M]$, $n \in [0, N]$. Modified Fourier series were chosen because they can satisfy the homogenous boundary conditions a priori. The coefficients b_n are the cosine coefficients of the interface temperature, and will be determined by the coupling with the base. Because of the strong discontinuity at the inlet corner, the fluid inlet temperature is expanded in basis functions with coefficients l_m. These two sets of coefficients are related to each other by setting the fluid inlet temperature equal to the interface temperature at the inlet corner. The relation is given by

$$l_m = \frac{-2 \sum_{n=1}^{N} b_n}{\gamma_m} \tag{3.3.23}$$

The discontinuity leads to oscillations and linear decay of the coefficients (Gibbs phenomenon); however, applying a Lancsoz filter reduces oscillation and improves convergence

away from the discontinuity

$$\sigma_n = \frac{\sin\left({}^{n\pi}/_{N}\right)}{{}^{n\pi}/_{N}} \tag{3.3.24}$$

Any derivative of the temperature distributions can be readily obtained by differentiating its series expansion. Applying the GM to the governing equations with the given basis functions, the following set of matrix equations is obtained

$${}^{G_1}/_{2}\mathbf{L}_1\mathbf{FI} + {}^{G_2}/_{4}\mathbf{D}_{2s}\mathbf{FI} + {}^{G_3}/_{4}\mathbf{IFD}_{2s} + {}^{1}/_{4}\mathbf{IFI} - {}^{1}/_{2}\mathbf{L}_2^T\mathbf{SI} = \mathbf{K}_1 \tag{3.3.25}$$

$${}^{1}/_{2}\mathbf{L}_2\mathbf{FI} - {}^{C_1}/_{4}\mathbf{D}_{2c}\mathbf{SI} - {}^{C_2}/_{4}\tilde{\mathbf{I}}\mathbf{SD}_{2s} - {}^{1}/_{4}\tilde{\mathbf{I}}\mathbf{SI} = \mathbf{K}_2 \tag{3.3.26}$$

where $\mathbf{F}$ and $\mathbf{S}$ are matrices of fluid and solid coefficients with $\mathbf{F}, \mathbf{S} \in \mathbb{R}^{N\times M}$. All other left hand side matrices are square, resulting from inner products of basis functions, and are calculated analytically

$$(\mathbf{D}_{2s})_{ij} = \begin{cases} \gamma_i^2, i = j \\ 0, i \neq j \end{cases}, (\mathbf{D}_{2c})_{ij} = \begin{cases} \varphi_i^2, i = j \\ 0, i \neq j \end{cases} \tag{3.3.27}$$

$$\begin{aligned} (\mathbf{L}_1)_{ij} &= \gamma_i \int_0^1 \cos(\gamma_i x)\sin(\gamma_j x)\,dx = \\ &= \begin{cases} \frac{1}{2} if\ i = j \\ -\dfrac{(2i+1)\left[(1+2i)(-1)^j(-1)^i - (1+2j)\right]}{[4(j-i)(1+j+i)]} otherwise \end{cases} \end{aligned} \tag{3.3.28}$$

$$(\mathbf{L}_2)_{ij} = \int_0^1 \cos(\varphi_i x)\sin(\gamma_j x)\,dx = \frac{2(2j+1)}{\pi\left[(1+2j)^2 - 4i^2\right]}, \tag{3.3.29}$$

$$(\mathbf{L}_3)_{ij} = \varphi_j \int_0^1 \mathrm{s}(\gamma_i x)\,\mathrm{s}(\varphi_j x)\,dx = \begin{cases} \dfrac{j(-1)^{(j-1)}}{2i-2j+1} - \dfrac{j(-1)^{(j+i)}}{2i+2j+1} \end{cases} \tag{3.3.30}$$

and $\tilde{\mathbf{I}}$ denotes the identity matrix with first element equal to 2. The right hand side matrices are defined by the boundary conditions

$$\begin{aligned} (\mathbf{K}_1)_{ij} &= \left(G_1(\mathbf{L}_3)_{ij} - G_2\gamma_i(\mathbf{L}_2)_{ij}\right){}^{b_i}/_{\gamma_j} - \left({}^{G_3}/_{2}(\mathbf{D}_{2s})_{ij} + {}^{1}/_{2}\mathbf{I}\right){}^{l_i}/_{\gamma_j} \\ (\mathbf{K}_2)_{ij} &= -{}^{C_1}/_{2}(\mathbf{D}_{2c})_{ij}\,{}^{b_i}/_{\gamma_j} - {}^{1}/_{2}(\mathbf{I})_{1j}l_i \end{aligned} \tag{3.3.31}$$

These equations represent a system of coupled linear equations for the coefficients f_{nm} and s_{nm}. In order to solve the system, it is convenient to use properties of the Kronecker product of matrices (given symbol $\otimes$) to cast the previous matrix equation in a matrix-vector product form. The resulting system, given by Eqn. (3.3.32), represents a skew-symmetric, square, sparse, linear system of $2NM \times 2NM$ with $3N^2M + NM$ non-zero elements. The matrix $\mathbf{P}_4$ is diagonal while the rest of the left hand side matrices are block diagonal.

$$\begin{bmatrix} \mathbf{P}_1 & \mathbf{P}_2 \\ -\mathbf{P}_2^T & \mathbf{P}_4 \end{bmatrix} \begin{bmatrix} vec\,(\mathbf{F}) \\ vec\,(\mathbf{S}) \end{bmatrix} = \begin{bmatrix} vec\,(\mathbf{K}_1) \\ vec\,(\mathbf{K}_2) \end{bmatrix} \tag{3.3.32}$$

The $vec\,()$ operator simply stacks the columns of a matrix. To exploit the diagonality of $\mathbf{P}_4$, the system is solved using its Schur complement; the fluid coefficients are therefore obtained directly by solving the $NM \times NM$ system

$$\left(\mathbf{P}_1 + \mathbf{P}_2\mathbf{P}_4^{-1}\mathbf{P}_2^T\right) vec\,(\mathbf{F}) = \left[vec\,(\mathbf{K}_1) - \mathbf{P}_2\mathbf{P}_4^{-1} vec\,(\mathbf{K}_2)\right] \tag{3.3.33}$$

The block diagonal structure of the Schur complement implies that its inverse will also be block diagonal. Hence, eachα-th column, $\mathbf{f}_\alpha$, of the fluid coefficient matrix can be obtained by solving the$N \times N$system

$$\left(\mathbf{P}_1 + \mathbf{P}_2\mathbf{P}_4^{-1}\mathbf{P}_2^T\right)_\alpha \mathbf{f}_\alpha = \left[vec\,(\mathbf{K}_1) - \mathbf{P}_2\mathbf{P}_4^{-1} vec\,(\mathbf{K}_2)\right]_\alpha \tag{3.3.34}$$

These matrices are full and well-conditioned, and are solved using a LU decomposition with partial pivoting. Once the α-th fluid coefficient column has been obtained, its solid counterpart is obtained by matrix-vector product

$$\mathbf{s}_\alpha = \left(\mathbf{P}_4^{-1}\right)_\alpha \left[vec(\mathbf{K}_2)_\alpha - {}^1\!/_2 \mathbf{J}_2^T \mathbf{f}_\alpha\right] \tag{3.3.35}$$

and the process is repeated for $\alpha \in [1, M]$. The temperatures and heat fluxes at any point (or grid) can be reconstructed using the definition of the series expansion solution given in Eqn. (3.3.21) & Eqn. (3.3.22); while average temperatures can be calculated directly from the coefficients. For example, the average solid interface temperature, which is used for Nusselt calculations, is given by

$$\overline{T_i\,(x)} = \int_0^1 T_i\,(x)\,dx = \int_0^1 b_n\,\mathrm{c}\,(\varphi_n x)\,dx = b_0 \tag{3.3.36}$$

The average Nusselt number (or any average performance parameter) can therefore be obtained without the additional computational time due to the reconstruction process. This fact is particularly useful in optimization studies in which local temperature distributions might not be of interest.

3.3.3.2 Finite Difference Solution

Finite difference solutions are more flexible than Galerkin Method solutions because the selection of the basis function is not always clear, especially when the coefficients of the equations are not constant. Furthermore, it was found that due to the discontinuity at the inlet corner, the convergence of the series solution to the actual function is arithmetic, while relatively dense matrices need to be solved. Because of these shortcomings, a Finite Difference (FD) discretization of the problem was also implemented. FD methods are quite general, easy to implement and can be devised in an efficient way. Although in this work only two dimensional, steady state problems will be addressed, it is of interest to devise a solution method that can easily be expanded to three dimensional and unsteady problems. Before the solution of the problem is explained, the notation used is discussed for clarity. The function at a given point on the grid (x_i, z_i) is defined as

$$f_{i,j} = f\left(x_i, z_j\right) \tag{3.3.37}$$

Three finite difference schemes will be used. A second order backward difference for the convective term and interface heat flux

$$f'_i = \frac{3f_i - 4f_{i-1} + f_{i-2}}{2\Delta x} \tag{3.3.38}$$

and a second order centered difference for the diffusive term with variable porosity

$$\frac{\partial}{\partial x}\left[\alpha\left(x\right)\frac{\partial f}{\partial x}\right] = \frac{\alpha\left(x_{i-1/2}\right)}{\Delta x^2} f_{i-1} - \frac{\alpha\left(x_{i+1/2}\right) + \alpha\left(x_{i-1/2}\right)}{\Delta x^2} f_i + \frac{\alpha\left(x_{i+1/2}\right)}{\Delta x^2} f_{i+1} \tag{3.3.39}$$

A derivation of the finite difference schemes and their local truncation errors are given in Appendix A. Note that no upwinding is necessary in the convective term since the velocity will always be in the positive x direction. In order to keep the second order convergence, the

adiabatic conditions at the interface are addressed using the ghost point idea

$$\left.\frac{\partial f}{\partial x}\right|_1 = \frac{f_2 - f_0}{2\Delta x} = 0 \rightarrow f_2 = f_0 \tag{3.3.40}$$

Using these discretizations, the scaled fluid energy equation derived in the previous section is discretizes as follows

$$\begin{aligned}
&F_1 \left(\frac{\langle u \rangle_{i,j}}{2\Delta x} \langle T_f \rangle^f_{i-2,j} + \frac{2\langle u \rangle_{i,j}}{\Delta x} \langle T_f \rangle^f_{i-1,j} - \frac{3\langle u \rangle_{i,j}}{2\Delta x} \right) \langle T_f \rangle^f_{i,j} + \\
&+ F_2 \left(\frac{\varepsilon_{f,i-1/2,j}}{\Delta x^2} \langle T_f \rangle^f_{i-1,j} - \frac{\varepsilon_{f,i-1/2,j} + \varepsilon_{f,i+1/2,j}}{\Delta x^2} \langle T_f \rangle^f_{i,j} + \frac{\varepsilon_{f,i+1/2,j}}{\Delta x^2} \langle T_f \rangle^f_{i+1,j} \right) + \\
&+ F_3 \left(\frac{\varepsilon_{f,i,j-1/2}}{\Delta z^2} \langle T_f \rangle^f_{i,j-1} - \frac{\varepsilon_{f,i,j-1/2} + \varepsilon_{f,i,j+1/2}}{\Delta z^2} \langle T_f \rangle^f_{i,j} + \frac{\varepsilon_{f,i,j+1/2}}{\Delta z^2} \langle T_f \rangle^f_{i,j+1} \right) + \\
&- h_{i,j} S_{w,ij} \langle T_f \rangle^f_{i,j} + h_{i,j} S_{w,ij} \langle T_s \rangle^s_{i,j}
\end{aligned} \tag{3.3.41}$$

The grid is assumed to be uniform with N and M panels in the x and z direction respectively ($N+1$ and $M+1$ grid points). A schematic of a 4×4grid is given in Figure 3.9. Since the temperature at the inlet and at the bottom of the channel is given, the fluid equation is solved on at $N \times M$points. Using the ghost point approximation given in Eqn. (3.3.40), at the outlet of the channel, $i = N$, the x diffusion term becomes

$$\left(\frac{\varepsilon_{f,N-3/2,j} + \varepsilon_{f,N+1/2,j}}{\Delta x^2} \right) \langle T_f \rangle^f_{N-1,j} - \left(\frac{\varepsilon_{f,N-3/2,j} + \varepsilon_{f,N+1/2,j}}{\Delta x^2} \right) \langle T_f \rangle^f_{N,j} \tag{3.3.42}$$

Similarly, at the top of the channel, $j = M$, the z diffusion term becomes

$$\left(\frac{\varepsilon_{f,i,M-3/2} + \varepsilon_{f,i,M+1/2}}{\Delta z^2} \right) \langle T_f \rangle^f_{M-1,j-1} - \left(\frac{\varepsilon_{f,i,M-3/2} + \varepsilon_{f,i,M+1/2}}{\Delta z^2} \right) \langle T_f \rangle^f_{M,j} \tag{3.3.43}$$

Similarly, using the second order scheme given in Eqn. (3.3.39), the discretized solid equation is

$$\begin{aligned}
&S_1 \left(\frac{\varepsilon_{s,i-1/2,j}}{\Delta x^2} \langle T_s \rangle^s_{i-1,j} - \frac{\varepsilon_{s,i-1/2,j} + \varepsilon_{s,i+1/2,j}}{\Delta x^2} \langle T_s \rangle^s_{i,j} + \frac{\varepsilon_{s,i+1/2,j}}{\Delta x^2} \langle T_s \rangle^s_{i+1,j} \right) + \\
&+ S_2 \left(\frac{\varepsilon_{s,i,j-1/2}}{\Delta z^2} \langle T_s \rangle^s_{i,j-1} - \frac{\varepsilon_{s,i,j-1/2} + \varepsilon_{s,i,j+1/2}}{\Delta z^2} \langle T_s \rangle^s_{i,j} + \frac{\varepsilon_{s,i,j+1/2}}{\Delta z^2} \langle T_s \rangle^s_{i,j+1} \right) + \\
&- h_{i,j} S_{w,ij} \langle T_s \rangle^s_{i,j} + h_{i,j} S_{w,ij} \langle T_f \rangle^f_{i,j} = 0
\end{aligned} \tag{3.3.44}$$

Note that since the boundary condition for the solid is adiabatic at the inlet, the solid equation is solved on $(N+1) \times M$grid points. The boundary conditions are again implemented

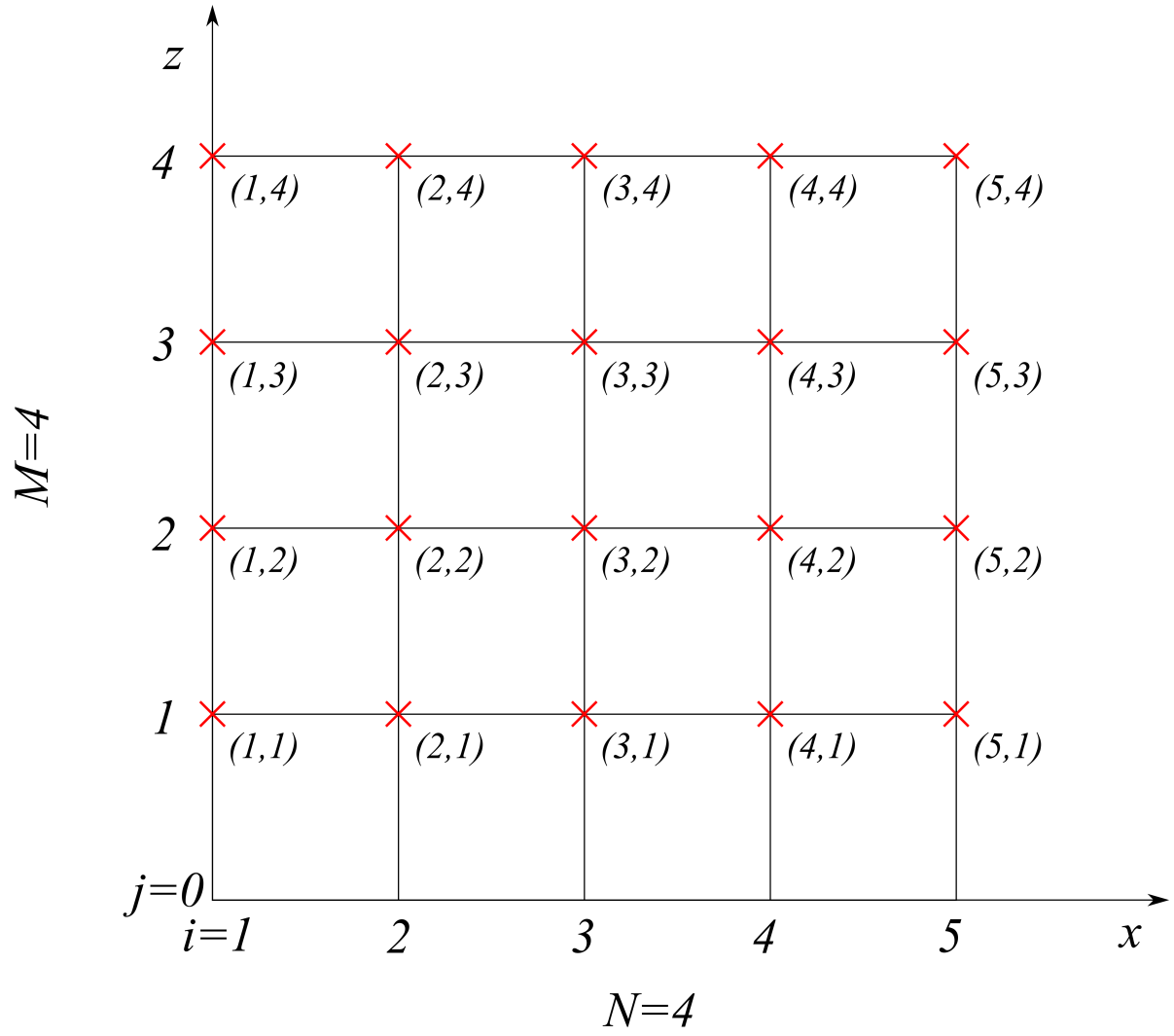

Figure 3.9: Example of a 4x4 Computational Grid

using the ghost point, at points $i = 1$and $i = N + 1$ the x diffusive term becomes

$$-\left(\frac{\varepsilon_{s,1/2,j}+\varepsilon_{s,3/2,j}}{\Delta x^2}\right)\langle T_s\rangle^s_{1,j}+\left(\frac{\varepsilon_{s,1/2,j}+\varepsilon_{s,3/2,j}}{\Delta x^2}\right)\langle T_s\rangle^s_{2,j} \tag{3.3.45}$$

$$\left(\frac{\varepsilon_{s,N+1/2,j}}{\Delta x^2}+\frac{\varepsilon_{s,N+3/2,j}}{\Delta x^2}\right)\langle T_s\rangle^s_{N,j}-\left(\frac{\varepsilon_{s,N+1/2,j}+\varepsilon_{s,N+3/2,j}}{\Delta x^2}\right)\langle T_s\rangle^s_{N+1,j} \tag{3.3.46}$$

while at $j = M$ the z diffusion term becomes

$$\left(\frac{\varepsilon_{s,i,M+1/2}+\varepsilon_{s,i,M+3/2}}{\Delta z^2}\right)\langle T_s\rangle^s_{i,M-1}-\left(\frac{\varepsilon_{s,i,M+1/2}+\varepsilon_{s,i,M+3/2}}{\Delta z^2}\right)\langle T_s\rangle^s_{i,M} \tag{3.3.47}$$

These discretized equations represent a set of coupled linear systems of size $2NM+2\left(N+1\right)M$ for the solid and fluid temperatures at the grid points. Two solutions for the given system have been developed: a direct method, and a pseudo transient method. In the direct method, the temperature at the grid points are expanded in a single vector

$$\mathbf{t}=\begin{bmatrix}\langle T_f\rangle^f_{1,1}\\ \langle T_f\rangle^f_{2,1}\\ \vdots\\ \langle T_f\rangle^f_{N,M}\\ \langle T_s\rangle^s_{1,1}\\ \langle T_s\rangle^s_{2,1}\\ \vdots\\ \langle T_s\rangle^s_{N+1,M}\end{bmatrix} \tag{3.3.48}$$

and the resulting linear system

$$\mathbf{At}=\mathbf{b} \tag{3.3.49}$$

is solved using MATLABs built in sparse solver. The matrix A is very sparse (see Figure 3.10) therefore the system can be solved quite efficiently for moderate grids. The vector **b** contains the boundary conditions, and it will be shown later that the ability of the direct solver to handle multiple right hand side vectors efficiently, will be exploited in the coupling of the interface condition. This type of solution is not very scalable since the computational time increases dramatically as the grid size increases, and it cannot be easily extended to transient problems. To address this shortcoming, a transient fractional step method was developed.

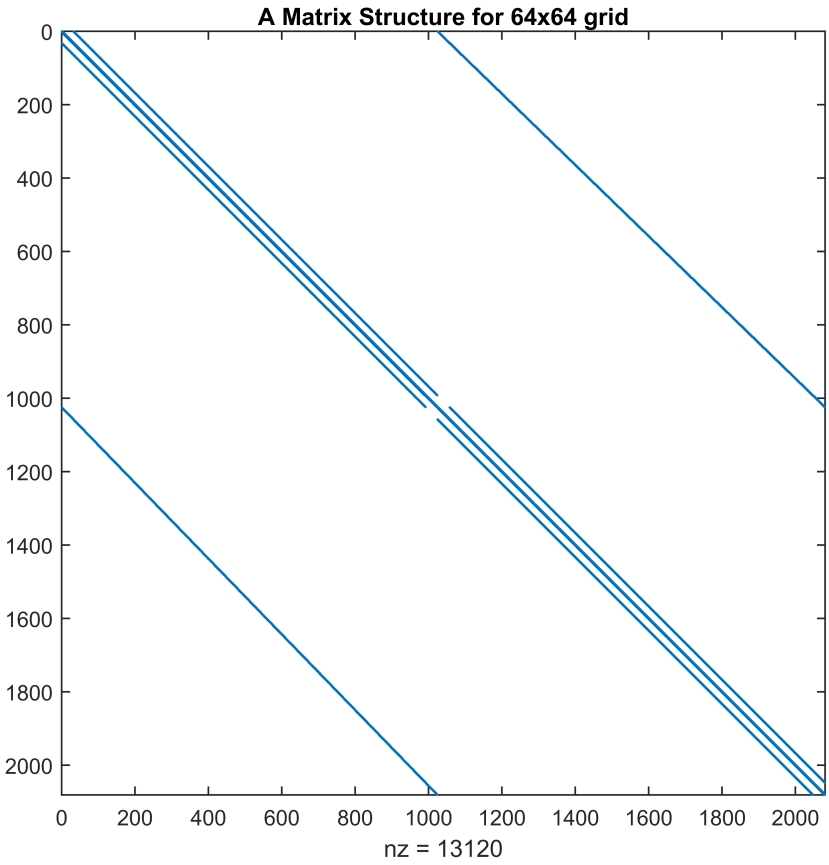

Figure 3.10: Matrix Structure of Coupled VAT Energy Equations

The idea behind this method of solution is to set up the previous system in the following way

$$\begin{aligned}\frac{\partial}{\partial t}\begin{bmatrix}\mathbf{T_f}\\ \mathbf{T_s}\end{bmatrix} &= -\begin{bmatrix}F_1\mathbf{C}_x & 0\\ 0 & 0\end{bmatrix}\begin{bmatrix}\mathbf{T_f}\\ \mathbf{T_s}\end{bmatrix}+\begin{bmatrix}F_2\mathbf{D}_{f,xx} & 0\\ 0 & S_1\mathbf{D}_{s,xx}\end{bmatrix}\begin{bmatrix}\mathbf{T_f}\\ \mathbf{T_s}\end{bmatrix}+\\ &+\begin{bmatrix}F_3\mathbf{D}_{f,zz} & 0\\ 0 & S_2\mathbf{D}_{s,zz}\end{bmatrix}\begin{bmatrix}\mathbf{T_f}\\ \mathbf{T_s}\end{bmatrix}+\begin{bmatrix}-\mathbf{H} & \mathbf{H}\\ \mathbf{H} & -\mathbf{H}\end{bmatrix}\begin{bmatrix}\mathbf{T_f}\\ \mathbf{T_s}\end{bmatrix}\end{aligned} \tag{3.3.50}$$

The main problem in the solution of the system is the coupling between the fluid and solid equations, which is represented by the last term in the equation. The coupling adds a non-zero diagonal far away from the banded diagonal terms, which significantly increases computational time. This is similar to the problem that is encountered in the solution of a two dimensional Laplace (or Poisson) equation, in which the second dimension add non-zero diagonal terms away from the main diagonal. The idea that was developed here is to address the problem in the same way it is addressed by ADI; use Strang splitting [151]. The idea is to split the solution of the system in three decoupled steps and use a trapezoidal method in time to ensure stability Step 1

$$\begin{aligned}\frac{\mathbf{T}_f^* - \mathbf{T}_f^k}{\Delta t/2} &= \frac{1}{2}\left(-F_1\mathbf{C}_x + F_2\mathbf{D}_{f,xx} + F_3\mathbf{D}_{f,zz} - \mathbf{H}\right)\mathbf{T}_f^k +\\ &+\frac{1}{2}\left(-F_1\mathbf{C}_x + F_2\mathbf{D}_{f,xx} + F_3\mathbf{D}_{f,zz} - \mathbf{H}\right)\mathbf{T}_f^* + \mathbf{H}\mathbf{T}_s^k\end{aligned} \tag{3.3.51}$$

Step 2

$$\frac{\mathbf{T}_s^{k+1} - \mathbf{T}_s^k}{\Delta t} = \frac{1}{2}\left(S_1\mathbf{D}_{s,xx} + S_2\mathbf{D}_{s,zz} - \mathbf{H}\right)\mathbf{T}_s^{k+1} + \frac{1}{2}\left(S_1\mathbf{D}_{s,xx} + S_2\mathbf{D}_{s,zz} - \mathbf{H}\right)\mathbf{T}_s^k + \mathbf{H}\mathbf{T}_f^* \tag{3.3.52}$$

Step 3

$$\begin{aligned}\frac{\mathbf{T}_f^{k+1} - \mathbf{T}_f^*}{\Delta t/2} &= \frac{1}{2}\left(-F_1\mathbf{C}_x + F_2\mathbf{D}_{f,xx} + F_3\mathbf{D}_{f,zz} - \mathbf{H}\right)\mathbf{T}_f^* +\\ &+\frac{1}{2}\left(-F_1\mathbf{C}_x + F_2\mathbf{D}_{f,xx} + F_3\mathbf{D}_{f,zz} - \mathbf{H}\right)\mathbf{T}_f^{k+1} + \mathbf{H}\mathbf{T}_s^{k+1}\end{aligned} \tag{3.3.53}$$

This splitting implies that now a NM system (twice) and a $(N+1)M$ system are solved separately. Note also, that, except at the initial and final step, Step 1 and Step 3 can be combined to reduce the computational time, which is the beauty of Strang splitting. In

addition, each step is further separated, and Peaceman-Rachford [152] ADI scheme can be applied. Using this idea, Step 1 and 3 are divided in two additional steps

$$\frac{\mathbf{T}_f^{**} - \mathbf{T}_f^k}{\Delta t/4} = \frac{1}{2}\left(-F_1\mathbf{C}_x + F_2\mathbf{D}_{xx} - \frac{1}{2}\mathbf{H}\right)\mathbf{T}_f^k + \frac{1}{2}\left(-F_1\mathbf{C}_x + F_2\mathbf{D}_{xx} - \frac{1}{2}\mathbf{H}\right)\mathbf{T}_f^{**} + \frac{1}{2}\mathbf{H}\mathbf{T}_s^k \tag{3.3.54}$$

$$\frac{\mathbf{T}_f^{*} - \mathbf{T}_f^{**}}{\Delta t/4} = \frac{1}{2}\left(F_3\mathbf{D}_{f,zz} - \frac{1}{2}\mathbf{H}\right)\mathbf{T}_f^k + \frac{1}{2}\left(F_3\mathbf{D}_{f,zz} - \frac{1}{2}\mathbf{H}\right)\mathbf{T}_f^{**} + \frac{1}{2}\mathbf{H}\mathbf{T}_s^k \tag{3.3.55}$$

Note that the first step requires the solution of a quad-diagonal system, while the second step requires the solution of a tri-diagonal system. The tri-diagonal system can be carried out efficiently using Thomas algorithm [149], while the quad-diagonal system can be solved using a slight variation of the same algorithm. The solid equation is also divided in two substeps,

$$\frac{\mathbf{T}_s^{**} - \mathbf{T}_s^k}{\Delta t/2} = \frac{1}{2}\left(S_1\mathbf{D}_{s,xx} - \frac{1}{2}\mathbf{H}\right)\mathbf{T}_s^{**} + \frac{1}{2}\left(S_1\mathbf{D}_{s,xx} - \frac{1}{2}\mathbf{H}\right)\mathbf{T}_s^k + \frac{1}{2}\mathbf{H}\mathbf{T}_f^* \tag{3.3.56}$$

$$\frac{\mathbf{T}_s^{k+1} - \mathbf{T}_s^{**}}{\Delta t/2} = \frac{1}{2}\left(S_2\mathbf{D}_{s,zz} - \frac{1}{2}\mathbf{H}\right)\mathbf{T}_s^{k+1} + \frac{1}{2}\left(S_2\mathbf{D}_{s,zz} - \frac{1}{2}\mathbf{H}\right)\mathbf{T}_s^{**} + \frac{1}{2}\mathbf{H}\mathbf{T}_f^* \tag{3.3.57}$$

and both steps reduce to solving a set of tri-diagonal matrices. The overall algorithm is given in Figure 3.11. This solution method is second order accurate in time and space, and absolutely stable. Also, the extension to a three dimensional system can be easily obtained by substituting the Peaceman-Rachford ADI method with a Douglas-Rachford [153] ADI method.

In the rest of this work, only steady state solutions will be considered. The direct method is implicitly steady state, while a steady state solution using the transient method can be obtained by evolving the system until

$$\frac{\partial}{\partial t}\begin{bmatrix}\mathbf{T_f}\\ \mathbf{T_s}\end{bmatrix} \leq tol \tag{3.3.58}$$

The absolute stability of the method developed implies that any time step can be used to obtain a steady state solution, however, the number of time steps required will vary significantly depending on the selection of the time step. When the intermediate transient solutions are not of interest, the selection of the optimal time step is an important parameter

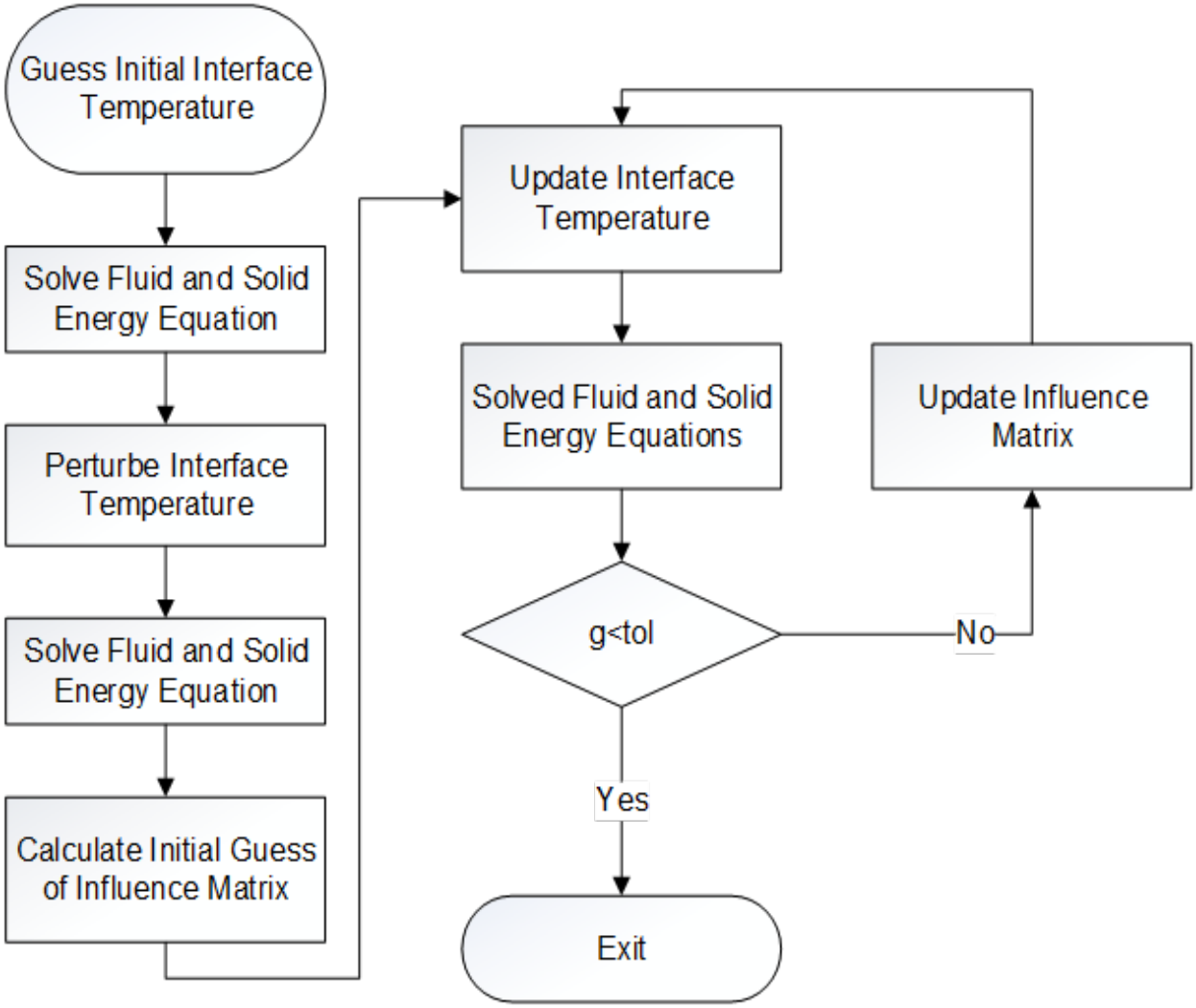

Figure 3.11: Flowchart of Iterative Energy Solution Procedure

in the problem.

It is a well-known fact that strongly elliptic equations lead to slow decay of the low frequency content of the solution. This issue is most often dealt with in Poissons equation, and has lead to the development of transform and multi-grid methods for its solution. In our case, the scaling in Section 3.2 revealed that diffusion is negligible in the fluid equation, while it is dominant in the solid equation. This suggest that the convergence will be limited by the convergence of the solid equation, and a time stepping method to accelerate its convergence will lead to a much faster steady state solution.

Douglas [153] developed a variable time stepping scheme that leads to improved convergence for a Poisson type equation. The idea is to develop a variable time stepping method that will lead to improve decay of the low frequency solution. The derivation carried out by Douglas is repeated for the Helmholtz type VAT solid energy equation, and a variable time step is found

$$\Delta t^k = \frac{4}{S_1 \left(\pi/2^k \Delta x\right)^2 + 1/2 h S_w} \tag{3.3.59}$$

where k is the iteration number. The Nyquist frequency of the grid is $k_{\max} = \log_2(N) + 1$, and the parameter k is varied in V sweeps. The derivation was carried out for constant coefficients and a one dimensional system, however, through numerical experiments, it was found that by adjusting the time step variation as

$$\Delta t^j = \frac{4}{\min(S_1, S_2) \left(\pi/2^j \Delta x\right)^2 + 1/2 \min(h S_w)} \tag{3.3.60}$$

a steady state solution is almost always obtained in two sweeps.

The solution methods developed in this section lead to an efficient calculation of the temperature distribution for a given interface temperature. However, this interface temperature is not known a priori, and will be determined by the interface energy conserving condition given in Eqn. (3.2.41). The implementation of this condition will be discussed in Section 3.3.5.

3.3.4 Base

The solution of the Laplace equation in the base is obtained analytically for the case of an applied heat flux. The derivation for a given temperature can be extended easily, but it

will not be discussed here. The solution of the Laplace equation for the given conditions can be found by separation of variables. The linearity of Laplaces equation implies that the problem can be separated into two separate solution. The first solution, $T_{b,1}(x,z)$, is found by a problem with the following boundary conditions

$$T_{b,1}(x,1) = 0,\ \left.\frac{\partial T_{b,1}}{\partial x}\right|_{x=0} = \left.\frac{\partial T_{b,1}}{\partial x}\right|_{x=1} = 0,\ \left.\frac{\partial T_{b,1}}{\partial z}\right|_{x=0} = -q''(x) \tag{3.3.61}$$

Applying separation of variables to Eqn. (3.2.37), it can be written

$$C_b^2 X''Z + XZ'' = 0 \rightarrow C_b^2 \frac{X''}{X} = -\frac{Z''}{Z} = -\lambda^2 \tag{3.3.62}$$

where since the first equation is a function of x only and the second equation is a function of z only, λ has to be a constant. This leads to two separate problems

$$C_b^2 X'' + \lambda^2 X = 0 \tag{3.3.63}$$

$$Z'' - \lambda^2 Z'' = 0 \tag{3.3.64}$$

The solution of the first equation is given by

$$X = a\cos\left(\frac{\lambda}{C_b}x\right) + b\sin\left(\frac{\lambda}{C_b}x\right) \tag{3.3.65}$$

Since both$a$ and b cannot be zero (or there would be no variation in x), by enforcing the boundary conditions, it is found that the following condition has to be satisfied

$$a\frac{\lambda}{C_b}\sin\left(\frac{\lambda}{C_b}x\right) = 0 \tag{3.3.66}$$

This condition is satisfied when λ takes the following form, for any integer multiple values of n,s

$$\lambda_n = n\pi C_b \tag{3.3.67}$$

Therefore, the x series solution is given by

$$X = a_n\cos(n\pi x) \tag{3.3.68}$$

Now that λ has been determined, it can easily be shown that a solution to Eqn. (3.3.64), is given by

$$Z = c_n\sinh\left[n\pi C_b(z-1)\right] + e_n\cosh\left[n\pi C_b(z-1)\right] \tag{3.3.69}$$

where the shift was applied to ensure that both boundary conditions can be applied. Applying the boundary condition at $z = 1$ implies that

$$Z(1) = 0 = e_n \tag{3.3.70}$$

and a solution to the problem is given by

$$T_{b,1}(x, z) = d_n \cos(\pi n x) \sinh[n\pi C_b (z - 1)] \tag{3.3.71}$$

In addition, a zero eigenvalue solution is added and,

$$T_{b,1}(x, z) = d_0 (z - 1) + d_n \cos(\pi n x) \sinh[n\pi C_b (z - 1)] \tag{3.3.72}$$

The coefficients d_n are the scaled cosine coefficients of the heat flux distribution $q(x)$ and can be determined using the orthogonality of cosines

$$\begin{aligned} d_0 &= -\int_0^1 q(x)\, dx = -q_{avg} \\ d_n &= -\frac{1}{\cosh[n\pi C_b]} \int_0^1 q(x) \cos(n\pi x)\, dx \end{aligned} \tag{3.3.73}$$

To satisfy the top boundary condition, a second solution to Laplaces equation is found, with the following boundary conditions

$$T_{b,2}(x, 1) = T_i(x), \quad \left.\frac{\partial T_{b,2}}{\partial x}\right|_{x=0} = \left.\frac{\partial T_{b,1}}{\partial x}\right|_{x=1} = 0, \quad \left.\frac{\partial T_{b,2}}{\partial z}\right|_{x=0} = 0 \tag{3.3.74}$$

Repeating the separation of variable procedure, but with the new boundary conditions, leads to the following solution

$$T_{b,2}(x, z_b) = a_0 + a_n \cos(n\pi x) \cosh(n\pi C_b z) \tag{3.3.75}$$

where the coefficients a_n are the modified cosine coefficients of the interface,

$$\begin{aligned} a_0 &= \int_0^1 T_i(x)\, dx = T_{i,avg} \\ a_n &= \frac{1}{\cosh(n\pi C_b)} \int_0^1 T_i(x) \cos(n\pi x)\, dx \end{aligned} \tag{3.3.76}$$

It can be easily verified that, by construction, the sum of these two solutions satisfy all the boundary conditions, and the governing equations. Therefore, a solution to the base conduction equation is given by

$$\begin{aligned} T_b(x, z_b) &= T_{i,avg} - q_{avg}(z-1) + \\ &+ \sum_{n=1}^{N} \cos(\varphi_n x) \left\{ a_n \cosh(C_b \varphi_n z) + d_n \sinh\left[C_b \varphi_n (z-1)\right] \right\} \end{aligned} \tag{3.3.77}$$

3.3.5 Interface Matching

The interface energy conservation boundary condition is given as a linear combination of fluid and solid heat fluxes, which are fully determined once an interface temperature is set. The condition is repeated here for convenience

$$K_1 \varepsilon_s(x,0) \left.\frac{\partial \langle T_s \rangle^s}{\partial z}\right|_{z=0} + \frac{K_1}{R_k} \varepsilon_f(x,0) \left.\frac{\partial \langle T_f \rangle^f}{\partial z}\right|_{z=0} = \left.\frac{\partial T_b}{\partial z_b}\right|_{z_b=1} \tag{3.3.78}$$

where $K_1 = \varepsilon_{s,avg} \hat{t}_b / \hat{H}_c$ and $R_k = \varepsilon_{s,avg} k_s / \varepsilon_{f,avg} k_f$. In previous computer codes developed, this condition was found by iterating the interface temperature at the grid points attempting to match the heat flux. The iteration procedure was computationally very expensive, due to the large number of iterations required. A new treatment, based on a spectral representation of the coefficients, is proposed here. The interface temperature, which is equal in the solid, fluid and base, is expanded in its cosine series

$$\langle T_s \rangle^s = \langle T_f \rangle^f = T_i(x) = b_n \cos(n\pi x) \tag{3.3.79}$$

where the coefficients b_n are unknown and will be determined to satisfy Eqn. (3.3.78). The idea is to express the heat fluxes at the interface in a cosine series and obtain an equation for its residual that is an implicit function of the coefficients b_n. Then, the interface temperature will be determined by the set of coefficients that minimizes the residual. Mathematically, the coefficients b_n are Lagrangian variables that enforce energy conservation at the interface, similar to the way that pressure can be seen as a Lagrangian variable that enforces mass conservation for incompressible flow. The solid and fluid heat flux at the interface are found using a second order backward difference given in Eqn. (3.3.38). Then, the cosine coefficients

defined as

$$
\begin{aligned}
s_0 &= \int_0^1 \varepsilon_s(x,0)\left.\frac{\partial\langle T_s\rangle^s}{\partial z}\right|_{z=0} dx \\
s_n &= \int_0^1 \varepsilon_s(x,0)\left.\frac{\partial\langle T_s\rangle^s}{\partial z}\right|_{z=0} \cos(n\pi x)\, dx
\end{aligned}
\tag{3.3.80}
$$

$$
\begin{aligned}
f_0 &= \int_0^1 \varepsilon_f(x,0)\left.\frac{\partial\langle T_f\rangle^f}{\partial z}\right|_{z=0} dx \\
f_n &= \int_0^1 \varepsilon_f(x,0)\left.\frac{\partial\langle T_f\rangle^f}{\partial z}\right|_{z=0} \cos(n\pi x)\, dx
\end{aligned}
\tag{3.3.81}
$$

can be obtained using a Discrete Cosine Transform (DCT). The base solution is already expressed in terms of its cosine series in the x direction. The base heat flux is found from the series solution

$$
\frac{\partial T_b}{\partial z} = -q_{w,avg} + \sum_{n=1}^{N} S_b\varphi_n \cos(\varphi_n x)\left\{d_n + a_n \sinh(S_b\varphi_n)\right\} \tag{3.3.82}
$$

Then, substituting these expressions in Eqn. (3.3.78), an equation in terms of the coefficients is obtained

$$
\begin{aligned}
K_1 s_n \cos(n\pi x) + \frac{K_1}{R_k} f_n \cos(n\pi x) &= -q_{w,avg} + \\
+ S_b\varphi_n \cos(\varphi_n x)\left\{d_n + a_n \sinh(S_b\varphi_n)\right\}&
\end{aligned}
\tag{3.3.83}
$$

Multiplying both sides by $\cos(\varphi_j x)$, integrating over the interface, and using the orthogonality of cosines, the following $N+1$ set of equations is obtained

$$
\begin{gathered}
j = 0 \\
[\mathbf{g}(\mathbf{b})]_0 = K_1 s_0 + \tfrac{K_1}{R_k} f_0 + q_{w,avg} = 0 \\
1 \le j \le N \\
[\mathbf{g}(\mathbf{b})]_j = {}^1\!/_2 K_1 s_n + {}^1\!/_2 \tfrac{K_1}{R_k} f_n - {}^1\!/_2 S_b\varphi_n \left\{d_n + a_n \sinh(S_b\varphi_n)\right\} = 0
\end{gathered}
\tag{3.3.84}
$$

The function $\mathbf{g}$ is the residual at the interface, and it is an implicit linear function of the coefficients $\mathbf{b}$. The problem now becomes an unconstrained minimization problem

$$
\text{minimize} \quad \mathbf{g}(\mathbf{b}) \tag{3.3.85}
$$

Due to the linearity of $\mathbf{g}$, given a starting point $\mathbf{b}^0$ for the coefficients, a new set $\mathbf{b}^*$, which will satisfy Eqn. (3.3.85), can be found by expanding the function $\mathbf{g}$ in a Taylor series expansion

$$\mathbf{g}\left(\mathbf{b}^*\right) = 0 = \mathbf{g}\left(\mathbf{b}^0\right) + \nabla \mathbf{g}|_{\mathbf{b}} \Delta \mathbf{b} \tag{3.3.86}$$

where $\Delta \mathbf{b} = \mathbf{b}^0 - \mathbf{b}^*$, and the influence matrix $\nabla \mathbf{g}|_{\mathbf{b}}$ is defined by

$$\left[\nabla \mathbf{g}|_{\mathbf{b}}\right]_{ij} = \frac{\partial g_i}{\partial b_j} \tag{3.3.87}$$

Then, a solution to Eqn. (3.3.86) is found by solving the linear system

$$\nabla \mathbf{g}|_{\mathbf{b}} \Delta \mathbf{b} = -\mathbf{g}\left(\mathbf{b}^0\right) \tag{3.3.88}$$

and the set of coefficients that satisfies Eqn. (3.3.84) is given by $\mathbf{b}^* = \mathbf{b}^0 + \Delta \mathbf{b}$. The evaluation of the influence matrix can be carried out in two ways: direct or iteratively. In the direct case, the matrix is evaluated by perturbing the starting point $\mathbf{b}^0$ by an amount δ in each direction$\mathbf{b}_{\delta,i} = \mathbf{b}_0 + \delta \mathbf{e}_i$, calculating the corresponding $g_{\delta,i}$ value, and calculating its derivative with a first order finite difference.

$$\frac{\partial g_i}{\partial b_j} = \frac{g_{\delta,i} - g_0}{\delta} \tag{3.3.89}$$

This type of evaluation of the influence matrix $\nabla \mathbf{g}|_{\mathbf{b}}$ requires the solution of the energy equations, and evaluation of coefficients f_n and s_n for $N + 2$ different input temperatures. When a direct solver is used to solve the energy equations, the influence matric can be calculated efficiently by carrying out the LU factorization of matrix $\mathbf{A}$ in Eqn. (3.3.49) once and then applying it to each right hand side vector $\mathbf{b}_{\delta,i}$. When an iterative solver is used for the energy equations, this type of solution is not advantageous since each right hand side vector has to be computed individually.

In such cases, an alternative solution is to guess a form of the influence matrix, and update it at each iteration. These types of solutions are called quasi-newton methods and are extensions of the bisection methods for 1D equations. In this work, a Broyden-Fletcher-Goldfarb-Shanno (BFGS) [154] update method is used (although without line search). In this study, an initial guess for the influence matrix is taken as a diagonal matrix, and its

inverse is directly updated at each step using the following formula

$$[\nabla \mathbf{g}]_k^{-1} = \left(I - \frac{\Delta \mathbf{b} \Delta \mathbf{g}^T}{\Delta \mathbf{g}^T \Delta \mathbf{b}}\right) [\nabla \mathbf{g}]_k^{-1} \left(I - \frac{\Delta \mathbf{g} \Delta \mathbf{b}^T}{\Delta \mathbf{b}^T \Delta \mathbf{g}}\right) + \frac{\Delta \mathbf{b} \Delta \mathbf{b}^T}{\Delta \mathbf{g} \Delta \mathbf{b}} \tag{3.3.90}$$

with $\Delta \mathbf{b} = \mathbf{b}^k - \mathbf{b}^{k-1}, \Delta \mathbf{g} = \mathbf{g}^k - \mathbf{g}^{k-1}$. The stability and efficiency of the solution depends on the initial guess. An initial guess is taken by assuming that the influence matrix is diagonally dominant, and solving the equations for two inputs $\mathbf{b}_0$, $\mathbf{b}_{\delta,i} = \mathbf{b}_0 + \delta$. Then an initial guess for the inverse of the influence matrix is given by

$$[\nabla \mathbf{g}]^{-1} = diag \left[\frac{\delta}{\mathbf{g}(\mathbf{b}_\delta) - \mathbf{g}(\mathbf{b}_0)}\right] \tag{3.3.91}$$

It was found that this initial guess is very good for cases in which most of the energy is conducted in the solid equation, but it can diverge when that is not the case. In general the iteration was found to converge to a tolerance of $1e-7$ within about $10-12$ iterations.

CHAPTER 4

Heat Sink VAT Model Limits

In the previous sections, the governing equations for fluid flow and heat transfer in a heat sink were developed, and numerical methods for their solutions were discussed. It was shown how the application of VAT to the complex multi-scale structures geometrically homogenizes the domain of the solution, and defines equations that are valid everywhere in the domain of the system. In this section, the accuracy and limits of the model are discussed. Determination of the limits of applicability of the model are crucial, in order to ensure that the results of the optimization procedure, which will be carried out in the next chapter, are not affected by shortcomings of the model.

The chapter is divided into three sections. In the first section, the limits for cases of constant porosity are discussed. Solution and closure methods are validated by comparing predicted and experimental results for several micro-channel and pin fin heat sinks. Subsequently, the limits of applicability of the model are determined by comparing the error between predicted results and high fidelity CFD results. In the second section, the procedure is repeated for heat sinks with linear porosity variation in the z-direction. In the third and last section of the chapter, the procedure is repeated for converging and diverging channels, to determine the limits of applicability of the model when variation in the x-direction are present.

The geometrical heat sink configurations, along with methods for the determination of porosity and specific surface, have been discussed in detail in Section 3.3.1. The friction factor closure correlation for channels is taken from the analytical solution for hydrodynamically fully developed flow between parallel plates,

$$f = \frac{24}{\mathrm{Re}_{d_h}} \tag{4.0.1}$$

The Nusslet number is taken from the asymptotic matching correlation proposed by Awad [155] for thermally developing flow for parallel plates with constant temperature,

$$Nu_{dh} = \left[\left(\frac{1.849}{x^{*1/3}} \right)^{3.5} + (7.514)^{3.5} \right]^{1/3.5} \tag{4.0.2}$$

where the developing length scale is defined as

$$x^* = \frac{L}{\mathrm{Re}_{d_h,avg} d_h \mathrm{Pr}_f} \tag{4.0.3}$$

The Reynolds number is always based on the local intrinsic velocity and the VAT hydraulic diameter defined in Eqn. (2.6.11). For variable geometries, the friction factor and Nusselt numbers are assumed to scale with the local hydraulic diameter i.e. for trapezoidal microchannels, the heat transfer coefficient will vary linearly with the Nusselt number in the z-direction. The accuracy of these assumptions and closure schemes will be discussed in detail the next sections.

A staggered pin fin heat sink is also considered. In this case, the friction factor the flow develops thermally and hydrodynamically within the first few rows, and the friction factor and Nusselt number correlations are taken from Zukauskas [156] experimental correlations. Khan [157] conveniently used Zukauskas data to develop a single correlation that includes the dependence on the pitches, diameter and Reynolds number

$$f = K_1 \frac{S_T^{387.6/S_T^{13.1/S_T}}}{\mathrm{Re}_D^{0.68/S_T^{1.29}}} \tag{4.0.4}$$

where K_1 is a correction factor given by

$$K_1 = 1.175 \frac{S_L}{S_T \, \mathrm{Re}_D^{0.3124}} + 0.5 \, \mathrm{Re}_D^{0.0807} \tag{4.0.5}$$

where S_T and S_L are the non-dimensional pitches

$$S_T = \frac{p_y}{D}, \quad S_L = \frac{p_x}{D} \tag{4.0.6}$$

The Nusselt number for staggered pin fins is taken directly from Zukauskas

$$\begin{aligned} Nu_D &= 1.04 \, \mathrm{Re}_D^{0.4} \, \mathrm{Pr}_f^{0.36} && \mathrm{Re}_D < 300 \\ Nu_D &= 0.71 \, \mathrm{Re}_D^{0.5} \, \mathrm{Pr}_f^{0.36} && 300 < \mathrm{Re}_D < 1000 \\ Nu_D &= 0.4 \, \mathrm{Re}_D^{0.6} \, \mathrm{Pr}_f^{0.36} && \mathrm{Re}_D > 1000 \end{aligned} \tag{4.0.7}$$

These correlations are based on a different length scale and velocity, therefore appropriate scaling parameters are applied to ensure that the velocity and length scales match the VAT definition. Lets also note that these correlations have been developed for long tubes held at constant temperature. Using these correlations, the VAT energy and momentum equations can be solved to model transport phenomena in these two types of heat sinks. Following the discussion from Chapter 2, the friction factor can in general be case in the form

$$f = \frac{A}{\mathrm{Re}_{dh}} + B \tag{4.0.8}$$

where the first term dominates at low to moderate Reynolds numbers, while the second term becomes dominant at large Reynolds, and it can be seen that this is indeed the case for the given geometries.

Numerical simulations of laminar, constant property flow in a heat sink using Computational Fluid Dynamics (CFD) are quite reliable. To ensure that no numerical errors are present in the CFD results, the solution is taken as converged, when the RMS residual is less than1 $\times$ 10^{-6}, and the imbalances in the domain are less than 1%. A mesh sensitivity study is also carried out to ensure that the solution is mesh independent. The mesh-independent results are then compared to experiments to ensure that the physics of the problem have been captured correctly by the numerical solution. Since experimental results for heat sinks with variable geometries are not available, the experimental validation of the CFD results is carried out only for heat sinks with constant geometry. To ensure that the physics of the problem are captured for variable geometry heat sinks, the mesh size is increased by 20%. This is probably an unnecessary step that will increase computational time, however, in our case accuracy is crucial so some computational efficiency can be sacrificed. All the numerical simulations are carried out using the ANSYS CFX package. The workflow of the CFD studies is given Figure 4.1. Since the flow is assumed to be hydrodynamically fully developed, a developing inlet section is added to the computational domain to ensure that it matches the VAT closure model. This also implies that any entrance constriction and outlet expansion pressure drops are not included in the two models. An example of the computational domain for a trapezoidal micro-channel is given in Figure 4.2. The definition of the geometries and the parameters that defined them for each heat sink configuration can

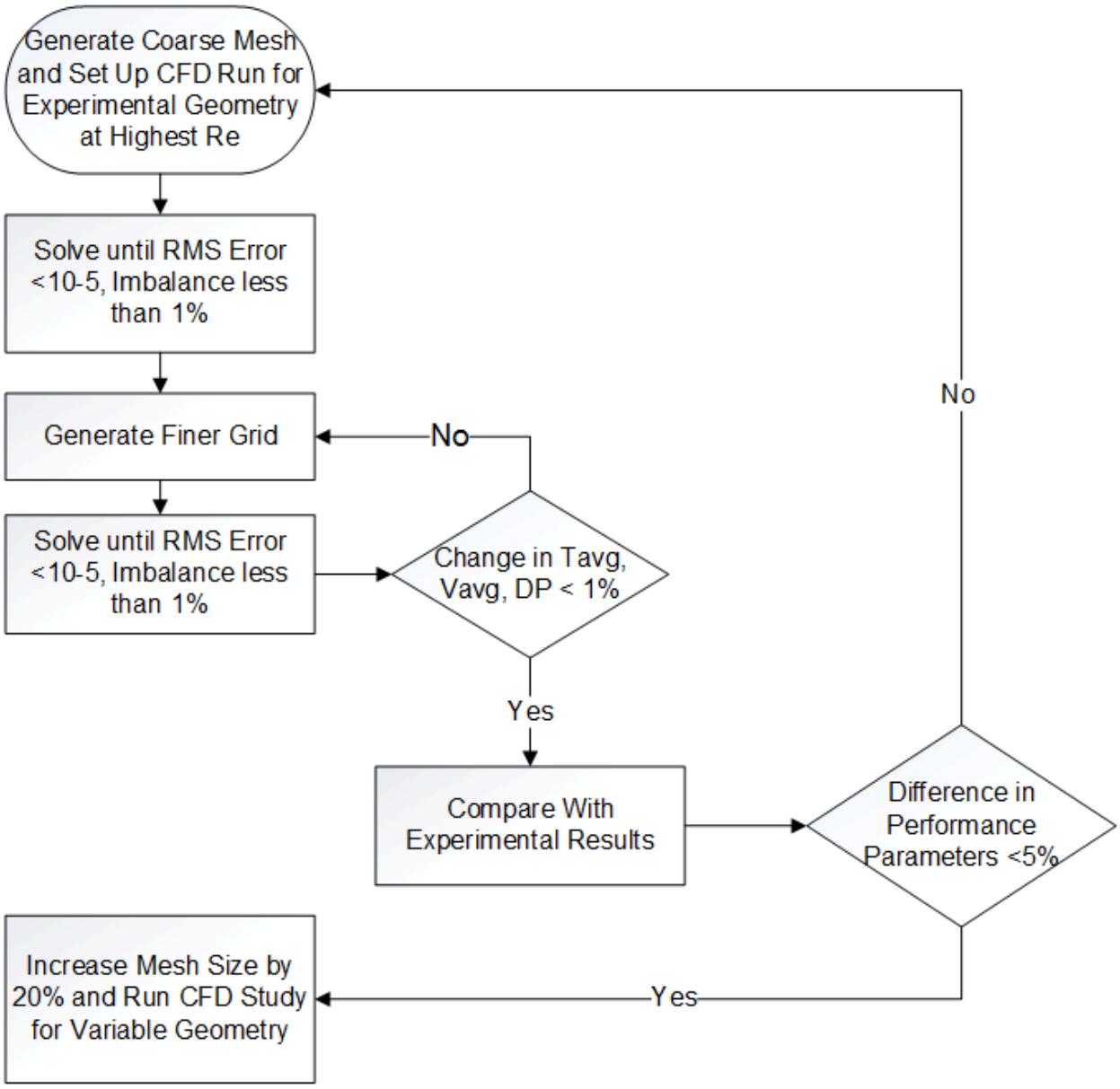

Figure 4.1: CFD Studies Workflow

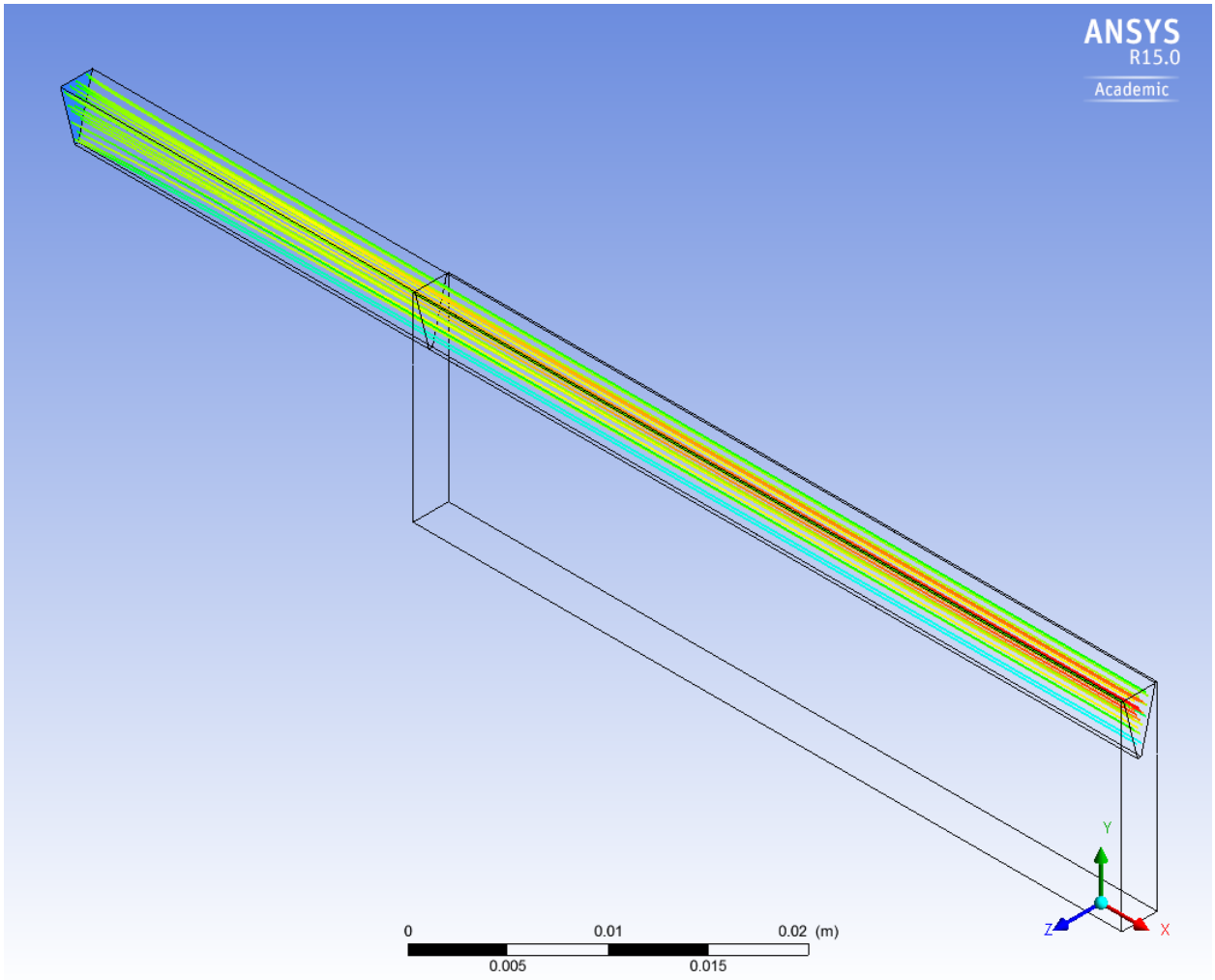

Figure 4.2: Example of Computational Domain for CFD Runs

be found in Section 3.3.1.

4.1 Heat Sinks with Uniform Geometry

Heat sinks without geometry variations are considered first in order to validate the model, the closure and the numerical solution. In addition, this allows us to show the computational advantages of using a VAT, compared to classic CFD modeling. The results obtained for a straight micro-channel and a staggered circular fin heat sink are compared to experimental results and numerical solutions.

4.1.1 Limiting Parameters

For constant porosity and specific surface, the scaled VAT conservation equation derived in Chapter 3

$$M_1 \frac{\partial^2 \langle u \rangle}{\partial z^2} - f \langle u \rangle^2 = \frac{d\langle p_f \rangle^f}{dx}, \tag{4.1.1}$$

$$F_1 \langle u \rangle \frac{\partial \langle T_f \rangle^f}{\partial x} = F_2 \frac{\partial^2 \langle T_f \rangle^f}{\partial x^2} + F_3 \frac{\partial^2 \left\langle \hat{T}_f \right\rangle^f}{\partial z^2} + h \left(\langle T_s \rangle^s - \langle T_f \rangle^f \right) \tag{4.1.2}$$

$$S_1 \frac{\partial^2 \langle T_s \rangle^s}{\partial x^2} + S_2 \frac{\partial^2 \langle T_s \rangle^s}{\partial z^2} - h \left(\langle T_s \rangle^s - \langle T_f \rangle^f \right) = 0 \tag{4.1.3}$$

Since porosity is constant, the characteristic values of porosity, specific surface and hydraulic diameter are simply the constant values

$$\begin{aligned} M_1 &= \frac{2\varepsilon_f}{f_{avg} \mathrm{Re}_{dh}} \left(\frac{d_h}{2H_c} \right)^2, \\ F_1 = \frac{\mathrm{Re}_{dh} \mathrm{Pr}_f}{2Nu_{dh}} \frac{C_x}{\varepsilon_f}, \quad F_2 &= \frac{C_x^2}{Nu_{dh}}, \quad F_3 = \frac{C_z^2}{Nu_{dh}}, \\ S_1 &= \frac{R_k}{Nu_{dh}} C_x^2, \quad S_2 = \frac{R_k}{Nu_{dh}} C_z^2, \end{aligned} \tag{4.1.4}$$

The heat transfer coefficient, and friction factors remain in the equation due to their variations in the z direction, however they are scaled quantities and are therefore of order 1.
The scaling of the momentum equation was carried out by assuming that the pressure gradient will be balanced by the momentum sink term. With this in mind, the parameter M_1 represents the ratio of frictional losses due to the no-slip condition at the system boundary,

to frictional losses due to the lower scale geometry. This is clear by the appearance of the ratio of length scales d_h/H_c , which is the ratio of the size of the internal geometry features to the size of the system.

In order to find the limits of applicability of the VAT equations, it is important to recall the main assumption at the base of the VAT model, which implies that the system scale is much larger than the lower geometry scale. In the current problem, this ratio is represented by that the ratio d_h/H_c . Note that this was one of the assumptions that was used in Chapter 2, and gives the averaging process statistical sense. In other words, when the two scales are not disparate, the averaging process does not make sense. Therefore, this suggests that a requirement for the validity of the VAT momentum conservation equation is

$$M_1 \ll 1 \tag{4.1.5}$$

Physically, this condition implies that most of the momentum loss in the system is due to the intricate lower scale geometry i.e. in a pin fin heat sink, pins are responsible for most of the pressure drop, and the pressure drop due to the base and/or top wall are negligible. If this parameters is not small, the lower and upper scale geometry are close, and lower scale phenomena will no longer depend only on the local velocity, but will be dependent on the velocity at other locations in the system. The product $f\mathrm{Re}_{dh}$, given the form of the friction factor given in Eqn. (4.0.8), implies that M_1 will be independent of the Reynolds number at low to moderate Re_{dh}, while it will be inversely proportional to it for large Re_{dh}. The assumption given in Eqn. (4.1.5), and the actual value that will delimit the validity of the equation will be discussed in Section 4.1.3. Mathematically, M_1 represents the curvature of the velocity profile, and Figure 4.3 shows that small values of M_1 result in a mostly uniform velocity profile.

Moving on to the energy equations, recall that the scaling was carried out by comparing each term to the interphase heat transfer term. Lets consider the fluid equation first. Following the previous discussion, the length scale ratios C_x and $C_z$are ratios of the lower scale geometry scale to the system scale. The multi-scale nature of the problem implies that they will be smaller than one, therefore, their squared values will be much smaller than one. In addition, the diffusive terms are divided by the Nusselt number, and they will be very small.

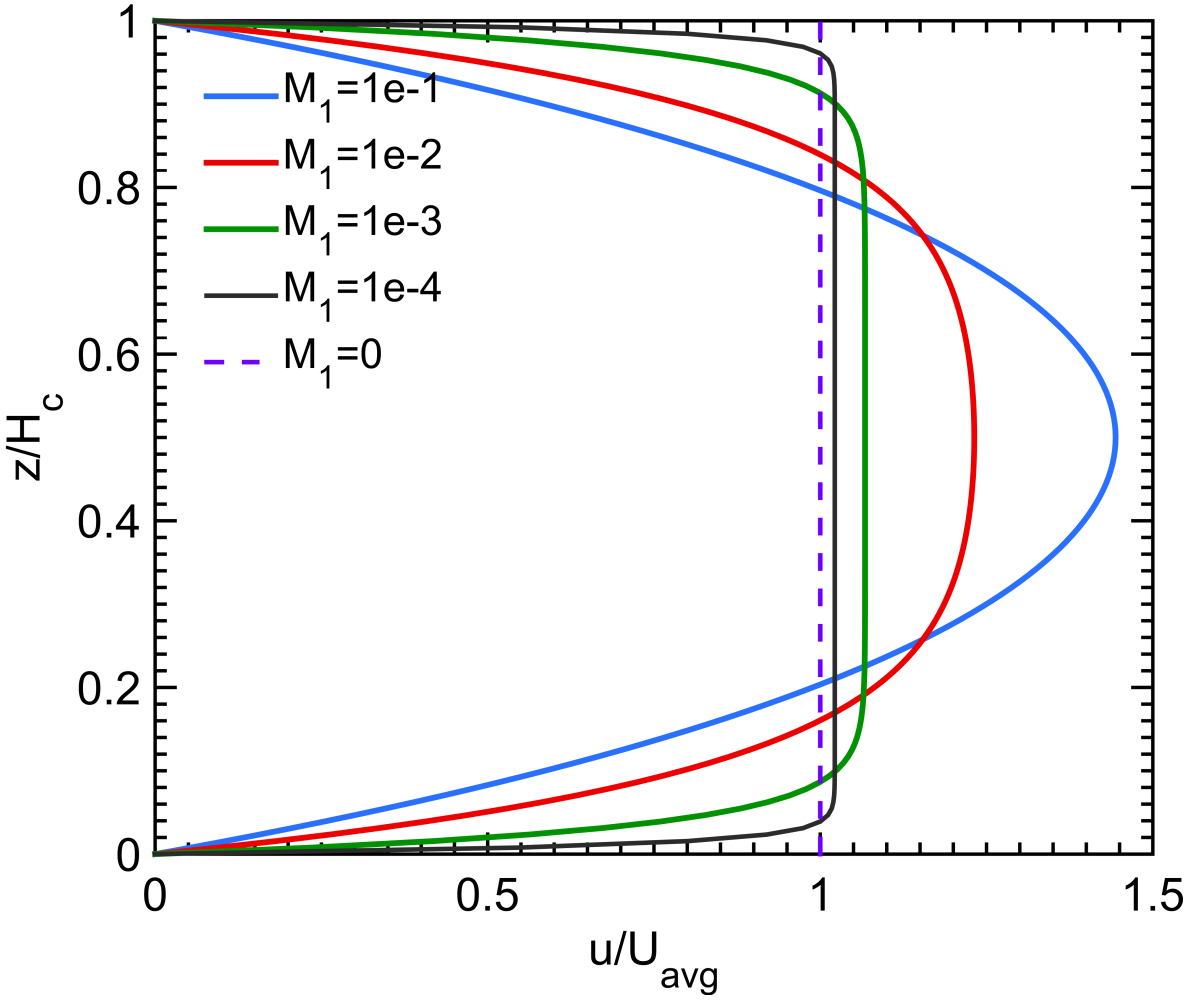

Figure 4.3: Velocity Profile for Different Values of M_1

This suggests the F_1 term, which is the ratio of the Peclet number to the Nusselt number will balance the interphase heat transfer term. Near the boundary at $z = 0$, the velocity goes to zero, therefore the convective term vanishes, and the fluid and solid temperature are assumed to be equal, so the interphase term is also zero. The scaling of the heat flux interface condition implies that, when the ratio of thermal conductivities is large (which is the case in almost all heat sinks), most of the heat from the base enters the solid phase, which implies that the fluid z-diffusive term will be small. In addition, the interphase fluid and solid temperature is assumed to be equal, which implies that near the boundary all terms in the fluid equations are small. Therefore, the diffusive terms in the fluid energy equation are small everywhere. Overall, the scaling revealed that heat enters through the solid phase, its diffused and transferred to the fluid through the fins, and it is then convected away. This is an accurate description of the heat transfer physics in a heat sink. The fact that the diffusive terms are negligible everywhere implies that the gradients of the velocity profile near the boundaries do not affect the energy equations strongly. As long as the velocity distribution is accurate in the bulk of the flow, the energy equations will be accurate. Because of this fact, when the limits of applicability of the equations are discussed, only the terms in the momentum equation will be considered.

4.1.2 Validation

In this section, the VAT heat sink model is validated by comparing the results to experimental data for two heat sink geometries and material combinations: a water cooled microchannel heat sink, and an air cooled staggered pin fin heat sink.

4.1.2.1 Microchannel Heat Sink

The geometry and experimental results for the microchannel heat sink, are taken from Lee and Garimella [158]. They fabricated five heat sinks by machining ten micro-channels, of different heights and widths, on a $25.4 \times 25.4 \times 70$ mm copper block. Four cartridge heaters were machined into the base, and used to heat deionized water flowing through at flow rates

Table 4.1: Micro-channel heat sink geometric parameters

Test	N_c	$w_c\,[mm]$	$H_c\,[mm]$	$L\,[mm]$	$W\,[mm]$	$D_h\,[mm]$	$\alpha_c\,(=H_c/w_c\,)$
1	10	0.194	0.884	25.4	25.4	318	4.56
2	10	0.229	1.250	25.4	25.4	387	5.46
3	10	0.300	1.520	25.4	25.4	501	5.07
4	10	0.339	1.895	25.4	25.4	575	5.59
5	10	0.534	2.910	25.4	25.4	902	5.45

of 0.1 to $2.2l/min$. They define the Nusselt and Reynolds numbers as

$$\mathrm{Nu}_{\mathrm{exp}} = \frac{hD_h}{k_f} = \frac{QD_h}{NA_f k_f\,(T_w - T_m)} \tag{4.1.6}$$

$$\mathrm{Re}_{\mathrm{exp}} = \frac{u_{avg} D_h}{\nu_f} \tag{4.1.7}$$

where $Q$is the heat input, $D_h = 2w_c H_c/(w_c + H_c)$ is the hydraulic diameter, $N$is the number of fins,$A_f = L\,(w_c + 2H_c)$ is the interface area per fin, T_w is the average wall temperature at the bottom of the channel, and T_m is the average of inlet and outlet fluid temperature. The average velocity u_{avg} is determined from the flow rate, the heat flux is kept at $45\,W/cm^2$, and all fluid properties are evaluated at T_m. The uncertainty in the experimental results is 6-17%, with the higher error occurring at higher flow rates. The geometric parameters for the five different heat sinks considered are given in Table 4.1.

The base of the heat sink is arbitrarily chosen to be 10 mm thick, which corresponds to a base aspect ratio S_b of about 0.4. This thickness is chosen to ensure that base conduction is not negligible; moreover, because of the high thermal conductivity, a uniform heat flux applied at the bottom of the base closely approximates experimental conditions (embedded cartridge heaters in 70 mm thick substrate). The porosity and specific surface can be found by analytically solving the integrals in Section 3.3.1.3.

$$\varepsilon_f = \frac{w_c}{p_y}, \quad S_w = \frac{2H_c + 2w_c}{H_c p_y} \tag{4.1.8}$$

The hydraulic diameter than becomes

$$d_h = 2w_c \tag{4.1.9}$$

which is consistent with the parallel plate length scale that was used in the closure. The parameter M_1 depends than on the inverse of the aspect ratio of the channel α. In all the cases, the aspect ratio is quite large, which leads to values of M_1 of $O\left(10^{-3}\right)$. The numerical results for overall Nusselt number and pressure drop as a function of Reynolds number are shown in Figure 4 4, along with the experimental results. Both VAT and CFX predicted values are in very good agreement with experimental data, with mean errors of 3.3% and 3.8%, respectively, which are well within experimental uncertainty. The error is defined as the absolute value of the relative difference of two values. The results for

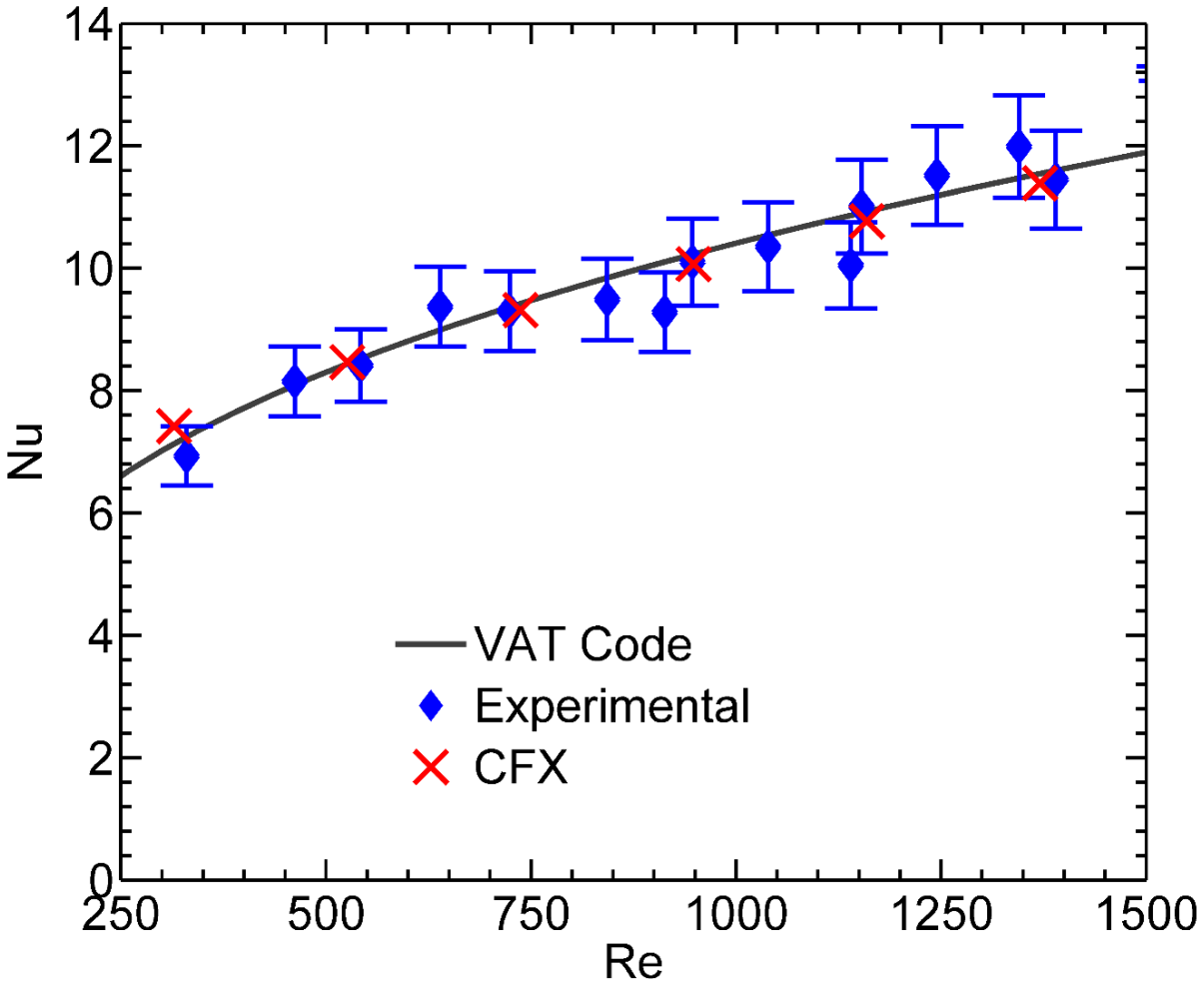

Figure 4.4: Comparison of Nusselt Number Obtained Numerically With Experimental Results for Test #3

pressure drop as a function of Reynolds number are shown in Figure 4.5, and the agreement is again very good with a mean error of 5.4%. The values obtained with the two codes

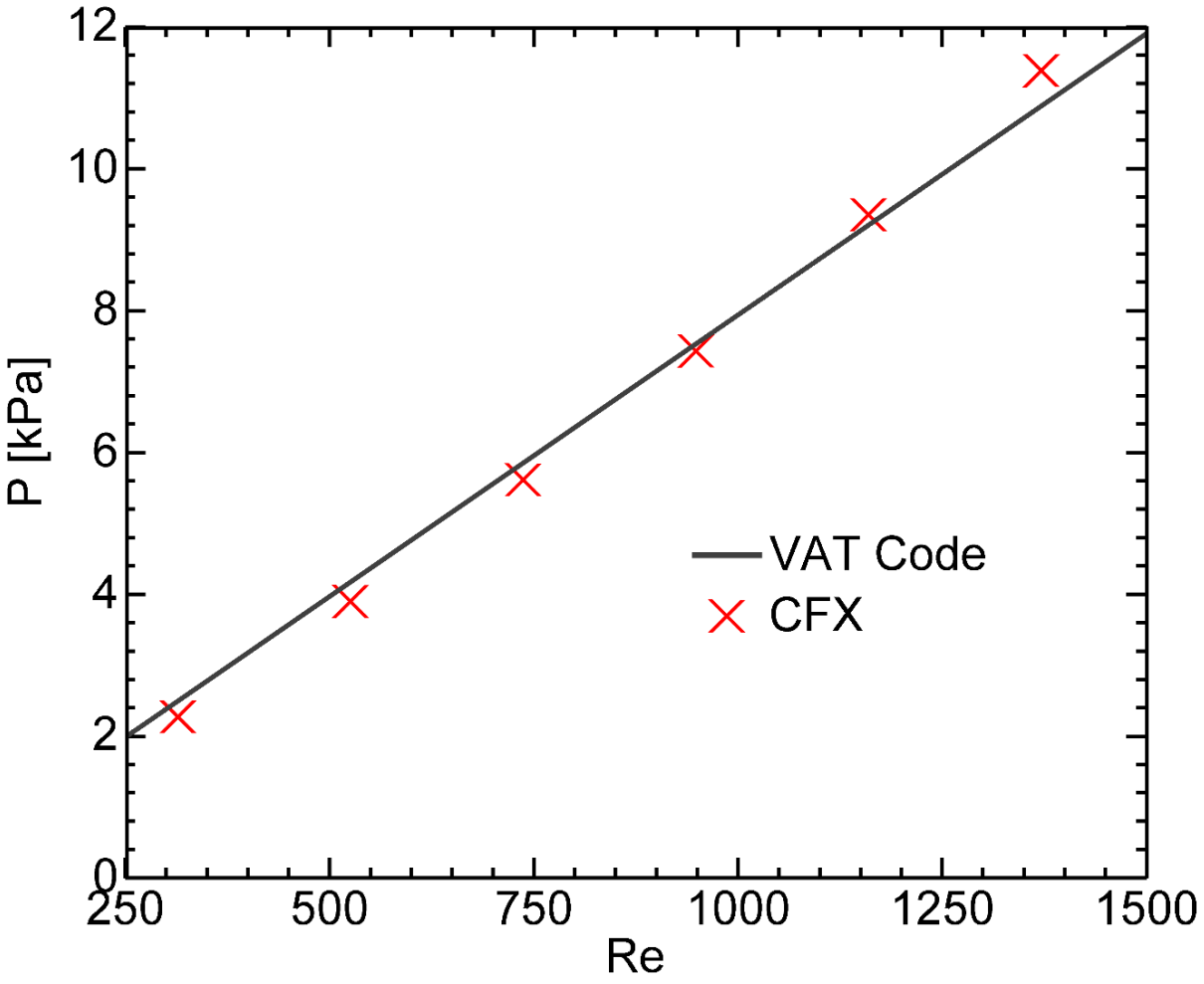

Figure 4.5: Comparison of Pressure Drop Obtained with VAT Code and CFX for Test #3

are in very good agreement with each other and with experimental data over the entire Reynolds number range considered, but the VAT code gives a solution 4.3×10^3 times faster than CFX. The accuracy of the VAT code is further validated by comparing the predicted Nusselt number for the remaining micro-channel geometries Table 4.1 with experimental data. In all cases, the lower and upper limits of the Reynolds numbers range were determined by the lowest experimental point available and transition to turbulence, respectively. The results for Nusselt vs. Reynolds number, given in Figure 4.6, show that the agreement with experimental data is excellent. In all geometric configurations and over the entire

range of Reynolds numbers, the predicted Nusselt number agrees well with experimental results, and the average error is less than 4.5%, which is again well within experimental uncertainty. It has been shown that the VAT code can very quickly and accurately predict the

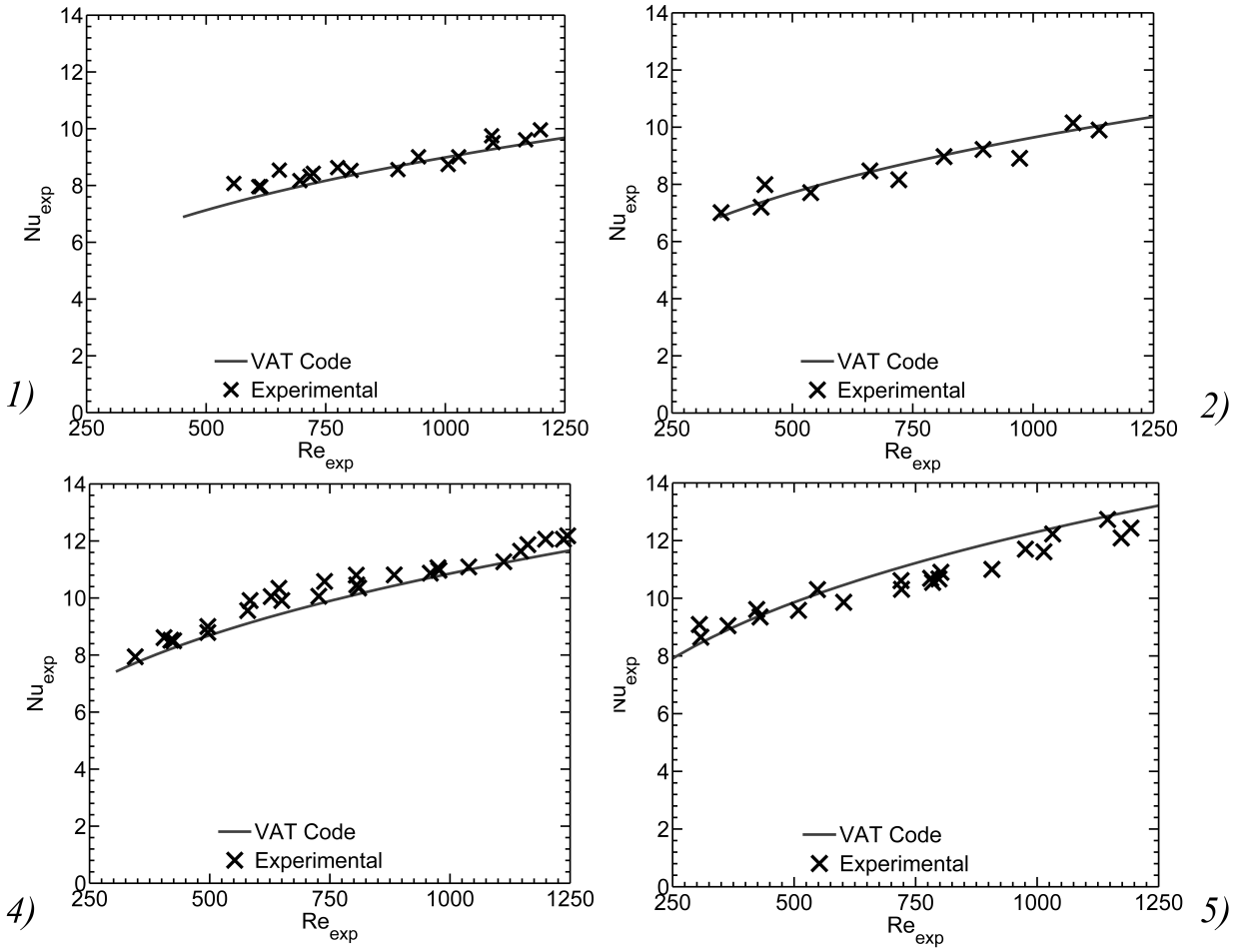

Figure 4.6: Comparison of Nusselt Number Obtained Numerically With Experimental Results for Tests #1-2, 4-5

average Nusselt and Reynolds number for several geometric configurations when a constant heat flux is applied. In order to check the accuracy of the VAT code in predicting base temperature distributions, its results are compared with those obtained using CFX for a heat sink with applied non-uniform heat flux. Test #3 is chosen because the CFX solution has been validated. A square heat flux is applied at the bottom of the base to simulate an

attached heat generating component, and Re = 948 is chosen. The component is given an arbitrary length of 10 mm, width equal to base width, and is located at the center of the base. The component is assumed to generate $45\,W/cm^2$ heat flux while the rest of the base is insulated. From a mathematical point of view, a two-dimensional slice of such an input is the difference of two shifted opposite Heaviside step functions $H(x)$'

$$q_w(x) = q_{w,\max}\left\{H\left[x - \left(x_c - {}^{W_c}/_2\right)\right] - H\left[x - \left(x_c + {}^{W_c}/_2\right)\right]\right\} \tag{4.1.10}$$

where $x_c$and W_c are the non-dimensional center and width of the input, respectively (see Figure 4.7). Numerically, the function can be approximated by

$$q_w(x) = \frac{q_{w,\max}}{2}\left\{\tanh\left[k\left(x - d^-\right)\right] - \tanh\left[k\left(x - d^+\right)\right]\right\} \tag{4.1.11}$$

where $d^{\pm} = (x_c \pm W_c/2\ )$, while k defines the sharpness of the transition. The average of the function can then be found analytically while the cosine coefficients are found numerically by using MATLABs built-in integrate function. It is found that $k = 200$ provides a good approximation of the step function, and is well approximated by a cosine series with $N = 128$. A schematic of the heat flux applied to CFX case, its approximation Eqn. (4.1.11), and its truncated cosine Fourier series are shown in Figure 4.7. It can be seen that, although the steep gradient causes some fluctuations in the cosine series, the agreement between all three functions is good. Figure 4.8 shows the temperature distribution at the bottom of the base obtained using the VAT code and CFX with applied non-uniform heat flux. The agreement between the two solutions is excellent with a maximum error of about 5%; however, while the CFX requires about 3500s to obtain a solution, the VAT code requires only 2s, which is approximately 1.8×10^3 times faster. The huge computational time reduction obtained with the combination of VAT and a faster solution procedure makes multi-parameter and multi-objective optimization possible. This solution procedure is not meant to replace full numerical solutions in all cases; rather, it demonstrates that if details of the flow are not of interest, accurate performance parameters and component temperatures can be obtained much more efficiently using the VAT based code. This study shows that the VAT code can quickly, and accurately predict the performance of micro-channels for a wide range of Reynolds numbers.

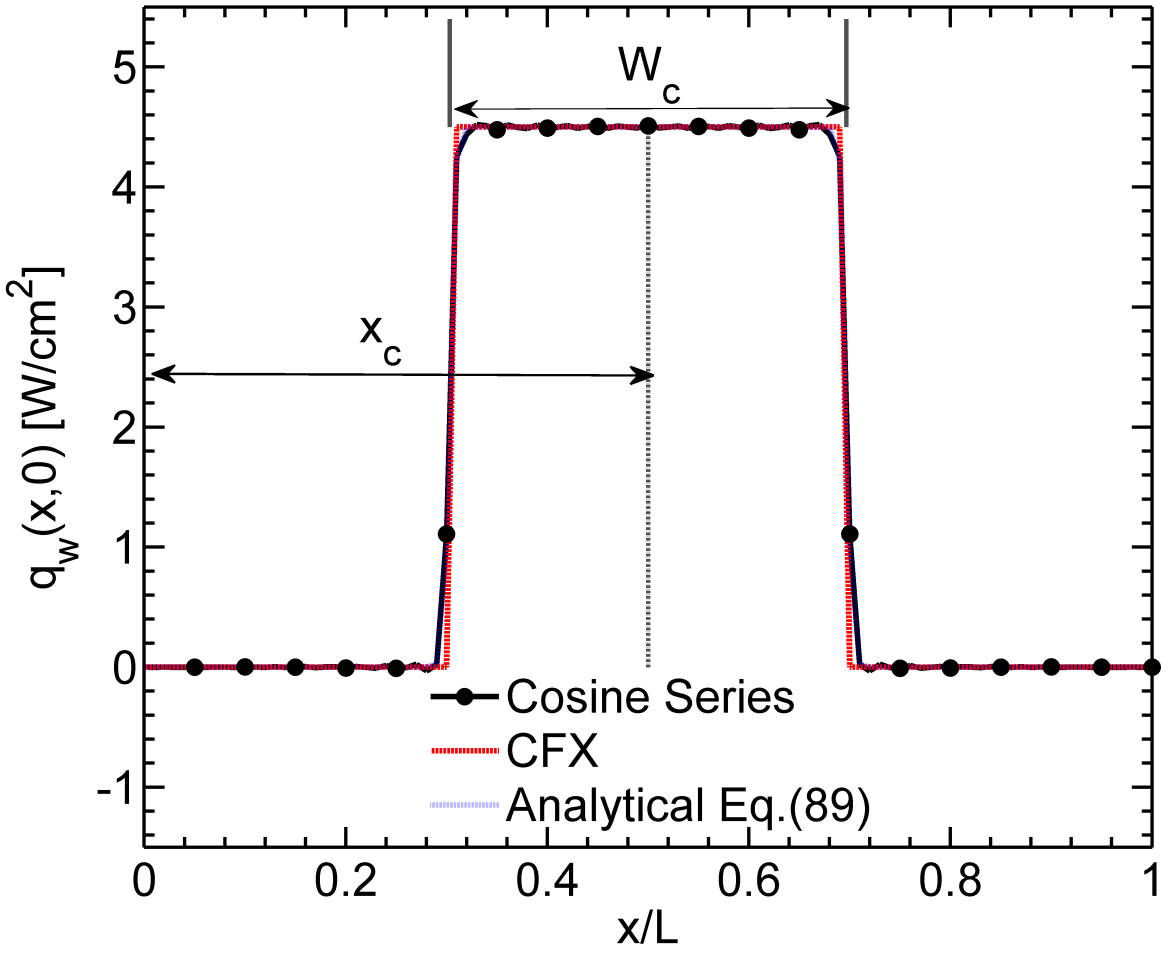

Figure 4.7: Non-uniform Heat Flux Applied at Bottom of Base to Test #3

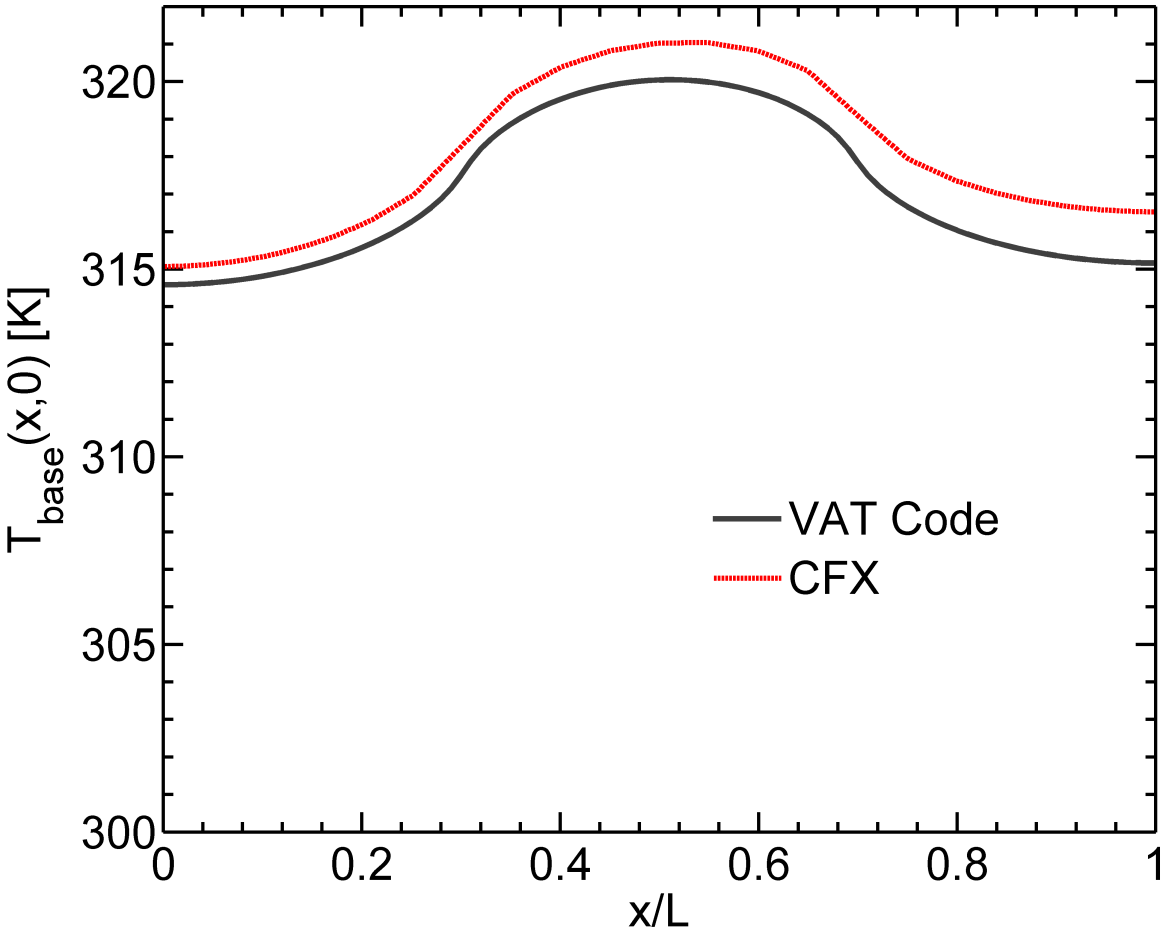

Figure 4.8: Base Bottom Temperature for Non-Uniform Heat Flux obtained with CFX and VAT Code

Next, in order to ensure that the solution is accurate for a wide range of porosities, four more micro-channel heat sinks are studied. The details of the geometry are given in Table 4.2. Their geometric parameters are somewhat randomly chosen, however, the aspect ratio is

Table 4.2: Geometrical Parameters of Straight Micro-channels used in Low M_1 Numerical Experiments

$L[mm]$	$W[mm]$	$H_c[mm]$	$p_y[mm]$	$w[mm]$	ε	M_1
50	50	13.5	2.5	2.25	0.9	3.75E-03
50	50	7.5	2.5	1.25	0.5	2.31E-03
50	50	1.5	2.5	0.5	0.2	9.41E-03
50	50	1.5	2.5	0.25	0.1	4.63E-04

kept high, to ensure that M_1 will be small. The Reynolds number has been fixed at 1100. The results for the overall friction factor and Nusselt number are given in Figure 4.9 and Figure 4.10, respectively. In addition, the percent error is plotted at each experimental point on the right axis, and it can be seen that for both Nusselt and friction factor, the error is always less than 4%. [ht!] It can be seen that once again the agreement between the values predicted by CFX and the VAT code are in excellent agreement.

4.1.2.2 Pin Fin Heat Sink

Pin fin heat sinks are also commonly used in thermal management of electronics. Stagnation points and vortex structures created by the pins improve the heat transfer performance of these types of heat sinks, when compared to simple straight channels. Two types of geometrical configurations are commonly found for pin fin heat sinks: inline and staggered. Staggered pin fins lead to better thermal performance, however, as often is the case, they also lead to an increase in pressure drop. Temperature, velocity and pressure distributions around cylinders are quite complicated due to the formation of transient trailing vortices (Von Karman vortices). Extensive CFD studies have been carried out to investigate these interesting phenomena; nonetheless, when the details of the flow around pins are not of interest, and all is required is performance evaluation of the entire heat sink, a VAT model

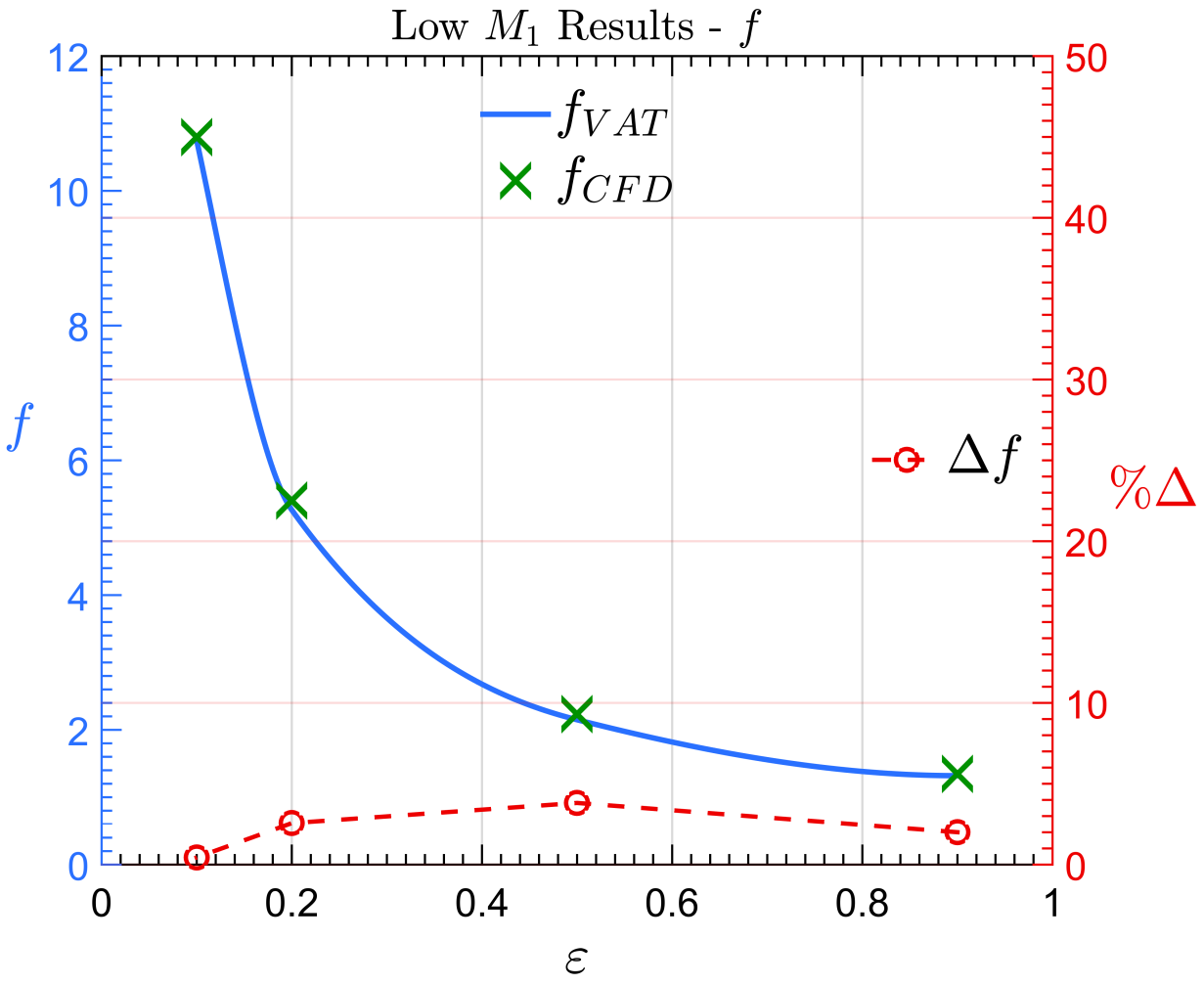

Figure 4.9: Friction Factor as a Function of Porosity for Four Heat Sinks with Low M_1

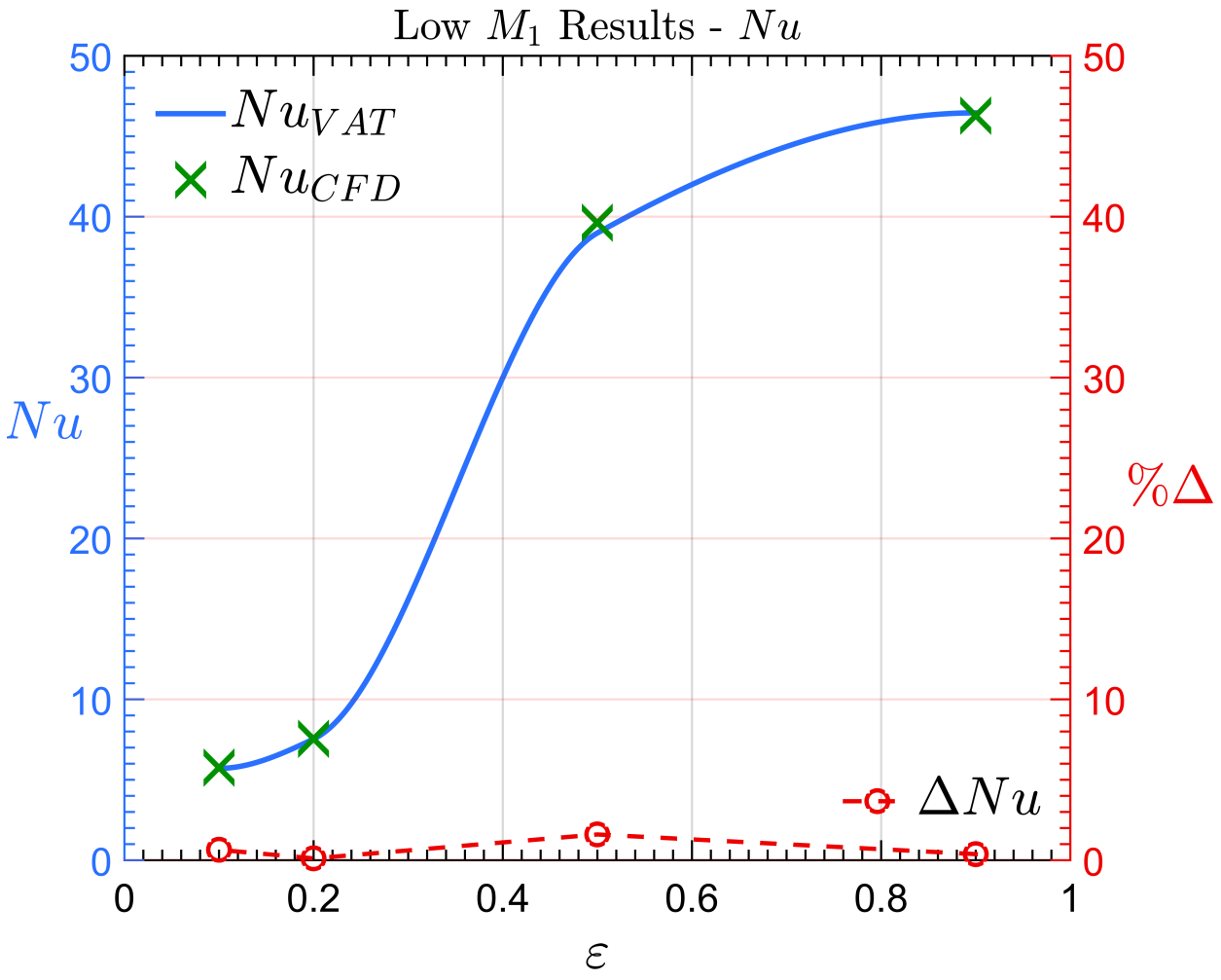

Figure 4.10: Nusselt Number as a Function of Porosity for Four Heat Sinks with Low M_1

Table 4.3: Geometric Parameter for Staggered Pin Fin Heat Sink

$L[mm]$	$W[mm]$	$H_c[mm]$	$t_b[mm]$	$D[mm]$	$p_x[mm]$	$p_y[mm]$	$T_{in}[K]$	$Q[W]$
114.3	114.3	38.1	8.25	3.175	3.3665	6.731	298	125

is a very efficient way to obtain it. The advantage of VAT lies in the fact that the same code developed in the previous section, with different closure parameters can be used to study these complex phenomena. The complexity of the lower flow structure is included in the closure parameters, while the quantities of interest are determined on the system scale. This type of separation is not possible using a full CFD solution, all the physics of the problem have to be calculated directly, leading to considerable computational times. Continuing our comparison with the continuum approach, different geometries are to VAT what different fluids are to the Navier-Stokes equations. The same Navier-Stokes equations are used to calculate velocity and pressure distribution in a system containing air or water. The molecular behavior of the two fluids is quite different however, when solving the Navier-Stokes equations, the only differences are the values of density and viscosity, which are the lower scale closure parameter. In this section, a VAT approach will be applied to determine performance parameters for a staggered pin fin heat sink. A schematic of a pin fin heat sink, along with the geometric parameters are shown in Figures 3.4 and 3.5. The results obtained using VAT will be validated by comparison with experimental results. The heat sink geometry and experimental results are taken from Rizzi [159]. The experiments were conducted by placing a staggered aluminum pin fin heat sink in a wind tunnel, and attaching it to a copper block with cartridge heaters inserted into it. The cooling fluid was air, and a shroud was inserted about the fin tips, to eliminate any flow bypass. The geometric and thermal input parameters are given in Table 4.3 The experimental Nusselt and Reynolds numbers are defined using the VAT hydraulic diameter and the average intrinsic velocity

$$\mathrm{Nu}_{\mathrm{exp}} = \frac{h d_h}{k_f}, \quad \mathrm{Re}_{\mathrm{exp}} = \frac{\langle u_f \rangle^f_{avg} \, d_h}{\nu_f} \tag{4.1.12}$$

The heat transfer coefficient is defined in terms of the maximum temperature difference

$$h = \frac{{}^{Q}/_{A_b}}{T_{b,\max} - T_{in}} \tag{4.1.13}$$

where $A_b = W \cdot L$ is the area of the base on which the heat load is applied. The porosity and specific surface for constant porosity can be found by analytically solving the integrals in Section 3.3.1.2.

$$\varepsilon_f = 1 - \frac{\pi D^2}{8 p_x p_y}, \quad S_w = \frac{\pi D}{2 p_x p_y} \tag{4.1.14}$$

The non-dimensional parameter M_1 for this heat sink was found to be $O\left(10^{-5}\right)$ or smaller, while volume fraction weighted thermal conductivity ratio R_h was of order $O\left(10^{-5}\right)$, therefore, all the assumptions discussed in the previous sections are still valid. The predicted friction factor and Nusselt number as a function of Reynolds number are shown in Figure 4.11, along with Rizzis experimental results [159, 160]. It can be seen that the agreement in for both parameters with experimental results is again excellent. The average error in the Nusselt number is 3.2% with a maximum error of 5.1%, while the average and maximum error for the friction factor are 2.6% and 4.5% respectively.

4.1.3 Determination of Limits on M_1

In the previous sections, it has been shown that when M_1 is small, the VAT code can accurately predict the thermal and hydraulic performance of two geometrically different systems. It is of interest now to find a limiting value of M_1, after which the VAT model is no longer applicable. To this purpose, the same study defined in Table 4.2 is repeated, but the height of the channel is kept fixed at 4 mm, such that as the width increases, the parameter M_1 increases. Although there is no Reynolds number dependence, for consistency, the Reynolds number is again kept fixed at 850. The results for the friction factor predicted by the VAT model and the CFD solution are shown in Figure 4.12. Also in Figure 4.12, the percentage difference between the two solutions is plotted on the right axis. It is quite clear that as predicted, the VAT model loses accuracy as M_1 increases. If an error of about 10% is considered acceptable, the limit of applicability of the VAT model for constant geometry is given by

$$M_1 < 0.04 \tag{4.1.15}$$

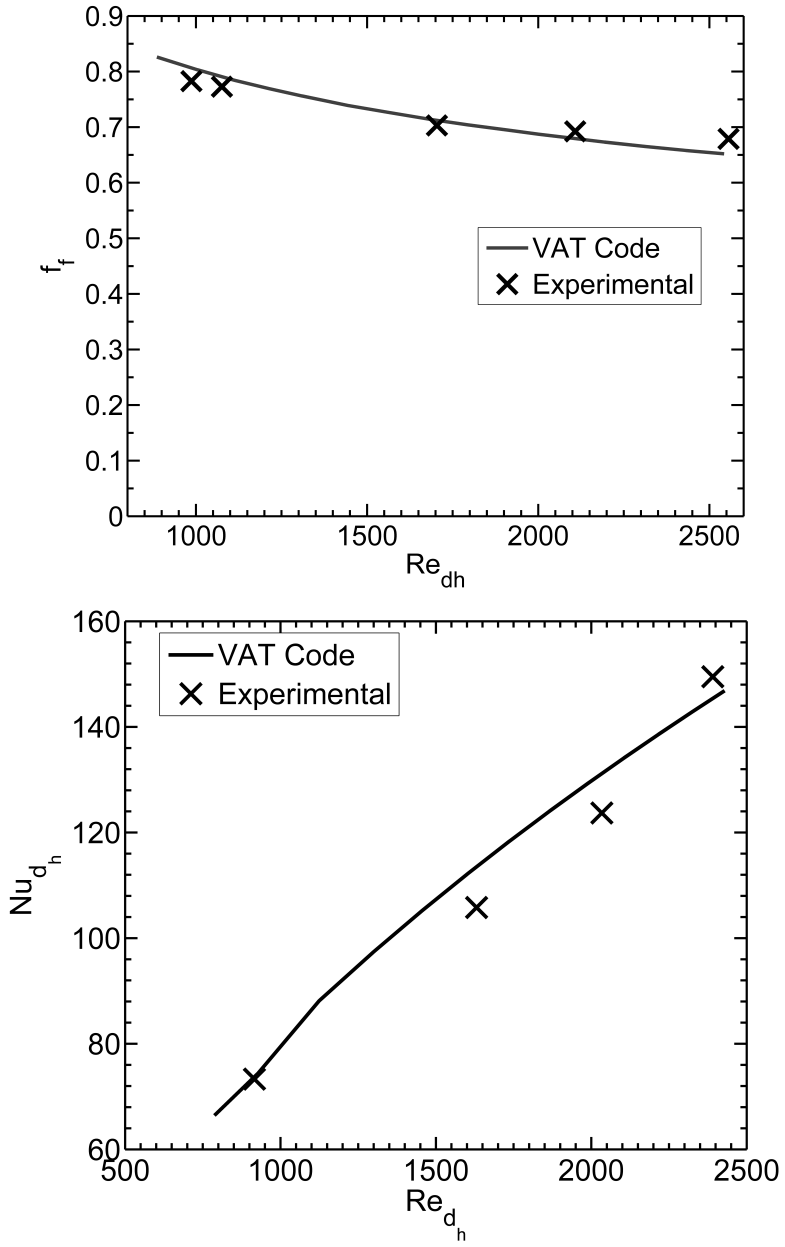

Figure 4.11: Comparison of Friction Factor and Nusselt Number for a Staggered Pin Fin Heat Sink with Experimental Results by Rizzi

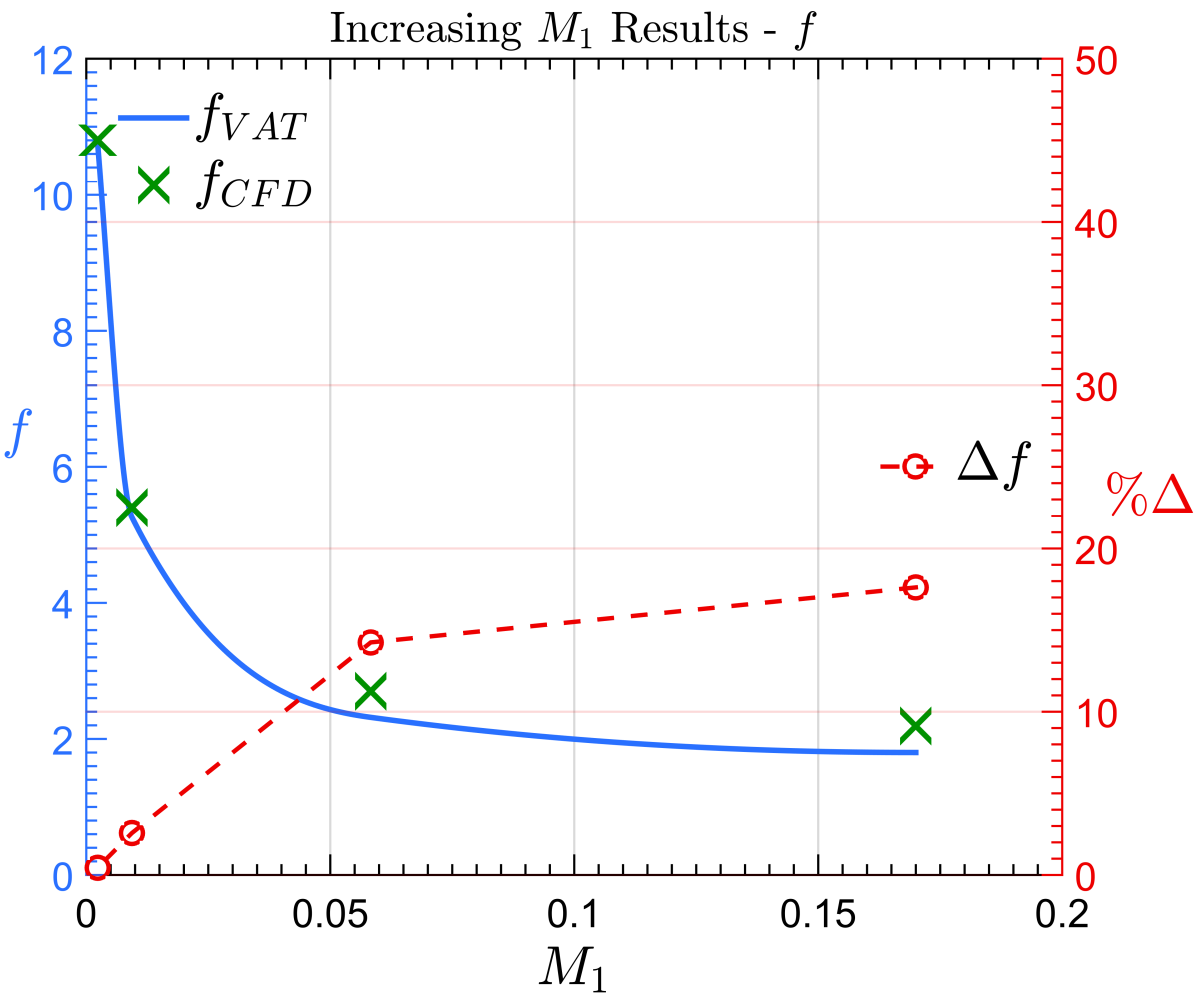

Figure 4.12: Friction Factors Predicted by VAT and CFX as a Function of M_1

In addition, the predicted Nusselt number is shown in Figure 4.13. It can be seen that the accuracy decreases with an increase in M_1, however the increase is much more gradual, and the accuracy is indeed limited by the momentum solution. In both the CFD and the VAT

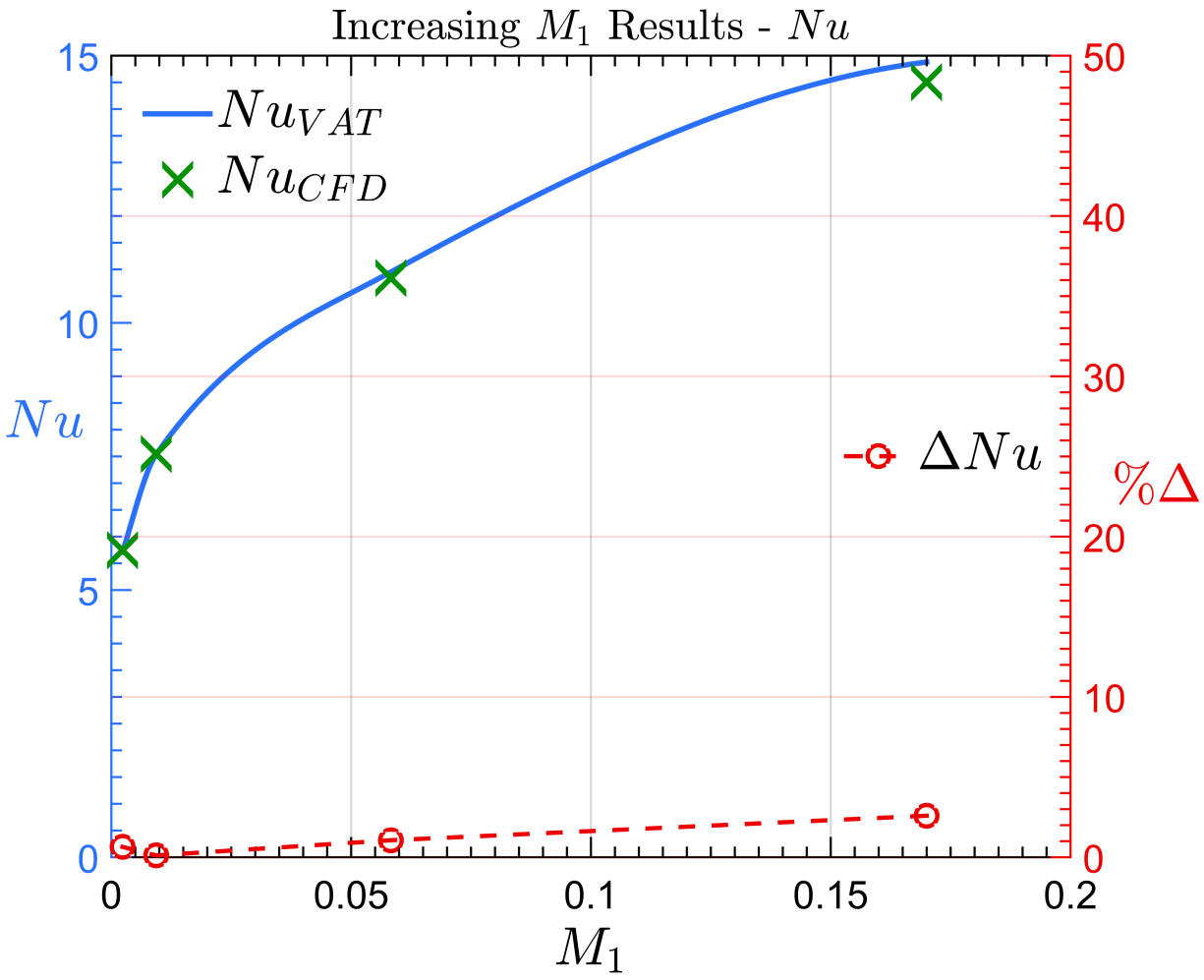

Figure 4.13: Nusselt Number Predicted by VAT and CFX as a Function of M_1

code, the average velocity was assumed to be the known quantity, which implies that the F_1 parameter is calculated correctly. Therefore, as discussed in Section 4.1.1, the error in the Nusselt number will be much smaller, which is evident by comparison of Figure 4.12 and Figure 4.13. The VAT model is geometry independent, therefore so should its limits. To prove that this is indeed the case, the last study is repeated for the staggered pin fin heat sink defined by Rizzi [160]. The geometry was reproduced in ANSYS CFX, and the height

was adjusted to study the effects of decreasing M_1 on the accuracy. The results for the pressure drop are shown in Figure 4.14. For pin fins, it is found that the error also increases

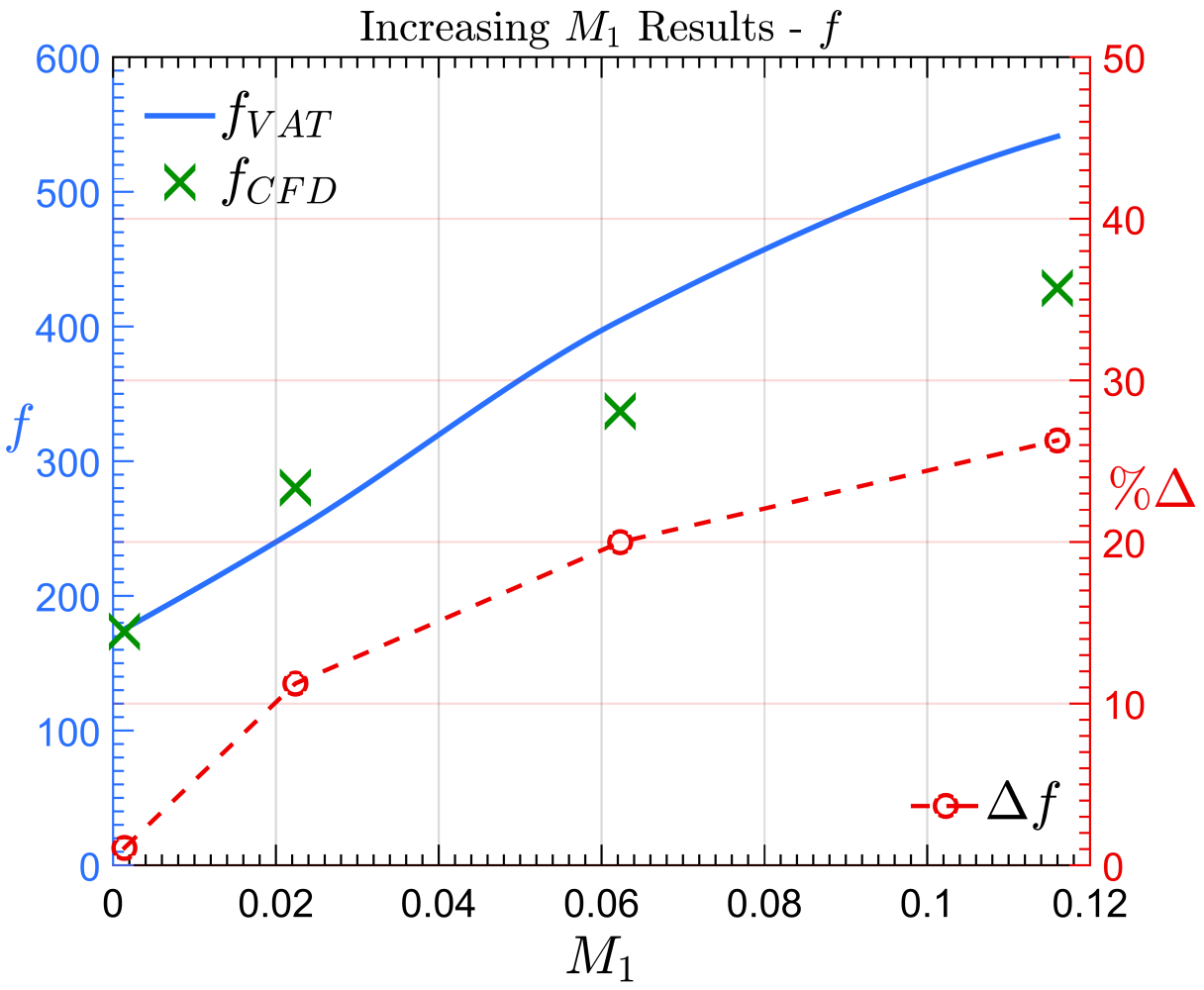

Figure 4.14: Friction Factors Predicted by VAT and CFX as a Function of M1 for Staggered Pin Fin Heat Sink

as a function of M_1 and it reaches 10% at $M_1 \approx 0.02$, which is a slightly lower limit than the one given in Eqn. (4.1.15). The fact that the error is larger for pin fins does not come as a surprise, since the lower scale flow and heat transfer structures are much more complicated than for straight channels, and, in general, the closure approximation will introduce a higher error. Nonetheless, it can be seen clearly that the increase in error trend and the order of magnitude of the limit are the same for both geometries.

4.2 Heat Sinks with Variable Geometry in Cross-Flow Direction

In the previous section, it has been shown that the parameter M1 determined the limits of applicability of the VAT model for constant geometry. In this section, a similar analysis is carried out for heat sinks in which the porosity varies in the z-direction only. These types of heat sinks include trapezoidal micro-channel heat sinks and tapered pin fin heat sinks. Although only linear profiles are considered here, the code and the model developed are independent of the profile.

4.2.1 Limiting Parameters

The VAT conservation equations derived in Chapter 3, when porosity variations are present in the z direction only, simplify to

$$M_1 \frac{\partial^2 \langle u \rangle}{\partial z^2} - S_w f \langle u \rangle^2 = \varepsilon_f \frac{d\langle p_f \rangle^f}{dx} \tag{4.2.1}$$

$$F_1 \langle u \rangle \frac{\partial \langle T_f \rangle^f}{\partial x} = F_2 \varepsilon_f \frac{\partial^2 \langle T_f \rangle^f}{\partial x^2} + F_3 \frac{\partial}{\partial z}\left(\varepsilon_f \frac{\partial \langle T_f \rangle^f}{\partial z}\right) + h S_w \left(\langle T_s \rangle^s - \langle T_f \rangle^f\right) \tag{4.2.2}$$

$$S_1 \varepsilon_s \frac{\partial^2 \langle T_s \rangle^s}{\partial x^2} + S_2 \frac{\partial}{\partial z}\left(\varepsilon_s \frac{\partial^2 \langle T_s \rangle^s}{\partial z^2}\right) - h S_w \left(\langle T_s \rangle^s - \langle T_f \rangle^f\right) = 0 \tag{4.2.3}$$

Following the discussion in the previous section, the accuracy of the equations will be limited by the accuracy of the momentum equation. Consequently, only its limits will be explored. The porosity dependence of the momentum equation, Eqn. (4.2.1), is hidden in the diffusive term. The diffusive term is expanded to explicitly show this dependence on the porosity variations (where it is assumed that porosity variation is linear, therefore its second order derivative is zero)

$$M_1 \varepsilon_f \frac{\partial^2 \langle u \rangle^f}{\partial z^2} + 2 M_1 \frac{\partial \varepsilon_f}{\partial z} \frac{\partial \langle u \rangle^f}{\partial z} - S_w f \langle u \rangle^2 = \varepsilon_f \frac{d\langle p_f \rangle^f}{dx} \tag{4.2.4}$$

It can be seen that a new parameter arises in the equation, that will be defined as M_2

$$M_2 = 2 M_1 \left|\frac{\partial \varepsilon_f}{\partial z}\right| = \frac{4\varepsilon_{f,c}}{f \mathrm{Re}_{dh}} \left(\frac{d_{h,c}}{H_c}\right)^2 \left|\frac{\partial \varepsilon_f}{\partial z}\right| \tag{4.2.5}$$

Note that this parameter depends on M_1 and the porosity gradient. This term represents the ratio of friction losses due to the lower scale geometry, to system scale friction losses due

to the porosity variations. The characteristic porosity and hydraulic diameter are taken as the average values.

Similar to the discussion that was carried out for the constant geometry, assuming that M_1 is small, large values of the porosity gradient (M_2 is significant) imply that the lower scale phenomena are not anymore dependent only on the local velocity, but are affected by variations at the system scale. Physically, this implies that in such cases, the porosity gradient is felt in large parts of the domain. The effects of M_2 on the velocity profile are shown in Figure 4.15, and it can be clearly seen that the magnitude of M_2 determines the steepness of the gradient in the z direction within the channel. This suggests that a condition

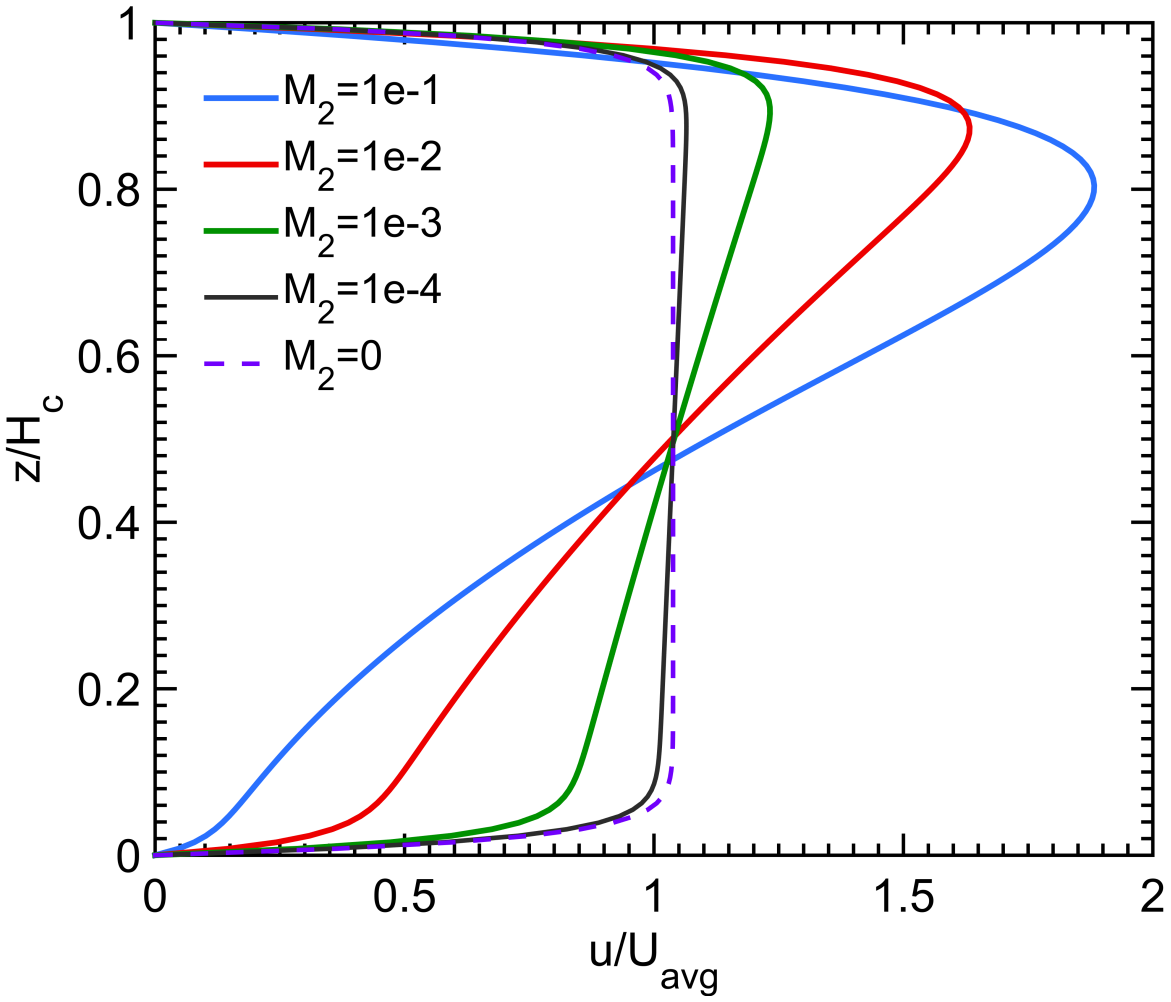

Figure 4.15: Velocity Profile as a Function of M_2

for the accuracy of the VAT momentum equation for variable porosity in the z-direction is

$$M_1 \ll 1, \quad M_2 \ll 1 \tag{4.2.6}$$

Eqn. (4.2.5) shows that the M_2 is a product of M_1 and the porosity gradient, therefore Eqn. (4.2.6) states that the aspect ratio of the channel has to be large, and porosity gradients have to be small. The determination of the limiting value of M_2 will be discussed in Section 4.2.3, but first, it is shown that when the conditions given are satisfied, the solution is indeed accurate.

4.2.2 Validation

A set of numerical experiments are carried out for cases in which Eqn. (4.2.6) is satisfied. The friction factor and Nusselt number obtained are compared to the VAT model to ensure that the two match. Five trapezoidal micro-channels were designed in such a way that the porosity gradient changes but Eqn. (4.2.6) is always satisfied. The geometry of the five micro-channels is given in Table 4.4. The Reynolds number, defined using the commonly

Table 4.4: Geometry for Low M_2 Trapezoidal Micro-channels

$\boldsymbol{L[mm]}$	$\boldsymbol{W[mm]}$	$\boldsymbol{H_c[mm]}$	$\boldsymbol{p_y[mm]}$	$\boldsymbol{w_b[mm]}$	$\boldsymbol{w_t[mm]}$	$\boldsymbol{\Delta\varepsilon_f}$
50	50	4	2.5	0.25	0.25	0
50	50	4	2.5	0.25	0.75	0.2
50	50	4	2.5	0.25	1.25	0.4
50	50	4	2.5	0.25	1.75	0.6
50	50	4	2.5	0.25	2.25	0.8

used definition of hydraulic diameter (see Eqn. (4.2.7)) and the average intrinsic velocity, was kept fixed at 1100.

$$D_h = \frac{2l + w_b + w_t}{H^{(w_b+w_t)}/_2} \tag{4.2.7}$$

l is the length of the sides of the trapezoidal channel. The Nusselt and friction factor were defined as follows

$$Nu = \frac{q'' D_h}{(T_{b,avg} - T_{in})\, k_f}, f = \frac{\Delta P}{{}^1/_2 \rho \left(\langle u \rangle^f \right)^2} \tag{4.2.8}$$

The friction factors obtained using CFX and the VAT model, along with their percent difference, as a function of the porosity gradient are shown in Figure 4.16. It can be seen

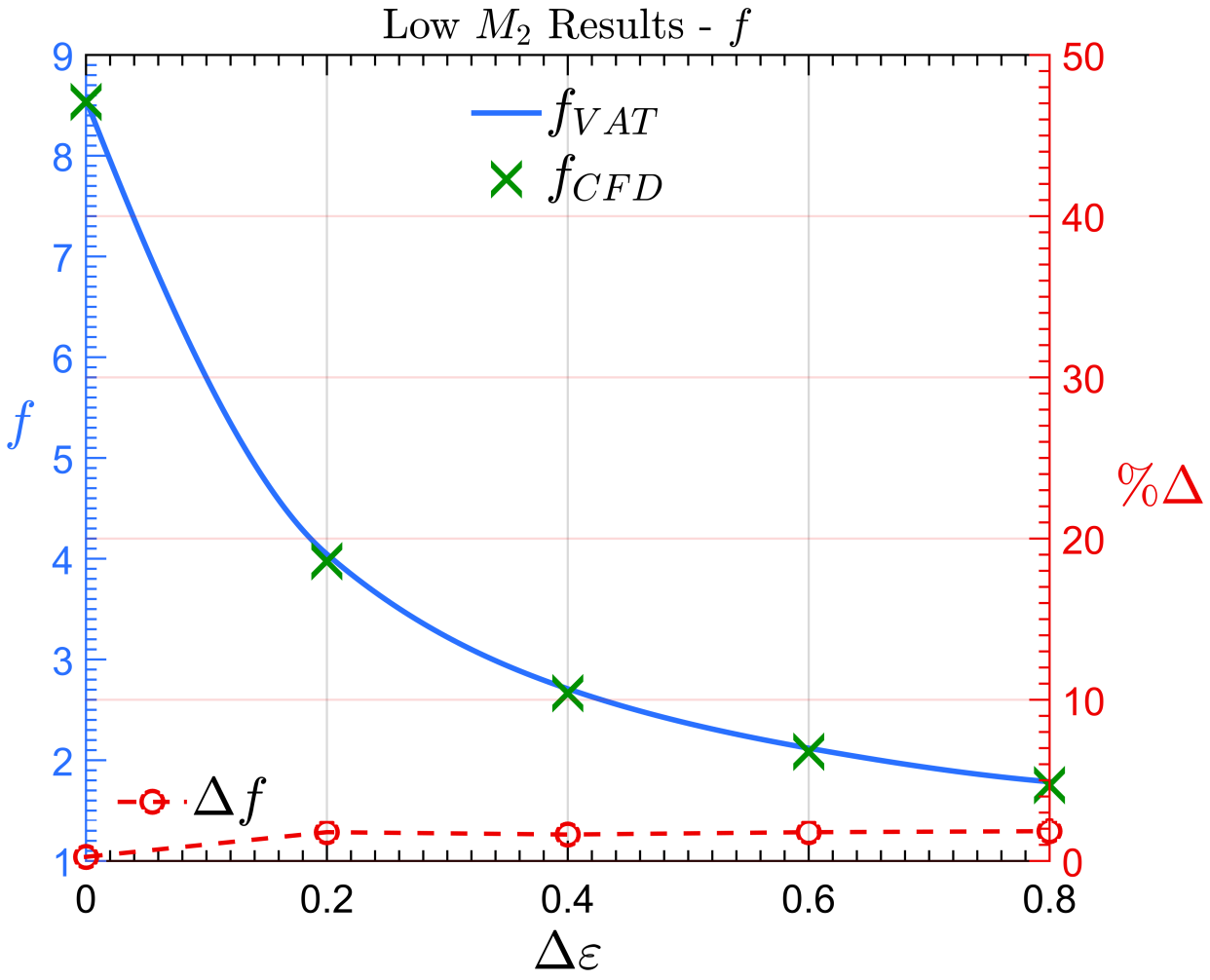

Figure 4.16: Comparison of CFD and VAT Friction Factor Predictions for Trapezoidal Microchannels with Low M_2

that, as hypothesized, the VAT model is very accurate over the entire range of porosity gradients, with a maximum error of about 2%. The results for the Nusselt number are shown in Figure 4.17, and once again the VAT model accurately predicts the behavior of the

system. This shows that indeed, when Eqn. (4.2.6) is satisfied, the VAT model can effectively

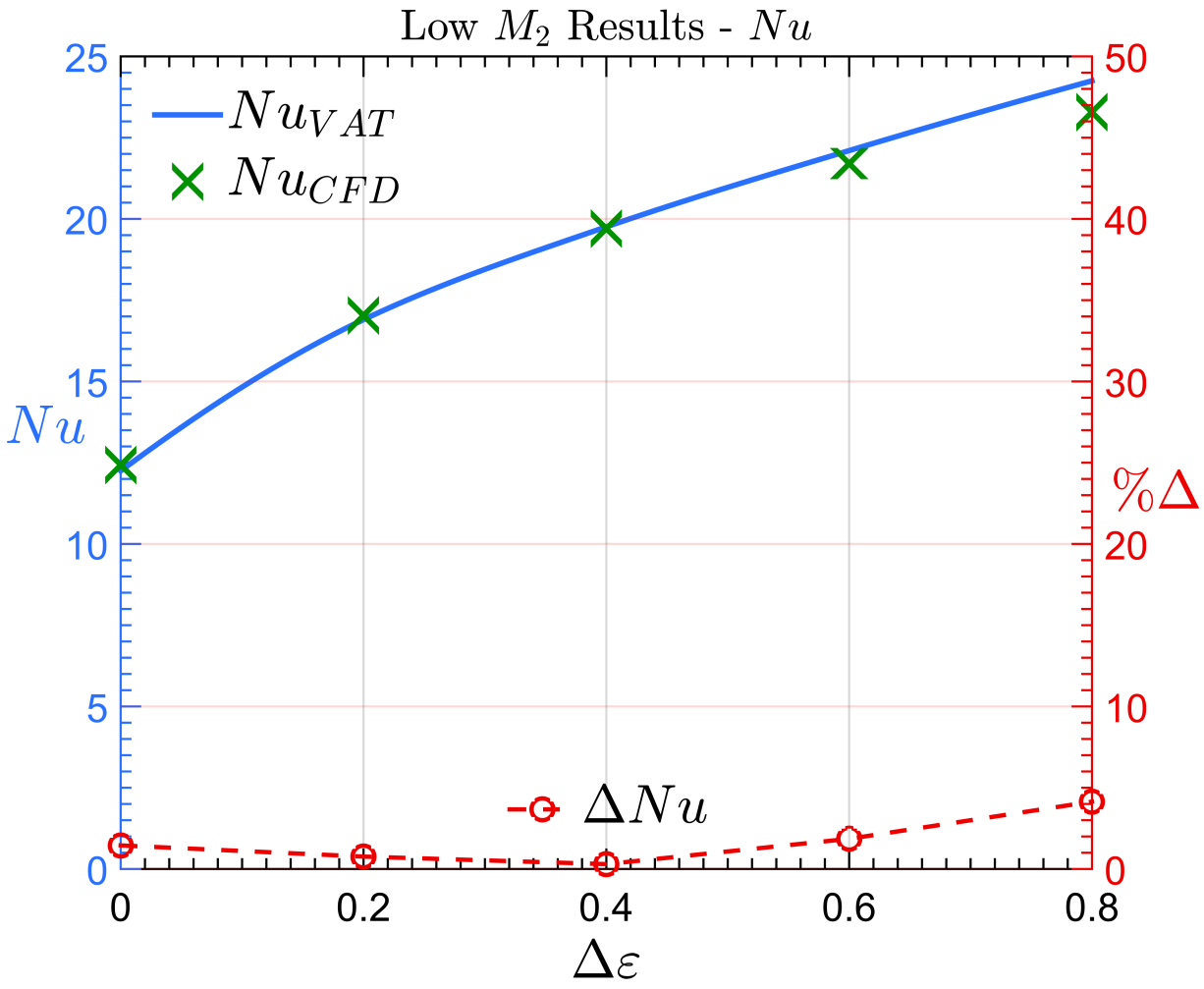

Figure 4.17: Comparison of CFD and VAT Nusselt Number Predictions for Trapezoidal Microchannels with Low M_2

predict the behavior of the system.

4.2.3 Determination of Limits on M_2

Now that it has been shown that the solution is accurate for low values of M_2, it is of interest to show that M_2 is indeed the limiting parameter for the accuracy of the VAT model, and to determine its limiting value. In order to achieve this, the previous numerical experiments are repeated by repeating the study for the larges porosity gradient (last configuration in

Table 4.4) and varying its height. Effectively, this process varies M_2, which allows us to study the limits of applicability.

The comparison of the friction factors and Nusselt number obtained using CFX and the VAT model, along with their percentage difference, are shown in Figure 4.18 and Figure 4.19, respectively. It can be seen that the error seems to grow quadratically as a function of

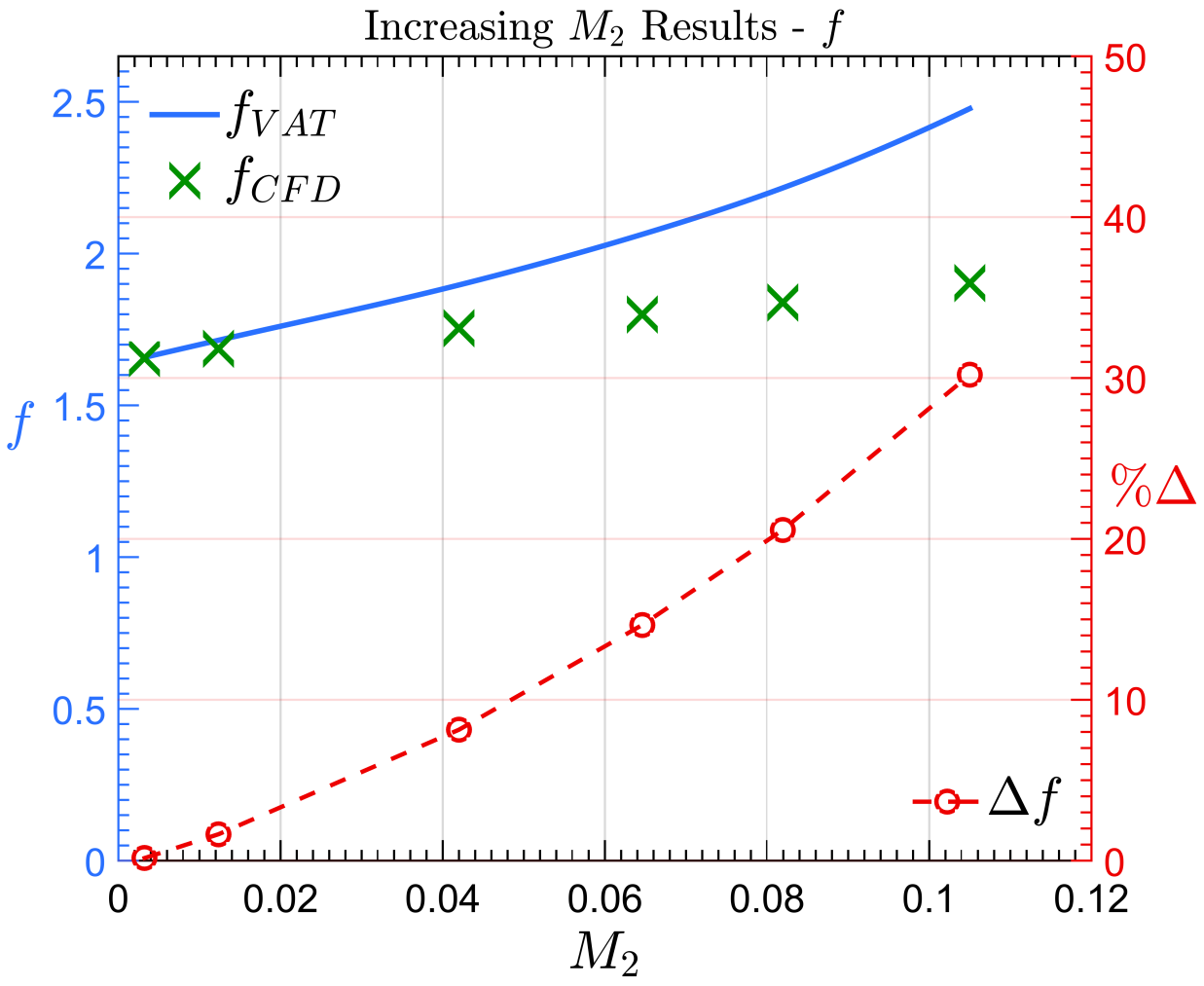

Figure 4.18: Comparison of CFD and VAT predicted friction factors as a function of M_2

M_2. If an error of about 10% is deemed as the bounding value, it seems that the limit of applicability of the VAT equation is given by

$$M_2 < 0.05 \tag{4.2.9}$$

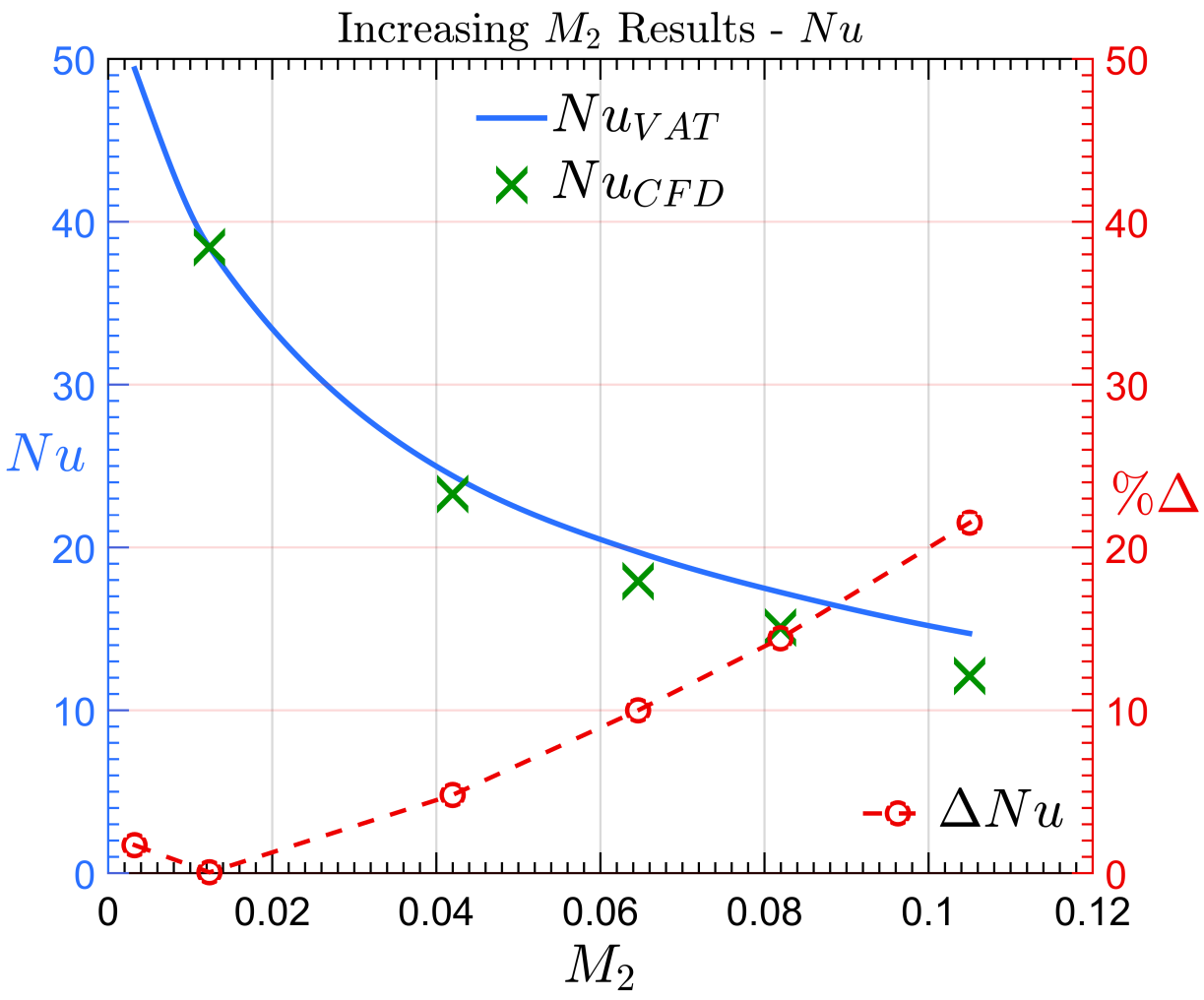

Figure 4.19: Comparison of CFD and VAT predicted Nusselt Number as a function of M_2

Therefore, it has been shown that the value of M_2 will determine the validity of the VAT model for geometries with porosity variations in the z-direction.

4.3 Heat Sinks with Variable Geometry in Streamwise Direction

In this section, the accuracy and limits of applicability of the VAT model for heat sinks with porosity variations in the x-direction is considered. These types of heat sinks include converging and diverging micro-channels, and pin fin heat sinks with variable diameter in the x-direction. The determination of parameters that define the accuracy of the model is carried out first. It is then shown that the model is accurate for low values of the given parameter by comparison with numerical experiments. A limit of the value is then determined by exploring the increase in error as a function of the limiting parameter.

4.3.1 Limiting Parameters

For porosity variations in the x-direction, the VAT equations derived in Chapter 3, become

$$M_1 \frac{\partial^2 \langle u \rangle}{\partial z^2} - \left[S_w f - M_3 \frac{\partial \varepsilon_f}{\partial x} \right] \langle u \rangle^2 = \varepsilon_f \frac{d \langle p_f \rangle^f}{dx} \tag{4.3.1}$$

$$F_1 \langle u \rangle \frac{\partial \langle T_f \rangle^f}{\partial x} = F_2 \frac{\partial}{\partial x} \left(\varepsilon_f \frac{\partial \langle T_f \rangle^f}{\partial x} \right) + F_3 \frac{\partial}{\partial z} \left(\varepsilon_f \frac{\partial \langle T_f \rangle^f}{\partial z} \right) + h S_w \left(\langle T_s \rangle^s - \langle T_f \rangle^f \right) \tag{4.3.2}$$

$$S_1 \frac{\partial}{\partial x} \left(\varepsilon_s \frac{\partial \langle T_s \rangle^s}{\partial x} \right) + S_2 \frac{\partial}{\partial z} \left(\varepsilon_s \frac{\partial \langle T_s \rangle^s}{\partial z} \right) - h S_w \left(\langle T_s \rangle^s - \langle T_f \rangle^f \right) = 0 \tag{4.3.3}$$

Once again, the accuracy of the model will be limited by the VAT momentum equation, therefore only its limits will be considered. Two constants are now present in the VAT momentum equation. The constants in the equations are repeated here for clarity

$$M_1 = \frac{2\varepsilon_{f,c}}{f_c \mathrm{Re}_{dh}} \left(\frac{d_{h,c}}{2H_c} \right)^2, \quad M_3 = \frac{1}{f_c} \left(\frac{d_{h,c}}{2L} \right) \left| \frac{\partial \varepsilon_f}{\partial x} \right| \tag{4.3.4}$$

The characteristic values have been chosen as the average values. The meaning of M_1 has been discussed in detail in the previous sections. The second parameter, represent the ratio of pressure drop (momentum sink/source) due to the porosity variations in the x-direction,

to the pressure drop due to the lower scale geometry. Although, unlikeM_1, this term does not directly multiply a gradient, it will determine the gradients of the velocity in the x-direction, through the mass conservation equation. This is due to the fact that, for variable porosity in x, the pressure gradient is now a function of x and it enforces conservation of mass at each x location. Therefore, porosity gradients in x lead to x variations in the pressure gradient, which in turn leads to velocity gradients in x. Therefore, like in the previous two cases, the value of M_3 quantifies velocity gradients in the x direction. Figure 4.20 shows the centerline velocity as a function of the scaled length for three different values of M_3, and it is clear that M_3 determines the gradients in the x-direction. Large gradients in the

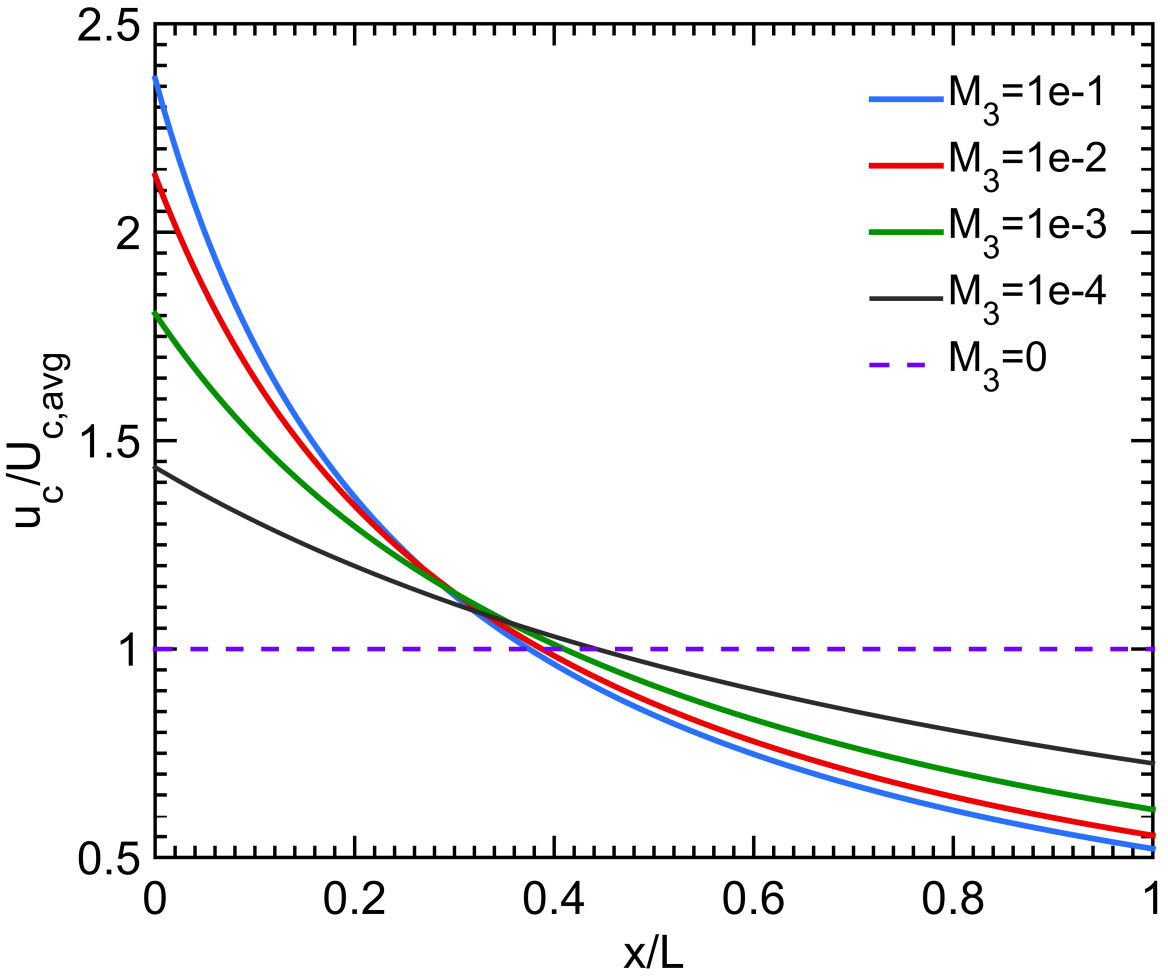

Figure 4.20: Centerline Velocity Profile as a Function of M_3

velocity profile away from the boundaries, imply that there are large variations of the velocity

within an averaging volume, which then implies that the lower scale phenomena are no longer dependent only on the local value of the velocity, and the closure condition breaks down. Therefore, the validity of the VAT momentum equation for variations in the x-direction is that the gradients in velocity induced by these variations, are relatively small. Since the parameters M_1 and M_3 quantify these gradients, the condition for the applicability of the VAT equations in the presence of porosity gradients in the x-direction is

$$M_1 \ll 1, \quad M_3 \ll 1 \tag{4.3.5}$$

Given the form of the friction factor given in Eqn. (4.0.8), for relatively low Reynolds numbers, M_3 will be proportional to the Reynolds number since the friction factor is inversely proportional to it. As the Reynolds number increases, the friction factor attains a constant value and M_3 will become independent of it. Although, as shown in previous sections, these bounds are not dependent on the geometry, to better understand the physical reasons behind this phenomenon, it helps to think about the case of converging (or diverging) channels. M_3 represents the degree of convergence (or divergence) of the channel, and for high values of M_3, flow upstream will be aware of the downstream conditions. For slowly converging channels, the downstream converging geometry will not significantly affect the downstream flow, and the approximation of the local dependence of the friction factor on the velocity is still accurate. As the gradient of porosity variations increases, the upstream flow starts significantly affecting the downstream conditions and the friction factor is no longer due only to the local flow. The Reynolds number dependence of the condition can similarly be explained. At lower Reynolds number the flow will be more aware of the downstream conditions due to the importance of the viscous effects, while at high Reynolds, inertia will take over and the flow downstream is less affected by the conditions upstream.

4.3.2 Validation

The hypothesis given in Eqn. (4.3.5) is first confirmed by first ensuring that when it is actually satisfied, our model can predict correctly the physics of the problem. This is carried out by carrying out a series of numerical experiments for converging and diverging channels

with various porosity gradients, keeping M_3small by adjusting the Reynolds number, and comparing the results with those predicted by the VAT model (M_1 is always kept small). The geometric and physical parameters of this study for converging and diverging channels are given in Table 4.5 and Table 4.6, respectively.

Table 4.5: Geometries and Reynolds Numbers for Low M_3 Converging Channels Study

$L[mm]$	$W[mm]$	$H_c[mm]$	$p_y[mm]$	$w_i[mm]$	$w_o[mm]$	$\Delta\varepsilon_f$	Re
50	50	13.5	2.5	2.25	2.25	0.00	850
50	50	13.5	2.5	2.25	1.58	0.268	100
50	50	13.5	2.5	2.25	0.92	0.532	37
50	50	13.5	2.5	2.25	0.25	0.800	35

Table 4.6: Geometries and Reynolds Numbers for Low M_3 Diverging Channels Study

$L[mm]$	$W[mm]$	$H_c[mm]$	$p_y[mm]$	$w_i[mm]$	$w_o[mm]$	$\Delta\varepsilon_f$	Re
50	50	1.5	2.5	0.25	0.25	0.00	850
50	50	2.5	2.5	0.25	0.34	0.036	121
50	50	2.5	2.5	0.25	0.75	0.200	121
50	50	8.5	2.5	0.25	1.4	0.460	51
50	50	15.0	2.5	0.25	2.4	0.860	20

The Poiseuille number f Re is plotted as a function of the porosity gradient for converging channels in Figure 4.21. The Poiseuille number is plotted in this case since the Reynolds number was not kept fixed. It can be seen that the VAT model accurately predicts the pressure drop over the entire range of porosity gradients, and the maximum error is about 4%. The results for diverging channels are shown in Figure 4.22, and once again for low M_3, the values predicted by the VAT model are in excellent agreement with experimental results, with a maximum error of 4%. Now that it has been shown that the code is accurate for cases in which Eqn. (4.3.5) is satisfied, it is of interest to determine what is the limiting value of M_3, after which the VAT approximation exceeds a given accuracy.

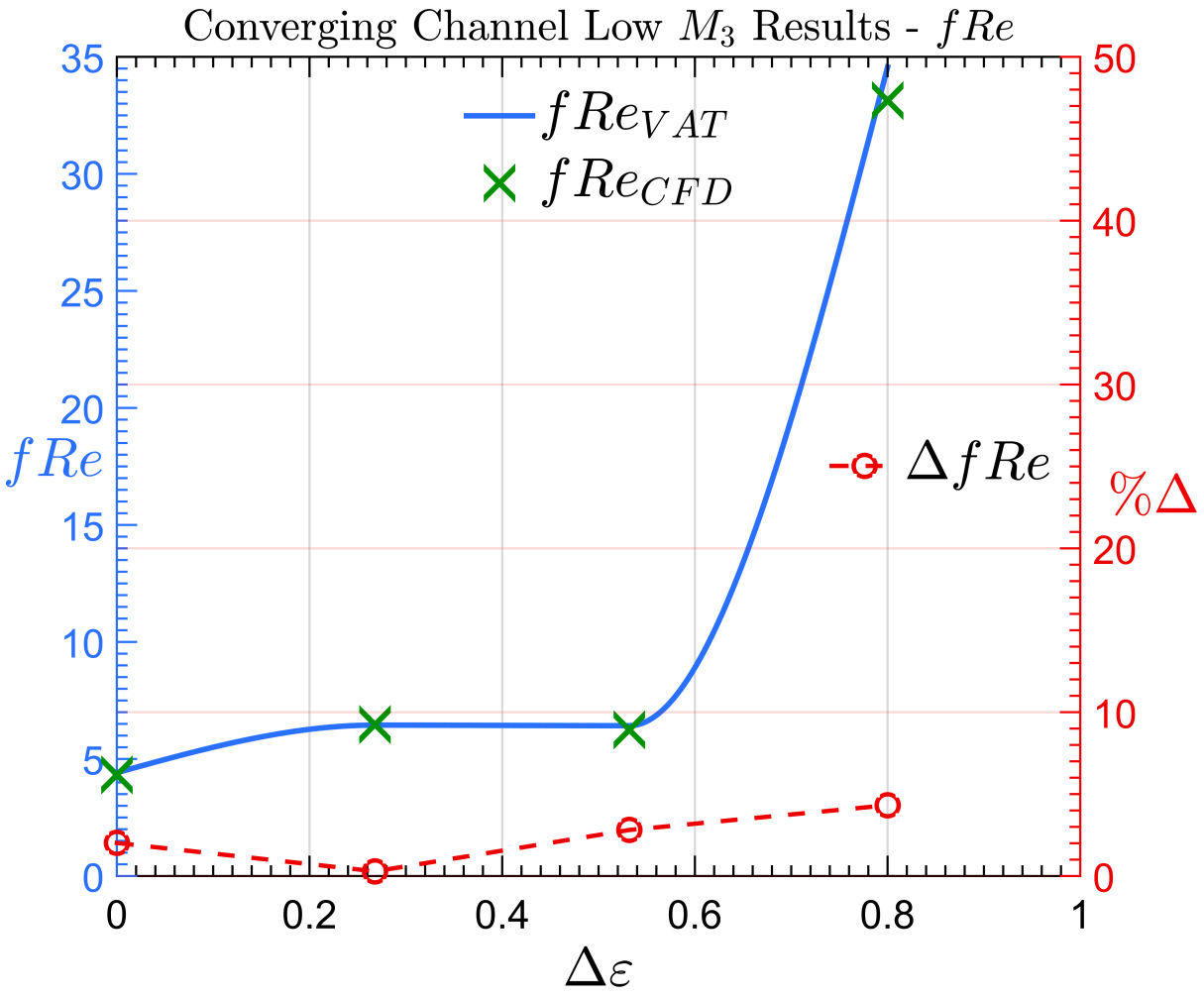

Figure 4.21: Poiseuille Number for Converging Channels as a Function of the Porosity Gradient for Low M_3

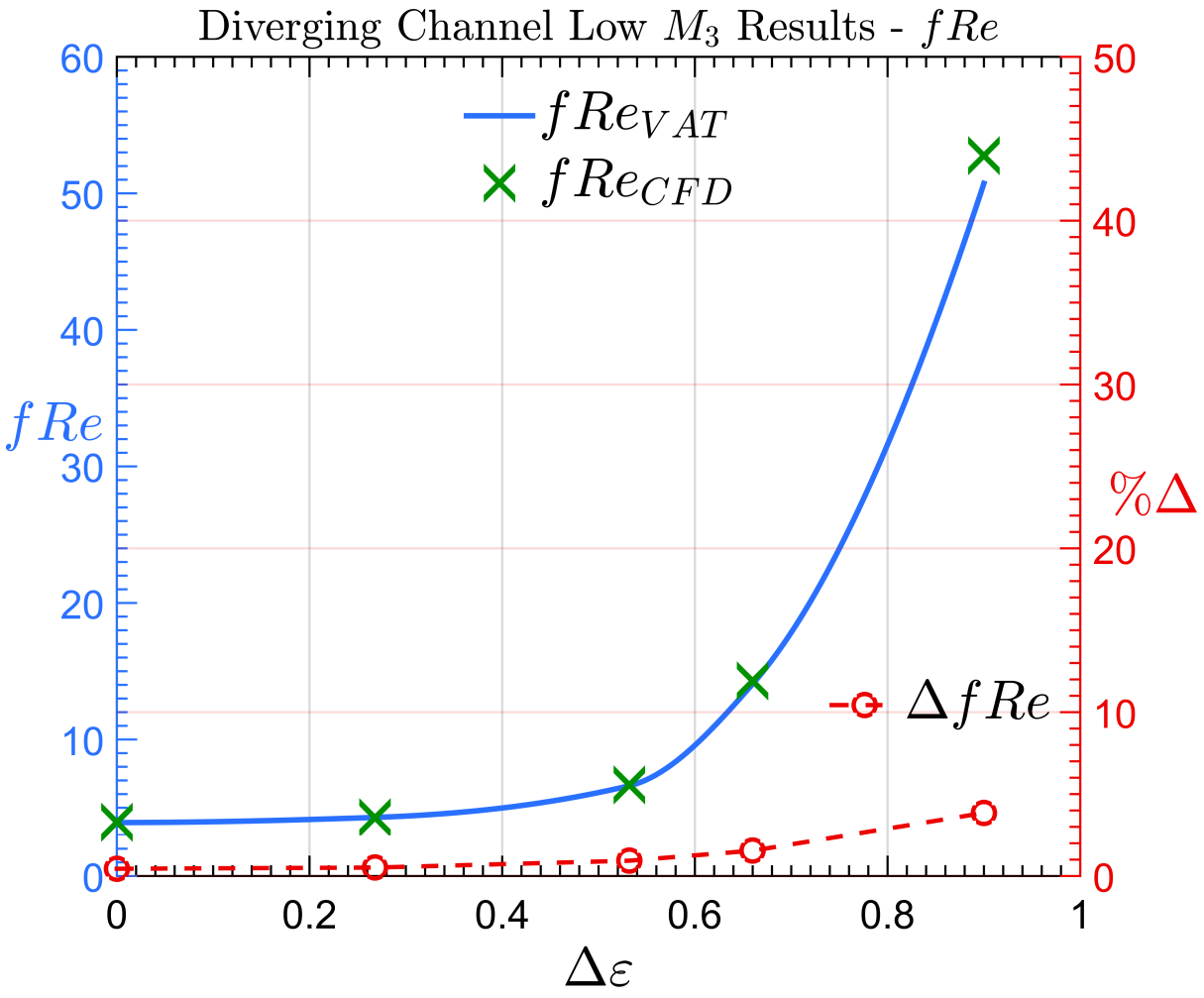

Figure 4.22: Poiseuille Number for Diverging Channels as a Function of the Porosity Gradient for Low M_3

4.3.3 Determination of Limits on M_3

To determine the limiting values, and confirm the Reynolds number dependence, two sets of numerical experiments are carried out and its results are compared to those predicted by the VAT model. First, a diverging channel with a porosity gradient of $\Delta\varepsilon_f = 0.2$ (third geometry in Table 4.6) is chosen and solved for four Reynolds numbers, which leads to variations in M_3 . The values of the Poiseuille number obtained with CFD and the VAT model, along with their percent difference, as a function of M_3 are shown in Figure 4.23. It can be seen,

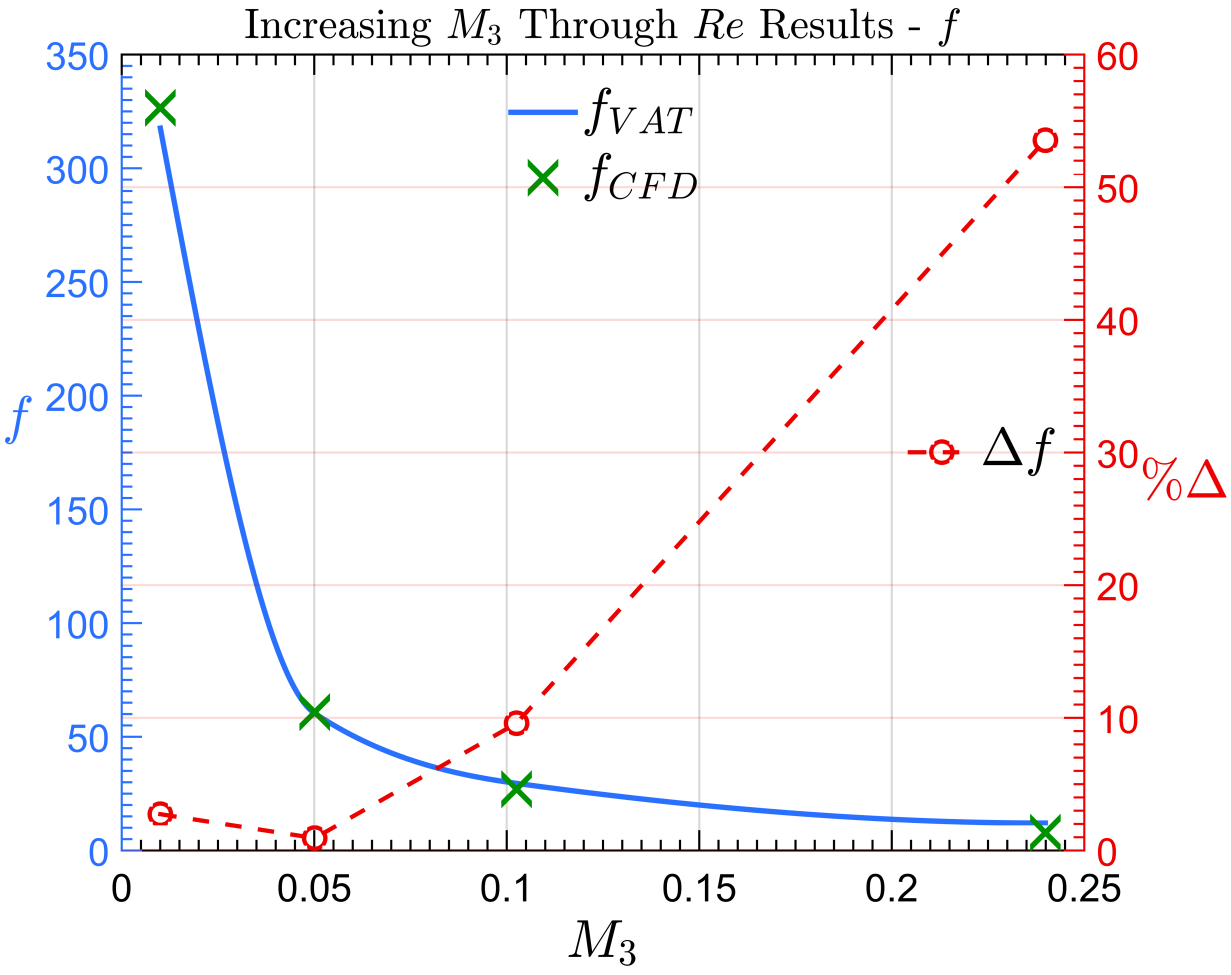

Figure 4.23: Poiseuille Number for Diverging Channels vs M_3 for Varying Reynolds Number

that as expected, the accuracy of the VAT model decreases with increasing M_3. If 10% is

chosen as an acceptable error in the model, a limiting condition is given by

$$M_3 < 0.1 \tag{4.3.6}$$

Next, to confirm the dependence of M_3 on the porosity gradient, the study given in Table 4.5, is repeated but this time the Reynolds number was kept fixed at 121. The results for the Poiseuille number predicted by the VAT model and the numerical experiments, along with their percent difference, as a function of M_3 are shown in Figure 4.24. As predicted, the

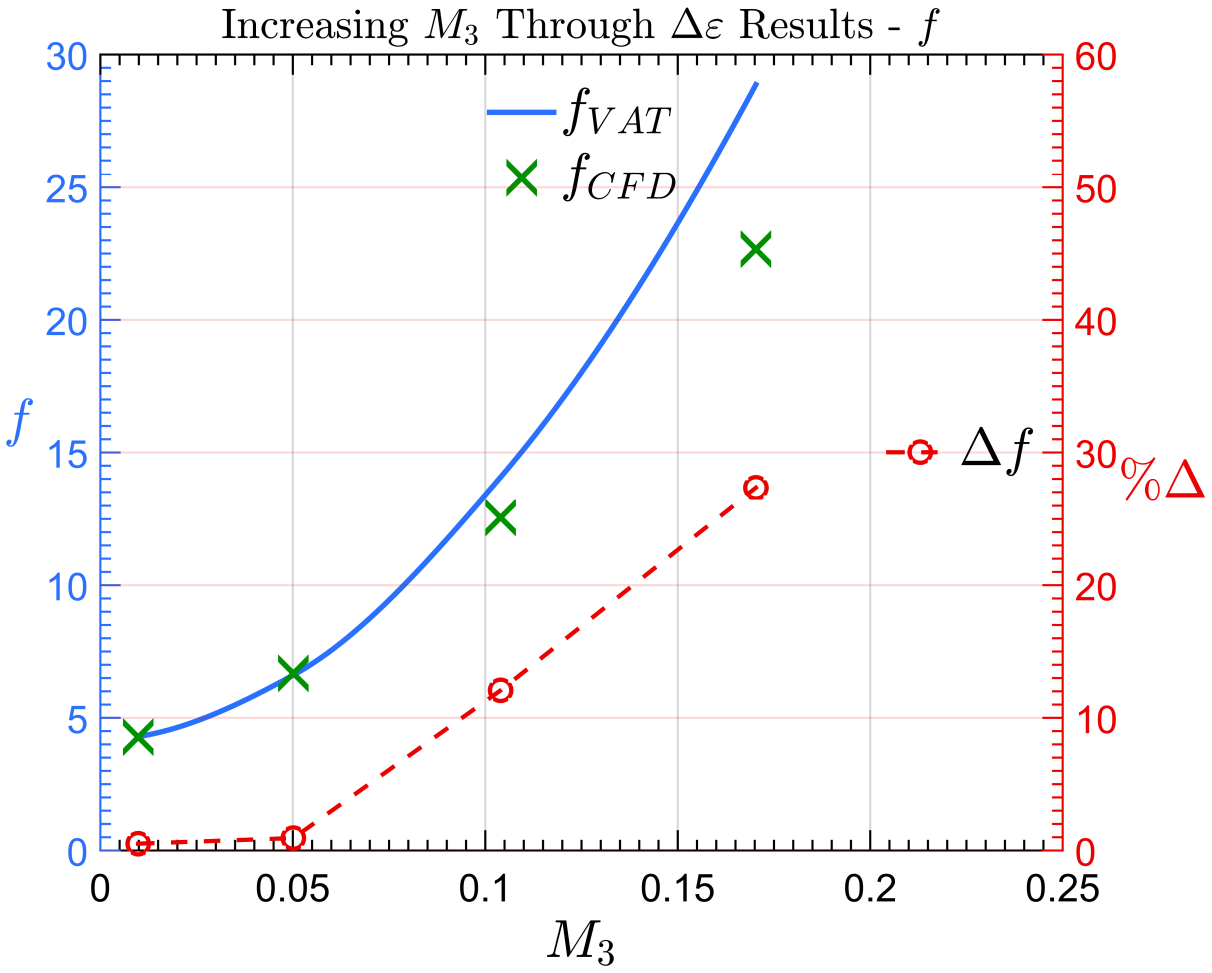

Figure 4.24: Poiseuille number for Converging Channels vs M_3 by Varying Porosity Gradient

VAT model only for low values of M_3, and the limit for a 10% accuracy in the results is given by same condition obtained by varying the Reynolds number. Although the study was not repeated for staggered pin fin heat sinks, it can be expected that the same behavior would

be observed, since the VAT model is itself independent of geometry, and therefore also its limits should be.

CHAPTER 5

Spatially Evolving Micro-channel Heat Sinks Optimization

The main goal behind the development of the VAT model described in the previous sections, is to exploit its computational efficiency to explore design parameters that will lead to a more efficient heat rejecting device. To this end, in this section the developed code is coupled to a population-based Genetic Algorithm (GA) to determine geometric that will optimized the performance of a micro-channel heat sink.

Genetic Algorithms are a subset of the larger group of optimization algorithms known as evolutionary algorithms. The name genetic algorithm, as well as the first application of the GA, is attributed to the pioneer work of Bagley [161]. In 1975, De Jong and Holland [162]carried out the first studies entirely dedicated to GAs, which was then significantly advanced in the 80s by Grefenstette [163], Baker [164] and Goldberg [165]. A complete review and description of GAs and other evolutionary computational methods can be found in Ashlocks book [166], and many other volumes on the subject. The application of GAs to heat transfer problems is more recent, and started approximately with the work by Queipo [167]. Since then, the number of publications on the subject was limited until 2005 when the GA start growing significantly in popularity in the heat transfer field. The major drawback of GAs for heat transfer application is the large number of function evaluations that are required by the algorithm; since each function evaluation implies the numerical solution of a complex CFD/FEM model, the required computational time can be prohibitive. Therefore, the recent popularity of the application of GAs to heat transfer problems is largely attributed to the improvement in computational efficiency of CFD/FEM methods, along with the advent of commercially available parallel processors.

Several researchers have tried to bypass the time-consuming performance evaluations of heat sinks using CFD, by using resistance models or algebraic correlations [168, 169, 170]. In these studies, the negligible computational time required for each function evaluation allowed the exploration of several parameters with wide parameter bounds. However, these models cannot effectively take into account the conjugate heat transfer phenomena in a heat sink, and their accuracy is limited. Other studies have been carried out by coupling a GA directly to a CFD/FEM solver [167, 171, 172, 173], which allows for a very accurate determination of the physics of the problem. Nonetheless, the extensive time required for the evaluation of each design implies that only small ranges and limited number of design parameters can be considered. In another effort to reduce computational times, Gosselin et al [174, 175] have used porous media models to optimize heat transfer in heat sinks. The use of a porous media approach allowed these researchers to reduce the computational time, and therefore expand the search space and consider the effect of several parameters on the heat transfer. Yet, the porous media models employed are based on empirical correlations and do not take into account the limitation of the model used, which could lead to physical inaccuracies. Most recently, Geb [138] used a VAT model and a GA to find a plane fin heat sink that exceeded state-of-the-art currently available heat sinks. In this work, the combination of the expanded VAT model and GA is used to determine the effects of geometry variations on heat sink efficiency.

A short description of the idea behind GAs is given here. This is meant to give the reader a general picture of how a GA leads to an optimum solution, and it is not meant to be a through description of it. For more detail refer to [176]. The GA is based on the Darwinian assumption of survival of the fittest. Each heat sink is treated as an individual. Each individual has its own DNA, which is a combination of its chromosomes (the design parameters). The length of the DNA is then equal to the number of design parameters that define each individual. Each individual is also assigned a fitness parameter, which for minimization problems can be seen as the negative of the function to be minimized (such as the fittest individuals have the largest value of the fitness function). An initial population of size N_P is generated as a random combination of the design parameter within the specified range.

Each individual is then assigned a fitness parameter by evaluation of the objective function. The population is then ranked, from fittest to least fit, and the top 5% of the population is advanced to the next generation. This step is called elitism. The rest of the population in the next generation is created by crossover and mutation. In the crossover process, two parents are taken and mated, and their child is a combination of their chromosomes. In the mutation process, children are created by mutating some of its parents chromosomes. A graphical explanation of elitism, crossover and mutation are shown in Figure 5.1. The

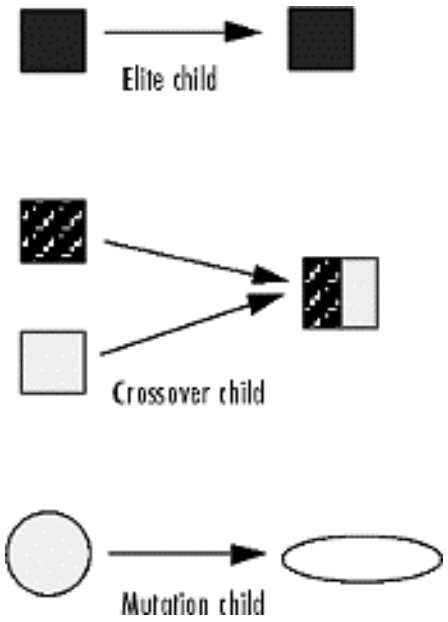

Figure 5.1: Graphical Explanation of Elitism, Crossover and Mutation [177]

elite children, along with the children obtained through crossover and mutation define a new population that takes the place of the previous population, and the process is repeated until a stopping criterion is met. A graphical representation of the GA is shown in Figure 5.2, In this work, the stopping criteria are either that the optimal (scaled) objective function has changed less than 10^{-6} over the last 20 iterations, or that the number of generations is less than N_G. If the second stopping criteria is met, it implies that an optimal solution might have not been reached yet, and the problem needs to be defined better, of the maximum number of generations needs to be increased. The definition of the fitness parameter for a heat sink is dependent on the goal of the design. Different researchers have defined different

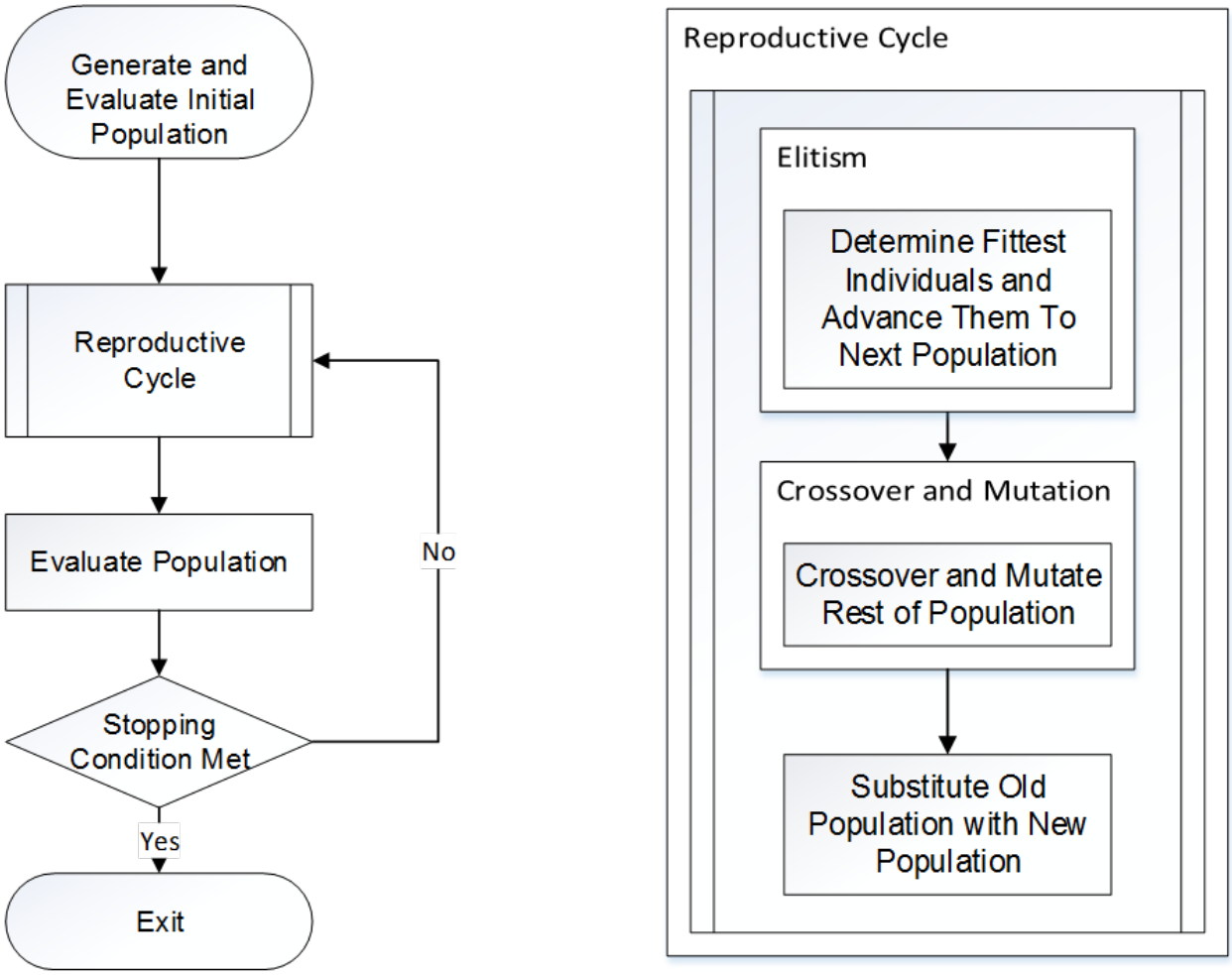

Figure 5.2: Schematic of Genetic Algorithm

efficiency parameters such as cost, entropy generation, thermo-hydraulic efficiency, thermal resistance etc. In this work, two types of commonly chosen optimization parameters will be minimized, entropy generation and thermal resistance. Entropy generation for a heat sink has been defined by Bejan [178],

$$\dot{S}_{gen} = Q\left(\frac{1}{T_{in}} - \frac{1}{T_b}\right) + \frac{PP}{\rho T_{in}} = \frac{Q^2}{T_{in}T_b}R_{th} + \frac{PP}{\rho T_{in}} \tag{5.0.1}$$

where pumping power and thermal resistance are defined as

$$R_{th} = \frac{T_{b,\max} - T_{in}}{Q}\left[\frac{K}{W}\right], \quad PP = N_c \dot{m} \Delta P\,[W] \tag{5.0.2}$$

and N_c is the number of channels in the heat sink and it will be equal to $N_c = p_y/W$. For fairness it should be pointed out that in its physical sense entropy generation is based on the

Table 5.1: Heat Sink Parameters Fixed in Optimization Studies

$\boldsymbol{L}\,[\boldsymbol{mm}]$	50
$\boldsymbol{W}\,[\boldsymbol{mm}]$	50
$\boldsymbol{T_{in}}\,[\boldsymbol{K}]$	300
$\boldsymbol{q}\,[\boldsymbol{W/m^2}]$	1.60E+05
$\boldsymbol{\Delta P}\,[\boldsymbol{Pa}]$	1000
Solid Material	Copper
Fluid	Water

average base temperature of the base $T_{b,avg}$, not on its maximum value $T_{b,\max}$ as defined here. Nonetheless, in this study the physical value of entropy generation is not of interest, but it is considered as a parameter that combines hydraulic and thermal performance. In addition, to quantify the effect of different geometries on the ability of the heat sink to spread heat, a hot spot factor (HSF) is defined as

$$HSF = \frac{T_{b,\max} - T_{f,avg}}{T_{b,avg} - T_{f,avg}} \tag{5.0.3}$$

This is a parameter commonly used in nuclear studies [179] to quantify temperature gradients within a reactor. The same concept is applied here to quantify temperature gradients that would be found on the heat generating component. Large temperature gradients on electronic components lead to thermal stresses, local electron migration and other performance degradation mechanisms, therefore a low value of the HSF is desirable. In the subsequent optimization studies, the HSF will not be taken into account in the definitions of the fitness function, therefore any improvement in spreading are only a by-product of the optimal configurations. For each geometry, two optimization studies will be carried out. In all cases, the heat sink materials, the pressure drop, the heat flux, the inlet temperature as well as the length and width of the heat sink are kept fixed. These parameters are given in Table 5.1. The entropy generation optimization study will be used to determine whether heat sinks with variable geometries are more efficient from an overall energy point of view, which takes into account a combination of pressure drop and heat transfer simultaneously. The thermal resistance optimization study will determine whether heat sinks with variable geometry are

a more efficient way to improve the heat transfer performance of the system. MATLABs global optimization toolbox GA was used, and an example script is given in Appendix D.

5.1 Straight Channel Heat Sink Optimization

In order to fairly compare the performance of heat sinks with variable geometry, the optimization study is first carried out for straight micro-channels (see Figure 5.3). For straight channels, the effect of four parameters on the fitness function is considered: the height of the channels H_c, the transverse pitch p_y, the width of the channel w and the thickness of the base t_b. The range of parameters is selected based on experience and other publications, and is given in Table 5.2. The constraints of the problem are given by the geometric constraint

Table 5.2: Range of Geometric Parameters for Constant Straight Micro-channels

	min	max
$\boldsymbol{H[mm]}$	2	6
$\boldsymbol{p_y[mm]}$	0.3	2.5
$\boldsymbol{w[mm]}$	0.1	1
$\boldsymbol{t_b[mm]}$	1	5

that the thickness of the fins has to be larger than a minimum value

$$p_y - w \leq D_{\min} = 0.1\,mm \tag{5.1.1}$$

and, following the discussion of the limits on the parameter M_1, the aspect ratio has to be greater than 3,

$$\frac{H_c}{w} > 3 \tag{5.1.2}$$

It was determined that a 128x128 grid provided an optimal balance between speed and accuracy for straight channels, and it will be therefore used in the optimization study. The maximum number of generation N_G was set at 200, and the initial population N_p at 100. First, the optimization study is carried out to minimize entropy generation. The GA found an optimal solution after 83 generations, and the evolution of the geometrical configuration

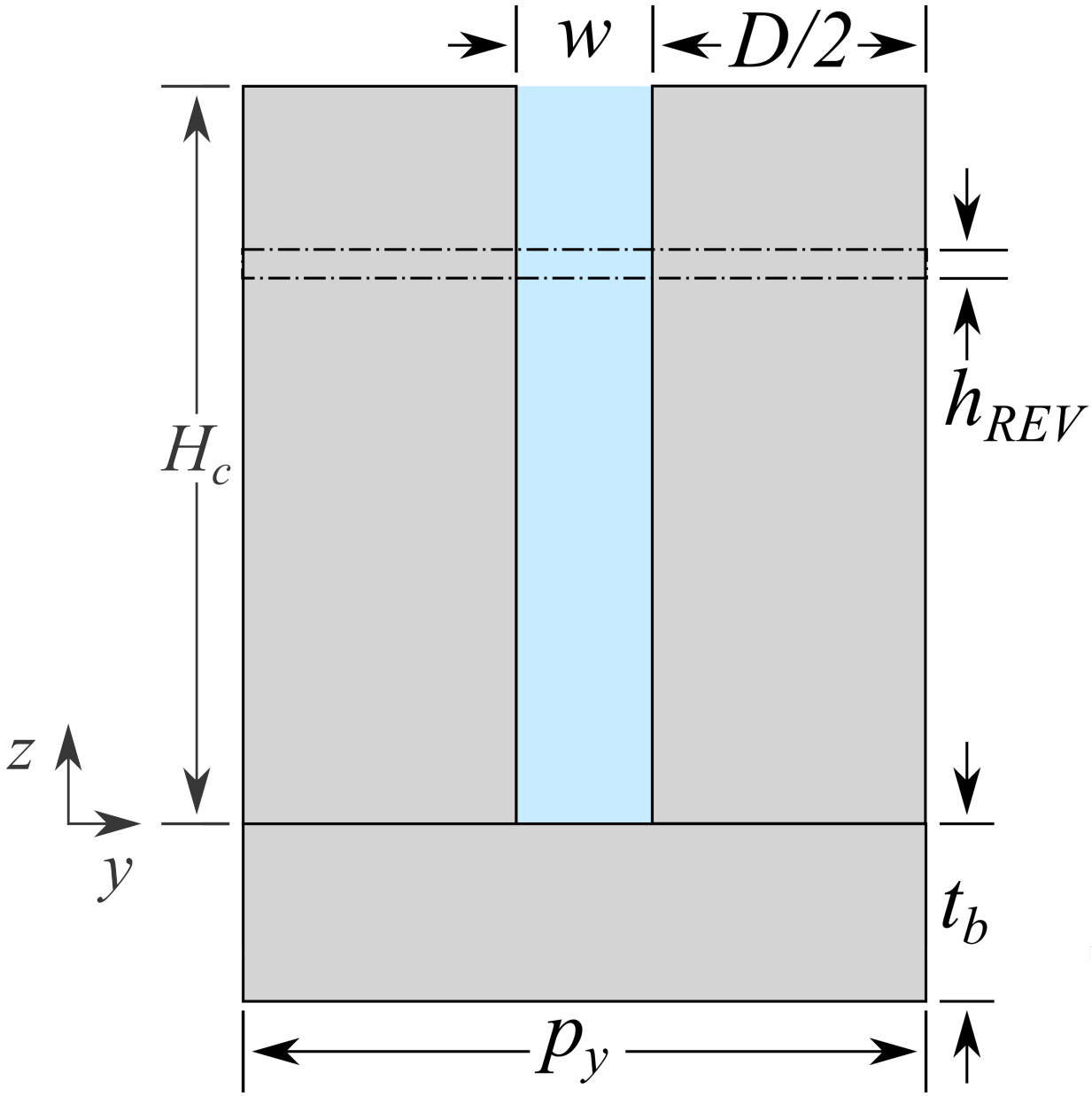

Figure 5.3: Straight Micro-channel Geometry Cross Section View

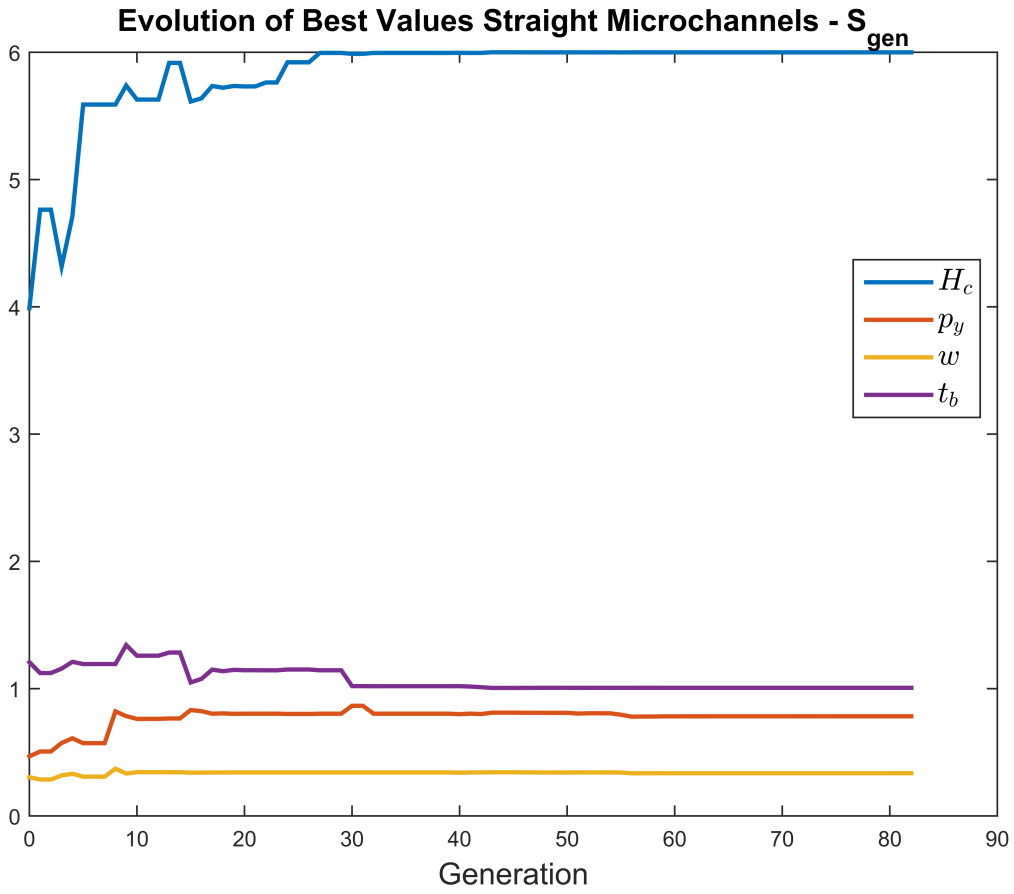

Figure 5.4: Evolution of Geometric Parameters of Minimum Entropy Generation Individual at Each Generation Straight Channels

of the fittest individual at each iteration is shown in Figure 5.4. The optimal configuration is found to be

$$\begin{aligned} H_c &= 6 \\ p_y &= 0.78 \\ w &= 0.34 \\ t_b &= 1 \end{aligned} \tag{5.1.3}$$

The optimal configuration selected has a minimum entropy generation value of $\dot{S}_{gen} = 2.77 \times 10^{-2}$ $[W/K]$, which corresponds to a pumping power $PP = 1.67\,W$, a thermal resistance of $R_{th} = 1.66 \times 10^{-2}$ $[K/W]$, and a hot spot factor of $HSF = 1.49$.The optimizer always chooses the minimum base thickness in the specified range. This is due to the fact that, for constant heat flux, the spreading effect of a thicker base is negligible, however large thicknesses lead to larger temperature gradients and increase the resistance in the base. The optimizer also chooses the maximum height since high channels will increase the heat transfer area without significantly affecting the pressure drop. The rest of the parameters are chosen within the specified range, which indicates that our bounds were properly selected.
Next, the study is repeated by setting the thermal resistance as the fitness parameter. The optimizer found an optimal solution after 69 iterations, and the geometrical configuration of the fittest individual at each generation is shown in Figure 5.5.

The optimal configuration with respect to thermal resistance is found to be

$$\begin{aligned} H_c &= 6 \\ p_y &= 0.74 \\ w &= 0.47 \\ t_b &= 1 \end{aligned} \tag{5.1.4}$$

with a value of the thermal resistance of $R_{th} = 1.33 \times 10^{-2}$ $[K/W]$, and a hot spot factor of $HSF = 1.17$. For the same reason discussed in the previous section, the optimizer chooses again the minimum base thickness. Indeed, this will always be the case for constant heat fluxes, therefore, base thickness will be kept fixed at 1 mm in subsequent studies. To optimize heat transfer, the optimizer chose a larger width and the maximum allowed height, since, for constant pressure drop, these parameters maximize flow speed, and therefore increase the

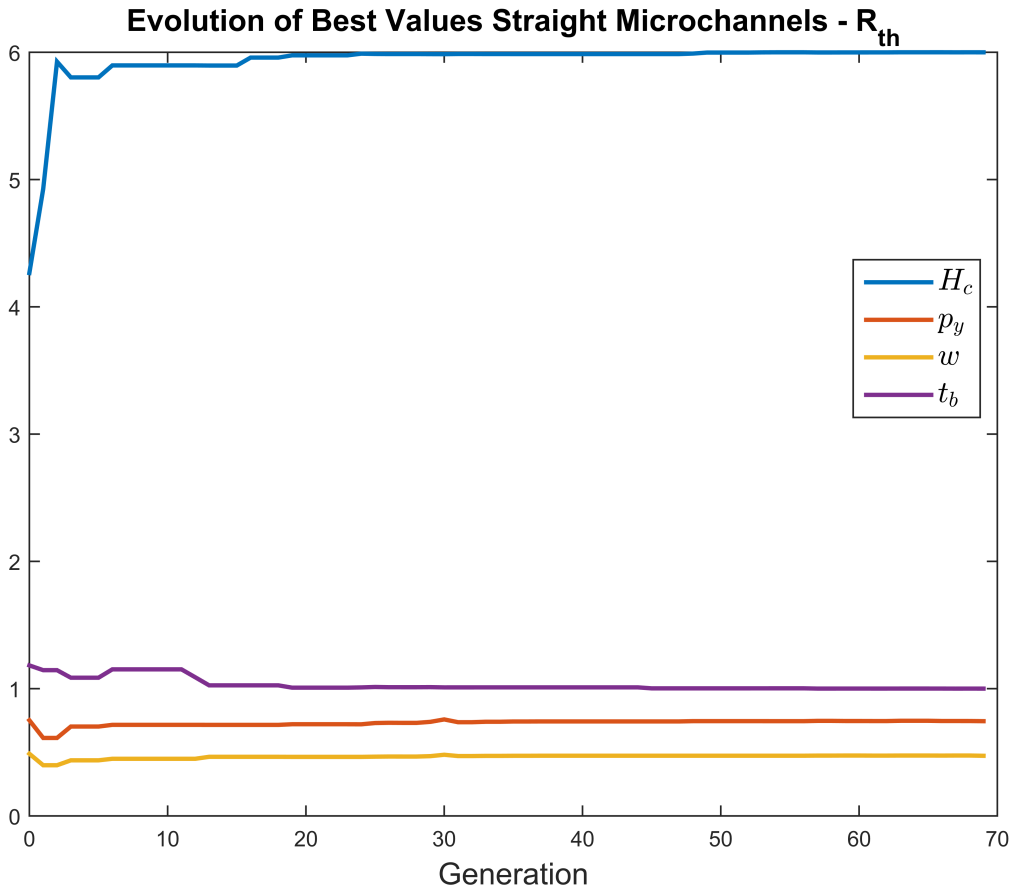

Figure 5.5: Evolution of Geometric Parameters of Minimum Thermal Resistance Individual at Each Generation Straight Channels

heat transfer coefficient. This configuration results in a 20% and 21% improvement in the thermal resistance and hot spot factor, respectively, over the minimum entropy configuration; however, the optimal heat transfer configuration requires a pumping power of $PP = 5.08\,W$, which is a 200% increase. This is due to the fact that, for straight micro-channels, the only way to increase the heat transfer is to squeeze the channel, which leads to a large increase in the pumping power. In both cases the optimal configuration has a high aspect ratio, which corresponds to values of M_1 less than 10^{-3}, therefore the optimal solutions are expected to be accurate. This also suggests that the limit on M_1 plays no role in the optimization studies.

5.2 Trapezoidal Channel Heat Sink Optimization

The optimization study is now repeated for trapezoidal micro-channels to determine if geometry changes in the z direction can improve the efficiency and heat transfer of the system. The number of parameters to be optimized in the problem now increases by one since two widths are now available: bottom and top width, w_b and w_t respectively (see Figure 5.6). In practice, since the base thickness was removed as a parameter, the number of variables to be optimized stays constant. The range of the two widths is kept the same as in the study for straight micro-channels (see Table 5.3). The constraints on the problem are given by

Table 5.3: Range of Parameters for Trapezoidal Micro-channel Optimization Studies

	min	max
$\boldsymbol{H[mm]}$	2	6
$\boldsymbol{p_y[mm]}$	0.3	2.5
$\boldsymbol{w_b[mm]}$	0.1	1
$\boldsymbol{w_t[mm]}$	0.1	1
$\boldsymbol{t_b[mm]}$	1	5

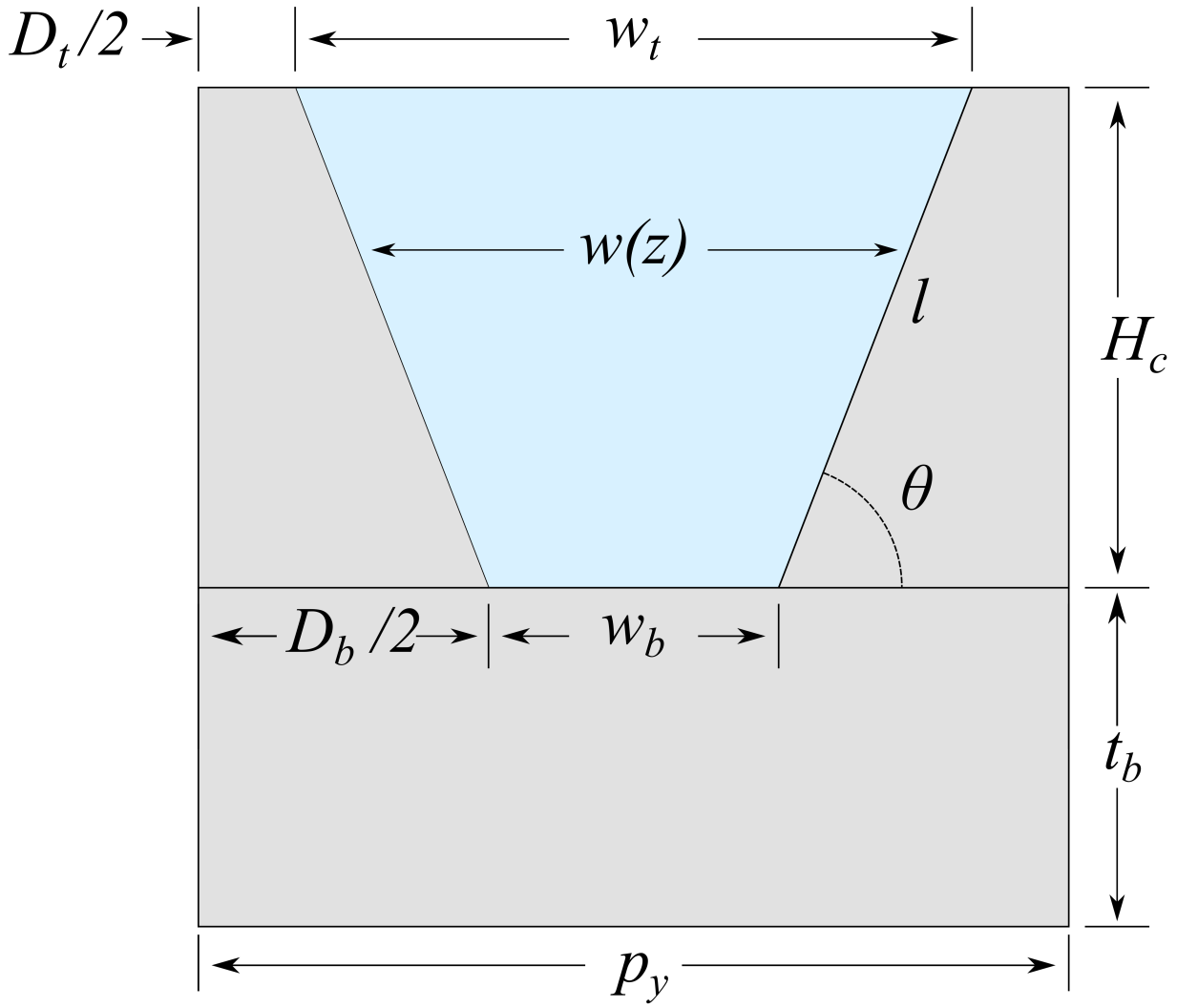

Figure 5.6: Schematic of Trapezoidal Micro-channel Geometry (Cross Section)

choosing a minimum fin thickness (equal to the straight channel one),

$$\begin{aligned} p_y - w_b &\leq D_{\min} = 0.1\,mm \\ p_y - w_t &\leq D_{\min} = 0.1\,mm \end{aligned} \tag{5.2.1}$$

and a maximum aspect ratio greater than 3, so that the condition on M_2discussed in the previous section is satisfied,

$$\frac{H_c}{w_b} > 3, \frac{H_c}{w_t} > 3 \tag{5.2.2}$$

It was found that again a 128x128 grid provides a good balance between accuracy and computational speed. Since the number of parameters is the same as in the previous discussion, the population size N_p is again set as 100, and the maximum number of iteration $N_G$is set at 200.

The GA optimizer is ran first using the entropy generation as the fitness parameter, and a converged solution was found after 103 generations. The evolution of the geometric parameters for the fittest individual at each generation is given in Figure 5.7. The values of the optimal solution are

$$\begin{aligned} H_c &= 6.0 \\ p_y &= 0.78 \\ w_b &= 0.36 \\ w_t &= 0.30 \end{aligned} \tag{5.2.3}$$

with a minimum entropy generation $\dot{S}_{gen} = 2.75 \times 10^{-2}$ $[W/K\,]$. This heat sink configuration implies that the pumping power required is $PP = 1.65\,W$, the thermal resistance is$R_{th} = 1.65 \times 10^{-2}$ $[K/W\,]$, and the hot spot factor is $HSF = 1.49$. The optimal solution is a slightly tapered micro-channel with wider channels at the bottom than at the top. The optimizer chooses this configuration because near the top of the fins, the heat transfer is usually weaker because the fin temperature will be close to the inlet temperature. Therefore, a wider channel near the bottom will speed up the flow in these areas and increase the heat transfer at the interface and in the bottom half of the fins, while keeping the pumping power close to its value for straight micro-channels. The difference between this heat sink configuration and the optimal entropy generation configuration with straight channels, is minimal with a reduction in entropy generation of only 0.5%. The pumping power decreases

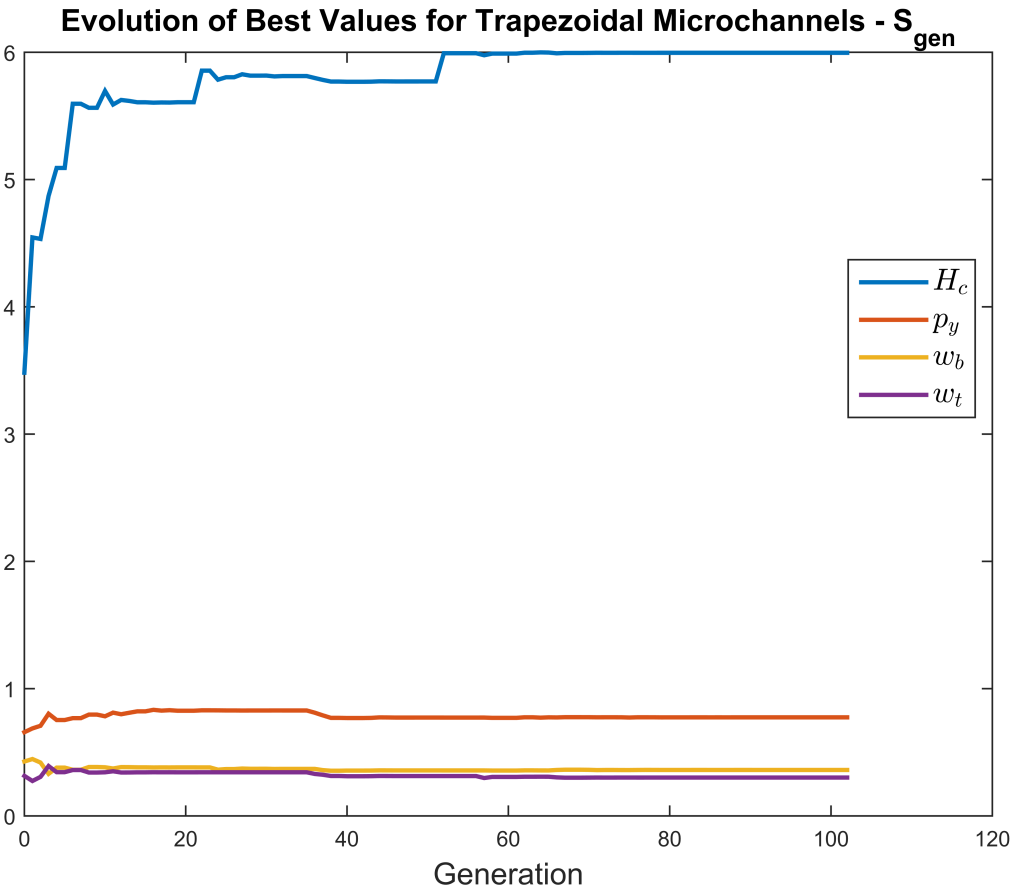

Figure 5.7: Evolution of Geometric Parameters of Minimum Entropy Generation Individual at Each Generation Trapezoidal Channels

by 1.5% while the thermal resistance was reduced by 0.6%. This is a modest improvement in the performance, which suggests that trapezoidal micro-channels do not provide significant improvements in the overall efficiency of the system. The optimization is then repeated taking the thermal resistance as the fitness parameter. The GA found a solution in 66 generations (see Figure 5 8), and the optimal configuration is found to be

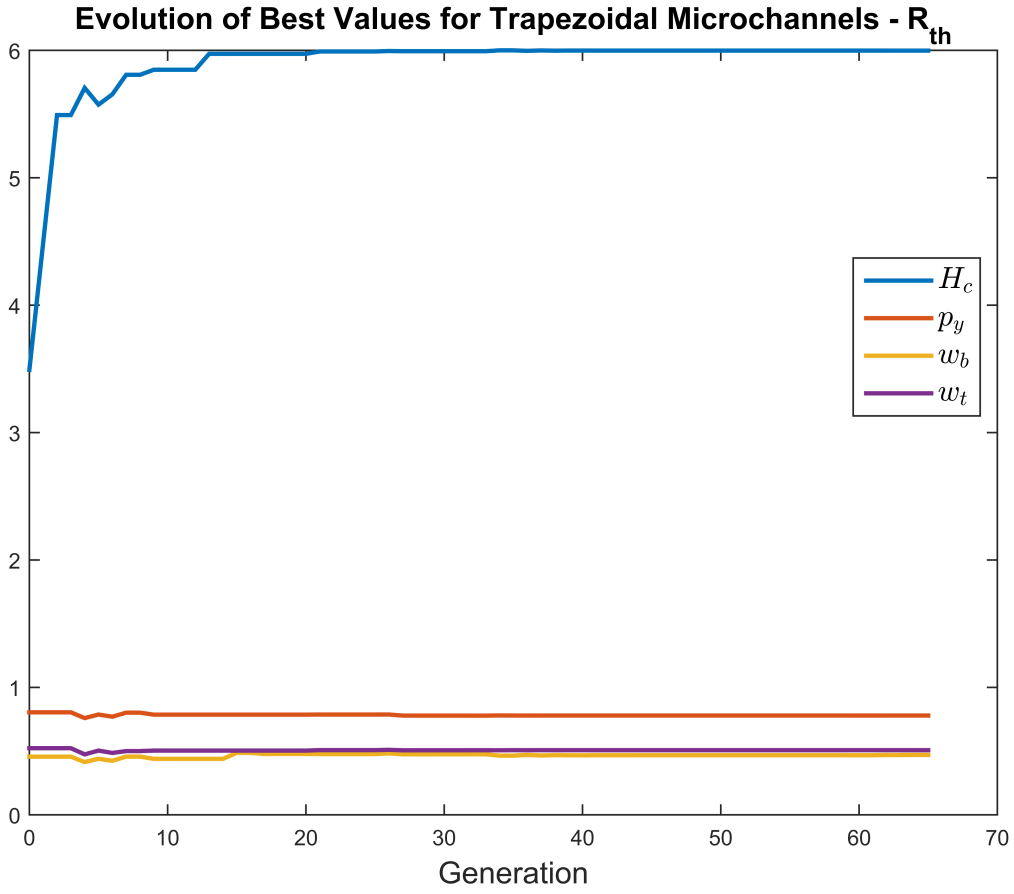

Figure 5.8: Evolution of Geometric Parameters of Minimum Thermal Resistance Individual at Each Generation Trapezoidal Channels

$$\begin{aligned} H_c &= 6.0 \\ p_y &= 0.79 \\ w_b &= 0.47 \\ w_t &= 0.51 \end{aligned} \tag{5.2.4}$$

with an optimal an optimal thermal resistance $R_{th} = 1.32 \times 10^{-2}$ $[K/W]$. It can be seen that again the optimizer chose a maximum height, and a slightly tapered fin to improve the heat transfer. However, the decrease in the thermal resistance, compared to a straight micro-channel is of only 1.5%, while the pumping power was found to be $PP = 5.12\,W$, which is a 0.8% decrease over the thermally optimized straight micro-channels. In both cases, although the optimizer chose a slightly tapered trapezoidal channel, it was found that the improvement in performance with respect to straight channels was minimal, and the added geometric variability in the z-direction did not lead to significant improvement in efficiency.

5.3 Converging/Diverging Channel Heat Sink Optimization

Two more optimization studies are carried out to study the effects of linearly converging or diverging channels on the performance of heat sinks. The optimization parameters are taken as the height of the channel, the inlet and outlet width and the longitudinal pitch (see Figure 5.9). For consistency, the bounds on the system are kept constant (see Table 5.4) The geometric bounds on the system are given by a minimum fin thickness,

Table 5.4: Range of Parameters for Converging \Diverging Micro-channel Optimization Studies

	min	max
$\boldsymbol{H[mm]}$	2	6
$\boldsymbol{p_y[mm]}$	0.3	2.5
$\boldsymbol{w_b[mm]}$	0.1	1
$\boldsymbol{w_t[mm]}$	0.1	1

$$\begin{aligned} p_y - w_i &\leq D_{\min} = 0.1\,mm \\ p_y - w_o &\leq D_{\min} = 0.1\,mm \end{aligned} \tag{5.3.1}$$

a minimum aspect ratio that satisfies the limits on M_1

$$\frac{H_c}{w_i} > 3, \frac{H_c}{w_o} > 3 \tag{5.3.2}$$

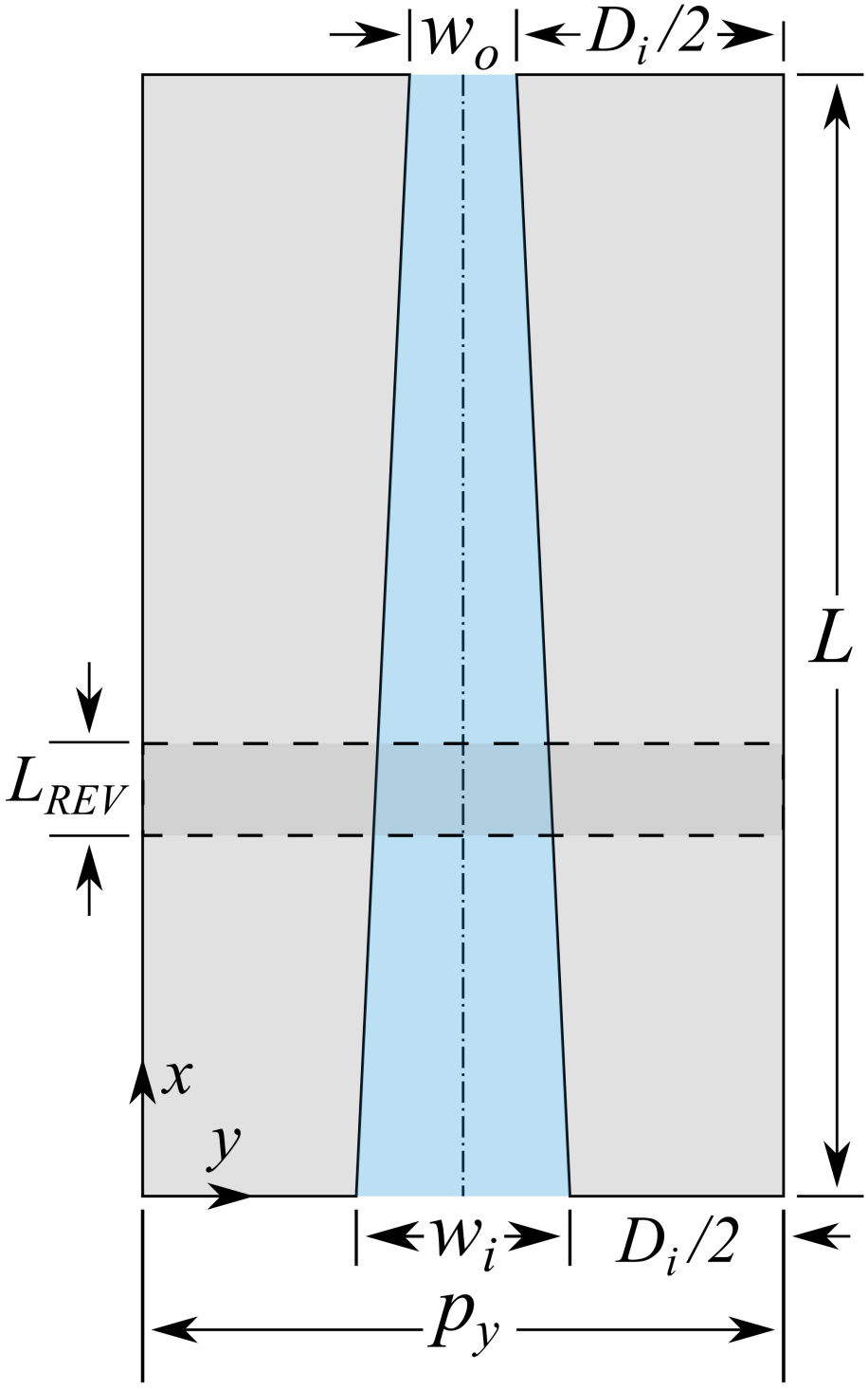

Figure 5.9: Schematic of Converging/Diverging Micro-channel Heat Sink (Top View)

The limits on M_3 are harder to implement, however the pressure drop has been chosen such that Reynolds numbers will be relatively low, therefore to ensure that the condition is met (or close), a bound on the porosity gradient is defined

$$0.5 \leq \frac{w_i}{w_o} \leq 2 \tag{5.3.3}$$

First, the GA optimization is carried out setting entropy generation as the fitness parameters. The initial population N_p was set at 100, and the maximum number of generation was set at $N_G$at 200. The optimizer found a solution after 66 generations, and the evolution of the geometric parameters of the fittest individual are shown in Figure 5.10. The optimal

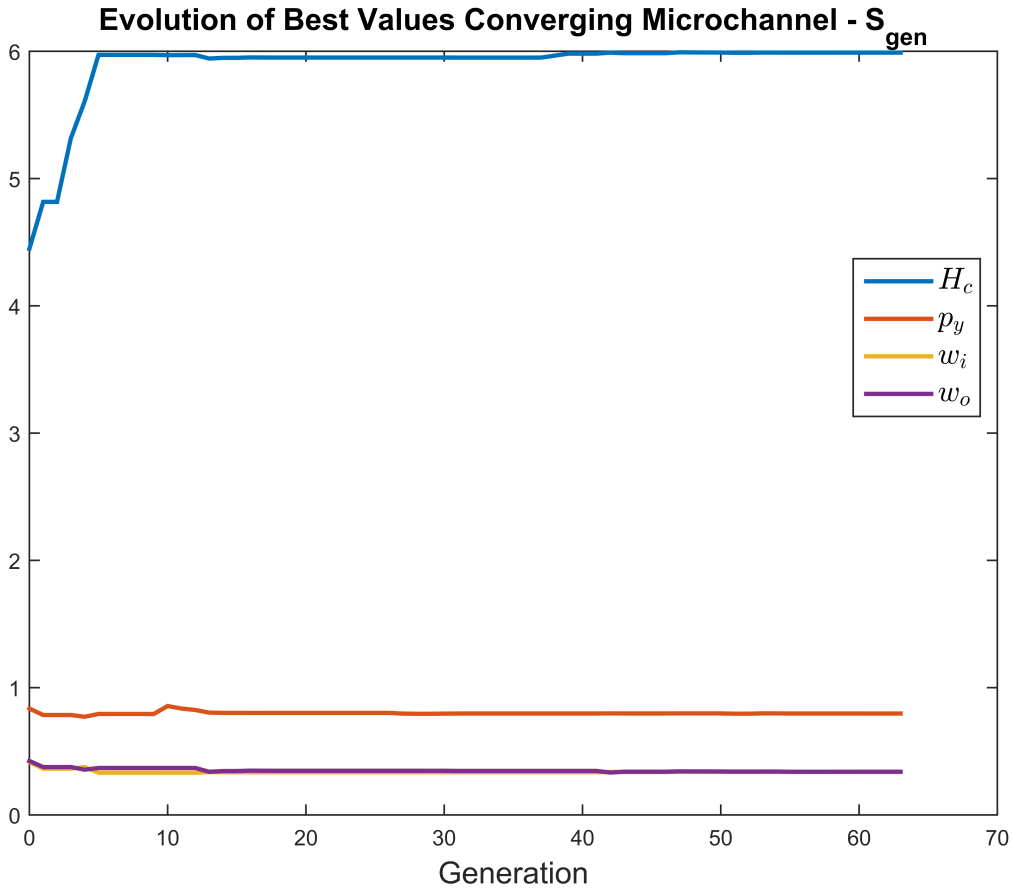

Figure 5.10: Evolution of Geometric Parameters of Minimum Entropy Generation Individual at Each Generation Converging Channels

configuration was found to be

$$\begin{aligned} H_c &= 6 \\ p_y &= 0.79 \\ w_i &= 0.34 \\ w_o &= 0.34 \end{aligned} \tag{5.3.4}$$

with a minimum entropy of $\dot{S}_{gen} = 2.77 \times 10^{-2}$ $[W/K\,]$. The thermal resistance, HSF and pumping power are $R_{th} = 1.66 \times 10^{-2}$ $[K/W\,]$, 1.48, and $1.66\,W$, respectively. It can be seen that the optimizer chose the same straight channel configuration given in Section 5.1. This means that in terms of overall entropy generation, straight channels are optimal.

Next, the optimization study was repeated by defining thermal resistance as the fitness parameter. The optimizer found a solution after 97 generations, and the evolution of the individual with the lowest thermal resistance at each generation is shown in Figure 5.11. The optimal parameters are found to be

$$\begin{aligned} H_c &= 6 \\ p_y &= 0.9 \\ w_i &= 0.59 \\ w_o &= 0.42 \end{aligned} \tag{5.3.5}$$

with a minimum value of the thermal resistance of $R_{th} = 1.25 \times 10^{-2}$ $[K/W\,]$ and a hot spot factor of 1.04, with a pumping power of $PP = 3.89\,W$. Compared with the minimal thermal resistance configuration found for straight micro-channels, this converging channel configuration leads to a 23% reduction in the pumping power, and a 6% improvement in the thermal resistance. Also, the temperature uniformity improves significantly, as determined by the 9% decrease in the hot spot factor. It was found that, M_3 for this solution is 8×10^{-2}, which implies that the results for the optimal solution is expected to be accurate. These last two optimization studies show that, although straight channels have the overall lowest entropy generation, converging channels are a more efficient way to improve the heat transfer of a heat sink. This is due to the fact that the only means for improving heat transfer in a straight channel is to increase the width, to improve the heat transfer coefficient. Since the width is adjusted everywhere, the heat transfer coefficient is improved everywhere in the

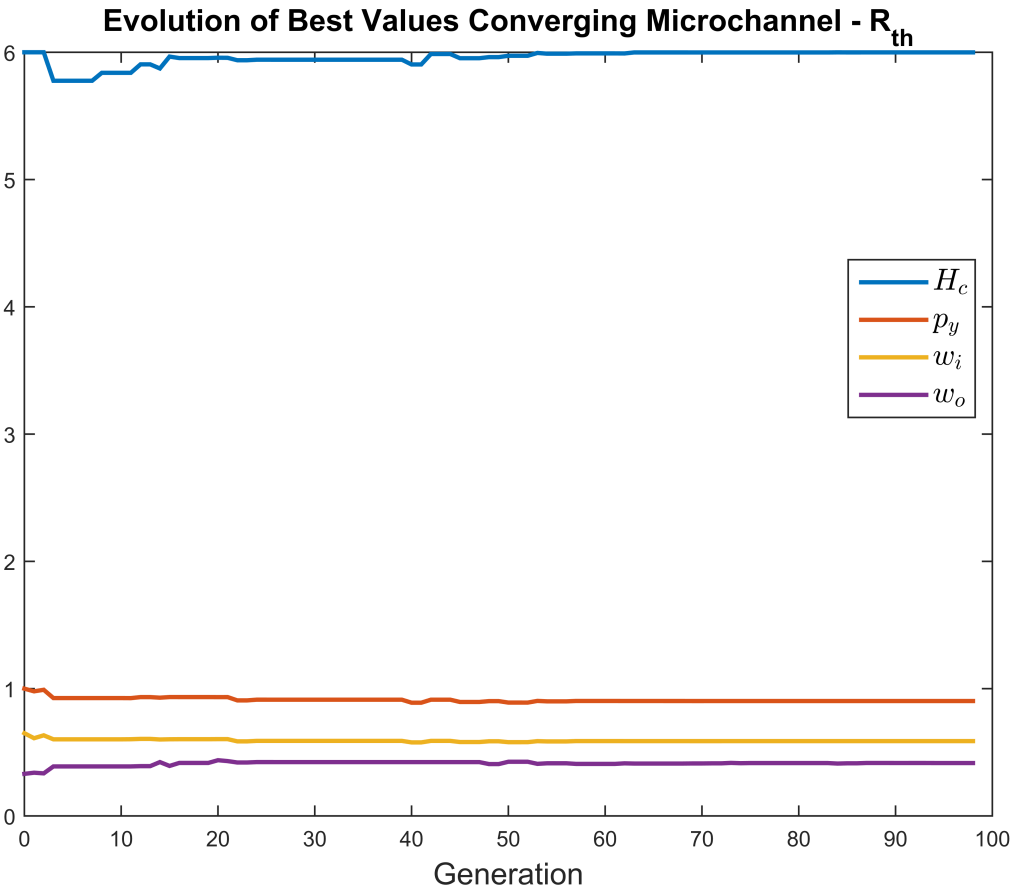

Figure 5.11: Evolution of Geometric Parameters of Minimum Thermal Resistance Individual at Each Generation Converging Channels

system, even in areas, such as near the entrance, where it is already quite high and heat transfer is diffusion controlled. On the contrary, the added geometric degree of freedom of a converging channel allows a selective local improvement of the heat transfer coefficient in areas where it is relatively low, e.g. away from the inlet, which leads to a reduction in the pumping power.

In a final step, the insight gained through the previous studies is used to design a heat sink with linear geometric variation in both x and z variation with the same performance thermal performance as the thermally optimized straight channel, but with reduced pumping power. It was found through iteration that a heat sink with the following geometrical design

$$\begin{aligned} H_c &= 6 \\ p_y &= 0.89 \\ w_b &= 0.68 \\ w_t &= 0.58 \\ w_o &= 0.41 \end{aligned} \tag{5.3.6}$$

has the same thermal resistance value as the thermally optimized straight micro-channel ($R_{th} = 1.32 \times 10^{-2}$ $[K/W]$), but a pumping power of only $PP = 2.82\,W$. This means that a heat sink with varying geometry in the x- and z direction, with the same thermal performance as a straight channel, will reduce the pumping power by 44%. In the process, the temperature uniformity of the system was also significantly improved, and it was found that this last configuration has a HSF of 1.02, which is a decrease of 11% with respect to straight channels. The scaled temperature at the base bottom is shown in Figure 5.12, and it can be seen that the trapezoidal converging micro-channel has an almost uniform temperature. The optimization studies have shown that, although from an entropy generation perspective, straight channels are optimal, there is no efficient way to improve their heat transfer performance. Converging channels present a better solution to improve the heat transfer in the system, and it has been shown that an optimized converging channel can reduce the thermal resistance by 6% while decreasing the pumping power by 23%, when compared to a thermally optimized straight channel. Finally, it was found that a combination of trapezoidal and converging channel can achieve the same thermal resistance as a thermally optimized

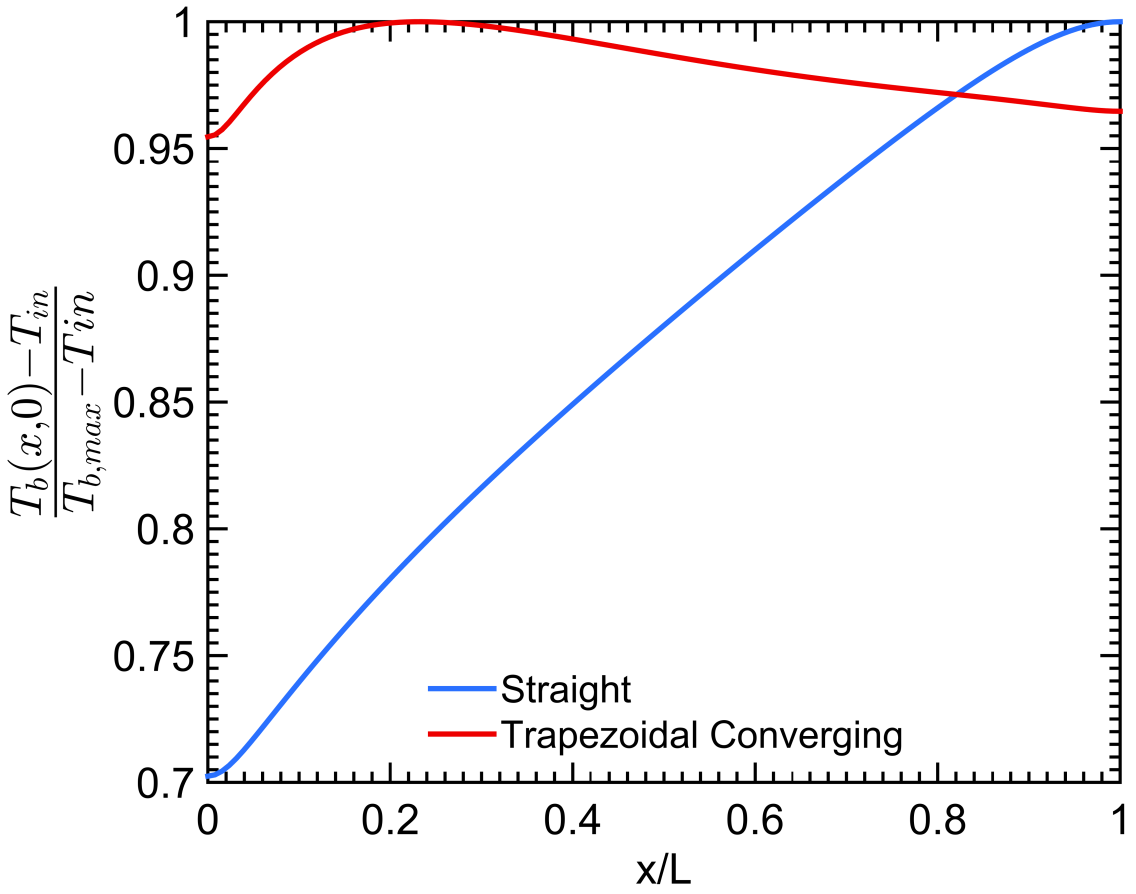

Figure 5.12: Comparison of Temperature Distribution at Base Bottom for Straight and Trapezoidal Converging Micro-channels

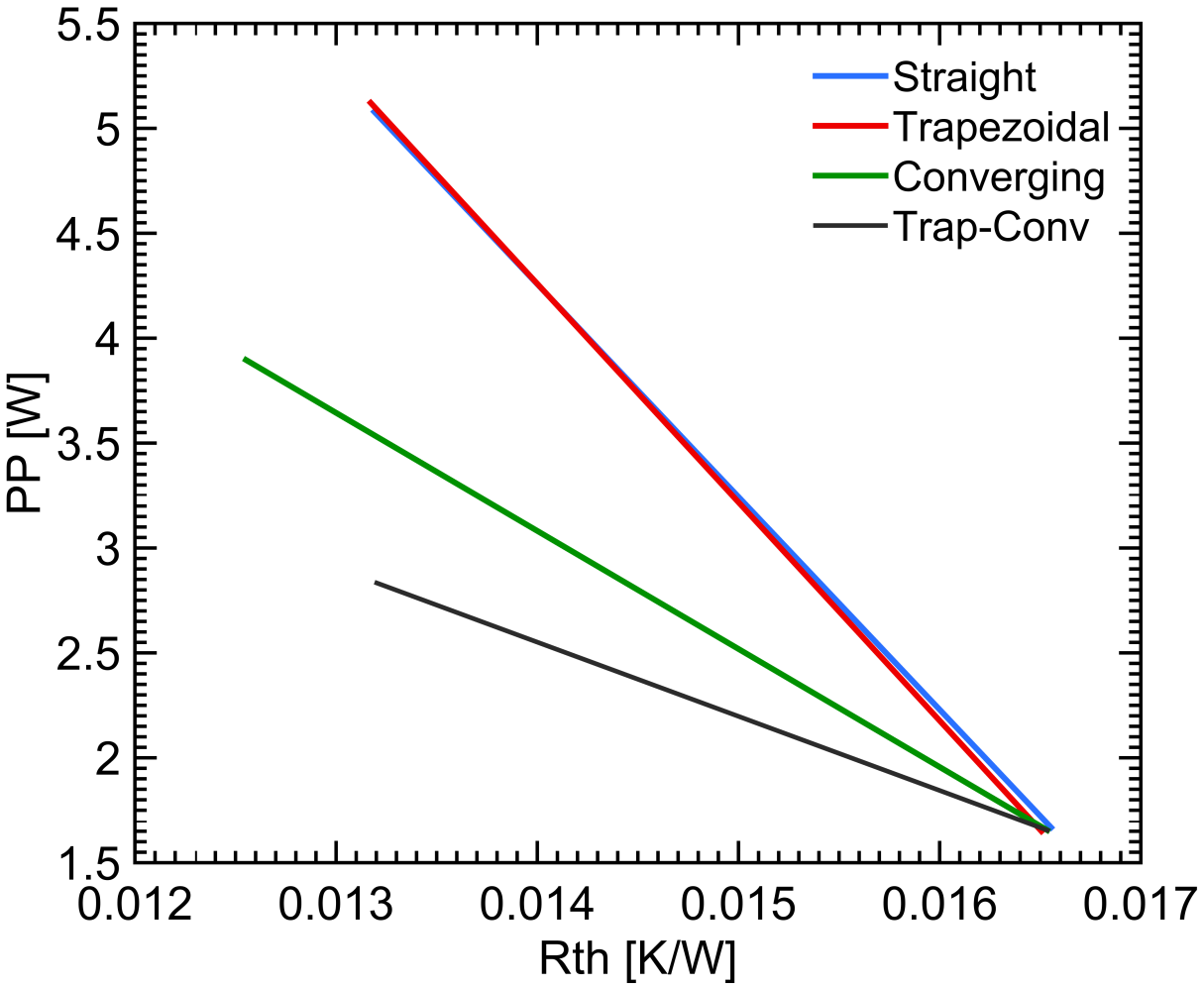

Figure 5.13: Summary of Pumping Power vs Thermal Resistance Results of Optimization Studies

straight channel, with a reduction in pumping power of 44%, and a significant reduction of temperature gradients. The fact that the added geometric degrees of freedom lead to a better way to improve heat transfer is clearly visible in Figure 5.13, where the thermal resistance versus pumping power were plotted for all the systems considered. The slope of the line (interpolated between only two points), shows the amount of energy input that is required to improve the heat transfer of the heat sink. It can be seen that with increasing degrees of freedom, the slope clearly decreases which shows that benefit of a trapezoidal converging channel. In order to validate the optimization results, the performance parameters for three optimal configurations were validated using CFX. The designs to be validated were chosen

as the three limiting designs in Figure 5.13: the minimum entropy straight channel, the minimum thermal resistance straight channel, and the optimal trapezoidal converging channel. The result of the validation study are shown in Table 5.5, It can be seen that the agreement

Table 5.5: Validation of Optimal Designs

Straight Channel Minimum S_{gen}, Eqn. (5.1.3)			
	VAT	**CFD**	**%Δ**
$\boldsymbol{PP[W]}$	1.67	1.66	0.60%
$\boldsymbol{R_{th}[W/K]}$	$1.66 \cdot 10^{-2}$	$1.65 \cdot 10^{-2}$	0.61%
Straight Channel Minimum R_{th}, Eqn. (5.1.4)			
	VAT	**CFD**	**%Δ**
$\boldsymbol{PP[W]}$	5.08	5.17	1.7%
$\boldsymbol{R_{th}[W/K]}$	$1.32 \cdot 10^{-2}$	$1.36 \cdot 10^{-2}$	2.9%
Trapezoidal Converging Channel Minimum R_{th}, Eqn. (5.3.6)			
	VAT	**CFD**	**%Δ**
$\boldsymbol{PP[W]}$	2.82	3.42	17.5%
$\boldsymbol{R_{th}[W/K]}$	$1.32 \cdot 10^{-2}$	$1.32 \cdot 10^{-2}$	0.3%

is excellent for the straight channel optimal configurations, and the error between VAT and CFD is within 3%. For the trapezoidal converging configuration, the actual pumping power is 17.5% higher than predicted, which is still a relatively good result considering the complicated nature of the geometry, and the fact that the interaction between the x and z direction variation has not been taken into account. Nonetheless, the CFD validation confirmed that the use of VAT leads to a heat sink geometric configuration which has approximately the same thermal performance of a straight channel, but a 34% reduction in pressure drop. This study was carried out with a fixed value of the pressure drop at 1000 Pa, therefore our solutions represent one point along the Pareto optimal curve. It is indeed possible that the results and conclusions would be different at different values of the pressure drop. Since the thermal resistance and pumping power represent the two energy parameters in the system, a multi-objective optimization study should be carried out to indeed determine the Pareto

optimal curve for a wide range of parameters. Nonetheless, the design shows that using a VAT base model allows the exploration of a wide range of design parameters, and the determination of an optimal solution in significantly reduced computational times. Since on average about 6000 function evaluations were required by the GA during the optimization studies, the determination of the optimal geometry that has been carried out in this chapter, would have required about 420 days using a full CFD solution of the conjugate problem.

CHAPTER 6

Conclusions

The main purpose of this work was to explore the effects of added geometric degrees of freedom on performance of heat rejecting devices. The importance and challenges of improving cooling solution models were discussed and provided in Chapter 1. Following recent studies, it was hypothesized that adding geometrical variations to a heat sink can lead to better cooling solutions. A VAT model was proposed as an efficient modeling alterative to reduce the considerable computational times required by CFD studies and allow the use of large scale optimization algorithms to find optimal configurations. In Chapter 2, the fundamentals of VAT were discussed, and the governing equations for laminar fluid flow and heat transfer through multi-scale systems were derived. Analogies between VAT, the continuum approach used in mechanics, and the LES methods of turbulence were used to show that these methods are similar in the way they deal with the multi-scale nature of the problem at hand. The analogies developed were used throughout the paper to explain some of the issues that arise from averaging techniques, and in particular, the need for closure schemes to account for information loss. Analysis of different closure schemes established that complete models, although more accurate, require too many unknowns to be determined, and simpler models lead to good results when all significant effects are properly accounted for. Issues due to length disparities at boundaries between a homogenous and porous media were identified, a few studies were reviewed, and further avenues of research to advance this theory were noted. The momentum and energy equations were closed using constitutive closure relations, and their determination using available data and numerical simulations were discussed. It was shown that the VAT hydraulic diameter and intrinsic velocity could be used to collapse data for a wide range of disparate geometries onto a single curve. Particular attention was

given to the determination of closure parameters using CFD, and a five step process was outlined that ensures the results give an accurate description of the momentum and energy transport at the lower scale. It was noted that the momentum pressure and drag terms could be obtained numerically using one REV with periodic boundary conditions, while six REVs were necessary to obtain a good representation of the heat transfer coefficient. It was also observed that the numerical boundary conditions used to determine the VAT defined heat transfer coefficient did not affect the results, and the heat transfer coefficient in the domain was constant everywhere except for very small regions near the boundaries of the computational domain.

In Chapter 3, the VAT model was applied to heat sinks with variable geometry. First, a scaling procedure was developed to reduce momentum conservation to a one dimensional equation. Then, numerical methods for the solution of the resulting set of partial differential equations were developed. The momentum equation was solved using finite differences and a Newton-Rhapson scheme for pressure updating. Two numerical methods were developed for the solution of the coupled system of energy conservation equations. A Galerkin methods solution, which has been shown to be useful for constant geometries, was discussed first. Next, a transient finite difference solution procedure was outlined. Strang splitting was used to address the coupling between the fluid and solid energy equations and reduce computational time. In addition, an ADI technique was used to reduce the solution of the entire system to the solution of a series of tri-diagonal systems. For steady-state cases, an optimal variable time-stepping technique was derived to improve the decay of the low frequency spectrum of the solid solution. An analytical solution of the Laplace equation for the temperature distribution in the homogenous base was derived for arbitrary heat fluxes. To address the coupling between the VAT energy equations and the homogenous base, the interface condition was posed as a minimization problem in spectral space, and a direct and iterative method was applied to find the optimal solution. It is found that the combination of the analytical and finite difference solutions of the equations, and the iterative solution of the interface minimization problem leads to significant improvement in code efficiency.

Chapter 4 was devoted to determining limitations of VAT applicability for heat sinks with

constant geometry, as well as for heat sinks with geometry variations in the x- and z- directions. The scaling developed in Chapter 3 was exploited to determine three non-dimensional parameters that define the limits of accuracy in these equations. The first parameter, M_1, is related to the ratio of the hydraulic diameter to the height of the channel, and it is independent of the Reynolds number. It was first shown that for low values of M_1 the VAT model was accurate by comparing the predicted values with numerical and empirical studies. Two geometries were considered: a water cooled micro-channel heat sink and an air cooled pin fin heat sink. In both cases, the error between the predicted values and the experimental and numerical values was less than 5%. Furthermore, several additional heat sinks geometries were studied to determine the error in the VAT model as a function of the parameter M_1, and a maximum error of 10% was deemed acceptable. It is determined that a $M_1 \leq 0.05$ was required for the VAT model to satisfy the accuracy condition. The study was then repeated for a trapezoidal micro-channel heat sink to study the effects of porosity variation in the z-direction on the accuracy. The second parameter resulting from scaling, M_2, is shown to be the determining factor for accuracy. When this parameter was small, the VAT model was shown to be again accurate, with a maximum error of 5% when compared to CFD results. It is also found that $M_2 \leq 0.05$ is the limiting value on the accuracy of the model. A third parameter, M_3, arose from scaling when porosity variations in the x-direction were present. It is shown that this parameter depends on the porosity gradient in the x-direction and the Reynolds number. It was confirmed that for low values of this parameter the VAT model was accurate by comparing predicted values for both converging and diverging channels to numerical experiments. The error again was found to be less than 5% when this condition was satisfied. The increase in error as a function of M_3 was then explored, and the limiting value is determined to be $M_3 \approx 0.1$. In Chapter 5, the computational savings obtained by using the VAT model, along with the numerical solution developed in Chapter 3, were exploited to conduct an optimization study. A Genetic Algorithm (GA) was employed to carry out two optimization studies for straight, trapezoidal, and converging micro-channel heat sinks. In one optimization study, the overall efficiency of the system was defined as the entropy generated by the heat sink, which combines its thermal and hydraulic perfor-

mance. It is found that trapezoidal micro-channels are optimal, although the difference in entropy generation with respect to straight micro-channels is minimal. In a second optimization study, the pressure drop was kept constant, and the thermal resistance was optimized. This study shows that converging channels are the most effective way to increase the heat transfer performance of the system. The thermally optimized converging channel provides a reduction in pumping power and thermal resistance of 6% and 23%, respectively, over a thermally optimized straight channel. Furthermore, the temperature uniformity of the heat source, quantified by the hot spot factor, improves by 9%. Lastly, variation in both directions were manually combined to design a trapezoidal converging heat sink which boasts the same thermal resistance of the thermally optimized straight channel, but a 44% reduction in pressure drop. It is also found that the uniformity of the component temperature improves by 13%. These results confirm that geometrical non-uniformity is an efficient way to improve the thermal performance of a heat sink. Several unanswered questions remain about the fundamentals of VAT, the numerical solutions of its equation, as well as of the determination of optimal heat sink configurations with variable geometry. From a theoretical point of view, boundary conditions of the VAT equations are an area that requires further research. In particular, better models for dispersion effects and momentum boundary conditions near walls need to be developed to extend the accuracy of the model to lower aspect ratio systems. Also, a better heat flux splitting model for the interface condition between the homogenous base, which takes into account the effects of geometry, Reynolds number, and thermal conductivity ratio would not only improve the rigor of the model, but also greatly reduce issues with the numerical iteration procedure currently carried out at the interface. From a numerical point of view, solution methods for the VAT two-dimensional momentum equations need to be developed. In general, the same numerical methods that are used for the solution of the Navier-Stokes equations could be applied, although the effects of the non-linear momentum sink term on the stability of solution methods for the N-S equations is not clear at the moment. Also, the numerical solution of the energy equation could be greatly improved by using a predictor-corrector method. The setup of the iteration procedure shown in Chapter 3 implies the interface temperature is a Lagrangian variable that enforces the

interface energy condition in a similar way that pressure enforces mass conservation for the N-S equations. Therefore, it is indeed possible to develop an equivalent of the pressure Poisson equation (and a KKT optimal condition), which is solved at every time step and used to update the interface temperature. The implementation of this type of solution method would significantly reduce the computational time. Although optimization studies like the one conducted here can give good indication of performance trends, the only way to define an optimal heat rejection system is to carry out a full multi-objective optimization study. As it has been shown, a model based on VAT gives a good balance between computational efficiency and accuracy, and it is therefore a good candidate for multi-objective optimization studies. Furthermore, if the improvements discussed above are properly implemented, the range of applicability of the VAT model would be expanded, its computational advantages improved, and very large scale optimization studies could be accomplished. My main goal for this work was to apply my physical and mathematical understanding of VAT to show how adding geometric degrees of freedom is a simple, yet efficient way of improving heat sink performance. My hopes are that the detailed discussion, examples, and analogies help to de-mystify the VAT process and also demonstrate, behind the somewhat convoluted mathematics, how the fundamental concepts are beautifully simple. I hope to convince the reader that, within its limits, VAT is an accurate modeling procedure, and that varying the heat sinks geometry is indeed an efficient way to enhance heat transfer. The next step in this research progression might be to use the developed model to explore the effects of non-linear geometry variations on thermal performance, as well as studies on variable geometry heat sinks for hot spot mitigation. Ultimately, I hope that this works theoretical and numerical treatment of VAT, and the demonstration of performance improvements with geometrically non-uniform heat sinks will lead to the application of these techniques to determine optimal configuration for a wide variety of heat transfer devices.

APPENDIX A

Derivation of Finite Difference Schemes and Truncation Errors

A.1 Forward Difference

Take the Taylor series expansion of f_{i+1} around i

$$f_{i+1} = f_i + f'_i \underbrace{(x_{i+1} - x_i)}_{\Delta x_{i+1}} + \frac{1}{2!} f''_i \Delta x_{i+1}^2 + \frac{1}{3!} f'''_i \ \Delta x_{i+1}^3 + \frac{1}{4!} f_i^{IV} \Delta x_{i+1}^4 + O\left(\Delta x_{i+1}^5\right) \quad \text{(A.1.1)}$$

and rearranging

$$f'_i = \frac{f_{i+1} - f_i}{\Delta x_{i+1}} - \frac{1}{2!} f''_i \Delta x_{i+1} - \frac{1}{3!} f'''_i \ \Delta x_{i+1}^2 - \frac{1}{3!} f_i^{IV} \Delta x_{i+1}^3 - O\left(\Delta x_{i+1}^4\right) \quad \text{(A.1.2)}$$

and the truncation error is defined as the leading term of the reminder

$$\tau_i = -\frac{1}{2!} f''_i \Delta x_{i+1} - \frac{1}{3!} f'''_i \ \Delta x_{i+1}^2 - \frac{1}{3!} f_i^{IV} \Delta x_{i+1}^3 - O\left(\Delta x_{i+1}^4\right) = O\left(\Delta x_{i+1}\right) \quad \text{(A.1.3)}$$

A.2 Backward Difference

Similarly, expanding f_{i-1} around i

$$\begin{aligned} f_{i-1} &= f_i + f'_i \underbrace{(x_{i-1} - x_i)}_{-\Delta x_i} + \frac{1}{2!} f''_i (-\Delta x_i)^2 + \frac{1}{3!} f'''_i \ (-\Delta x_i)^3 + \frac{1}{4!} f_i^{IV} (-\Delta x_i)^4 + O\left(\Delta x_i^5\right) = \\ &= f_i - f'_i \Delta x_i + \frac{1}{2!} f''_i \Delta x_i^2 - \frac{1}{3!} f'''_i \ \Delta x_i^3 + \frac{1}{4!} f_i^{IV} \Delta x_i^4 + O\left(\Delta x_i^5\right) \end{aligned} \quad \text{(A.2.1)}$$

Then rearranging

$$f'_i = \frac{f_i - f_{i-1}}{\Delta x_i} + \frac{1}{2!} f''_i \Delta x_i - \frac{1}{3!} f'''_i \ \Delta x_i^2 + \frac{1}{4!} f_i^{IV} \Delta x_i^3 + O\left(\Delta x_i^4\right) \quad \text{(A.2.2)}$$

and the truncation error is given by

$$\tau_i = \frac{1}{2!} f''_i \Delta x_i - \frac{1}{3!} f'''_i \ \Delta x_i^2 + \frac{1}{4!} f_i^{IV} \Delta x_i^3 + O\left(\Delta x_i^4\right) = O\left(\Delta x_i\right) \tag{A.2.3}$$

A.3 Centered Difference

Lets take the difference between the $D_+ f - D_- f$

$$\begin{aligned} f_{i+1} &= f_i + f'_i \Delta x_{i+1} + \frac{1}{2!} f''_i \Delta x_{i+1}^2 + \frac{1}{3!} f'''_i \Delta x_{i+1}^3 + O\left(\Delta x_{i+1}^4\right) \\ -f_{i-1} &= f_i - f'_i \Delta x_i + \frac{1}{2!} f''_i \Delta x_i^2 - \frac{1}{3!} f'''_i \Delta x_i^3 + O\left(\Delta x_i^4\right) \\ \hline f_{i+1} - f_{i-1} &= f'_i \left(\Delta x_{i+1} + \Delta x_i\right) + \frac{1}{2!} f''_i \left(\Delta x_{i+1}^2 - \Delta x_i^2\right) + \\ &\quad + \frac{1}{3!} f'''_i \left(\Delta x_{i+1}^3 + \Delta x_i^3\right) + O\left(\Delta x_{i+1}^4 + \Delta x_i^4\right) \end{aligned} \tag{A.3.1}$$

Then rearranging

$$f'_i = \frac{f_{i+1} - f_{i-1}}{\left(\Delta x_{i+1} + \Delta x_i\right)} - \frac{1}{2!} f''_i \frac{\left(\Delta x_{i+1}^2 - \Delta x_i^2\right)}{\left(\Delta x_{i+1} + \Delta x_i\right)} - \frac{1}{3!} f'''_i \ \frac{\left(\Delta x_{i+1}^3 + \Delta x_i^3\right)}{\left(\Delta x_{i+1} + \Delta x_i\right)} + O\left(\frac{\Delta x_{i+1}^4 + \Delta x_i^4}{\left(\Delta x_{i+1} + \Delta x_i\right)}\right) \tag{A.3.2}$$

and the local truncation error is

$$\tau_i = -\frac{1}{2!} f''_i \frac{\left(\Delta x_{i+1}^2 - \Delta x_i^2\right)}{\left(\Delta x_{i+1} + \Delta x_i\right)} - \frac{1}{3!} f'''_i \ \frac{\left(\Delta x_{i+1}^3 + \Delta x_i^3\right)}{\left(\Delta x_{i+1} + \Delta x_i\right)} + O\left(\frac{\Delta x_{i+1}^4 + \Delta x_i^4}{\left(\Delta x_{i+1} + \Delta x_i\right)}\right) = O\left(\frac{\Delta x_{i+1}^2 - \Delta x_i^2}{\Delta x_{i+1} + \Delta x_i}\right) \tag{A.3.3}$$

It can be seen that if $\Delta x_{i+1} = \Delta x_i$ the first term in the local truncation error will cancel and the approximation will be second order as expected. But for the case of non-uniform meshes, the order of the truncation error is still one.

A.4 2^{nd} Order Forward Difference

A 2nd order forward difference to the first derivative is needed at the interface, therefore, a method is developed. First, expand the f_{i+2} around i

$$f_{i+2} = f_i + f'_i \underbrace{(x_{i+2} - x_i)}_{\substack{x_{i+2}-x_{i+1}+x_{i+1}-x_i= \\ =\Delta x_{i+2}+\Delta x_{i+1}}} + \frac{1}{2!}f''_i(\Delta x_{i+2} + \Delta x_{i+1})^2 + \frac{1}{3!}f'''_i(\Delta x_{i+2} + \Delta x_{i+1})^3 +$$
$$+ O\left((\Delta x_{i+2} + \Delta x_{i+1})^4\right) = f_i + f'_i\left(\Delta x_{i+2} + \Delta x_{i+1}\right) + \frac{1}{2!}f''_i(\Delta x_{i+2} + \Delta x_{i+1})^2 +$$
$$+ \frac{1}{3!}f'''_i\ \left(\Delta x_{i+2} + \Delta x_{i+1}\right)^3 + O\left((\Delta x_{i+2} + \Delta x_{i+1})^4\right) \tag{A.4.1}$$

Then, we seek a combination of f_{i+1} and f_{i+2} to obtain second order accuracy. Lets create a linear combination of the two

$$-(\alpha+\beta)f_i + \alpha f_{i+1} + \beta f_{i+2} = f'_i\left[\alpha\Delta x_{i+1} + \beta\left(\Delta x_{i+2} + \Delta x_{i+1}\right)\right] +$$
$$+ f''_i\left[\frac{\alpha}{2}\Delta x_{i+1}^2 + \frac{\beta}{2}(\Delta x_{i+1} + \Delta x_{i+2})^2\right] + f'''_i\ \left[\frac{\alpha}{3!}\Delta x_{i+1}^3 + \frac{\beta}{3!}(\Delta x_{i+1} + \Delta x_{i+2})^3\right] +$$
$$+ O\left((\Delta x_{i-1} + \Delta x_i)^4\right) \tag{A.4.2}$$

we want to arrange the coefficients in such a way to obtain as high an accuracy as possible. Therefore, we choose a solution to the system

$$\begin{bmatrix} \Delta x_i & (\Delta x_{i-1} + \Delta x_i) \\ \frac{\Delta x_i^2}{2} & \frac{1}{2}(\Delta x_{i-1} + \Delta x_i)^2 \end{bmatrix} \begin{bmatrix} \alpha \\ \beta \end{bmatrix} = \begin{bmatrix} 1 \\ 0 \end{bmatrix} \tag{A.4.3}$$

A solution is given by

$$\alpha = \frac{(\Delta x_{i+1} + \Delta x_{i+2})}{\Delta x_{i+1}\Delta x_{i+2}}$$
$$\beta = -\frac{\Delta x_{i+1}}{\Delta x_{i+2}\left(\Delta x_{i+1} + \Delta x_{i+2}\right)} \tag{A.4.4}$$

Therefore, the scheme can be written as

$$f'_i = -\left(\frac{(\Delta x_{i+1} + \Delta x_{i+2})^2 - \Delta x_{i+1}^2}{\Delta x_{i+1}\Delta x_{i+2}\left(\Delta x_{i+1} + \Delta x_{i+2}\right)}\right) f_i +$$
$$+ \frac{(\Delta x_{i+1} + \Delta x_{i+2})^2}{\Delta x_{i+1}\Delta x_{i+2}\left(\Delta x_{i+1} + \Delta x_{i+2}\right)} f_{i+1} - \frac{\Delta x_{i+1}^2}{\Delta x_{i+2}\Delta x_{i+1}\left(\Delta x_{i+1} + \Delta x_{i+2}\right)} f_{i+2} \tag{A.4.5}$$

with truncation error

$$\tau_i = -\frac{1}{6} f'''_i \left[\frac{(\Delta x_{i+1} + \Delta x_{i+2})\,\Delta x_{i+1}}{\Delta x_{i+2}} \Delta x_{i+1} - \frac{(\Delta x_{i+1} + \Delta x_{i+2})\,\Delta x_{i+1}}{\Delta x_{i+2}} (\Delta x_{i+1} + \Delta x_{i+2}) \right] + \\ + O\left((\Delta x_{i-1} + \Delta x_i)^4\right) \tag{A.4.6}$$

Now, assuming that $\Delta x_{i-1} = \Delta x_i$, this gives

$$\begin{aligned} \alpha &= \frac{4}{2\Delta x} \\ \beta &= -\frac{1}{2\Delta x} \end{aligned} \tag{A.4.7}$$

and the scheme is given by

$$f'_i = -\left(\frac{3}{2\Delta x}\right) f_i + \frac{4}{2\Delta x} f_{i+1} - \frac{1}{2\Delta x} f_{i+2} - \frac{1}{4} f'''_i\ \Delta x^2 + O\left(\Delta x^3\right) \tag{A.4.8}$$

This difference will be used to calculate the heat flux at the interface, therefore, at z=0, j=1, the solution gives

$$f'_1 = -\left(\frac{(\Delta x_2 + \Delta x_3)^2 - \Delta x_2^2}{\Delta x_2 \Delta x_3 (\Delta x_2 + \Delta x_3)}\right) f_i + \frac{(\Delta x_2 + \Delta x_3)^2}{\Delta x_2 \Delta x_3 (\Delta x_2 + \Delta x_3)} f_{i+1} - \frac{\Delta x_2^2}{\Delta x_2 \Delta x_3 (\Delta x_2 + \Delta x_3)} f_{i+2} \tag{A.4.9}$$

Recall that: $\Delta x_i = x_i - x_{i-1}$

A.5 2^{nd} Order Backward Difference

A 2nd order backward difference to the first derivative is needed at the interface, therefore, a method is developed. First, expand f_{i-2} around i

$$f_{i-2} = f_i + f'_i \underbrace{(x_{i-2} - x_i)}_{\substack{x_{i-2} - x_{i-1} + x_{i-1} - x_i = \\ = -(\Delta x_{i-1} + \Delta x_i)}} + \frac{1}{2!} f''_i (-(\Delta x_{i-1} + \Delta x_i))^2 + \frac{1}{3!} f'''_i (-(\Delta x_{i-1} + \Delta x_i))^3 + \\ + O\left((\Delta x_{i-1} + \Delta x_i)^4\right) = f_i - f'_i (\Delta x_{i-1} + \Delta x_i) + \frac{1}{2!} f''_i (\Delta x_{i-1} + \Delta x_i)^2 + \\ - \frac{1}{3!} f'''_i (\Delta x_{i-1} + \Delta x_i)^3 + O\left((\Delta x_{i-1} + \Delta x_i)^4\right) \tag{A.5.1}$$

And recall

$$f_{i-1} = f_i - f'_i \Delta x_i + \frac{1}{2!} f''_i \Delta x_i^2 - \frac{1}{3!} f'''_i\ \Delta x_i^3 + \frac{1}{4!} f_i^{IV} \Delta x_i^4 + O\left(\Delta x_i^5\right) \tag{A.5.2}$$

Then, we seek a combination of f_{i-1} and f_{i-2} to obtain second order accuracy. Lets create a linear combination of the two

$$\begin{aligned}&-(\alpha+\beta)f_i+\alpha f_{i-1}+\beta f_{i-2}=\left[-\alpha\Delta x_i-\beta\left(\Delta x_{i-1}+\Delta x_i\right)\right]f'_i+\\&\left[\frac{\alpha}{2}\Delta x_i^2+\frac{\beta}{2}(\Delta x_{i-1}+\Delta x_i)^2\right]f''_i-\left[\frac{\alpha}{3!}\Delta x_i^3+\frac{\beta}{3!}f'''_i\ \left(\Delta x_{i-1}+\Delta x_i\right)^3\right]f'''_i\ \ +O\left(\Delta x_i^4\right)\end{aligned} \tag{A.5.3}$$

we want to arrange the coefficients in such a way to obtain as high an accuracy as possible. Therefore, we choose a solution to the system

$$\begin{bmatrix}-\Delta x_i & -(\Delta x_{i-1}+\Delta x_i)\\ \frac{\Delta x_i^2}{2} & \frac{1}{2}(\Delta x_{i-1}+\Delta x_i)^2\end{bmatrix}\begin{bmatrix}\alpha\\ \beta\end{bmatrix}=\begin{bmatrix}1\\ 0\end{bmatrix} \tag{A.5.4}$$

A solution is given by

$$\begin{aligned}\alpha&=\frac{(\Delta x_{i-1}+\Delta x_i)}{\Delta x_i\left[\Delta x_i-(\Delta x_{i-1}+\Delta x_i)\right]}=-\frac{(\Delta x_{i-1}+\Delta x_i)}{\Delta x_i\Delta x_{i-1}}\\ \beta&=-\frac{\Delta x_i}{-(\Delta x_{i-1}+\Delta x_i)^2+\Delta x_i\left(\Delta x_{i-1}+\Delta x_i\right)}=\frac{\Delta x_i}{\Delta x_{i-1}\left(\Delta x_{i-1}+\Delta x_i\right)}\end{aligned} \tag{A.5.5}$$

Now, assuming that , this gives

$$\begin{aligned}\alpha&=-\frac{4}{2\Delta x}\\ \beta&=\frac{1}{2\Delta x}\end{aligned} \tag{A.5.6}$$

and the scheme is given by

$$f'_i=\frac{3f_i-4f_{i-1}+f_{i-2}}{2\Delta x}+\frac{1}{4}f'''_i\ \Delta x^2+O\left(\Delta x^4\right) \tag{A.5.7}$$

A.6 2^{nd} Order Centered Second Difference

In order to derive a second order approximation of the second derivative, lets take a linear combination of f_{i-1} and f_{i+1}

$$\begin{aligned}&\beta f_{i-1}-(\alpha+\beta)f_i+\alpha f_{i+1}=f'_i\left(\alpha\Delta x_{i+1}-\beta\Delta x_i\right)+\frac{1}{2}f''_i\left(\alpha\Delta x_{i+1}^2+\beta\Delta x_i^2\right)+\\&+\frac{1}{3!}f'''_i\ \left(\alpha\Delta x_{i+1}^3-\beta\Delta x_i^3\right)+\frac{1}{4!}f_i^{IV}\left(\alpha\Delta x_{i+1}^4+\beta\Delta x_i^4\right)+O\left(\Delta x_i^5\right)\end{aligned} \tag{A.6.1}$$

And we have the following conditions on the coefficients

$$\begin{bmatrix} \Delta x_{i+1} & -\Delta x_i \\ {\Delta x_{i+1}^2}/{2} & {\Delta x_i^2}/{2} \end{bmatrix} \begin{bmatrix} \alpha \\ \beta \end{bmatrix} = \begin{bmatrix} 0 \\ 1 \end{bmatrix} \tag{A.6.2}$$

and the solution is found to be

$$\begin{aligned} \alpha &= \frac{2}{\Delta x_{i+1}\left(\Delta x_{i+1} + \Delta x_i\right)} = \frac{1}{\Delta x_{i+1}\Delta \bar{x}_i} \\ \beta &= \frac{2}{\Delta x_i^2 + \Delta x_{i+1}\Delta x_i} = \frac{1}{\Delta x_i \Delta \bar{x}_i} \end{aligned} \tag{A.6.3}$$

Also, using the notation

$$\frac{\left(\Delta x_i + \Delta x_{i+1}\right)}{2} = \frac{x_i - x_{i-1} + x_{i+1} - x_i}{2} = \frac{x_{i+1} - x_{i-1}}{2} = \Delta \bar{x}_i \tag{A.6.4}$$

And the solution can be written as

$$\begin{aligned} {f''}_i'' = \frac{2}{\left(\Delta x_{i+1} + \Delta x_i\right)} \frac{\left[\Delta x_{i+1} f_{i-1} - \left(\Delta x_i + \Delta x_{i+1}\right) f_i + \Delta x_i f_{i+1}\right]}{\Delta x_i \Delta x_{i+1}} + \\ -\frac{1}{6} {f'''}_i \ \frac{\left(\alpha \Delta x_{i+1}^3 - \beta \Delta x_i^3\right)}{{}^1/_2 \left(\alpha \Delta x_{i+1}^2 + \beta \Delta x_i^2\right)} - \frac{1}{4!} f_i^{IV} \frac{\left(\alpha \Delta x_{i+1}^4 + \beta \Delta x_i^4\right)}{{}^1/_2 \left(\alpha \Delta x_{i+1}^2 + \beta \Delta x_i^2\right)} + O\left(\Delta x_i^5\right) \end{aligned} \tag{A.6.5}$$

So the scheme is

$$f_i'' = \frac{1}{\Delta \bar{x}_i} \frac{\left[\Delta x_{i+1} f_{i-1} - \left(\Delta x_i + \Delta x_{i+1}\right) f_i + \Delta x_i f_{i+1}\right]}{\Delta x_i \Delta x_{i+1}} \tag{A.6.6}$$

And the truncation error is given by

$$\tau_i = -\frac{1}{3} {f'''}_i \ \frac{\left(\Delta x_{i+1}^2 - \Delta x_i^2\right)}{\left(\Delta x_{i+1} + \Delta x_1\right)} - \frac{1}{12} f_i^{IV} \frac{\left(\Delta x_{i+1}^3 + \Delta x_i^3\right)}{\left(\Delta x_{i+1} + \Delta x_1\right)} + O\left(\Delta x_i^5\right) \tag{A.6.7}$$

For the first interior point, this can be written as

$${f_2}'' = \frac{2}{\left(\Delta x_3 + \Delta x_2\right)} \frac{\left[\Delta x_3 f_1 - \left(\Delta x_2 + \Delta x_3\right) f_2 + \Delta x_2 f_3\right]}{\Delta x_2 \Delta x_3} \tag{A.6.8}$$

It can be seen that when the spacing is uniform, this becomes

$$f_i'' = \frac{\left[f_{i-1} - 2 f_i + f_{i+1}\right]}{\Delta x^2} \tag{A.6.9}$$

with a truncation error

$$\tau_i = -\frac{1}{12} f_i^{IV} \Delta x^2 + O\left(\Delta x_i^5\right) \tag{A.6.10}$$

which is the well-known second order scheme.

In the solution of the equations, we will also need to calculate the Laplacian of the following function

$$f = \varepsilon T \tag{A.6.11}$$

in this case, the schemes will not change, and the second derivative is now given by

$$\begin{aligned} \frac{\partial^2 (\varepsilon T)}{\partial x^2} &= \frac{1}{\Delta \bar{x}_i} \frac{\left[\Delta x_{i+1} (\varepsilon T)_{i-1} - (\Delta x_i + \Delta x_{i+1}) (\varepsilon T)_i + \Delta x_i (\varepsilon T)_{i+1}\right]}{\Delta x_i \Delta x_{i+1}} \\ \frac{\partial^2 (\varepsilon T)}{\partial z^2} &= \frac{1}{\Delta \bar{z}_i} \frac{\left[\Delta z_{i+1} (\varepsilon T)_{i-1} - (\Delta z_i + \Delta z_{i+1}) (\varepsilon T)_i + \Delta z_i (\varepsilon T)_{i+1}\right]}{\Delta z_i \Delta z_{i+1}} \end{aligned} \tag{A.6.12}$$

and the truncation errors will be

$$\begin{aligned} \tau_i &= -\frac{1}{3} (\varepsilon T)_i''' \frac{\left(\Delta x_{i+1}^2 - \Delta x_i^2\right)}{(\Delta x_{i+1} + \Delta x_1)} - \frac{1}{12} (\varepsilon T)_i^{IV} \frac{\left(\Delta x_{i+1}^3 + \Delta x_i^3\right)}{(\Delta x_{i+1} + \Delta x_1)} + O\left(\Delta x_i^5\right) = \\ &= -\frac{1}{3} \left[T_i \left(\varepsilon_i'''\right) + \varepsilon_i \left(T_i'''\right)\right] \frac{\left(\Delta x_{i+1}^2 - \Delta x_i^2\right)}{(\Delta x_{i+1} + \Delta x_1)} - \frac{1}{12} \left[T_i \left(\varepsilon_i{}^{IV}\right) + \varepsilon_i \left(T_i{}^{IV}\right)\right] \frac{\left(\Delta x_{i+1}^3 + \Delta x_i^3\right)}{(\Delta x_{i+1} + \Delta x_1)} + O\left(\Delta x_i^5\right) \end{aligned} \tag{A.6.13}$$

It can be seen that the LTE now will depend on the derivative, as well as the point values of the quantities.

A.7 2^{nd} Order Centered Second Difference with Variable Coefficients

To obtain a second order approximation of the following type of diffusive term

$$\nabla (\alpha \nabla f) \tag{A.7.1}$$

then using the divergence theorem on a volume around the gridpoint, it can be written

$$\int_{\Delta V} \nabla (\alpha \nabla f) \, dV = \int_{\Delta S} (\alpha \nabla f) \cdot \mathbf{n} dS \tag{A.7.2}$$

In a one-dimensional case, when the volume is $dx/2$ in each direction around point x_i this becomes

$$\frac{1}{\Delta x} \int_{x_i - \Delta x/2}^{x_i + \Delta x/2} \frac{\partial}{\partial x} \left[\alpha (x) \frac{\partial f}{\partial x}\right] dx = \frac{1}{\Delta x} \left[\alpha \left(x_{i+1/2}\right) \left.\frac{\partial f}{\partial x}\right|_{x_{1+1/2}} - \alpha \left(x_{i-1/2}\right) \left.\frac{\partial f}{\partial x}\right|_{x_{1-1/2}}\right] \tag{A.7.3}$$

Then, approximating the two derivatives using a forward difference

$$\frac{1}{\Delta x}\int\limits_{x_i-\Delta x/2}^{x_i+\Delta x/2}\frac{\partial}{\partial x}\left[\alpha\left(x\right)\frac{\partial f}{\partial x}\right]dx=\frac{1}{\Delta x}\left[\alpha\left(x_{i+1/2}\right)\frac{f_{i+1}-f_i}{\Delta x}-\alpha\left(x_{i-1/2}\right)\frac{f_i-f_{i-1}}{\Delta x}\right] \tag{A.7.4}$$

the following scheme is obtained

$$\frac{\partial}{\partial x}\left[\alpha\left(x\right)\frac{\partial f}{\partial x}\right]=\frac{\alpha\left(x_{i-1/2}\right)}{\Delta x^2}f_{i-1}-\frac{\alpha\left(x_{i+1/2}\right)+\alpha\left(x_{i-1/2}\right)}{\Delta x^2}f_i+\frac{\alpha\left(x_{i+1/2}\right)}{\Delta x^2}f_{i+1} \tag{A.7.5}$$

APPENDIX B

Definition of Porosity Variations

The variations in the x and z directions for the diameter are assumed to be separable functions. In CAD models, the easiest way to define these types of variations is to define an inlet profile and then extrude it along guide lines. The inlet profile can be seen as the z variation of the diameter (or width) and the guide lines are the x variations. The subsequent section discusses the determination of the parameters in the equations for different cases.

B.1 Linear x —Linear z

The first combination considered is a linear-linear combination

$$D(x,z) = (a_x + b_x x)(a_z + b_z z) \tag{B.1.1}$$

Following the previous discussion, the parameters are defined as

$$D_{00} = D(0,0), D_{0H} = D(0,H), \quad D_{L0} = D(L,0) \tag{B.1.2}$$

Using these definitions, the parameters in Eqn. (B.1.1) can be found

$$D_{00} = a_x a_z \rightarrow a_x = a_z = \sqrt{D_{00}} \tag{B.1.3}$$

$$D_{0H} = a_x a_z + a_x b_z H \rightarrow b_z = \frac{D_{0H} - D_{00}}{H\sqrt{D_{00}}} \tag{B.1.4}$$

$$D_{L0} = a_x a_z + a_z b_x L \rightarrow b_x = \frac{D_{L0} - D_{00}}{L\sqrt{D_{00}}} \tag{B.1.5}$$

Therefore, when the three parameters given in Eqn. (B.1.2) are given, the diameter is set.

B.2 Quadratic x —Linear z

The second combination considered is a quadratic in x and linear in z

$$D(x,z) = \left(a_x + b_x x + c_x x^2\right)(a_z + b_z z) \tag{B.2.1}$$

The parameters in this case are

$$\begin{gathered} D_{00} = D(0,0), D_{0H} = D(0,H), \quad D_{x_{\max}0} = D(x_{\max},0), \\ \frac{\partial D}{\partial x}\Big|_{x_{\max},0} = 0 \end{gathered} \tag{B.2.2}$$

Using these definitions, the parameters in Eqn. (B.2.1) can be found

$$D_{00} = a_x a_z \rightarrow a_x = a_z = \sqrt{D_{00}} \tag{B.2.3}$$

$$D_{0H} = a_x a_z + a_x b_z H \rightarrow b_z = \frac{D_{0H} - D_{00}}{H\sqrt{D_{00}}} \tag{B.2.4}$$

$$D_{x_{\max}0} = a_x a_z + a_z b_x x_{\max} + a_z c_x x_{\max}^2 \rightarrow \begin{bmatrix} a_z x_{\max} & a_z x_{\max}^2 \end{bmatrix} \begin{bmatrix} b_x \\ c_x \end{bmatrix} = D_{x_{\max}0} - D_{00} \tag{B.2.5}$$

$$\frac{\partial D}{\partial x}\Big|_{x_{\max},0} = a_z b_x + 2a_z c_x x_{\max} = \begin{bmatrix} a_z & 2a_z x_{\max} \end{bmatrix} \begin{bmatrix} b_x \\ c_x \end{bmatrix} = 0 \tag{B.2.6}$$

The last two equations represent a set of 2 equations in 2 unknowns and can be easily solved to find that

$$\begin{aligned} b_x &= 2\frac{D_{x_{\max}0} - D_{00}}{x_{\max}\sqrt{D_{00}}} \\ c_x &= -\frac{D_{x_{\max}0} - D_{00}}{x_{\max}^2\sqrt{D_{00}}} \end{aligned} \tag{B.2.7}$$

To check that the solution is correct, the solution is substituted in the governing equations

$$\begin{aligned} &D_{x_{\max}0} - D_{00} = 2\left(D_{x_{\max}0} - D_{00}\right) - \left(D_{x_{\max}0} - D_{00}\right) \\ &2\frac{D_{x_{\max}0} - D_{00}}{x_{\max}} - 2\frac{D_{x_{\max}0} - D_{00}}{x_{\max}} = 0 \end{aligned} \tag{B.2.8}$$

and it can be seen that the equations are satisfied.

B.3 Linear x —Quadratic z

The third combination considered is linear in x and quadratic in z

$$D(x,z) = (a_x + b_x x)\left(a_z + b_z z + c_z z^2\right) \tag{B.3.1}$$

The parameters in this case are

$$\begin{gathered} D_{00} = D(0,0), D_{0z_{\max}} = D(0,z_{\max}), \quad D_{L0} = D(L,0), \\ \frac{\partial D}{\partial z}\Big|_{0,z_{\max}} = 0 \end{gathered} \tag{B.3.2}$$

The set of equations defining the parameters are

$$D_{00} = a_x a_z \rightarrow a_x = a_z = \sqrt{D_{00}} \tag{B.3.3}$$

$$D_{L0} = a_z a_x + a_z b_x L \rightarrow b_x = \frac{D_{L0} - D_{00}}{L\sqrt{D_{00}}} \tag{B.3.4}$$

$$D_{0z_{\max}} = a_x a_z + a_x b_z z_{\max} + a_x c_z z_{\max}^2 \tag{B.3.5}$$

$$\left.\frac{\partial D}{\partial z}\right|_{0,z_{\max}} = 0 = a_x b_z + 2a_x c_z z_{\max} \tag{B.3.6}$$

The last two equations represent a system of two equations in two unknowns and the solution can be found to be

$$\begin{aligned} b_z &= 2\frac{D_{0z_{\max}} - D_{00}}{z_{\max}\sqrt{D_{00}}} \\ c_z &= -\frac{D_{0z_{\max}} - D_{00}}{z_{\max}^2\sqrt{D_{00}}} \end{aligned} \tag{B.3.7}$$

And by substitution, it can be confirmed that they are solution to the given equations

$$\begin{gathered} \frac{D_{0z_{\max}} - D_{00}}{z_{\max}\sqrt{D_{00}}} = 2\frac{D_{0z_{\max}} - D_{00}}{z_{\max}\sqrt{D_{00}}} - \frac{D_{0z_{\max}} - D_{00}}{z_{\max}\sqrt{D_{00}}} \\ 2\frac{D_{0z_{\max}} - D_{00}}{z_{\max}} - 2\frac{D_{0z_{\max}} - D_{00}}{z_{\max}} = 0 \end{gathered} \tag{B.3.8}$$

B.4 Quadratic x —Quadratic z

The fourth combination considered is quadratic in x and quadratic in z

$$D(x,z) = \left(a_x + b_x x + c_x x^2\right)\left(a_z + b_z z + c_z z^2\right) \tag{B.4.1}$$

The parameters in this case are

$$\begin{gathered} D_{00} = D\left(0,0\right), D_{0z_{\max}} = D\left(0,z_{\max}\right), \quad D_{x_{\max}0} = D\left(x_{\max},0\right), \\ \frac{\partial D}{\partial x}\big|_{x_{\max},0} = 0, \frac{\partial D}{\partial z}\big|_{0,z_{\max}} = 0 \end{gathered} \tag{B.4.2}$$

The set of equations defining the parameters are

$$D_{00} = a_x a_z \rightarrow a_x = a_z = \sqrt{D_{00}} \tag{B.4.3}$$

$$D_{x_{\max}0} = a_x a_z + a_z b_x x_{\max} + a_z c_x x_{\max}^2 \tag{B.4.4}$$

$$\left.\frac{\partial D}{\partial x}\right|_{x_{\max},0} = 0 = a_z b_x + 2 a_z c_x x_{\max} \tag{B.4.5}$$

$$D_{0z_{\max}} = a_x a_z + a_x b_z z_{\max} + a_x c_z z_{\max}^2 \tag{B.4.6}$$

$$\left.\frac{\partial D}{\partial z}\right|_{0,z_{\max}} = 0 = a_x b_z + 2 a_x c_z z_{\max} \tag{B.4.7}$$

The last four equations represent a system of four equations in four unknowns. Since the x and z equations are independent, except for the constant terms which are set by Eqn. (B.4.3) , the solution to the two independent systems are given by the ones given in Eqns. (B.2.7) and (B.3.7), and are repeated here

$$\begin{aligned} b_x &= 2\frac{D_{x_{\max}0} - D_{00}}{x_{\max}\sqrt{D_{00}}}, c_x = -\frac{D_{x_{\max}0} - D_{00}}{x_{\max}^2\sqrt{D_{00}}} \\ b_z &= 2\frac{D_{0z_{\max}} - D_{00}}{z_{\max}\sqrt{D_{00}}}, c_z = -\frac{D_{0z_{\max}} - D_{00}}{z_{\max}^2\sqrt{D_{00}}} \end{aligned} \tag{B.4.8}$$

APPENDIX C

Derivation of Integral VAT Conservation Equations

C.1 Mass and Momentum Conservation

The momentum equation is integrated over the entire domain

$$\int_0^1 \int_0^1 \frac{\partial \langle u \rangle}{\partial x} dxdz = 0 \rightarrow \int_0^1 \langle u \rangle_{x=1} dz - \int_0^1 \langle u \rangle_{x=0} dz = 0 \tag{C.1.1}$$

which is simply a statement that the volume mass flow rate at the outlet is equal to the mass flow rate at the outlet. The momentum equation given, is integrated over the domain

$$\int_0^1 \int_0^1 \left[-M_1 \frac{\partial^2 \langle u \rangle}{\partial z^2} + M_2 (x,z) \langle u \rangle^2 \right] dxdz = \int_0^1 \int_0^1 M_3 (x,z)\, dxdz \tag{C.1.2}$$

The shear stress term can be rearranged using the independence of the integration limits from x and z

$$- M_1 \left[\int_0^1 \frac{\partial \langle u \rangle}{\partial z}\bigg|_{z=1} dx - \int_0^1 \frac{\partial \langle u \rangle}{\partial z}\bigg|_{z=0} dx \right] \tag{C.1.3}$$

These are the energy losses due to the shear stress. The z-derivatives at the boundaries are integrated using a second order one sided finite difference. The other two terms are simply integrated entirely over the domain. The first term,

$$\int_0^1 \int_0^1 \left[M_2 \langle u \rangle^2 \right] dxdz \tag{C.1.4}$$

represent the losses due to the lower scale geometry. The RHS represents the energy supplied to the system through pressure

$$\int_0^1 \int_0^1 M_3 dxdz \tag{C.1.5}$$

In order for the forces to match, the difference between the LHS and RHS of the equations should be small. A convergence criterion for the code is that the momentum imbalance is less than 1%. All the integrals are calculated using a trapezoidal method over the solution grid to obtain second order accuracy.

C.2 Energy Conservation

The fluid energy equation is integrated over the domain

$$\int_0^1 \int_0^1 \left[F_1 \langle u \rangle \frac{\partial \langle T_f \rangle^f}{\partial x} - F_2 \frac{\partial}{\partial x} \left(\varepsilon_f \frac{\partial \langle T_f \rangle^f}{\partial x} \right) - F_3 \frac{\partial}{\partial z} \left(\varepsilon_f \frac{\partial \langle T_f \rangle^f}{\partial z} \right) - F_4 \left(\langle T_s \rangle^s - \langle T_f \rangle^f \right) \right] dxdz \tag{C.2.1}$$

The convective term can be rearranged as

$$F_1 \int_0^1 \int_0^1 \langle u \rangle \frac{\partial \langle T_f \rangle^f}{\partial x} dxdz = F_1 \int_0^1 \left[\langle u \rangle \langle T_f \rangle^f \Big|_0^1 - \int_0^1 \frac{\cancel{\partial \langle u \rangle}}{\cancel{\partial x}} \langle T_f \rangle^f \right] dz \tag{C.2.2}$$

where the second term cancels by continuity. The term can then be arranged as

$$F_1 \int_0^1 \int_0^1 \langle u \rangle \frac{\partial \langle T_f \rangle^f}{\partial x} dxdz = F_1 \int_0^1 \langle u \rangle \langle T_f \rangle^f \Big|_{x=1} dz - \int_0^1 \langle u \rangle \langle T_f \rangle^f \Big|_{x=0} dz \tag{C.2.3}$$

This term represents the heat that convected away by the fluid. The x diffusive term can be rearranged as

$$F_2 \int_0^1 \left[\varepsilon_f \frac{\cancel{\partial \langle T_f \rangle^f}}{\cancel{\partial x}} \right]_{x=1} - \left[\varepsilon_f \frac{\partial \langle T_f \rangle^f}{\partial x} \right]_{x=0} dz = F_2 \int_0^1 \left[-\varepsilon_f \frac{\partial \langle T_f \rangle^f}{\partial x} \right]_{x=0} dz \tag{C.2.4}$$

where the first term is zero by the boundary condition. The temperature gradient in the second term will always be positive (for heating) because as the fluid enters, its temperature increases for the inlet temperature as it comes to contact with the fins, and from conduction from the hotter fluid ahead. In general, this term represent heat exiting the domain by back conduction at the inlet and should in general be small. The z diffusive term can similarly

be rearranged as

$$F_3 \int_0^1 \int_0^1 \frac{\partial}{\partial z}\left(\varepsilon_f \frac{\partial \langle T_f \rangle^f}{\partial z}\right) dz dx = F_3 \int_0^1 \left[\varepsilon_f \frac{\partial \langle T_f \rangle^f}{\cancel{\partial z}}\right]_{z=1} - \left[\varepsilon_f \frac{\partial \langle T_f \rangle^f}{\partial z}\right]_{z=0} dx = \\ = F_3 \int_0^1 \left[-\varepsilon_f \frac{\partial \langle T_f \rangle^f}{\partial z}\right]_{z=0} dx \tag{C.2.5}$$

where the first term is zero due to the boundary conditions. The remaining term represents the heat entering in the channel through the base. The inter REV heat transfer term is simply integrated over the entire domain

$$\int_0^1 \int_0^1 F_4 \left(\langle T_s \rangle^s - \langle T_f \rangle^f\right) dx dz \tag{C.2.6}$$

and represent the heat entering the fluid through the fins.

The solid energy equation is also integrated over the domain to obtain

$$Q_s = \int_0^1 \int_0^1 \left[S_1 \frac{\partial}{\partial x}\left(\varepsilon_s \frac{\partial \langle T_s \rangle^s}{\partial x}\right) + S_2 \frac{\partial}{\partial z}\left(\varepsilon_s \frac{\partial \langle T_s \rangle^s}{\partial z}\right) - S_3 \left(\langle T_s \rangle^s - \langle T_f \rangle^f\right)\right] dx dz \tag{C.2.7}$$

The x diffusion term can easily be shown to be zero by using the boundary conditions

$$S_1 \int_0^1 \left[\varepsilon_s \frac{\partial \langle T_s \rangle^s}{\partial x}\right]_{x=0}^{x=1} dz = S_1 \int_0^1 \left[\varepsilon_s \frac{\partial \langle T_s \rangle^s}{\cancel{\partial x}}\right]_{x=1} dz - S_1 \int_0^1 \left[\varepsilon_s \frac{\partial \langle T_s \rangle^s}{\cancel{\partial x}}\right]_{x=0} dz \tag{C.2.8}$$

Using again the boundary conditions, the z diffusion term can be rewritten as

$$S_2 \int_0^1 \int_0^1 \frac{\partial}{\partial z}\left(\varepsilon_s \frac{\partial \langle T_s \rangle^s}{\partial z}\right) dx dz = S_2 \int_0^1 \int_0^1 \frac{\partial}{\partial z}\left(\varepsilon_s \frac{\partial \langle T_s \rangle^s}{\partial z}\right) dz dx = \\ = S_2 \int_0^1 \left[\varepsilon_s \frac{\partial \langle T_s \rangle^s}{\partial z}\right]_{z=1}^{z=0} dx = S_2 \int_0^1 \left[\varepsilon_s \frac{\partial \langle T_s \rangle^s}{\cancel{\partial z}}\right]_{z=1} dx - S_2 \int_0^1 \left[\varepsilon_s \frac{\partial \langle T_s \rangle^s}{\partial z}\right]_{z=0} dx = \\ = S_2 \int_0^1 \left[-\varepsilon_s \frac{\partial \langle T_s \rangle^s}{\partial z}\right]_{z=0} dx \tag{C.2.9}$$

where the last term represents the heat entering the solid through the base. The inter REV term is simply integrated over the domain

$$\int_0^1 \int_0^1 S_3 \left(\langle T_s \rangle^s - \langle T_f \rangle^f\right) dx dz \tag{C.2.10}$$

and represent the heat loss in the solid due to transfer to the fluid. An overall energy conservation equation is obtained by subtracting the fluid and solid integral conservation equations. In this case, the interphase heat transfer cancels out and the only terms remaining are

$$F_1 \int_0^1 \langle u \rangle \langle T_f \rangle^f \Big|_{x=1} dz - \int_0^1 \langle u \rangle \langle T_f \rangle^f \Big|_{x=0} dz - F_2 \int_0^1 \left[-\varepsilon_f \frac{\partial \langle T_f \rangle^f}{\partial x} \right]_{x=0} dz + \\ - F_3 \int_0^1 \left[-\varepsilon_f \frac{\partial \langle T_f \rangle^f}{\partial z} \right]_{z=0} dx - S_2 \int_0^1 \left[-\varepsilon_s \frac{\partial \langle T_s \rangle^s}{\partial z} \right]_{z=0} dx = 0 \tag{C.2.11}$$

An overall conservation of energy gives that the all of the heat entering through the base has to be transferred to the fluid, and then advected away at the outlet and conducted through the inlet which is expressed from the previous equation. This can be easily seen if the equation is rearranged as

$$\underbrace{F_1 \int_0^1 \langle u \rangle \langle T_f \rangle^f \Big|_{x=1} dz - F_1 \int_0^1 \langle u \rangle \langle T_f \rangle^f \Big|_{x=0} dz}_{Q_{conv,out}} \underbrace{- F_2 \int_0^1 \left[-\varepsilon_f \frac{\partial \langle T_f \rangle^f}{\partial x} \right]_{x=0} dz}_{Q_{cond,out}} = \\ \underbrace{= F_3 \int_0^1 \left[-\varepsilon_f \frac{\partial \langle T_f \rangle^f}{\partial z} \right]_{z=0} dx + S_2 \int_0^1 \left[-\varepsilon_s \frac{\partial \langle T_s \rangle^s}{\partial z} \right]_{z=0} dx}_{Q_{in,HS}} + \Delta Q_{HS} \tag{C.2.12}$$

where ΔQ_{HS} is the imbalance due to numerical errors between the energy exiting the system and the energy entering the system. Ideally, the heat conducted in the heat sink should be equal to the heat conducted in the base; however, in the interface process, some of the energy contained in the truncated part of the base series is lost. Persevals theorem states that the energy content in the full energy series is the same as its actual function, however since the series in the solution is truncated, some energy is lost. To assess the amount of energy lost, another energy imbalance condition is given by

$$\underbrace{F_3 \int_0^1 \left[-\varepsilon_f \frac{\partial \langle T_f \rangle^f}{\partial z} \right]_{z=0} dx + S_2 \int_0^1 \left[-\varepsilon_s \frac{\partial \langle T_s \rangle^s}{\partial z} \right]_{z=0} dx}_{Q_{in,HS}} - Q_{in,base} = \Delta Q_{\text{int}} \tag{C.2.13}$$

and ΔQ_{int} is the energy lost at the interface due to numerical errors. In general, one of the convergence criteria is that the imbalances in the integral conservation equations are less than 1%. In general, for 128x128 grids, this imbalances are always satisfied.

APPENDIX D

Optimization Source Code

```
% This script runs the PSO optimization of the heat sink
close all
clc
if exist('outputs/bestValues.mat', 'file')==2
  delete('outputs/bestValues.mat');
end

% addpath 'F:\Documents\Research\MATLAB Accesories\psopt'
curDir = pwd;
funPath=fullfile(curDir,'vatCodeX');
addpath(funPath)

%%%%%%%%%%%%%%%%%% SET CONSTRATINTS FOR CONSTANT GEOMETRY %%%%%%%%%%
%%%%%
% Microchannels
% Inputs are Hc, py, wi, wo, tb
minThick=-0.1;  % minimum fin thickness
minAR = 2;      % minimum aspect ratio
minPor = 0.65;  % minimum porosity
maxGrad = 0.5;
A=zeros(4,4); b=zeros(4,1);
A(1,:)=[0, -minPor*1, 1, 0]; b(1)=0;   % Constraint that bottom width
 is less than py (py-wb)>=tMin --> -py+wb<=-tMin
A(2,:)=[0, -minPor*1, 0, 1]; b(2)=0;   % Constraint that top width is
 less than py (py-wt)>=tMin --> -py+wt<=-tMin
% A(3,:)=[-1, 0, minAR*1, 0]; b(3)=0;    % Constraint that minimum
 aspect ratio is less than minimum minAR*wb-H<=0
% A(4,:)=[-1, 0, 0, minAR*1]; b(4)=0;    % Constraint that minimum
 aspect ratio is less than minimum minAR*wt-H<=0
A(3,:)=[0, 0, maxGrad*1, -1]; b(3)=0;  % Constraint that maximum width
 variation is less than minimum gradient
A(4,:)=[0, 0, -1/maxGrad*1, 1]; b(4)=0;    % Constraint that minimum
 aspect ratio is less than minimum minAR*wt-H<=0
LB = [3; 0.3; 0.1; 0.1];   % Lower bounds
UB = [6; 1; 1; 1];         % Upper bounds

%%%%%%%%%%%%%%%%%%%%%%%%%%%%%%%%%%%%%%%%%%%%%%%%%%%%%%%%%%%%%%%%%%%%
%%%%

%%%%%%%%%%%%%%%%%%%%%%% RUN OPTIMIZER %%%%%%%%%%%%%%%%%%%%%%%%%%%%%%
%%%%%
tStartOpt = tic;    % start timer

% Set GA options
% Plot best function value (and mean) vs generation and vector values
 of
% the best individual.
% Set parallel option to be true.
% Set creation function such that every member is feasible.
% Set mutation function and cross over functions to maintain
 feasibility.
% Set initial population size
```

```
options=gaoptimset('PlotFcns',
{@gaplotbestf,@gaPlotValuesEvol},'UseParallel',true,...

  'CreationFcn',@gacreationlinearfeasible,'MutationFcn',@mutationadaptfeasible,...

  'CrossoverFcn',@crossoverarithmetic,'PopulationSize',100,'OutputFcns',@gaValuesE

% Run GA optimizer
[x,fval,exitflag,output] = ga(@(x) mainOptimX(x),4,A,b,[],[],LB,UB,
[],options);


tEndOpt = toc(tStartOpt); % end timer

% Sound to notify of end run
load gong
sound(0.2*y,Fs)
clc
```

PRINT RESULTS AND PLOT

Output results

```
fprintf('Optimization run has terminated in %2g mins with message
 \n',round(tEndOpt/60,3,'significant'))
fprintf([output.message ' \n'])
fprintf('The optimal configuration is p_y=%3.3e [mm], w_i=%3.3e [mm],
 w_0=%3.3e [mm] \n',x(1),x(2),x(3))
fprintf('with a minimum optimal parameter of %3.3e \n',fval)

% % Load evolution of parameters and copy results in outputs directory
load('bestValues.mat')  % Load results
s=regexprep(datestr(dateTime),'\W','');    % string with date and time
save(['outputs/results'
 s '.mat'],'bestValues','dateTime','x','fval','output','A','b')
delete('bestValues.mat');

% Plot evolution of best parameters
figure
plot(0:output.generations,bestValues,'-','linewidth',2)
title('Evolution of Best Values Converging Microchannel -
 R_{th}','fontsize',14)
xlabel('Generation','fontsize',14)
hLegend = legend('$H_c$','$p_y$','$w_i$','$w_o$','Location','Best');
hLegend.Interpreter='latex';
hLegend.FontSize=14;
```

Published with MATLAB® R2015a

APPENDIX E

Heat Sink Source Code

Table of Contents


```
function outputs=main(varargin)

%MAIN   Solve 2D VAT mom and energy
%
%   This function is the main function for the solution of the two
%   phase (fluid-solid) VAT energy and momentum equations.
%
%   outputs=main returns an outputs structure array containing the
 results
%   obtained from solving the equations with inputs extracted from the
%   first set of inputs from file inputs.txt assumed to be in the same
%   folder
%
%   outputs=main(inputs) returns an output structure array contining
 the
%   results obtained from solving the equations with inputs specified
 in
%   the array inputs. inputs is a regular array of at least 25 inputs
%
%   outputs=main(inputs,testType) runs the code and runs the test
 specified
%   by the string testType. testType options are given in testHSwB and
 can
%   be 'all','ener','mom','base',interface','solver'.


maxArg=3;
narginchk(0,maxArg)
% Maximum number of inputs of cell array
maxNumParam=25;
switch nargin
    case 0
        % Load first case from the inputs.txt file located in the
 folder
        try
            fid=fopen('inputs.txt');
            inputTot=textscan(fid,'%u%f%f%f%f%f%f%s%u%q%f%f%u%f%u%f%u
%u%f%f%u%u%f%f%f','Headerlines',1);
```

```
            fclose(fid);
            inputs = cell(maxNumParam,1);
            for i=1:maxNumParam
                inputs{i} = inputTot{i}(1);
            end

        catch
            error('Unable to run standalone. Possibly no inputs.txt in
 same folder as main')
        end
        % No test
        testDef='';
        testMode='reg';
        fprintf('-------------------- STANDALONE MODE
 ------------------------ \n \n \n')
        % Plot
        wannaPlot='yes';
    case 1
        % Run in test mode
        % Load first case from the inputs.txt file located in the
 folder
        try
            fid=fopen('inputs.txt');
            inputTot=textscan(fid,'%u%f%f%f%f%f%f%s%u%q%f%f%u%f%u%f%u
%u%f%f%u%u%f%f%f','Headerlines',1);
            fclose(fid);
            inputs = cell(maxNumParam,1);
            for i=1:maxNumParam
                inputs{i} = inputTot{i}(1);
            end

        catch
            error('Unable to run test. Possibly no inputs.txt in same
 folder as main')
        end
        % Run specified test with regular outputs
        testDef=varargin{1};
        testMode='reg';
        fprintf('-------------------- TEST MODE
 ------------------------ \n \n \n')
        wannaPlot='no';
    case 2
                % Run in test mode
        % Load first case from the inputs.txt file located in the
 folder
        try
            fid=fopen('inputs.txt');
            inputTot=textscan(fid,'%u%f%f%f%f%f%f%s%u%q%f%f%u%f%u%f%u
%u%f%f%u%u%f%f%f','Headerlines',1);
            fclose(fid);
            inputs = cell(maxNumParam,1);
            for i=1:maxNumParam
                inputs{i} = inputTot{i}(1);
            end
```

```
        catch
            error('Unable to run test. Possibly no inputs.txt in same
 folder as main')
        end
        testDef=varargin{1};
        testMode=varargin{2};
        wannaPlot='no';
    case 3
        testDef=varargin{1};
        testMode=varargin{2};
        inputs=varargin{3};
        wannaPlot='no';
end

------------------- STANDALONE MODE ------------------------
```

EXTRACT DATA FROM INPUTS ARRAY

```
% Get start time
tStart=tic;
% Start parameter counter
paramCount=1;
% Type of geometry
geomType=inputs{1}; paramCount=paramCount+1;
% Heat Sink Length
geomL=inputs{paramCount}*1e-3; paramCount=paramCount+1;
% Heat Sink Width
geomW=inputs{paramCount}*1e-3; paramCount=paramCount+1;
% Channel height
geomHc=inputs{paramCount}*1e-3; paramCount=paramCount+1;
% Obstacle width
geomD=inputs{paramCount}*1e-3; paramCount=paramCount+1;
% Obstacle pitch in transverse direction
geomPy=inputs{paramCount}*1e-3; paramCount=paramCount+1;
% Obstacle pitch in longitudinal direction
geomPx=inputs{paramCount}*1e-3; paramCount=paramCount+1;
% Parameter to be varied
varParam=inputs{paramCount}; paramCount=paramCount+1;
% Function type of input
porosityVarType=inputs{paramCount}; paramCount=paramCount+1;
% Function parameters
funParam=inputs{paramCount}; paramCount=paramCount+1;
% Base Thickness
geomtb=inputs{paramCount}*1e-3; paramCount=paramCount+1;
% Inlet Temperature
enerBcTin=inputs{paramCount}; paramCount=paramCount+1;
% Type of boundary condition at bottom of base
enerBcType=inputs{paramCount}; paramCount=paramCount+1;
% Value of boundadry condition at bottom of the base
enerBcVal=inputs{paramCount}; paramCount=paramCount+1;
```

```
% Type of boundary condition for momentum
momBcType=inputs{paramCount}; paramCount=paramCount+1;
% Value of boundary condition for momentum
momBcVal=inputs{paramCount}; paramCount=paramCount+1;
% Solid Material
propTypeS=inputs{paramCount}; paramCount=paramCount+1;
% Fluid Material
propTypeF=inputs{paramCount}; paramCount=paramCount+1;
% Number of Basis functions in x
N=inputs{paramCount}; paramCount=paramCount+1;
% Number of Basis functions in z
M=inputs{paramCount}; paramCount=paramCount+1;
% Solver type:
% 1 - Finite Difference
% 2 - Galerkin Method
solverType=inputs{paramCount}; paramCount=paramCount+1;
% Convection scheme:
% 1 - First order upwind
% 2 - Second order upwind
convScheme=inputs{paramCount}; paramCount=paramCount+1;

% Extra inputs for variable heat flux
switch enerBcType
    case 1
        % Sharpness of step input
        enerBcKs = 0;
        % Width of step input
        enerBcWc = 0;
        % Center of step input
        enerBcXc = 0;
        % Add three to counter
        paramCount=paramCount+2;

    case 2
        % Sharpness of step input
        enerBcKs = inputs{paramCount}(1); paramCount=paramCount+1;
        % Width of step input
        enerBcWc = inputs{paramCount}(1); paramCount=paramCount+1;
        % Center of step input
        enerBcXc = inputs{paramCount}(1);

    otherwise
        error('Wrong energy boundary type specification')

end
% Check that all parameters have been inputted
assert(paramCount==maxNumParam,'Input parameters do not match');
% Clear the input cell
clearvars inputs;

tIO = toc(tStart);  % Time to extract data from text file
```

EXTRACT FLUID AND SOLID PROPERTIES

Fluid and solid properties are specified here in SI units.

```
prop=propHandler(propTypeS,propTypeF);
```

GENERATE GRID

```
griddata= gridGen(N,M,solverType);

tGrid = toc(tStart)-tIO;    % Time to generate grid
```

GEOMETRY, REFERENCE AND DERIVED VALUES

```
geom=geomCalc(geomType,geomL,geomW,geomHc,geomD,geomPx,geomPy,geomtb,varParam,poro

tGeom = toc(tStart)-tGrid;  % Time to calculate geometrical parameters
```

INITIALIZE SOLUTION AND GRIDS

```
[ ener, mom, griddata, rundata,util ] = initHSwBase( solverType,
 convScheme, enerBcTin, enerBcType, enerBcVal, enerBcKs, enerBcWc,
 enerBcXc, momBcType, momBcVal, griddata, geom, prop);

tInitialized = toc(tStart);

--------------- Finite Difference Solver --------------------

------------- 2nd Order Backward Conv Scheme ----------------
```

MOMENTUM SOLUTION

Solve the momentum equation for the superficial velocity

```
tMomStart = tic;

[mom, clos] = vatMomSolver(geom,prop,mom,griddata);
% Copy Re and ff numbers in closure structure
clos.Redh=mom.Redh;

% If the Re is turbulent, print out a warning.
if max(max(mom.Redh)) >= 2300;

    warning(['Turbulent flow. Re_dh = ' num2str(max(max(mom.Redh)))])
```

```
end


tMom = toc(tMomStart);
fprintf('------------------- Momentum Solved -------------------------
 \n')
fprintf('---------------- Execution time %3.3e s ----------------- \n
 \n',tMom)
```

```
Momentum converged 70 total iterations, errM = 9.032e-09 errP =
 2.815e-07
------------------- Momentum Solved -------------------------
---------------- Execution time 7.037e-01 s -----------------
```

NUSSELT NUMBER CALCULATIONS

```
tEnerStart = tic;

clos = nuss(geom,prop,mom,clos);

% Calculate average Nusselt
ener.h = clos.Nudh*prop.f.k./geom.dh;
ener.hAve = trapz(griddata.xv,trapz(griddata.zv,ener.h,2));
ener.hND = ener.h/ener.hAve;
ener.NuAve = ener.hAve * geom.dhAve/prop.f.k;
```

ENERGY SOLUTION

```
%%%%%%%%%%%%%%%% NON-DIMENSIONAL PARAMETERS %%%%%%%%%%%%%%%%%%%%%%%%
%%%%%%
% Temperature nondimensional scale Q/(m_dot*cp)
ener.scaleT=(ener.bc.Q/(mom.mdot(1)*prop.f.cp));

% Non-dimensional heat flux scale tb/(ks*DT);
ener.qScale = geom.tb/(prop.s.k*(ener.scaleT));

% Porosity weighted thermal conductivity ratio
ener.Rk=geom.epscAve*prop.s.k/(geom.epsAve*prop.f.k);

%%%%%%%%%%%% Fluid equation non dimensional parameters  %%%%%%%%%%%%
%%%%%%
% Convective Term Non-Dimensional Constant
ener.G1 = mom.ReAve*prop.f.Pr/(2*ener.NuAve)*(geom.Cx/geom.epsAve);
% x diffusion Term Constant
ener.G2 = (geom.Cx^2)/ener.NuAve;
% z diffusion Term Constant
ener.G3 = (geom.Cz^2)/ener.NuAve;
% Inter REV transfer Matrix
ener.G4 = ener.hND.*geom.SwND;

%%%%%%%%%%%% Solid equation non dimensional parameters  %%%%%%%%%%%%
%%%%%%
```

```
% x diffusion Term Constant
if geom.conn ==0;       % Disconnected geometry
    ener.C1=0;
elseif geom.conn ==1;   % Connected geometry
    ener.C1=ener.Rk/ener.NuAve*geom.Cx^2;
end

% z diffusion Term Constant
ener.C2 = ener.Rk/ener.NuAve*geom.Cz^2;

% Inter REV transfer Matrix
ener.C3 = ener.hND.*geom.SwND;


%%%%%%%%%%%%%%%% Interface nondimensional parameters   %%%%%%%%%%%%%%
%%%%%%
ener.K1 = geom.epscAve.*geom.tb/geom.Hc;
ener.K2 = 1/ener.Rk*geom.epscAve.*geom.tb/geom.Hc;

%%%%%%%%%%%%%%%% Apply nondimensionalization %%%%%%%%%%%%%%%%%%%%%%%%
%%%%%%
% Non-dimensionalize heat flux
ener.qAveND = ener.bc.qAve*ener.qScale;
ener.bc.D = ener.bc.D.*ener.qScale;

%%%%%%%%%%%%%%%% SOLVE EQUATIONS %%%%%%%%%%%%%%%%%%%%%%%%%%%%%%%%%%%%
%%%%%%
% Perturbation size
eps_b = 0.01;

switch rundata.solver
    case 'Finite Difference'
        % Guess initial bottom temperature coefficients
        B=zeros(griddata.Nx+1,1);
        B(1)=1; % Constant temperature equal to 1

        % Perturbe coefficients by eps_b
        B1 = [B repmat(B,1,griddata.Nx+1)+diag(eps_b*ones(griddata.Nx
+1,1))];

        % Reconstruct bottom wall temperature on the grid
        scalingFactor=sqrt(2/(N+1))*ones(N+1,N+2);
        scalingFactor(1,:)=sqrt(1/(N+1))*ones(1,N+2);
        Twall=idct(B1./scalingFactor);

        % Obtain flux for all inputs

 soln=FDSolver(rundata.convScheme,ener,mom,geom,griddata,Twall);

        % Take DCT of the flux
        soln.s=dct(repmat(geom.epscND(:,1),1,griddata.Nx
+2).*soln.DTsDz);
        soln.f=dct(repmat(geom.epsND(:,1),1,griddata.Nx
+2).*soln.DTfDz);
```

```
        % Scale
        soln.s=soln.s.*scalingFactor;
        soln.f=soln.f.*scalingFactor;

        % Generate vector to account for different value for n=0 of
 cosine
        delC = [1; 0.5*ones(griddata.N,1)];
        % phi value for base
        phi = ((0:griddata.N)*pi)';
        % Calculate value of interface condition with initial guess B
        f0 =
 (ener.K1.*delC).*soln.s(:,1)+(ener.K2.*delC).*soln.f(:,1)-
(delC.*geom.Sb.*phi).*(ener.bc.D
+B.*tanh(geom.Sb*phi))+ener.qAveND.*[1;zeros(griddata.N,1)];

        % Calculate influence matrix
        infM=zeros(griddata.N+1,griddata.N+1);
        for i=2:griddata.N+2    % Calculate Jacobian entries Jij=fij-
f0
            infM(:,i-1) =
 (ener.K1.*delC).*soln.s(:,i)+(ener.K2.*delC).*soln.f(:,i)-
(delC.*geom.Sb.*phi).*(ener.bc.D
+B1(:,i).*tanh(geom.Sb*phi))+ener.qAveND.*[1;zeros(griddata.N,1)]-f0;
        end

        % Divide influence matrix by perturbation size
        infM = infM./eps_b;
        % Clear B1 variable
        clearvars B1;

        % Solve for dB
        dB = -infM\f0;
        % Calculate new interface coefficients
        B = B + dB;

        % Reconstruct wall temperature on grid with new coefficients
        Twall=idct(B./scalingFactor(:,1));

        % Evaluate f with new B

 soln=FDSolver(rundata.convScheme,ener,mom,geom,griddata,Twall);

        % Take DCT of the flux
        soln.s=dct(geom.epscND(:,1).*soln.DTsDz);
        soln.f=dct(geom.epsND(:,1).*soln.DTfDz);

        % Scale
        soln.s=soln.s.*scalingFactor(:,1);
        soln.f=soln.f.*scalingFactor(:,1);

        % Calculate final of interface condition with new B
        fNext = (ener.K1.*delC).*soln.s(:)+(ener.K2.*delC).*soln.f(:)-
(delC.*geom.Sb.*phi).*(ener.bc.D
+B.*tanh(geom.Sb*phi))+ener.qAveND.*[1;zeros(griddata.N,1)];
```

```
        % Calculate residual in interface condition
        errI = norm(fNext,inf);

        % Store final vector of interface coefficients
        soln.B=B;

        tEner = toc(tEnerStart);

        fprintf('-------------------- Energy solved
 ------------------------- \n')
        fprintf('-------------- Max Error in interface %3.3e
 ------------ \n', errI)
        fprintf('-------------- Energy solution time %3.3e s
 ------------ \n \n',tEner)

        % Recombine base basis
        soln=basisRecomb(soln,ener,util,geom,griddata,rundata.solver);

        % Add boundary and match to meshgrid
        Tf = zeros(N+1,M+1);     Tf(2:N+1,2:M+1)=soln.Tf;
        Tf(:,1) = Twall;     soln.Tf = Tf';
        Ts = zeros(N+1,M+1);     Ts(:,2:M+1)=soln.Ts;
        Ts(:,1) = Twall;     soln.Ts = Ts';
        tTot = toc(tStart);
        fprintf('-------------- Total solution time %3.3e s
 ------------ \n \n',tTot)



    case 'Galerkin Method'
        % Extract data for run
        N=rundata.N;
        M=rundata.M;
        % Guess bottom wall temperature
        B=zeros(N+1,1);
        B(1)=1;
        % Compute perturbed solution
        B1 = [B repmat(B,1,N+1)+diag(eps_b*ones(N+1,1))];
        % Calculate coefficients for perturbed solution
        [soln,util]=FGSolver(ener,util,B1);

        % Calculate value of interface condition with initial guess B
        f0 = 1/2*ener.K1*util.Jdelc*reshape(soln.S(:,1),N+1,M
+1)*util.gamZ + ener.K2*util.J2*reshape(soln.F(:,1),N+1,M+1)*util.gamZ
  ...
            - util.Jdelc*(B1(:,1).*tanh(geom.Sb*util.phi)+ener.bc.D) +
 (ener.qAveND+ener.K2*util.gamZ'*soln.I(:,1))*util.k;

        % Calculate Jacobian
        infM=zeros(N+1,N+1);
        for i=2:N+2
            % Calculate Jacobian entries Jij=fij-f0
```

```
            infM(:,i-1) = 1/2*ener.K1*util.Jdelc*reshape(soln.S(:,i),N
+1,M+1)*util.gamZ + ener.K2*util.J2*reshape(soln.F(:,i),N+1,M
+1)*util.gamZ +...
                -
 util.Jdelc*(B1(:,i).*tanh(geom.Sb*util.phi)+ener.bc.D) + (ener.qAveND
+ener.K2*util.gamZ'*soln.I(:,i)).*util.k-f0;

        end
        % Divide Jacobian by perturbation distance
        infM = infM./eps_b;
        % Choose dB by solving the linear system
        dB = -infM\f0;
        % Calculate new interface coefficients
        B = B + dB;
        % Evaluate f with new B
        [soln,util]=FGSolver(ener,util,B);
        % Calculate value of f with new B
        fNext = 1/2*ener.K1*util.Jdelc*(soln.S*util.gamZ) +
 ener.K2*util.J2*(soln.F*util.gamZ)  ...
            - util.Jdelc*(B.*tanh(geom.Sb*util.phi)+ener.bc.D) +
 (ener.qAveND+ener.K2*util.gamZ'*soln.I)*util.k;
        % Calculate residual in f
        errI = norm(fNext,inf);
        tEner = toc(tEnerStart);
        % Store final vector of interface coefficients
        soln.B=B;

        fprintf('---------------- Coefficients Obtained
 ---------------------- \n')
        fprintf('-------------- Max Error in interface %3.3e
 ------------- \n', errI)
        fprintf('----------------- Execution time %3.3e s
 ---------------- \n',tEner)

        soln=basisRecomb(soln,ener,util,geom,griddata,rundata.solver);
        tTot=toc(tStart);

        fprintf('---------------- Solution Evaluated on Grid
 ----------------- \n')
        fprintf('--------------- Total Execution time %3.3e s
 ------------ \n \n',tTot)

    otherwise
        error('Solver type could not be recognized in iterative
 process');
end
```

```
-------------------- Energy solved --------------------------
-------------- Max Error in interface 2.670e-11 -------------
-------------- Energy solution time 3.266e+00 s -------------

-------------- Total solution time 4.960e+00 s  -------------
```

POST-PROCESSING AND PLOTTING

Calculate non-dimensional outlet temperature

```
TfAveOut = trapz(griddata.zv,mom.uSuperf(griddata.Nx
+1,:).*soln.Tf(:,griddata.Nx+1)',2)./
trapz(griddata.zv,mom.uSuperf(griddata.Nx+1,:),2);

% Dimensionalize all quantities
soln.TfAveOut = TfAveOut.*ener.scaleT+ener.bc.Tin;

% Dimensionalize temperatures
soln.Tf=soln.Tf.*ener.scaleT+ener.bc.Tin;
soln.Ts=soln.Ts.*ener.scaleT+ener.bc.Tin;
soln.Tb=soln.Tb.*ener.scaleT+ener.bc.Tin;


postData = postProc(soln,ener,mom,griddata,prop,geom);

% CALCULATE IMBALANCES
% MASS BALANCE
massImb = (trapz(griddata.zv,mom.uND(griddata.Nx
+1,:))-trapz(griddata.zv,mom.uND(1,:))))./
trapz(griddata.zv,mom.uND(griddata.Nx+1,:));
fprintf('The mass imbalance in the system is: %3.2f %%
 \n',massImb*100);
% MOMENTUM BALANCE
% Shear stress at the two walls
SS = trapz(griddata.xv,(3*mom.uND(:,griddata.Nz
+1)-4*mom.uND(:,griddata.Nz)+mom.uND(:,griddata.Nz-1))/
(2*griddata.dz))...
    - trapz(griddata.xv,(-3*mom.uND(:,1)+4*mom.uND(:,2)-mom.uND(:,3))/
(2*griddata.dz));
SS = mom.M1*SS;
% Momentum sink
MS=mom.M2.*mom.uND.^2; MS(isnan(MS))=0;
MS = trapz(griddata.xv,trapz(griddata.zv,MS,2));
% Pressure contour integral
intP = trapz(griddata.xv,trapz(griddata.zv,mom.M3,2));
% Imbalance
momImb = -SS + MS -intP;
fprintf('The momentum imbalance in the system is: %3.2f %%
 \n',momImb*100);

% Calculate heat load from integral VAT energy
HL =
 prop.f.rho*prop.f.cp*geom.Hc*geom.W*(trapz(griddata.zv,mom.uSuperf(griddata.Nx
+1,:).*soln.Tf(:,griddata.Nx+1)')-
trapz(griddata.zv,mom.uSuperf(1,:).*soln.Tf(:,1)'));
% Solid flux
Qs = -
prop.s.k*geom.W*geom.L*geom.epscAve*geom.epscNDzv(1)*trapz(griddata.xv,geom.epscND
soln.Ts(3,:))./(2*griddata.dz*geom.Hc));
```

```
% Fluid flux
Qf = -
prop.f.k*geom.W*geom.L*geom.epsAve*geom.epsNDzv(1)*trapz(griddata.xv,geom.epsNDxv'
soln.Tf(3,:))./(2*griddata.dz*geom.Hc));
% Energy lost to back conduction at inlet
backLoss = -prop.f.k*geom.Hc*geom.W*trapz(griddata.zv,
(-3*soln.Tf(:,1)+4*soln.Tf(:,2)-soln.Tf(:,3))./
(2*griddata.dx*geom.L));
% Energy entering from the base
interfQ = Qs+Qf;
% Imbalance between what is applied to the base and what enters the
 domain
imbalB = (Qs+Qf-ener.bc.Q)/ener.bc.Q;
% Imbalance between what enters the channel and what exits
imbalDomain = (HL-(Qs+Qf+backLoss) ) / interfQ;
fprintf('The given heat input into the base is: %3.3e \n',ener.bc.Q);
fprintf('The heat load entering the channel is: %3.3e \n',interfQ);
fprintf('The imbalance between channel heat input and bottom heat load
 is: %3.2f %% \n',(imbalB*100));
fprintf('The sensible heat input in the channel is: %3.3e \n',HL);
fprintf('The imbalance in the channel domain is: %3.2f %% \n \n',
(imbalDomain*100));


% Extract grid data
x=griddata.x;
z=griddata.z;
xb=griddata.xb;
zb=griddata.zb;
xv=griddata.xv;


plotCount=1;

switch wannaPlot
    case 'yes'
        figure(plotCount)
        surf(x,z,soln.Tf);
        xlabel('x/L')
        ylabel('z/H_c')
        zlabel('T_f')
        title('Fluid Solution')
        plotCount=plotCount+1;

        figure(plotCount)
        surf(x,z,soln.Ts)
        xlabel('x/L')
        ylabel('z/H_c')
        zlabel('T_s')
        title('Solid Solution')
        plotCount=plotCount+1;

        figure(plotCount)
        surf(xb,zb,soln.Tb)
```

```
        xlabel('x/L')
        ylabel('z/t_b')
        zlabel('T_b')
        title('Base Solution')
        plotCount=plotCount+1;

        figure(plotCount)

 plot(xv,soln.Tf(1,:),xv,soln.Ts(1,:),'o',xv,soln.Tb(griddata.Nzb
+1,:),'x')
        xlabel('x/L')
        ylabel('T')
        legend('Fluid','Solid','Base','Location','Best')
        title('Interface Temperature')
        plotCount=plotCount+1;

        figure(plotCount)

 plot(xv,soln.Tb(1,:),xv,soln.Tf(floor(griddata.Nz/2),:),xv,soln.Ts(floor(griddata
        xlabel('x/L')
        ylabel('T')
        legend('Bottom Base Temperature','Fluid T @ z=0.5','Solid T @
 z=0.5','Location','Best')
        plotCount=plotCount+1;

        figure(plotCount)

 plot(soln.Tf(:,floor(griddata.Nx/2)),griddata.zv,soln.Ts(:,floor(griddata.Nx/2)),
        xlabel('z/H')
        ylabel('T')
        legend('Fluid T @ x=0.5','Solid T @ x=0.5','Location','Best')
        plotCount=plotCount+1;

        figure(plotCount)
        surf(griddata.xv,griddata.zv,mom.uIntr')
        xlabel('x/L')
        ylabel('z/Hc')
%         legend('Superficial Velocity','Intersticial Velocity')
        title('Velocity')
        plotCount=plotCount+1;

        figure(plotCount)
        plotyy(griddata.zv,geom.eps,griddata.zv,geom.Sw)
        xlabel('z/H_c')
        legend('Porosity','Specific Surface','Location','Best')
        title('Geometric Parameters')
        plotCount=plotCount+1;

        figure(plotCount)
        fillColor = [0.25 0.25 0.25];
        h=fill([0; -geom.D(1)/2; -geom.D(griddata.Nz+1)/2; 0;
 geom.D(griddata.Nz+1)/2; geom.D(1)/2; 0],[0; 0; geom.Hc; geom.Hc;
 geom.Hc; 0; 0],fillColor);
        title('Fin Profile')
```

```
%         axis equal

        rundata.numFig=plotCount;

    case 'no'
        rundata.numFig=0;
end

% Define the number of figures created by the main code
```

```
The mass imbalance in the system is: 0.00 %
The momentum imbalance in the system is: -0.05 %
The given heat input into the base is: 3.810e+02
The heat load entering the channel is: 3.781e+02
The imbalance between channel heat input and bottom heat load is:
 -0.76 %
The sensible heat input in the channel is: 3.743e+02
The imbalance in the channel domain is: -0.99 %
```

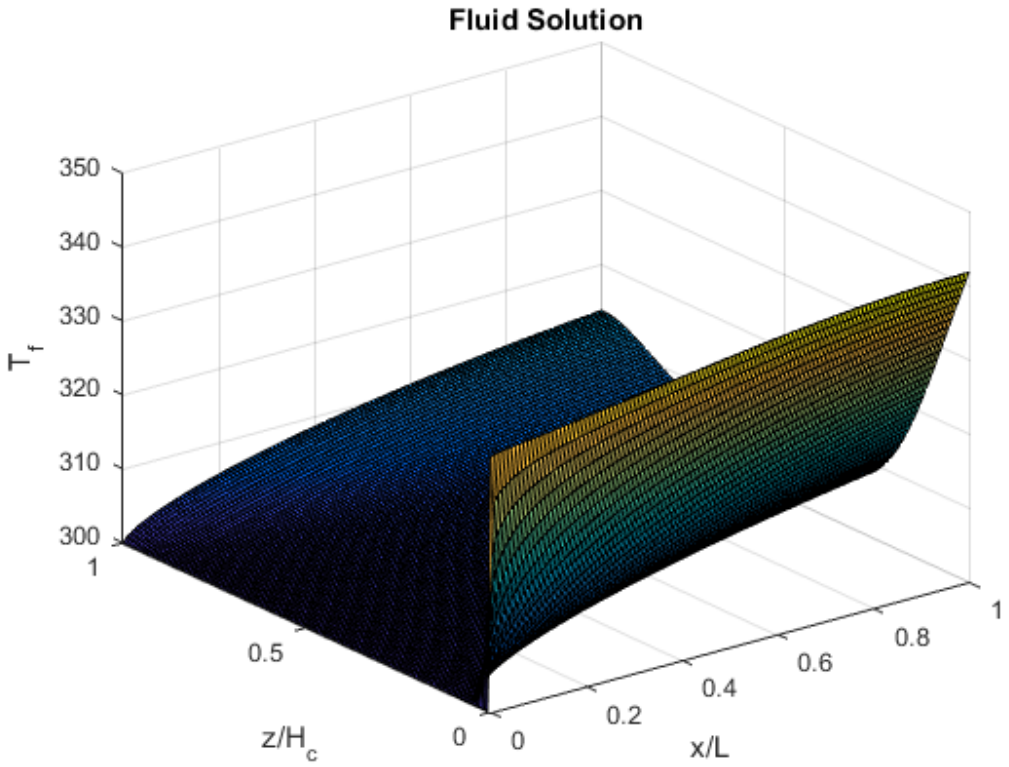

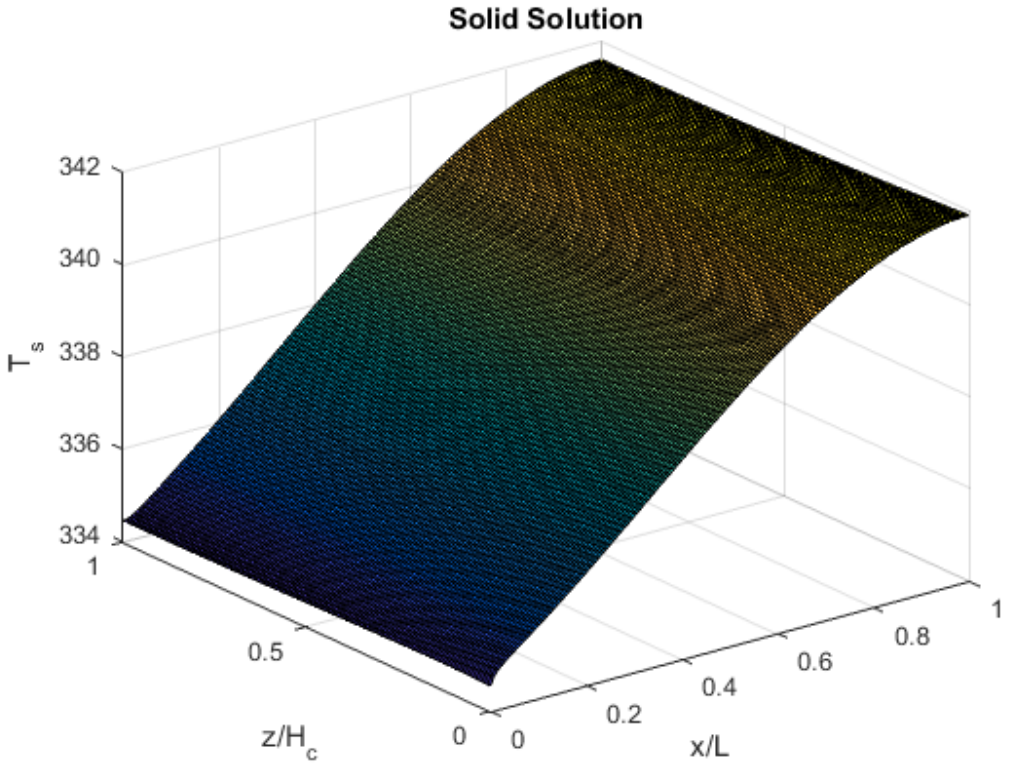
Solid Solution
342
340
338
336
334
T_s
1
0.5
0
z/H_c
0
0.2
0.4
0.6
0.8
1
x/L

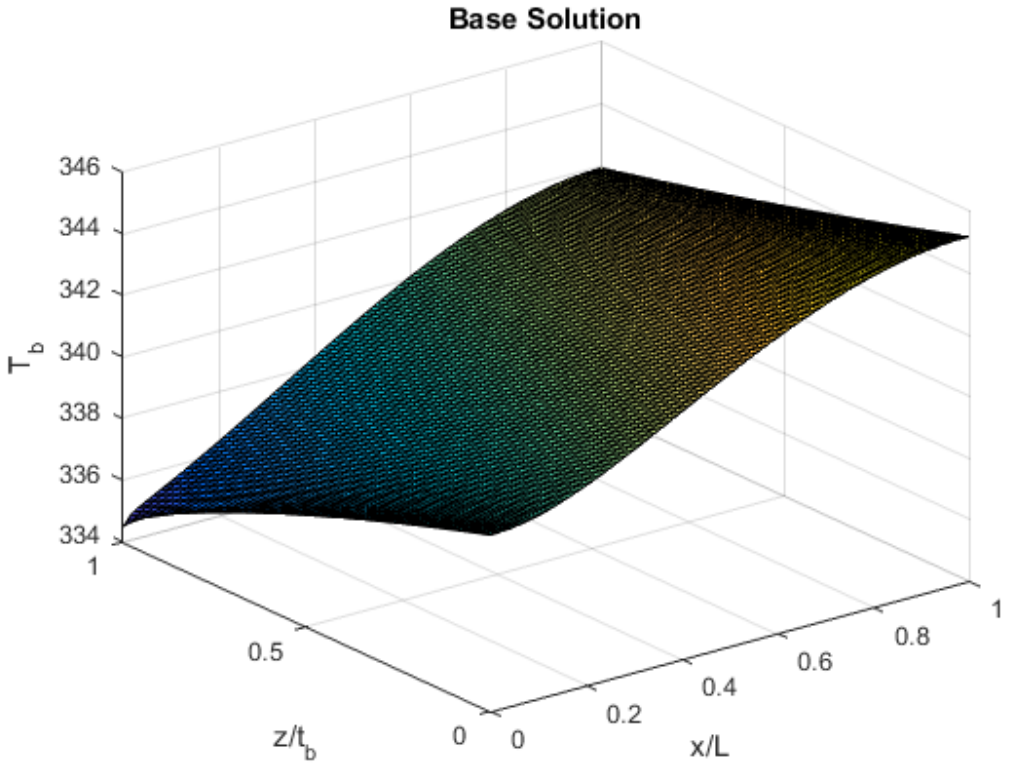
Base Solution
346
344
342
340
338
336
334
T_b
1
0.5
0
z/t_b
0
0.2
0.4
0.6
0.8
1
x/L

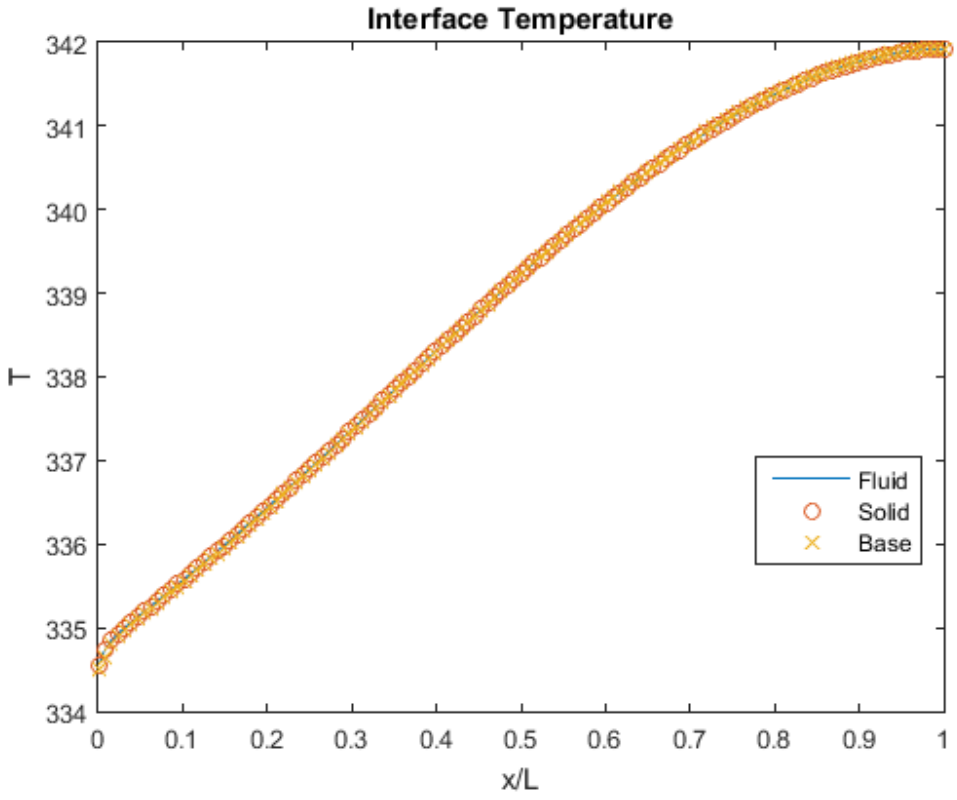
Interface Temperature
342
341
340
339
338
337
336
335
334
T
0
0.1
0.2
0.3
0.4
0.5
0.6
0.7
0.8
0.9
1
x/L
Fluid
Solid
Base

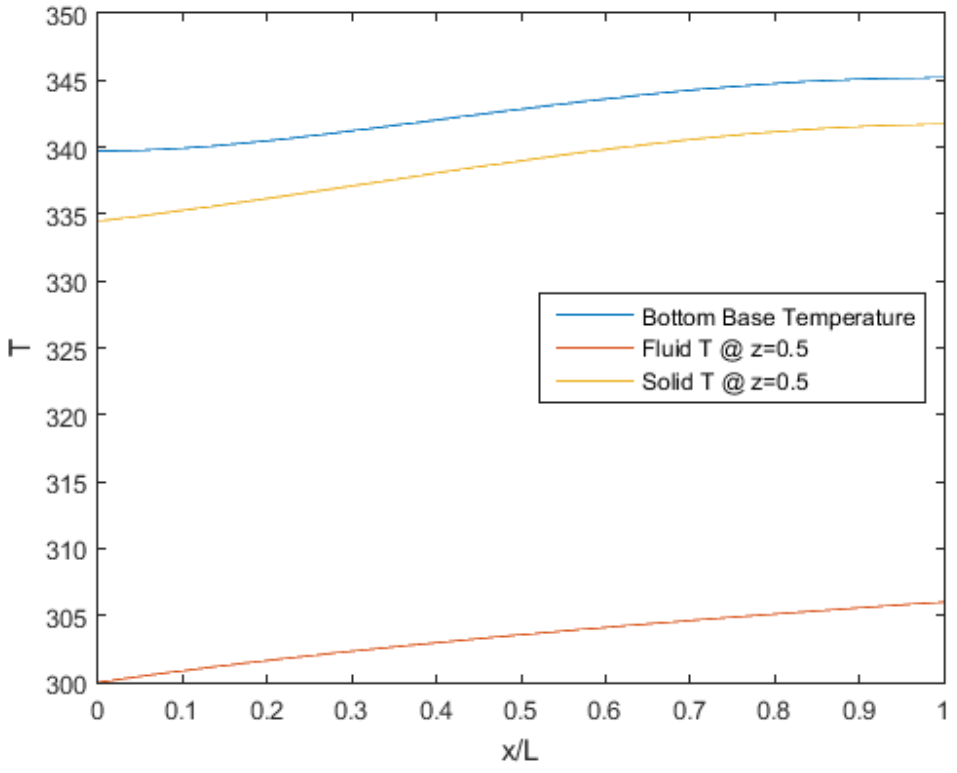
350
345
340
335
330
325
320
315
310
305
300
T
0
0.1
0.2
0.3
0.4
0.5
0.6
0.7
0.8
0.9
1
x/L
Bottom Base Temperature
Fluid T @ z=0.5
Solid T @ z=0.5

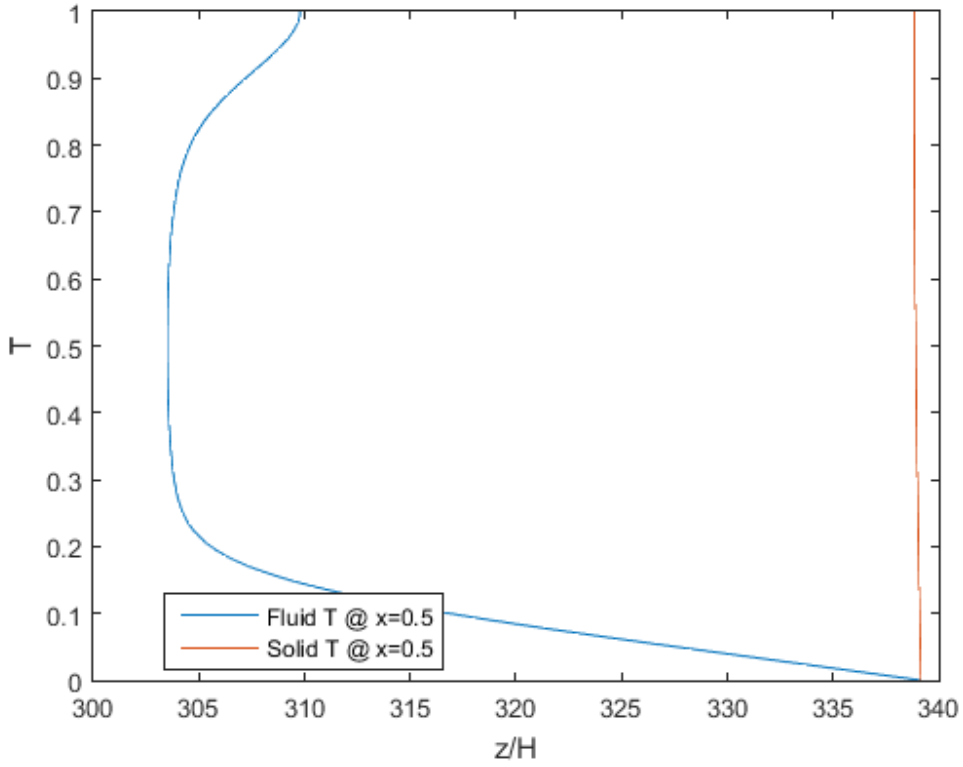
T
z/H
Fluid T @ x=0.5
Solid T @ x=0.5

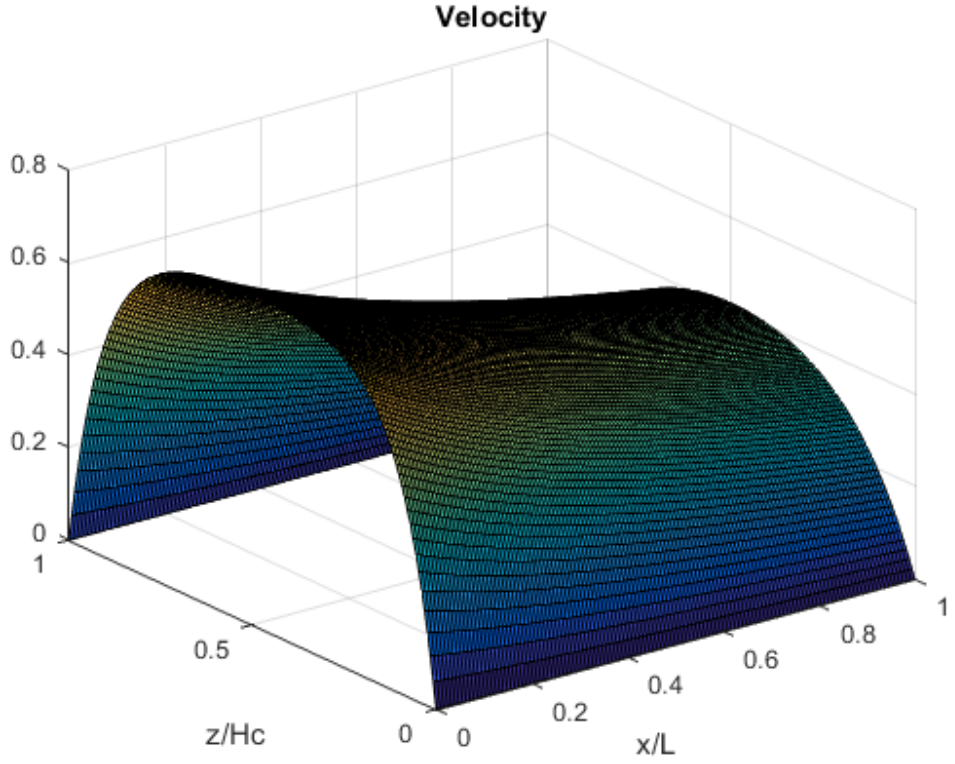
Velocity
z/Hc
x/L

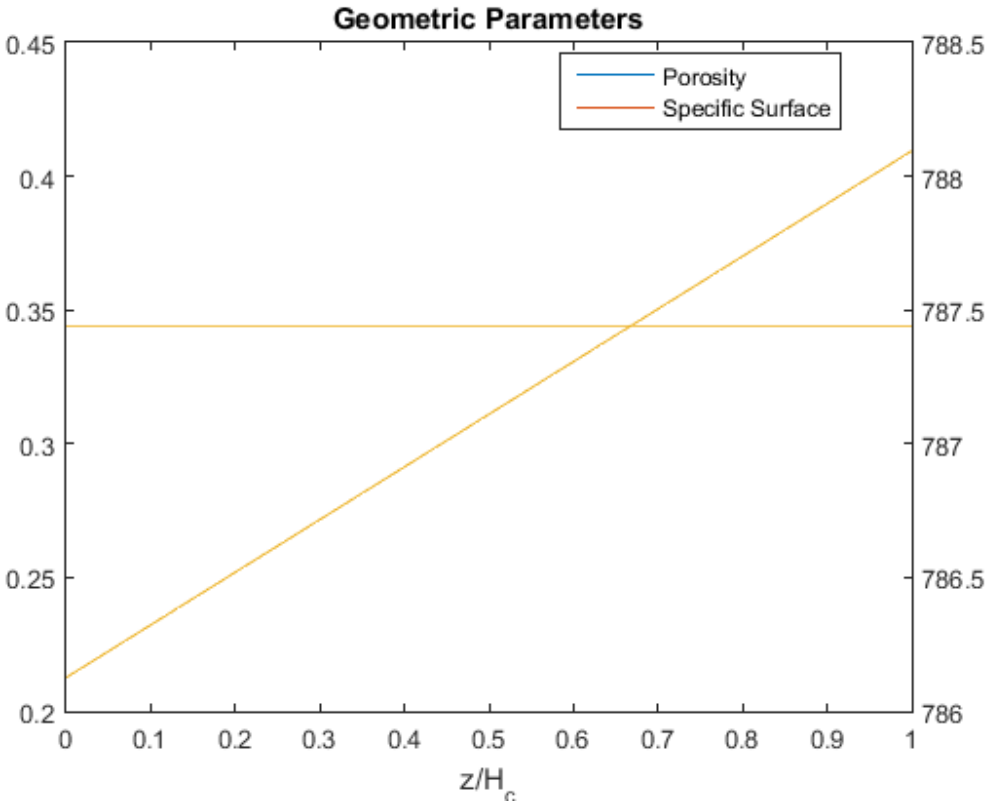
Geometric Parameters
Porosity
Specific Surface
0.45
0.4
0.35
0.3
0.25
0.2
788.5
788
787.5
787
786.5
786
0
0.1
0.2
0.3
0.4
0.5
0.6
0.7
0.8
0.9
1
z/H_c

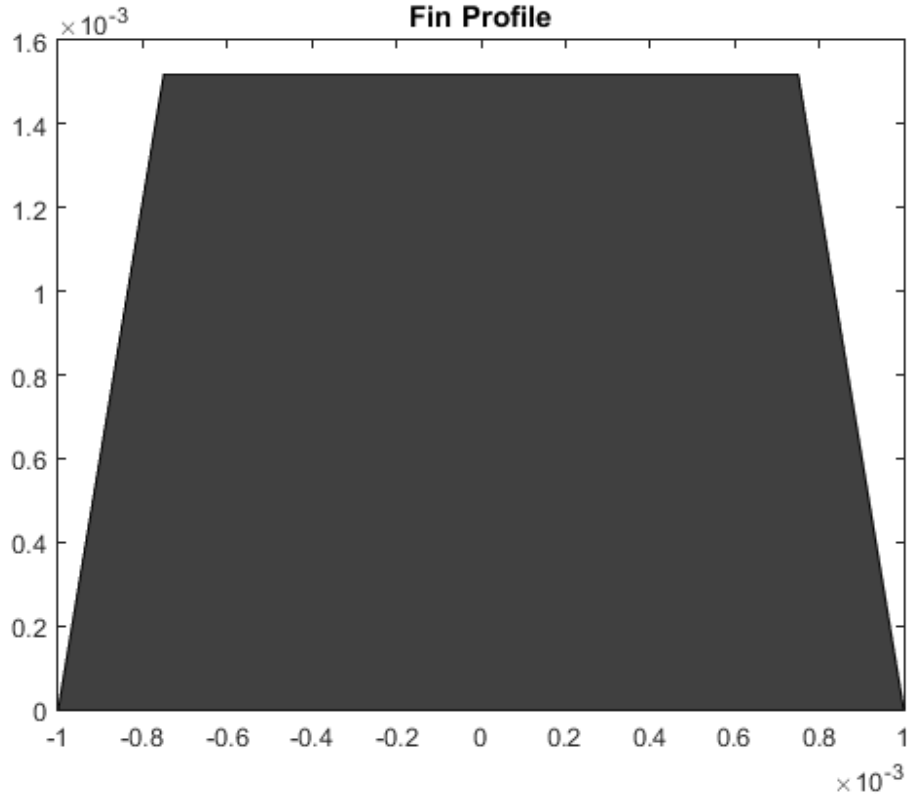
Fin Profile
×10^-3
1.6
1.4
1.2
1
0.8
0.6
0.4
0.2
0
-1
-0.8
-0.6
-0.4
-0.2
0
0.2
0.4
0.6
0.8
1
×10^-3

CALCULATE DATA NECESSARY IN POSTPROCESSING

```
% Save data to outputs structure
outputs.mom=mom;
outputs.geom=geom;
outputs.ener=ener;
outputs.griddata=griddata;
outputs.rundata=rundata;
outputs.clos=clos;
outputs.soln=soln;
outputs.util=util;
outputs.postData=postData;
outputs.prop=prop;
outputs.time=[tInitialized, tGrid, tGeom, tMom, tEner, tTot];


if strcmp(testDef,'')==0;
    % Run specified test
    fprintf('---------------------- Running Tests
 ------------------------ \n \n')
    testHSwB(outputs,testDef,testMode);
else
end

end
```

```
ans =

         mom: [1x1 struct]
        geom: [1x1 struct]
        ener: [1x1 struct]
    griddata: [1x1 struct]
     rundata: [1x1 struct]
        clos: [1x1 struct]
        soln: [1x1 struct]
        util: []
    postData: [1x1 struct]
        prop: [1x1 struct]
        time: [0.9264 0.2901 0.5718 0.7037 3.2658 4.9595]
```

Published with MATLAB® R2015a

References

[1] C. V. N. Index, "Global mobile data traffic forecast update, 2010-2015," *White Paper, February*, 2011.

[2] J. Watson and G. Castro, "High-temperature electronics pose design and reliability challenges." `http://www.analog.com/library/analogdialogue/archives/46-04/high_temp_electronics.html`, 2012.

[3] M. Bach, "Impact of temperature on intel cpu performance." `https://www.pugetsystems.com/labs/articles/Impact-of-Temperature-on-Intel-CPU-Performance-606/`, 2014.

[4] R. C. Chu, "The challenges of electronic cooling: Past, current and future," *Journal of Electronic Packaging*, vol. 126, no. 4, pp. 491–500, 2004.

[5] S. V. Garimella, A. S. Fleischer, J. Y. Murthy, A. Keshavarzi, R. Prasher, C. Patel, S. H. Bhavnani, R. Venkatasubramanian, R. Mahajan, Y. Joshi, B. Sammakia, B. A. Myers, L. Chorosinski, M. Baelmans, P. Sathyamurthy, and P. E. Raad, "Thermal challenges in next-generation electronic systems," *Components and Packaging Technologies, IEEE Transactions on*, vol. 31, no. 4, pp. 801–815, 2008.

[6] R. Hannemann, "Thermal control for mini- and microcomputers: the limits of air cooling," *Bulletin of the International Centre for Heat and Mass Transfer*, vol. 3, pp. 65–83, 1989.

[7] K. Azar, *LIMITS OF AIR COOLINGA METHODICAL APPROACH*. CRC Press, Boca Raton, FL, 1996.

[8] K. Azar, "The thermal millennium!," *Electronics Cooling*, vol. 6, no. 1, p. 1, 2000.

[9] K. Azar, "Advanced cooling concepts and their challenges," in *Int. Workshop Thermal Investigations ICs and Systems (THERMINIC), Madrid, Spain*, 2002.

[10] K. A. Gardner, "Efficiency of extended surface," *American Society of Mechanical Engineers – Transactions*, vol. 67, no. 8, pp. 621–628, 1945.

[11] W. Elenbaas, "Heat dissipation of parallel plates by free convection," *Physica*, vol. 9, no. 1, pp. 1–28, 1942.

[12] W. Elenbaas, "Dissipation of heat by free convectionpart ii," *Philips Res. Rept*, vol. 3, pp. 450–465, 1948.

[13] K. Starner and H. McManus Jr, "An experimental investigation of free-convection heat transfer from rectangular-fin arrays," *Journal of Heat Transfer*, vol. 85, p. 273, 1963.

[14] D. Van de Pol and J. Tierney, "Free convection nusselt number for vertical u-shaped channels," *Journal of Heat Transfer*, vol. 95, p. 542, 1973.

[15] T. Aihara and S. Maruyama, "Optimum design of natural cooling heat sinks with vertical rectangular fin arrays," in *Cooling Technology for Electronic Equipment*, pp. 35–54, Hemisphere New York, 1988.

[16] G. Ellison, "Generalized computations of the gray body shape factor for thermal radiation from a rectangular u-channel," *Components, Hybrids, and Manufacturing Technology, IEEE Transactions on*, vol. 2, no. 4, pp. 517–522, 1979.

[17] A. Zukauskas, "Convective heat transfer in cross flow," *Handbook of single-phase convective heat transfer*, pp. 6.1–6.46, 1987.

[18] A. Zukauskas, "Heat transfer from tubes in cross-ow," *advances in heat transfer*, vol. 18, p. 87, 1987.

[19] S. Whitaker, "Forced convection heat transfer correlations for flow in pipes, past flat plates, single cylinders, single spheres, and for flow in packed beds and tube bundles," *AIChE Journal*, vol. 18, no. 2, pp. 361–371, 1972. 10.1002/aic.690180219.

[20] D. B. Tuckerman and R. F. W. Pease, "High-performance heat sinking for vlsi," *Electron Device Letters, IEEE*, vol. 2, no. 5, pp. 126–129, 1981.

[21] W. Qu and I. Mudawar, "Analysis of three-dimensional heat transfer in micro-channel heat sinks," *International Journal of Heat and Mass Transfer*, vol. 45, no. 19, pp. 3973–3985, 2002.

[22] M. B. Bowers and I. Mudawar, "Two-phase electronic cooling using mini-channel and micro-channel heat sinks: part 1design criteria and heat diffusion constraints," *Journal of Electronic Packaging*, vol. 116, no. 4, pp. 290–297, 1994.

[23] K. Dae Whan, E. Rahim, A. Bar-Cohen, and H. Bongtae, "Thermofluid characteristics of two-phase flow in micro-gap channels," in *Thermal and Thermomechanical Phenomena in Electronic Systems, 2008. ITHERM 2008. 11th Intersociety Conference on*, pp. 979–992, IEEE, 2008.

[24] A. Bar-Cohen and E. Rahim, "Modeling and prediction of two-phase refrigerant flow regimes and heat transfer characteristics in microgap channels," in *ASME 2007 5th International Conference on Nanochannels, Microchannels, and Minichannels*, pp. 1141–1160, American Society of Mechanical Engineers, 2007.

[25] R. L. Linton and D. Agonafer, "Coarse and detailed cfd modeling of a finned heat sink," *Components, Packaging, and Manufacturing Technology, Part A, IEEE Transactions on*, vol. 18, no. 3, pp. 517–520, 1995.

[26] C. L. Chapman, S. Lee, and B. L. Schmidt, "Thermal performance of an elliptical pin fin heat sink," in *Semiconductor Thermal Measurement and Management Symposium, 1994. SEMI-THERM X., Proceedings of 1994 IEEE/CPMT 10th*, pp. 24–31, IEEE, 1994.

[27] D. Liu and S. V. Garimella, "Analysis and optimization of the thermal performance of microchannel heat sinks," *International Journal of Numerical Methods for Heat and Fluid Flow*, vol. 15, no. 1, pp. 7–26, 2005.

[28] R. Walchli, T. Brunschwiler, B. Michel, and D. Poulikakos, "Combined local microchannel-scale cfd modeling and global chip scale network modeling for electronics cooling design," *International Journal of Heat and Mass Transfer*, vol. 53, no. 56, pp. 1004–1014, 2010.

[29] S. Whitaker, "Advances in theory of fluid motion in porous media," *Industrial and Engineering Chemistry*, vol. 61, no. 12, pp. 14–28, 1969. doi: 10.1021/ie50720a004.

[30] M. Quintard and S. Whitaker, "Transport in ordered and disordered porous media i: The cellular average and the use of weighting functions," *Transport in Porous Media*, vol. 14, no. 2, pp. 163–177, 1994.

[31] M. Quintard and S. Whitaker, "Transport in ordered and disordered porous media ii: Generalized volume averaging," *Transport in Porous Media*, vol. 14, no. 2, pp. 179–206, 1994.

[32] M. Quintard and S. Whitaker, "Transport in ordered and disordered porous media iii: Closure and comparison between theory and experiment," *Transport in Porous Media*, vol. 15, no. 1, pp. 31–49, 1994.

[33] M. Quintard and S. Whitaker, "Transport in ordered and disordered porous media iv: Computer generated porous media for three-dimensional systems," *Transport in Porous Media*, vol. 15, no. 1, pp. 51–70, 1994.

[34] M. Quintard and S. Whitaker, "Transport in ordered and disordered porous media v: Geometrical results for two-dimensional systems," *Transport in Porous Media*, vol. 15, no. 2, pp. 183–196, 1994.

[35] M. Quintard, F. Cherblanc, and S. Whitaker, "Dispersion in heterogeneous porous media: One-equation non-equilibrium model," *Transport in Porous Media*, vol. 44, no. 1, pp. 181–203, 2001.

[36] W. G. Gray, "A derivation of the equations for multi-phase transport," *Chemical Engineering Science*, vol. 30, no. 2, pp. 229–233, 1975.

[37] W. G. Gray and K. O'Neill, "On the general equations for flow in porous media and their reduction to darcy's law," *Water Resour. Res.*, vol. 12, 1976.

[38] V. S. Travkin and I. Catton, "Transport phenomena in heterogeneous media based on volume averaging theory," *Advances in Heat Transfer*, vol. 34, pp. 1–144, 2001. doi: DOI: 10.1016/S0065-2717(01)80011-3.

[39] V. Travkin and I. Catton, "Turbulent flow and heat transfer modeling in a flat channel with regular highly rough walls," *International Journal of Fluid Mechanics Research*, vol. 27, no. 2-4, 2000.

[40] V. S. Travkin, I. Catton, and L. Gratton, "Single phase turbulent transport in prescribed non-isotropic and stochastic porous media," *ASME-PUBLICATIONS-HTD*, vol. 240, pp. 43–43, 1993.

[41] V. Travkin and I. Catton, "A two-temperature model for turbulent flow and heat transfer in a porous layer," *Journal of Fluids Engineering*, vol. 117, no. 1, pp. 181–188, 1995.

[42] V. Travkin and I. Catton, "Turbulent transport of momentum, heat and mass in a two-level highly porous media," in *INSTITUTION OF CHEMICAL ENGINEERS SYMPOSIUM SERIES*, vol. 135, pp. 399–399, HEMSPHERE PUBLISHING CORPORATION, 1994.

[43] V. Travkin and I. Catton, "Models of turbulent thermal diffusivity and transfer coefficients for a regular packed bed of spheres," *ASME-PUBLICATIONS-HTD*, vol. 193, pp. 15–15, 1992.

[44] A. Horvat and I. Catton, "Modeling of forced convection in an electronic device heat sink as porous media flow," *ASME Conference Proceedings*, vol. 2002, no. 3638X, pp. 207–212, 2002.

[45] A. Horvat and B. Mavko, "Hierarchic modeling of heat transfer processes in heat exchangers," *International Journal of Heat and Mass Transfer*, vol. 48, no. 2, pp. 361–371, 2005. doi: DOI: 10.1016/j.ijheatmasstransfer.2004.08.015.

[46] A. Vadnjal, *Modeling of a heat sink and high heat flux vapor chamber*. Ph.d., University of California, Los Angeles, 2009. Copyright - Copyright ProQuest, UMI Dissertations Publishing 2009 Last updated - 2011-10-26 DOI - 1997562861; 47920981; 66569; 9781109688269; 3401691 First page - n/a.

[47] A. Vadnjal and I. Catton, "Optimization of micro channel morphology," in *2006 ASME International Mechanical Engineering Congress and Exposition, IMECE2006, November 5, 2006 - November 10, 2006*, American Society of Mechanical Engineers, Heat Transfer Division, (Publication) HTD, American Society of Mechanical Engineers, 2006. Compilation and indexing terms, Copyright 2010 Elsevier Inc. 20072310641234 Heat fin design Parallel plates Volume averaging theory (VAT).

[48] F. Kuwahara, Y. Kameyama, S. Yamashita, and A. Nakayama, "Numerical modeling of turbulent flow in porous media using a spatially periodic array," *Journal of Porous Media*, vol. 1, no. 1, 1998.

[49] A. Nakayama, F. Kuwahara, M. Sugiyama, and G. Xu, "A two-energy equation model for conduction and convection in porous media," *International journal of heat and mass transfer*, vol. 44, no. 22, pp. 4375–4379, 2001.

[50] F. Kuwahara, A. Nakayama, and H. Koyama, "A numerical study of thermal dispersion in porous media," *Journal of Heat Transfer*, vol. 118, no. 3, pp. 756–761, 1996.

[51] F. Kuwahara, M. Shirota, and A. Nakayama, "A numerical study of interfacial convective heat transfer coefficient in two-energy equation model for convection in porous media," *International Journal of Heat and Mass Transfer*, vol. 44, no. 6, pp. 1153–1159, 2001.

[52] O. A. Plumb and S. Whitaker, "Dispersion in heterogeneous porous media 1. local volume averaging and large-scale averaging," *Water Resour. Res.*, vol. 24, 1988.

[53] M. Quintard and S. Whitaker, "Transport in chemically and mechanically heterogeneous porous media. i: Theoretical development of region-averaged equations for slightly compressible single-phase flow," *Advances in Water Resources*, vol. 19, no. 1, pp. 29 – 47, 1996.

[54] B. Goyeau, T. Benihaddadene, D. Gobin, and M. Quintard, "Averaged momentum equation for flow through a nonhomogenenous porous structure," *Transport in Porous Media*, vol. 28, no. 1, pp. 19–50, 1997.

[55] J. Cushman and T. R. Ginn, "Nonlocal dispersion in media with continuously evolving scales of heterogeneity," *Transport in Porous Media*, vol. 13, no. 1, pp. 123–138, 1993.

[56] M. Sahraoui and M. Kaviany, "Slip and no-slip velocity boundary conditions at interface of porous, plain media," *International Journal of Heat and Mass Transfer*, vol. 35, no. 4, pp. 927–943, 1992.

[57] A. Horvat and I. Catton, "Application of galerkin method to conjugate heat transfer calculation," *Numerical Heat Transfer: Part B: Fundamentals*, vol. 44, no. 6, pp. 509–531, 2003.

[58] K. Hu, *Flow and heat transfer over rough surfaces in porous media*. Ph.d., University of California, Los Angeles, 2002. Copyright - Copyright UMI - Dissertations Publishing 2002 Last updated - 2014-01-21 First page - n/a.

[59] D. Nield and A. Kuznetsov, "Local thermal nonequilibrium effects in forced convection in a porous medium channel: a conjugate problem," *International journal of heat and mass transfer*, vol. 42, no. 17, pp. 3245–3252, 1999.

[60] L. Gosselin and A. Bejan, "Tree networks for minimal pumping power," *International Journal of Thermal Sciences*, vol. 44, no. 1, pp. 53–63, 2005.

[61] D. Pence, "Reduced pumping power and wall temperature in microchannel heat sinks with fractal-like branching channel networks," *Microscale Thermophysical Engineering*, vol. 6, no. 4, pp. 319–330, 2003.

[62] C. A. Rubio-Jimenez, S. G. Kandlikar, and A. Hernandez-Guerrero, "Numerical analysis of novel micro pin fin heat sink with variable fin density," *Components, Packaging and Manufacturing Technology, IEEE Transactions on*, vol. 2, no. 5, pp. 825–833, 2012.

[63] A. Bejan and S. Lorente, "The constructal law and the thermodynamics of flow systems with configuration," *International Journal of Heat and Mass Transfer*, vol. 47, no. 1416, pp. 3203–3214, 2004.

[64] Y. Davit, C. G. Bell, H. M. Byrne, L. A. Chapman, L. S. Kimpton, G. E. Lang, K. H. Leonard, J. M. Oliver, N. C. Pearson, and R. J. Shipley, "Homogenization via formal multiscale asymptotics and volume averaging: How do the two techniques compare?," *Advances in Water Resources*, vol. 62, pp. 178–206, 2013.

[65] S. S. Girimaji, "Partially-averaged navier-stokes model for turbulence: A reynolds-averaged navier-stokes to direct numerical simulation bridging method," *Journal of Applied Mechanics*, vol. 73, no. 3, pp. 413–421, 2006.

[66] Y. Sone, K. Aoki, S. Takata, H. Sugimoto, and A. V. Bobylev, "Inappropriateness of the heatconduction equation for description of a temperature field of a stationary gas in the continuum limit: Examination by asymptotic analysis and numerical computation of the boltzmann equation," *Physics of Fluids (1994-present)*, vol. 8, no. 2, pp. 628–638, 1996.

[67] S. Whitaker, *The method of volume averaging*. Dordrecht: Kluwer Academic Publishers, 1999.

[68] S. Whitaker, "Diffusion and dispersion in porous media," *AIChE Journal*, vol. 13, no. 3, pp. 420–427, 1967.

[69] M. Quintard and S. Whitaker, "Two-phase flow in heterogeneous porous media: The method of large-scale averaging," *Transport in Porous Media*, vol. 3, no. 4, pp. 357–413, 1988.

[70] H. Darcy, "Les fontaines publiques de la ville de dijon," 1856.

[71] H. Brinkman, "On the permeability of media consisting of closely packed porous particles," *Applied Scientific Research*, vol. 1, no. 1, pp. 81–86, 1949.

[72] P. Forchheimer, "Wasserbewegungd urch der boden," *VDI Z*, no. 49, pp. 1736–1749, 1901.

[73] J. C. Slattery, "Flow of viscoelastic fluids through porous media," *AIChE Journal*, vol. 13, no. 6, pp. 1066–1071, 1967. 10.1002/aic.690130606.

[74] C. Marle, "Ecoulements monophasiques en milieu poreux," *Rev. Inst. Francais du Petrole*, vol. 22, no. 10, pp. 1471–1509, 1967.

[75] P. Zolotarev and L. Radushkevich, "An approximate analytical solution of the internal diffusion problem of dynamic absorption in the linear region of an isotherm," *Russian Chemical Bulletin*, vol. 17, no. 8, pp. 1818–1820, 1968.

[76] R. G. Carbonell and S. Whitaker, *Heat and Mass Transfer in Porous Media*, vol. 82 of *NATO ASI Series*, book section 3, pp. 121–198. Springer Netherlands, 1984.

[77] O. A. Plumb and S. Whitaker, "Diffusion, adsorption and dispersion in porous media: Small-scale averaging and local volume averaging," *Dynamics of Fluids in Hierarchical Porous Media*, vol. Academic Press, Inc., no. San Diego, California, pp. 97–148, 1990.

[78] J. Bear, *Dynamics of Fluids in Porous Media*. Civil and Mechanical Engineering, New York: Elsevier, 1998.

[79] M. Kaviany, *Principles of Heat Transfer in Porous Media*. Springer, 2nd ed., 1995.

[80] A. Nakayama and F. Kuwahara, "A quasi-three-dimensional numerical calculation procedure for periodically fully-developed heat and fluid flow," *International Journal of Numerical Methods for Heat and Fluid Flow*, vol. 15, no. 4, pp. 379–393, 2005.

[81] A. Nakayama and F. Kuwahara, *Three-Dimensional Flow and Heat Transfer within Highly Anisotropic Porous Media*, pp. 235–265. CRC Press, 2005. doi:10.1201/9780415876384.ch6.

[82] C. T. Hsu and P. Cheng, "Thermal dispersion in a porous medium," *International Journal of Heat and Mass Transfer*, vol. 33, no. 8, pp. 1587–1597, 1990.

[83] J. A. Ochoa-Tapia and S. Whitaker, "Momentum transfer at the boundary between a porous medium and a homogeneous fluidi. theoretical development," *International Journal of Heat and Mass Transfer*, vol. 38, no. 14, pp. 2635–2646, 1995.

[84] M. d. Lemos, *Turbulence in Porous Media*. Elsevier, 2006.

[85] D. Lasseux, A. Ahmadi, X. Cleis, and J. Garnier, "A macroscopic model for species transport during in vitro tissue growth obtained by the volume averaging method," *Chemical engineering science*, vol. 59, no. 10, pp. 1949–1964, 2004.

[86] K. Khanafer and K. Vafai, "The role of porous media in biomedical engineering as related to magnetic resonance imaging and drug delivery," *Heat and mass transfer*, vol. 42, no. 10, pp. 939–953, 2006.

[87] A. Nakayama and F. Kuwahara, "A general bioheat transfer model based on the theory of porous media," *International Journal of Heat and Mass Transfer*, vol. 51, no. 1112, pp. 3190–3199, 2008.

[88] A. Nakayama, F. Kuwahara, and W. Liu, "A macroscopic model for countercurrent bioheat transfer in a circulatory system," *Journal of Porous Media*, vol. 12, no. 4, pp. 289–300, 2009.

[89] A. Nakayama, F. Kuwahara, and W. Liu, "A general set of bioheat transfer equations based on the volume averaging theory," *Porous Media: Applications in Biological Systems and Biotechnology*, pp. 1–44, 2011.

[90] K. Khanafer, A. AlAmiri, I. Pop, and J. L. Bull, *Flow and heat transfer in biological tissues: application of porous media theory*, pp. 237–259. Springer, 2008.

[91] K. Khanafer and K. Vafai, *Macromolecular transport in arterial walls: current and future directions*, pp. 219–235. Springer, 2008.

[92] M. Hassanizadeh and W. G. Gray, "General conservation equations for multi-phase systems: 1. averaging procedure," *Advances in Water Resources*, vol. 2, pp. 131–144, 1979.

[93] P. Adler, *Porous Media: Geometry and Transports*. Butterworth-Heinemann, 1992.

[94] H. Brenner, "Dispersion resulting from flow through spatially periodic porous media," *Philosophical Transactions of the Royal Society of London*, vol. 297, no. 1430, pp. 81–133, 1980.

[95] J. Slattery, *Momentum, energy, and mass transfer in continua*. McGraw-Hill New York, 1972.

[96] H. Bertin, M. Quintard, V. Corpel, and S. Whitaker, "Two-phase flow in heterogeneous porous media iii: Laboratory experiments for flow parallel to a stratified system," *Transport in Porous Media*, vol. 5, no. 6, pp. 543–590, 1990.

[97] M. Quintard and S. Whitaker, "Two-phase flow in heterogeneous porous media i: The influence of large spatial and temporal gradients," *Transport in Porous Media*, vol. 5, no. 4, pp. 341–379, 1990.

[98] M. Quintard and S. Whitaker, "Two-phase flow in heterogeneous porous media ii: Numerical experiments for flow perpendicular to a stratified system," *Transport in Porous Media*, vol. 5, no. 5, pp. 429–472, 1990.

[99] S. Whitaker, *Coupled Transport in Multiphase Systems: A Theory of Drying*, vol. Volume 31, pp. 1–104. Elsevier, 1998.

[100] D. Nield, "Modelling high speed flow of a compressible fluid in a saturated porous medium," *Transport in Porous Media*, vol. 14, no. 1, pp. 85–88, 1994.

[101] J. P. Harvey, *Oscillatory compressible flow and heat transfer in porous media: application to cryocooler regenerators*. PhD thesis, Georgia Institute of Technology, 2003.

[102] P. a. Moin, K. Squires, W. Cabot, and S. Lee, "A dynamic subgrid-scale model for compressible turbulence and scalar transport," *Physics of Fluids A: Fluid Dynamics (1989-1993)*, vol. 3, no. 11, pp. 2746–2757, 1991.

[103] W. A. Sirignano, "Volume averaging for the analysis of turbulent spray flows," *International journal of multiphase flow*, vol. 31, no. 6, pp. 675–705, 2005.

[104] F. Zhou, *Development of Closure for Heat Exchangers Based on Volume Averaging Theory*. PhD thesis, UCLA, 2014.

[105] S. Ergun, "Fluid flow through packed columns," *Chemical Engineering Progress*, vol. 48, no. 2, pp. 89–94, 1952. Compilation and indexing terms, Copyright 2009 Elsevier Inc. 19520007399.

[106] H. P. A. Souto and C. Moyne, "Dispersion in two-dimensional periodic porous media. part i. hydrodynamics," *Physics of Fluids (1994-present)*, vol. 9, no. 8, pp. 2243–2252, 1997.

[107] H. P. A. Souto and C. Moyne, "Dispersion in two-dimensional periodic porous media. part ii. dispersion tensor," *Physics of Fluids (1994-present)*, vol. 9, no. 8, pp. 2253–2263, 1997.

[108] I. Macdonald, M. El-Sayed, K. Mow, and F. Dullien, "Flow through porous media-the ergun equation revisited," *Industrial and Engineering Chemistry Fundamentals*, vol. 18, no. 3, pp. 199–208, 1979.

[109] J. P. Du Plessis and S. Woudberg, "Pore-scale derivation of the ergun equation to enhance its adaptability and generalization," *Chemical Engineering Science*, vol. 63, no. 9, pp. 2576–2586, 2008.

[110] F. Zhou and I. Catton, "Numerical evaluation of flow and heat transfer in plate-pin fin heat sinks with various pin cross-sections," *Numerical Heat Transfer, Part A: Applications*, vol. 60, no. 2, pp. 107–128, 2011.

[111] F. Zhou and I. Catton, "Volume averaging theory (vat) based modeling and closure evaluation for fin-and-tube heat exchangers," *Heat and Mass Transfer*, vol. 48, no. 10, pp. 1813–1823, 2012.

[112] F. Zhou and I. Catton, "A numerical investigation of turbulent flow and heat transfer in rectangular channels with elliptic scale-roughened walls," *Journal of Heat Transfer*, vol. 135, no. 8, p. 081901(9), 2013.

[113] F. Zhou, G. W. DeMoulin, D. J. Geb, and I. Catton, "Modeling of pin fin heat sinks based on volume averaging theory," in *ASME-JSME-KSME 2011 Joint Fluids Engineering Conference*, pp. 1357–1365, American Society of Mechanical Engineers, 2011.

[114] F. Zhou, G. W. DeMoulin, D. J. Geb, and I. Catton, "Closure for a plane fin heat sink with scale-roughened surfaces for volume averaging theory (vat) based modeling," *International Journal of Heat and Mass Transfer*, vol. 55, no. 2526, pp. 7677–7685, 2012.

[115] F. Zhou, D. Geb, and I. Catton, "Cooling performance comparisons of five different plate-pin compound heat sinks based on two different length scale," in *ASME 2011 Pacific Rim Technical Conference and Exhibition on Packaging and Integration of Electronic and Photonic Systems*, pp. 47–57, American Society of Mechanical Engineers, 2011.

[116] F. Zhou, D. Geb, and I. Catton, "Numerical investigation on air side performance of fin-and-tube heat exchangers with large diameter tubes and large number of tube rows," in *ASME 2011 International Mechanical Engineering Congress and Exposition*, pp. 805–813, American Society of Mechanical Engineers, 2011.

[117] F. Zhou, G. W. DeMoulin, D. J. Geb, and I. Catton, "Modeling of pin fin heat sinks based on volume averaging theory," in *ASME-JSME-KSME 2011 Joint Fluids Engineering Conference*, pp. 1357–1365, American Society of Mechanical Engineers, 2011.

[118] F. Zhou, N. Hansen, and I. Catton, "Determining the computational domain length to obtain closure for vat based modeling by 3d numerical simulation and field synergy analysis," in *ASME 2010 International Mechanical Engineering Congress and Exposition*, pp. 593–602, American Society of Mechanical Engineers, 2010.

[119] F. Zhou, N. Hansen, and I. Catton, "Obtaining closure for heat exchanger modeling based on volume averaging theory (vat)," in *2010 14th International Heat Transfer Conference*, pp. 693–701, American Society of Mechanical Engineers, 2010.

[120] F. Zhou, N. Hansen, and I. Catton, "Vat based modeling of heat exchanger and obtaining closure from cfd solution," in *ASME 2010 International Mechanical Engineering Congress and Exposition*, pp. 583–591, American Society of Mechanical Engineers, 2010.

[121] F. Zhou, N. Hansen, and I. Catton, "Numerical predictions of thermal and hydraulic performances of heat sinks with enhanced heat transfer capability," in *Proc. ASME/JSME 2011 8th Thermal Engineering Joint Conference, AJTEC*, 2011.

[122] F. Zhou, N. Hansen, and I. Catton, "Vat based modeling of plate-pin fin heat sink and obtaining closure from cfd solution," in *ASME/JSME 2011 8th Thermal Engineering Joint Conference*, pp. T10085–T10085, American Society of Mechanical Engineers, 2011.

[123] F. Zhou, N. E. Hansen, D. J. Geb, and I. Catton, "Determination of the number of tube rows to obtain closure for volume averaging theory based model of fin-and-tube heat exchangers," *Journal of Heat Transfer*, vol. 133, no. 12, p. 121801, 2011.

[124] F. Zhou, N. E. Hansen, D. J. Geb, and I. Catton, "Obtaining closure for fin-and-tube heat exchanger modeling based on volume averaging theory (vat)," *Journal of Heat Transfer*, vol. 133, no. 11, p. 111802, 2011.

[125] G. Taylor, "Dispersion of soluble matter in solvent flowing slowly through a tube," in *Proceedings of the Royal Society of London A: Mathematical, Physical and Engineering Sciences*, vol. 219, pp. 186–203, The Royal Society, 1953.

[126] R. Aris, "On the dispersion of a solute in a fluid flowing through a tube," in *Proceedings of the Royal Society of London A: Mathematical, Physical and Engineering Sciences*, vol. 235, pp. 67–77, The Royal Society, 1967.

[127] F. Kuwahara, C. Yang, K. Ando, and A. Nakayama, "Exact solutions for a thermal nonequilibrium model of fluid saturated porous media based on an effective porosity," *Journal of Heat Transfer*, vol. 133, no. 11, p. 112602, 2011.

[128] F. Kuwahara, Y. Sano, J. Liu, and A. Nakayama, "A porous media approach for bifurcating flow and mass transfer in a human lung," *Journal of Heat Transfer*, vol. 131, no. 10, p. 101013, 2009.

[129] A. Nakayama, F. Kuwahara, and T. Hayashi, "Numerical modelling for three-dimensional heat and fluid flow through a bank of cylinders in yaw," *Journal of Fluid Mechanics*, vol. 498, pp. 139–159, 2004.

[130] C. Yang and A. Nakayama, "A synthesis of tortuosity and dispersion in effective thermal conductivity of porous media," *International Journal of Heat and Mass Transfer*, vol. 53, no. 15, pp. 3222–3230, 2010.

[131] C. Hsu and P. Cheng, "Closure schemes of the macroscopic energy equation for convective heat transfer in porous media," *International communications in heat and mass transfer*, vol. 15, no. 5, pp. 689–703, 1988.

[132] A. G. Dixon and D. L. Cresswell, "Theoretical prediction of effective heat transfer parameters in packed beds," *AIChE Journal*, vol. 25, no. 4, pp. 663–676, 1979.

[133] M. Quintard and S. Whitaker, "One-and two-equation models for transient diffusion processes in two-phase systems," *Advances in heat transfer*, vol. 23, no. C, pp. 369–464, 1993.

[134] M. Quintard, M. Kaviany, and S. Whitaker, "Two-medium treatment of heat transfer in porous media: numerical results for effective properties," *Advances in Water Resources*, vol. 20, no. 2, pp. 77–94, 1997.

[135] D. Handley and P. Heggs, "Momentum and heat transfer mechanisms in regular shaped packings," *Transactions of the Institution of Chemical Engineers and the Chemical Engineer*, vol. 46, no. 9, pp. T251–and, 1968.

[136] N. Wakao and S. Kagei, *Heat and mass transfer in packed beds*, vol. 1. Taylor and Francis, 1982.

[137] D. Geb, A. Lerro, K. Sbutega, and I. Catton, "Internal transport coefficient measurements in random fiber matrix heat exchangers," *Journal of Thermal Science and Engineering Applications*, vol. 6, no. 1, p. 011005, 2014.

[138] D. Geb, *Hierarchical Modeling for Population-Based Heat Exchanger Design.* PhD thesis, UCLA, 2013.

[139] D. J. Geb and I. Catton, "Non-intrusive heat transfer coefficient determination in a packed bed of spheres," *ASME Conference Proceedings*, vol. 2010, no. 49415, pp. 901–910, 2010.

[140] J. A. Ochoa-Tapia and S. Whitaker, "Momentum transfer at the boundary between a porous medium and a homogeneous fluidii. comparison with experiment," *International Journal of Heat and Mass Transfer*, vol. 38, no. 14, pp. 2647–2655, 1995.

[141] J. A. Ochoa-Tapia and S. Whitaker, "Heat transfer at the boundary between a porous medium and a homogeneous fluid," *International Journal of Heat and Mass Transfer*, vol. 40, no. 11, pp. 2691–2707, 1997.

[142] F. J. Valds-Parada, B. Goyeau, and J. A. Ochoa-Tapia, "Jump momentum boundary condition at a fluidporous dividing surface: Derivation of the closure problem," *Chemical Engineering Science*, vol. 62, no. 15, pp. 4025–4039, 2007.

[143] M. Sahraoui and M. Kaviany, "Slip and no-slip temperature boundary conditions at interface of porous, plain media: conduction," *International journal of heat and mass transfer*, vol. 36, no. 4, pp. 1019–1033, 1993.

[144] M. Sahraoui and M. Kaviany, "Slip and no-slip temperature boundary conditions at the interface of porous, plain media convection," *Int. J. Heat Mass Transfer*, vol. 37, no. 6, pp. 1029–1044, 1994.

[145] B. Alazmi and K. Vafai, "Constant wall heat flux boundary conditions in porous media under local thermal non-equilibrium conditions," *International Journal of Heat and Mass Transfer*, vol. 45, no. 15, pp. 3071–3087, 2002.

[146] P.-X. Jiang and X.-C. Lu, "Numerical simulation and theoretical analysis of thermal boundary characteristics of convection heat transfer in porous media," *International Journal of Heat and Fluid Flow*, vol. 28, no. 5, pp. 1144–1156, 2007.

[147] G. R. Imani, M. Maerefat, and K. Hooman, "Estimation of heat flux bifurcation at the heated boundary of a porous medium using a pore-scale numerical simulation," *International Journal of Thermal Sciences*, vol. 54, no. 0, pp. 109–118, 2012.

[148] X.-L. Ouyang, P.-X. Jiang, and R.-N. Xu, "Thermal boundary conditions of local thermal non-equilibrium model for convection heat transfer in porous media," *International Journal of Heat and Mass Transfer*, vol. 60, pp. 31–40, 2013.

[149] L. Thomas, "Elliptic problems in linear differential equations over a network: Watson scientific computing laboratory," *Columbia Univ., NY*, 1949.

[150] B. Adcock, "Univariate modified fourier methods for second order boundary value problems," *BIT Numerical Mathematics*, vol. 49, no. 2, pp. 249–280, 2009.

[151] G. Strang, "On the construction and comparison of difference schemes," *SIAM Journal on Numerical Analysis*, vol. 5, no. 3, pp. 506–517, 1968.

[152] D. W. Peaceman and J. H. H. Rachford, "The numerical solution of parabolic and elliptic differential equations," *Journal of the Society for Industrial and Applied Mathematics*, vol. 3, no. 1, pp. 28–41, 1955.

[153] J. Douglas, Jim and J. Rachford, H. H., "On the numerical solution of heat conduction problems in two and three space variables," *Transactions of the American Mathematical Society*, vol. 82, no. 2, pp. 421–439, 1956.

[154] R. Fletcher, *Practical methods of optimization*. John Wiley and Sons, 2013.

[155] M. Awad, "Heat transfer for laminar thermally developing flow in parallel-plates using the asymptotic method," in *Thermal Issues in Emerging Technologies Theory and Applications (ThETA), 2010 3rd International Conference on*, pp. 371–387, IEEE, 2010.

[156] A. Zukauskas and R. Ulinskas, "Efficiency parameters for heat transfer in tube banks," *Heat Transfer Engineering*, vol. 6, no. 1, pp. 19–25, 1985.

[157] W. A. Khan, *Modeling of fluid flow and heat transfer for optimization of pin-fin heat sinks*. Thesis, University of Waterloo, 2004.

[158] P.-S. Lee, S. V. Garimella, and D. Liu, "Investigation of heat transfer in rectangular microchannels," *International Journal of Heat and Mass Transfer*, vol. 48, no. 9, pp. 1688–1704, 2005.

[159] M. Rizzi, *An Experimental Study of Pin Fin Heat Sinks and Determination of End Wall Heat Transfer*. University of California, Los Angeles, 2002.

[160] M. Rizzi and I. Catton, "An experimental study of pin fin heat sinks and determination of end wall heat transfer," in *ASME 2003 Heat Transfer Summer Conference*, pp. 445–452, American Society of Mechanical Engineers, 2003.

[161] J. D. Bagley, *The behavior of adaptive systems which employ genetic and correlation algorithms*. PhD thesis, University of Michigan, 1967.

[162] K. A. De Jong, *Analysis of the behavior of a class of genetic adaptive systems*. PhD thesis, University of Michigan, 1975.

[163] J. J. Grefenstette, "Optimization of control parameters for genetic algorithms," *Systems, Man and Cybernetics, IEEE Transactions on*, vol. 16, no. 1, pp. 122–128, 1986.

[164] J. E. Baker, "Reducing bias and inefficiency in the selection algorithm," in *Proceedings of the second international conference on genetic algorithms*, pp. 14–21, 1987.

[165] D. E. Goldberg and M. P. Samtani, "Engineering optimization via genetic algorithm," in *Electronic Computation*, pp. 471–482, ASCE, 1986.

[166] D. Ashlock, *Evolutionary computation for modeling and optimization*. Springer Science and Business Media, 2006.

[167] N. Queipo, R. Devarakonda, and J. A. C. Humphrey, "Genetic algorithms for thermosciences research: application to the optimized cooling of electronic components," *International Journal of Heat and Mass Transfer*, vol. 37, no. 6, pp. 893–908, 1994.

[168] S. Manivannan, P. S. Devi, and R. Arumugam, "Optimization of flat plate heat sink using genetic algorithm," in *Electrical Energy Systems (ICEES), 2011 1st International Conference on*, pp. 78–81, IEEE, 2011.

[169] S. Mohsin, A. Maqbool, and W. A. Khan, "Optimization of cylindrical pin-fin heat sinks using genetic algorithms," *IEEE Trans. Compon. Packag. Technol. IEEE Transactions on Components and Packaging Technologies*, vol. 32, no. 1, pp. 44–52, 2009.

[170] S. Ndao, Y. Peles, and M. K. Jensen, "Multi-objective thermal design optimization and comparative analysis of electronics cooling technologies," *International Journal of Heat and Mass Transfer*, vol. 52, no. 19-20, pp. 4317–4326, 2009. 483FO Times Cited:2 Cited References Count:45.

[171] G. Fabbri, "A genetic algorithm for fin profile optimization," *International Journal of Heat and Mass Transfer*, vol. 40, no. 9, pp. 2165–2172, 1997.

[172] G. Fabbri, "Heat transfer optimization in corrugated wall channels," *International Journal of Heat and Mass Transfer*, vol. 43, no. 23, pp. 4299–4310, 2000.

[173] Z. Jian-hui, Y. Chun-xin, and Z. Li-na, "Minimizing the entropy generation rate of the plate-finned heat sinks using computational fluid dynamics and combined optimization," *Applied Thermal Engineering*, vol. 29, no. 8-9, pp. 1872–1879, 2009.

[174] M. Tye-Gingras and L. Gosselin, "Thermal resistance minimization of a fin-and-porous-medium heat sink with evolutionary algorithms," *Numerical Heat Transfer, Part A: Applications*, vol. 54, no. 4, pp. 349–366, 2008.

[175] P. Wildi-Tremblay and L. Gosselin, "Layered porous media architecture for maximal cooling," *International Journal of Heat and Mass Transfer*, vol. 50, no. 34, pp. 464–478, 2007.

[176] M. Mitchell, *An introduction to genetic algorithms*. MIT press, 1998.

[177] MATLAB, "version 8.6 (r2015b)," 2015.

[178] A. Bejan, *Entropy generation minimization: the method of thermodynamic optimization of finite-size systems and finite-time processes*. CRC press, 1995.

[179] N. Govindha Rasu, K. Velusamy, T. Sundararajan, and P. Chellapandi, "Simultaneous development of flow and temperature fields in wire-wrapped fuel pin bundles of sodium cooled fast reactor," *Nuclear Engineering and Design*, vol. 267, pp. 44–60, 2014.